# Development of fast and radiation hard Monolithic Active Pixel Sensors (MAPS) optimized for open charm meson detection >with the CBM - vertex detector

Michael Deveaux

# Development of fast and radiation hard Monolithic Active Pixel Sensors (MAPS) optimized for open charm meson detection with the CBM - vertex detector

**Dissertation zur Erlangung des Doktorgrades**
der Naturwissenschaften

vorgelegt beim Fachbereich Physik
der Johann Wolfgang Goethe - Universität
in Frankfurt am Main

**Thèse présentée pour obtenir le grade de Docteur**
de l'Université Louis Pasteur Strasbourg 1

Discipline: Physique

**Michael Deveaux**
aus/né à Idar-Oberstein

Frankfurt/Strasbourg (2007)
(D30)

Revision: 1.04

# Contents

Contents

*Contents*

# Acknowledgments

*Contents*

# Sommaire français

## Contexte général

L'expérience CBM (*Compressed Baryonic Matter*) [3], qui sera installée auprès du futur accélérateur international FAIR (*Facility for Antiproton and Ion Research*) à Darmstadt[1], explorera les propriétés de la matière nucléaire avec des énergies de faisceau comprises entre 10 et 40 $AGeV$. Cette gamme d'énergie a été choisie pour permettre l'étude de collisions d'ions lourds à la plus haute densité de baryons possible accessible en laboratoire (jusqu'à 10 fois la densité de la matière nucléaire ordinaire). L'expérience CBM sera donc capable d'explorer le diagramme de phase de la matière nucléaire dans la région de haute densité baryonique, jusqu'ici peu connue tant du point de vue expérimental que théorique.

Les principaux objectifs de cette expérience seront la recherche d'un changement de phase entre la matière hadronique et le plasma de quarks et de gluons (QGP), la mise en évidence du point critique QCD, la recherche de signatures d'une restauration de la symétrie chirale, et l'étude de l'équation d'état de la matière nucléaire à haute densité baryonique. Une connaissance accrue de la matière nucléaire à de telles densités baryoniques permettra également une meilleure compréhension des objets astrophysiques massifs comme l'intérieur des étoiles à neutrons.

L'étude de la production de mésons charmés "ouverts[1]" ($D^+$, $D^-$, $D^0$), est l'un des principaux thèmes de physique de l'expérience CBM. Cet axe de recherche est principalement motivé par le fait que la production et la propagation du charme dans les collisions d'ions lourds sont sensibles aux effets de haute densité et aux transitions de phase. Cette sensibilité devrait être particulièrement poussée aux énergies de *FAIR* (proches du seuil cinématique de production).

La théorie prévoit que la formation du plasma QGP conduit à une forte suppression de la production de mésons charmés "fermés". À ce titre, une suppression de la production de mésons $J/\psi$, compatible avec l'apparition du QGP a déjà été observée. Néanmoins, des interprétations alternatives existent. L'étude des mésons-D dans CBM constituera un complément important de mesures sur les mésons "charmés fermés", et facilitera l'interprétation des résultats obtenus antérieurement.

## Problématique

Aux énergies du FAIR, les mésons charmés sont rares car la production a lieu au voisinage du seuil cinématique. De plus la durée de vie de ces particules est très courte: $\beta\gamma c\tau$ est typicment de l'ordre de $\sim$ 100 - 500 $\mu m$. Ceci impose des contraintes fortes sur le système de détection. Celui-ci doit être capable d'identifier les rares mésons $D$ parmi un bruit de fond très important de particules chargées. La nécessité de mesurer la position des vertex secondaires provenant de la désintégration des mésons D avec une résolution meilleure que $\sim$ 100 $\mu m$ constituera un défi technologique majeur de ce projet. En effet, ces événements comporteront une très grande multiplicité en traces (jusqu'à quelques $\sim 10^9$ traces/seconde).

---

[1]On entend par méson charmé ouvert, un méson comportant un quark de valence $c$ et un quark léger et par méson charmé "fermé", un méson comportant deux quarks charmés.

*Contents*

Aucun détecteur à pixels actuel ne remplit les conditions requises à la fois en termes de radio-résistance et de résolution. Pour résoudre ce problème, il est proposé de développer et d'utiliser des capteurs de type MAPS (*Monolithic Active Pixel Sensors*). En effet, ces nouveaux détecteurs semblent susceptibles de répondre aux contraintes de résolution spatiale et dans une certaine mesure de radio-résistance, et constituent aujourd'hui le meilleur compromis technologique disponible.

Le but principal du travail de thèse a été d'explorer la faisabilité de la réalisation d'un détecteur de vertex pour CBM fondé sur la technologie MAPS. Répondre à cette problématique a été compliqué par le fait que le concept général de l'expérience CBM était en pleine évolution. Le cahier des charges demeure donc préliminaire. Par ailleurs, en tant que technologie relativement récente, les performances ultimes des MAPS restaient à définir. Ce travail consistait donc parallèlement à explorer la technologie des MAPS elle-même et à préciser le design du détecteur de vertex de l'expérience CBM.

La comparaison du cahier des charges du détecteur de vertex défini par le CDR (*Conceptual Design Report*) de CBM et des performances établies des MAPS a permis d'identifier deux paramètres critiques: la vitesse de lecture et la radio-résistance. La vitesse de lecture initialement demandée était de l'ordre de quelques dizaines de nanosecondes alors que les MAPS conventionnels atteignent une vitesse de l'ordre de quelques millisecondes. D'autre part, la radio-résistance établie des MAPS était légèrement inférieure à $10^{12}$ $n_{eq}/cm^2$ tandis que la dose annuelle attendue est de l'ordre de $10^{15}$ $n_{eq}/cm^2$ pour une luminosité nominale. Enfin, une estimation globale du budget de matière tenant compte du support mécanique, de l'alimentation, du système de refroidissement restait à définir.

**Approches**

Une simple optimisation des capteurs actuels en vue de satisfaire le cahier des charges du concept de détecteur CBM apparaît insuffisante au regard des performances exsistantes des MAPS. Une révision globale de l'approche initiale, incluant une estimation réaliste des performances accessibles, a du être entreprise. Celle-ci comprenait un ajustement des différentes possibilités et limites de la technologie elle-même et une optimisation de la géométrie et de la reconstruction de traces.

Une estimation des performances de détection des mésons $D^0$ a été utilisée comme critère principal de comparaison. Cette particule est en effet considérée comme particulièrement difficile à reconstruire.

L'étude sous-jacente à la thèse est consacrée également aux questions de radio-résistance et de temps de vie des MAPS dans l'environnement du détecteur de vertex de CBM. Ce travail s'est inscrit dans le cadre d'un programme de recherche dédié conduit par l'IPHC (Strasbourg), le GSI (Darmstadt) et l'université de Frankfort. Des simulations spécifiques ont été réalisées afin d'estimer les doses ionisantes et non ionisantes attendues.

Les aspects concernant l'amélioration de la vitesse de lecture des MAPS ont été couverts par un travail séparé dans le cadre la collaboration CBM. Ce document ne présente donc qu'une synthèse des travaux réalisés dans ce domaine. Toutefois, ces résultats ainsi que leurs conséquences sur le design du détecteur sont discutés en détail.

À partir de ces études, un design préliminaire d'un plan de capteurs intégré dans le détecteur a été réalisé afin d'obtenir une estimation réaliste du budget de matière du détecteur de vertex. Ce modèle a ensuite été introduit dans le programme global de simulation de CBM. Enfin, des simulations de physique tenant compte de la durée de vie limitée des capteurs MAPS ont permis, d'une part, d'améliorer la géométrie globale du détecteur de vertex de CBM et, d'autre

part, de démontrer la capacité d'un tel détecteur à reconstruire un nombre suffisant de mésons $D^0$.

### Résultats et performances de la technologie

**Radio-résistance:** Le travail a porté sur une étude de la radio-résistance de différentes architectures de pixels portés par sept générations successives de micro-circuits. Celle-ci a permis d'identifier la plupart des mécanismes, jusqu'ici mal connus, détériorant les performances des capteurs de cette technologie. De nouvelles architectures conduisant à une amélioration de la radio-résistance ont été proposées, réalisées et testées. Une résistance aux rayonnements ionisant excédant 1 $MRad$ a ainsi pu être démontrée. Les capteurs de prochaine génération devraient encore améliorer ces performances.

La résistance aux rayonnements non-ionisants a également été portée jusqu'à $2 \times 10^{12}$ $n_{eq}/cm^2$. Certaines approches devraient permettre d'atteindre une radio-résistance de l'ordre de $10^{13}$ $n_{eq}/cm^2$, mais nécessitent le développement de prototypes exploratoires.

Comme les dommages causés par les interactions non-ionisantes affectent le principe même de fonctionnement des MAPS, cette valeur de $10^{13}$ $n_{eq}/cm^2$ constitue probablement une limite ultime de la radio-résistance de cette technologie. Elle devrait donc imposer une limite du temps de vie du détecteur de vertex de CBM.

D'après les simulations réalisées dans le cadre de cette thèse, une dose annuelle de $10^{15}$ $n_{eq}/cm^2$ correspond à une luminosité nominale de l'expérience. Il est peu probable que les MAPS puissent un jour supporter de telles doses. Il est donc proposé de remplacer régulièrement les plans de capteurs les plus irradiés. En effet, puisque les plans sont aisément accessibles de par la géométrie en cible fixe de l'expérience, le temps de maintenance et de remplacement devrait rester relativement bas. Les coûts de cette opération demeurent réduits du fait de la faible surface totale du détecteur et du fait que les MAPS sont compatibles avec les processus CMOS standards. On peut ainsi entrevoir une production industrielle massive et relativement peu onéreuse de capteurs. D'après les simulations discutées plus loin, un taux de remplacement modeste devraient permettre de maintenir une détection efficace des mésons charmés ouverts et donc de réaliser pleinement le programme de physique de CBM.

**Vitesse de lecture et résolution temporelle :** La stratégie envisagée pour améliorer la résolution temporelle des MAPS est discutée en détail. Cette étude permet de conclure que les MAPS ne peuvent aujourd'hui atteindre une résolution temporelle meilleure que $\sim 10$ $\mu s$. Une séparation entre les collisions nucléaires successives ne peut être réalisée au delà d'un taux de $10^5$ collisions par seconde. Ce chiffre correspond à 1 % du taux de collision nominal de l'expérience CBM. À la luminosité maximale, un empilement allant jusqu'à 100 collisions, produisant quelques $10^4$ traces chargées, est attendu pour chaque cycle de lecture. Grace à l'excellente granularité des MAPS, le taux d'occupation restera raisonnablement bas dans ces conditions. Toutefois, la reconstruction des traces serait alors significativement compliquée. La faisabilité d'une telle reconstruction est à l'étude.

Par ailleurs, cette contrainte forte sur la résolution temporelle impose une surface active des capteurs reduite, conduisant à la nécessité d'avoir des plans double-couches.

**Design des plans du détecteur de vertex et budget de matière :** Les deux contraintes majeures sur le design du détecteur proviennent de cette nécessité de disposer de plans double-couches et du besoin d'opérer dans le vide. Une des solutions proposées est de disposer les deux couches de

chaque plan de part et d'autre d'un support constitué de fibres de carbone. Ce support pourrait également comporter des micro-tubes permettant la circulation d'un liquide de refroidissement, celui-ci étant probablement nécessaire pour évacuer la chaleur dissipée. Un design préliminaire a donc été réalisé fournissant ainsi une estimation du budgert de matière. Il a été démontré que le budget de matière de chaque plan pourrait être maintenu en dessous de quelques pour-mille de longueur de radiation.

### Simulations du détecteur de vertex de CBM

**Modèle pour la simulation :**    Les paramètres clefs obtenus à partir des études précédentes ont été intégrés dans la simulation complète du détecteur, comprenant trois plans de MAPS. La position et la géométrie de ces couches ont été optimisées de manière systématique dans le but d'obtenir un nombre maximal de mésons charmés reconstruits tout au long de la durée de vie du détecteur. Cette dernière dépend en effet de la dose reçue qui dépend elle-même fortement de la géométrie.

La simulation comprenait un ajustement de trace réaliste mais un algorithme de recherche de trace idéal. Ce dernier point ne se justifie que pour un faisceau à basse luminosité, où l'empilement des événements reste faible.

**Résultats:**    Ce travail a permis de démontrer qu'en modifiant substantiellement la géométrie initiallement prévue par la collaboration, on pouvait améliorer notablement les performances de la reconstruction. Pour cela, la distance entre la cible et les plans du détecteur a été augmentée de 5 à 10 $cm$. Ce changement réduit légèrement les performances de détection mais augmente significativement la durée de vie des capteurs.

La simulation, fondée sur une statistique importante ($2.4 \times 10^7$ collisions centrales), a permis de démontrer qu'un détecteur de vertex équipé de MAPS pouvait permettre de reconstruire quelques $10^4$ $D^0$ avec une significance supérieure à $Sign. = 130^{+30}_{-40}$ et un rapport signal-à-bruit (S/B) $S/B = 2.0$ ($> 0.53$ avec une probabilité de 95 % ), en utilisant à la fois le trajectographe, le détecteur de vertex et d'autres parties du détecteur comme le système de mesure de temps de vol.

### Conclusion et perspectives

Ce travail a permis de démontrer que l'utilisation de la technologie des MAPS pour la détection des mésons charmés ouverts dans les collisions d'ions lourds (Au+Au, $\gtrsim 25$ $AGeV$) est viable. Quelques $10^4$ mésons $D^0$ peuvent être reconstruits lors de la vie complète d'un détecteur. Ces performances satisfont le cahier des charges défini par la collaboration CBM.

Cette conclusion est valide sous la condition que le détecteur est opéré dans les conditions adaptées et définies par ce travail, ce qui implique en particulier la présence d'un système de refroidissement. De plus, une réduction du taux de collisions d'au moins un ordre de grandeur par rapport au taux nominal est recommandée pour les mesures touchants à la physique des mésons charmés ouverts. Il a cependant été démontré que cette réduction de la sensibilité statistique est compensée par une excellente rejection du bruit de fond.

Certaines incertitudes demeurent sur le nombre absolu de remplacements du détecteur de vertex nécessaires pour assurer le succès du programme de physique de CBM. Celles-ci proviennent essentiellement de la prédiction de la multiplicité de la production de mésons charmés "ouverts", des incertitudes concernant la radio-résistance (et donc de la durée de vie des détecteurs) et

de la vitesse de lecture des capteurs des prochaines générations. Les prochaines études devront s'attacher à réduire ces incertitudes.

*Contents*

16

# Deutsche Zusammenfassung

## Motivation

Das Compressed Baryonic Matter Experiment (CBM) ist ein Fixed-Target-Schwerionenexperiment, das zurzeit am zukünftigen FAIR-Beschleuniger in Darmstadt vorbereitet wird. Es soll die Eigenschaften von Kernmaterie bei Schwerionenstößen mit Strahlenergien zwischen 10 und 40 $AGeV$ untersuchen. In diesem Energiebereich werden voraussichtlich die höchsten experimentell zugänglichen Baryonendichten erreicht, die diejenigen der Atomkerne um bis zu einem Faktor 10 übersteigen können. Das ermöglicht es dem CBM-Experiment, das Phasendiagram der nuklearen Materie im bisher experimentell und theoretisch weitgehend unerforschten Bereich hoher Baryonendichten zu untersuchen.

Zu den Aufgaben des Experiments gehören die Suche nach der postulierten Phasengrenze zwischen hadronischer und partonischer Materie und dem kritischen Punkt der QCD, die Suche nach Hinweisen für eine Wiederherstellung der chiralen Symmetrie sowie die Vermessung des Phasendiagrams bei hoher Baryonendichte. Die hierdurch gewonnenen Informationen über das Verhalten von Kernmaterie unter extremen Bedingungen ist nicht zuletzt für ein tieferes Verständnis der Astronomie, z.B. der Physik von Neutronensternen von großer Bedeutung.
Eines der Hauptziele des CBM-Experiments ist die Untersuchung von Open-Charm-Mesonen ($D^+$, $D^-$, $D^0$), die aus einem Charm-Quark und einem leichten Quark aufgebaut sind. Diese sind deshalb von Bedeutung, weil ihre Produktion und Ausbreitung von der Dichte und dem eventuellen Phasenübergang des Feuerballs beeinflusst werden. Im Energiebereicht von FAIR, der nahe der minimalen Energie für die Erzeugung des Charm-Quarks liegt, ist dieser Einfluss besonders stark.

Für den Fall einer Ausbildung von Quark Gluon Plasma wird eine starke Unterdrückung der Produktion von Hidden-Charm-Mesonen vorhergesagt. Eine Unterdrückung der Produktion of $J/\Psi$-Mesonen, die mit dem Auftreten von QGP kompatibel ist wurde kürzlich beobachtet. Allerdings müssen existierende alternative Erklärungsmodelle ausgeschlossen werden. Die Untersuchung von $D$-Mesonen in CBM wird die Messungen von Hidden-Charm-Mesonen ergänzen und die Interpretation ihrer Resultate erleichtern.

## Fragestellung dieser Arbeit

Da die Strahlenergie des FAIR-Beschleunigers die minimale Energie für die Erzeugung von Open-Charm-Mesonen nur wenig übersteigt, sind die Erzeugungsquerschnitte sehr gering. Da außerdem ist die Lebenszeit der Mesonen außerordentlich kurz ist, $\beta\gamma c\tau$ im Laborsystem beträgt typischerweise 100-500 $\mu m$, stellt ihre Rekonstruktion enorme Anforderungen an das Detektorsystem. Dieses muss die seltenen Proben aus einer Vielzahl von Spuren geladener Teilchen filtern, wofür eine Rekonstruktion des Zerfallsvertex der D-Mesonen mit einer Präzision von besser als 100 $\mu m$ benötigt wird.

Diese präzise Rekonstruktion von Zerfallsvertices in einem Strahlenfeld mit bis zu einigen $10^9$ Spuren pro Sekunde ist eine beispiellose technologische Herausforderung. Etablierte Pixeldetektoren erreichen entweder nicht die notwendige Strahlenhärte oder nicht die notwendige Ortsauflösung um für den Micro Vertex Detector (MVD) von CBM in Frage zu kommen. Um

diesen Zielkonflikt zu überwinden, wurde der Einsatz von CMOS-Monolithic Active Pixel Sensoren (MAPS) vorgeschlagen. Diese neue Detektortechnologie, die gleichzeitig über die notwendige Ortsauflösung und gute Strahlenhärte verfügt, bietet mutmaßlich den besten heute erreichbaren technischen Kompromiss zwischen beiden Parametern.

Das Ziel dieser Arbeit besteht darin, die Machbarkeit der Open-Charm-Rekonstruktion mit einem MAPS basierten CBM-Vertexdetektor zu prüfen. Diese Aufgabe wurde dadurch erschwert, dass sich das CBM-Experiment noch in der frühen Planungsphase befand und die genauen Anforderungen an den Vertexdetektor nicht abschließend definiert waren. Gleichzeitig waren die Fähigkeiten der neu entwickelten MAPS noch weitgehend unerforscht. Eine Machbarkeitsstudie musste sich daher gleichzeitig mit der Technologie der Detektoren und dem globalen Aufbau des CBM-Experiments befassen.

Vergleicht man die vorläufigen Anforderungen[1] an einen Vertexdetektor, der bei der vollen Kollisionsrate von CBM betrieben werden soll, mit den Fähigkeiten der MAPS-Detektoren, erscheinen ihre die Zeitauflösung und Strahlenhärte als besonders kritische Parameter. Während eine Zeitauflösung in der Größenordnung weniger zehn Nanosekunden benötigt wird, um einzelne Stöße zeitlich zu trennen, liegt die Zeitauflösung klassischer MAPS in der Größenordnung weniger Millisekunden. Die Strahlenhärte dieser frühen Prototypen lag etwas unter $10^{12}$ $n_{eq}/cm^2$ während eine Dosis von bis zu $10^{15}$ $n_{eq}/cm^2$ pro Jahr zu erwarten ist. Die Anforderungen an die Ortsauflösung und die Dicke der Detektoren erschienen hingegen weniger kritisch.

**Der Ansatz dieser Arbeit**

Eine Optimierung einzelner Komponenten erschien nicht hinreichend, um die Kluft zwischen dem Anspruch des Detektorkonzepts von CBM und den Möglichkeiten der Detektortechnik zu überwinden. Deshalb wurde das globale Messkonzept von CBM für Open-Charm-Mesonen im Hinblick auf die Leistungsfähigkeit aktueller und absehbarer Detektoren einer Revision unterzogen. Hierbei wurde besonderes Augenmerk auf eine Abstimmung der Detektortechnologie, der Detektorgeometrie und der Datenanalyse gelegt. Als Maßstab für den Erfolg des überarbeiteten Messkonzeptes wurde die Fähigkeit von CBM zur Rekonstruktion von $D^0$-Mesonen gewählt. Diese Teilchen galt wegen seiner kurzen Lebensdauer als besonders schwierig zu rekonstruieren.

Ein Schwerpunkt dieser Arbeit wurde auf Fragen der Strahlenhärte gelegt. Diese Studien, die in ein eigens gestartetes F&E-Programm des IPHC (Strasbourg), der GSI (Darmstadt) und der Johann-Wolfgang-Goethe Universität (Frankfurt) eingebettet waren, ermittelten erstmals umfassend die Strahlenhärte von MAPS. Zusätzlich wurden die in CBM zu erwartenden Strahlendosen simuliert.

Die Verbesserung der Zeitauflösung von MAPS wurde in einer unabhängigen Arbeit innerhalb der CBM-Kollaboration abgedeckt. Die dort erzielten Ergebnisse werden zusammengefasst ihr Einfluss auf das Design und die Messstrategie von CBM wird diskutiert.

Ein vorläufiges Design für die Integration individueller MAPS-Chips in eine Detektorebene wurde entwickelt um sinnvolle Annahmen über das Materialbudget des Vertexdetektors zu erhalten.

Ein aus den technischen Studien abgeleitetes Simulationsmodell wurde in den CBM-Simulation-Framework übernommen. Physiksimulationen unter Berücksichtigung der begrenzten Lebensdauer der MAPS-Chips wurden durchgeführt, um die Geometrie des Vertexdetektors zu verbessern und seine Fähigkeiten zur Messung einer ausreichenden Zahl von $D^0$-Mesonen zu belegen.

**Ergebnisse der technischen Studien**

**Strahlenhärte**  Im Rahmen dieser Arbeit, wurde die Strahlenhärte zahlreicher verschiedener MAPS-pixel studiert, die in sieben verschiedene Prototypen integriert waren. Es war möglich, die meisten der bis dahin praktisch unbekannten Strahlenschadensmechanismen in der MAPS-Technik aufzuklären. Pixel mit verbesserter Strahlenhärte wurden vorgeschlagen und getestet. Mit diesen konnte eine Strahlenhärte von MAPS gegen ionisierende Dosen von 1 $MRad$ nachgewiesen werden. Es wird erwartet, dass diese Zahl mit zukünftigen Chips noch deutlich übertroffen werden kann.

Die Strahlenhärte gegen nicht ionisierende Dosen konnte auf wenige $2 \times 10^{12}$ $n_{eq}/cm^2$ gesteigert werden. Konzepte für Detektoren mit einer Strahlenhärte gegen nicht ionisierende Dosen von $10^{13}$ $n_{eq}/cm^2$ wurden erarbeitet. Sie müssen sich jedoch noch in der Praxis bewähren. Da die Strahlenschäden durch nicht ionisierende Strahlung die Funktion von MAPS fundamental beeinflusst, ist es wahrscheinlich, dass dieser Wert gleichzeitig die maximale Strahlenhärte von MAPS darstellt. Sie dürfte daher die Lebenserwartung des CBM-Vertexdetektors begrenzen.

Den durchgeführten Simulationen der jährlichen Strahlendosis im CBM-Vertexdetektor zu folge, wird diese Dosis bei $\sim 10^{15}$ $n_{eq}/cm^2$ liegen, sofern der Detektor bei seiner maximalen Kollisionsrate betrieben wird. Trotz der erreichten und noch zu erwartenden technischen Fortschritte dürfte die Lebenserwartung eines auf MAPS basierender Vertexdetektor unter diesen Bedingungen kaum die Laufzeit des CBM-Experiments erreichen. Es wird daher vorgeschlagen, Teile des MVD regelmäßig auszutauschen. Dieser Ansatz wird durch die Fixed-Target-Geometrie von CBM begünstigt, die einen einfachen Zugang zum Detektor erlaubt. Die entstehenden Kosten sollten sich wegen der geringen Oberfläche des Vertexdetektors, sowie der Option, MAPS in günstiger industrieller Massenproduktion herzustellen, im Rahmen halten. Ausgehend von den Ergebnissen der noch zu erläuternden Physiksimulationen sollten wenige Ersatzdetektoren ausreichen, um die physikalischen Ziele von CBM zu erreichen.

**Zeitauflösung und Auslesestrategie der MAPS**  Die Strategie der F&E-Programmes zur Verbesserung der Zeitauslösung der MAPS wird diskutiert und einige Schlüsselergebnisse werden gezeigt. Es wird aufgezeigt, dass mit heutigen CMOS-Prozessen keine MAPS mit einer besseren Zeitauflösung als $\sim 10$ $\mu s$ herzustellen sind. Einzelne Kollisionen können deshalb nur für Kollisionsraten bis $10^5$ Kollisionen pro Sekunde aufgelöst werden, was 1 % der vorgesehenen Rate des CBM-Experimentes entspricht. Sollte die vorgesehene Rate verwendung finden, muss mit einer Überlagerung der Spuren von bis zu 100 Kollisionen im Vertexdetektor gerechnet werden. Wegen der sehr hohen Granulatität der MAPS wird der Anteil der getroffenen Pixel auch unter diesen Bedingungen akzeptabel bleiben. Die Spurrekonstruktion ist unter diesen Umständen jedoch erschwert; ihre Machbarkeit wird noch untersucht.

Die Notwendigkeit, MAPS mit einer sehr guten Zeitauflösung zu bauen hat auch einen Einfluss auf den mechanischen Aufbau des Vertexdetektors, da die aktive Oberfläche von sehr schnellen MAPS aus technischen Gründen auf etwa die Hälfte der Chipoberfläche reduziert werden muss. Es werden daher in jeder Detektorebene zwei sich ergänzende Detektorschichten benötigt.

**Aufbau der Ebenen des Vertexdetektors und Materialbudget**  Die Notwendigkeit, pro Detektorebene zwei Ebenen mit MAPS-Chips im Vakuum zu betreiben, wurde als zentrale Anforderung an das Design der Detektorebenen betrachtet. Es wird vorgeschlagen, die MAPS-Chips auf beiden Seiten einer Schicht von Mikroröhren zu installieren, die gleichzeitig der mechanischen Stabilisierung und der Flüssigkeitskühlung der Detektorebene dienen. Ein vorläufiges Design, das mittelfristig einer fachmännischen Überarbeitung bedarf, wird diskutiert und zur Abschätzung

des Materialbudgets des Vertexdetektors herangezogen. Es wird gezeigt, dass die Dicke einer Detektorebene auf wenige 0.1 % $X_0$ (Strahlungslängen) gesenkt werden kann.

## Simulation der Empfindlichkeit des CBM-Vertexdetektors

**Simulationsmodel** Auf Basis der Ergebnisse der technischen Studien wurde ein Simulationsmodell eines Vertexdetektors mit drei Detektorebenen erstellt. Die genaue Position und Geometrie der Ebenen wurde systematisch variiert um die Zahl der $D^0$-Mesonen, die ein Vertexdetektor innerhalb seiner Lebenserwartung rekonstruieren kann, zu maximieren. Diese Lebenszeit hängt von den Strahlendosen im Detektor ab, die ihrerseits sehr stark von den Details der Geometrie beeinflusst werden.

Um eine gute Lösung zu finden, wurde für verschiedene Detektorgeometrien zunächst die individuelle Strahlendosis simuliert und nachfolgend die Rekonstruktionseffizienz des Systems für $D^0$-Mesonen abgeschätzt. Die Kombination beider Ergebnisse erlaubte es, die Zahl der Mesonen zu ermitteln, die das System in seiner Lebenszeit rekonstruieren kann.

Um einen ersten quantitativen Eindruck bezüglich der Machbarkeit der $D^0$-Rekonstruktion zu gewinnen, wurde diese anhand der mutmaßlich besten Detektorgeometrie mit sehr hoher Statistik ($2.4 \times 10^7$ zentrale Kollisionen äquivalent) simuliert.

**Resultate der Simulation** Die Simulation, die auf Au+Au-Kollisionen bei einer Strahlenergie von 25 $AGeV$ beruhte, demonstriert die außerordentliche Empfindlichkeit eines MAPS basierten Vertexdetektors. Ihre Ergebnisse legen nahe, dass die Lebenserwartung eines Vertexdetektors ausreichend ist, um $\sim 2.5 \times 10^4$ $D^0$-Mesonen mit einem $S/B = 2.0$ ($> 0.53$ mit einer Wahrscheinlichkeit von 95 %) und einer exzellenten Signifikanz von $Sign. = 130^{+30}_{-40}$ zu detektieren.

## Schlußfolgerungen

Als Schlussfolgerung dieser Arbeit wird festgestellt, dass ein CBM-Vertexdetektor auf der Basis von MAPS innerhalb seiner Lebenszeit einige $10^4$ Open-Charm-Mesonen rekonstruieren kann. Dieses Ergebnis erfüllt die von der CBM-Kollaboration definierten Ansprüche. Dieses Ergebnis gilt für Strahlenergien $\gtrsim 25$ $AGeV$ und unter der Annahme, dass die vorhergesagten Erzeugungsquerschnitte für Open-Charm-Mesonen bis auf kleine Faktoren zutreffend sind. Außerdem müssen die Einsatzbedingungen der MAPS bestimmten Bedingungen genügen. Dies gilt insbesondere für die Betriebstemperatur, die zum Erreichen der nötigen Strahlenhärte $\sim -20\ ^\circ C$ nicht überschreiten sollte. Darüber hinaus wird dringend empfohlen, während der Messung von Open-Charm-Mesonen die sehr hohe nominale Kollisionsrate des Experiments um ein bis zwei Größenordnungen abzusenken um die Überlagerung zu vieler Kollisionen im Vertexdetektor zu unterbinden. Die hierdurch entstehende Absenkung der Messstatistik wird durch die hervorragende Untergrundunterdrückung des Detektors hinreichend ausgeglichen.

Unsicherheiten verbleiben insbesondere wegen der Unsicherheiten in der Vorhersage der Erzeugungsquerschnitte der Open-Charm-Mesonen bei FAIR-Energien, der begrenzten Statistik der Simulationen und schließlich der Notwendigkeit, die technischen Fortschritte der MAPS-Detektoren über mehrere Jahre vorherzusagen. Um diese Unsicherheiten abzusenken, werden weitere Studien empfohlen.

# Introduction

The Compressed Baryonic Matter experiment (CBM) planned at the future international accelerator Facility for Antiproton and Ion Research (FAIR) in Darmstadt will investigate the properties of nuclear matter at beam energies between 10 and 40 $AGeV$. This energy range allows for studying the phase diagram of nuclear matter in the high baryon density region, which is only little explored both experimentally and theoretically. Among the primary goals of CBM are the search for the phase boundary between hadronic matter and the Quark Gluon Plasma (QGP) and the search for the QCD critical point.

The study of open charmed D-mesons ($D^+$, $D^-$, $D^0$) is one of the main physics topics of the CBM experiment. It is motivated by the fact that the production and propagation of charm in heavy-ion collisions is sensitive to the high-density effects and phase transitions. This sensitivity is particularly enhanced at FAIR energies, as open charm is produced close to the kinematic production threshold.

The foreseen detection strategy for open charm mesons in CBM aims to identify the particles by reconstructing their decay vertex.

Because of the short lifetime of those particles (typically only few 100 $\mu m$ in the laboratory frame), the location of their vertex must be measured with an accuracy substantially better than 100 $\mu m$. This imposes strong constraints on the design of the vertex detector. The latter must be highly granular to provide a very good spatial resolution, very close to the interaction point and very thin in order to reduce multiple scattering effects. Moreover, because of the low D-meson production multiplicities, the vertex detector must be very fast to operate at high collision rates required for particle production, and sufficiently radiation hard to cope with the very high particle flux inherent to the proximity of the target.

Since usual pixel technologies do not provide a satisfactory trade-off between these antagonistic requirements, the adequacy of CMOS Monolithic Active Pixel Sensors (MAPS) was investigated. The objective of this thesis was to demonstrate that these devices could allow to measure a satisfactory amount of $D$-mesons produced in heavy ion collisions.

In order to achieve the required sensitivity of a MAPS based vertex detector, a dedicated R&D aiming to establish and improve the performances of these novel pixel detectors was carried out. It also necessitated the development of a concept allowing to integrate the individual MAPS chips into detector stations and to arrange those stations into an optimized vertex detector geometry. To demonstrate the feasibility of open charm measurements with the proposed design of the vertex detector, detailed simulations were performed.

The R&D work on the MAPS detectors had in particular to answer the question, which radiation tolerance and time resolution could be reached with this technology. To do so it was necessary to study systematically the performances of existing devices and to search for possible improvements. Based on the outcome of this study, the progresses expected for the next 2-3 years had to be predicted.

A particular focus was laid on the issue of radiation tolerance of MAPS detectors, which was for the first time studied and improved in a systematic way. The studies showed in particular that a satisfactory radiation can only be reached if the detectors are operated at low temperatures

$-20\ °C$. Additional constraints came from the the results of the R&D on time resolution, which was done in parallel to this work. It was shown that a significant fraction of the detector chips would host micro-circuits used for signal processing, which are not sensitive.

Based on this input, a concept for the integration of individual chips into a vertex detector station was developed. This concept had to prove that it is possible to operate MAPS in vacuum and to cool them despite of their sizable power dissipation. Moreover, the passive area of a MAPS chip had to be covered by the active area of the neighboring chip. A particular challenge was introduced by the fact that the material budget of the individual station was not allowed to exceed few hundred micrometers in order to avoid multiple scattering effects.

After a solution was found, the detector stations had to be arranged into a vertex detector. The particular challenge was to find a good compromise between the charm tagging abilities of the detector (calling for a small distance between target and detector) and a good detector lifetime (calling for an increase of this distance). Methods for estimating and benchmarking the performances of the different vertex detector geometries considered had to be worked out.

Based on the information obtained, a specific detection concept for reconstructing $D$-mesons with a MAPS based vertex detector was developed. This concept had to consider for the specific strong and weak points of the detector, which are very different from the ones of the hybrid pixel detectors initially considered for the vertex detector. In particular it had to account for the limited radiation hardness and time resolution of MAPS, which do not allow open charm measurements at the full collision rate ($10^7$ collisions/s) of CBM.

The feasibility of $D$-meson detection was studied with a high statistics simulation of $D^0 \rightarrow K+\pi$ assuming an adapted collision rate. It could be shown that the excellent spatial resolution of MAPS dominates the drawbacks originating from moderate statistics. As the $D^0$ particle has a lower lifetime than the $D^\pm$, the study is considered as representative also for those charged mesons.

The thesis is organized as follows:

- In chapter 1, the physics motivation and the detector concept of CBM will be introduced. It will be demonstrated that conventional pixel detectors do not match the requirements of the experiment.

- In chapter 2, the technology of MAPS will be presented. The possibilities and the limits of this technology will be discussed.

- In chapter 3, the strategy and the status of the R&D program on time resolution will be given. The consequences of the need for fast detector chips will be discussed and the potential geometry of future detector chips will be introduced. Based on this information, a design proposal for the individual vertex detector stations will be presented. An estimate on the material budget of the detector station will be derived and discussed.

- In chapters 4-7, the radiation hardness of MAPS, will be addressed. After an introduction into the physics of radiation damage, the methods used for measuring the effects of different types of radiation on the detector will be discussed. The impact of radiation damage on different detector designs will be shown and possible explanations of the effects will be discussed. Moreover, the outcome of the R&D program on improving the radiation hardness of MAPS will be summarized. It will be concluded, that in spite of significant progresses, the optimization of the detector chips alone is not sufficient to operate the vertex detector for a sizable period at the full collision rate of CBM .

- In chapter 8, an improved measurement concept for open charm will be proposed. It will be shown that the excellent secondary vertex resolution, which can be achieved with MAPS, will allow detailed measurements of open charm mesons even with moderated beam intensities, which are in reach of the technology. Moreover, it will be demonstrated that slight

modifications of the vertex detector geometry further reduces the radiation doses without substantially deteriorating the detection efficiency of the system. Results of a GEANT simulation, which validates the newly proposed concept, will be shown and it will be concluded, that the performances of MAPS are sufficient to match the physics goals of CBM.

- In the last chapter, the results obtained in this thesis will be summarized and the main conclusions will be presented.

*Contents*

# 1. The CBM experiment: Physics motivations and detector concept

In this chapter, a brief introduction into the physics goals of the Compressed Baryonic Matter (CBM) experiment is given. The methods used to search for signatures of a phase transition to a deconfined phase of quarks and gluons and a (partial) restoration of the spontaneously broken chiral symmetry by means of heavy ion collisions will be introduced. Experimental challenges will be discussed and the approach used in the CBM experiment will be motivated. It will be shown, in particular, that the measurement of charm production in nuclear collisions will provide valuable information about the nuclear phase diagram.

Hereafter, the global design of the CBM experiment will be shown before focusing on its vertex detector to which this work is dedicated. Starting from its proposed layout it will be demonstrated that the use of highly granular and very thin pixel sensors is mandatory to allow for open charm detection. Moreover, it will be shown that established pixel detector technologies are not sufficient to meet the requirements.

The aim of this work, which is studying the feasibility of using Monolithic Active Pixel Sensors as technology for the CBM vertex detector, will be introduced.

## 1.1. The physics of the CBM experiment

### 1.1.1. Motivation

Today's knowledge of the strong interaction is still insufficient to predict the collective properties of strong interacting many body systems. This is in particular true if the many body systems are set out to extreme conditions for example in terms of temperature and pressure.

The ground state of nuclear matter, the atomic nuclei, is understood as a so called liquid phase of nuclear matter. At a given temperature, the binding forces between the nucleons inside the nuclei are insufficient to sustain the stability of the nuclei and therefore the protons and neutrons escape to a gaseous phase, the so called hadron gas.

The CBM experiment addresses a phase transition predicted by QCD for temperatures far above the one required for evaporating nuclei. It is the phase transition from hadronic gas to the so-called Quark Gluon Plasma (QGP).

The difference between this hadronic matter and QGP is defined by the occurrence of a deconfinement of quarks. This deconfinement is predicted for extremely high particle densities, which reduces the distances between quarks of neighboring hadrons to values comparable to the ones of the quarks forming a hadron. In this case, the confining "potentials" of the hadrons start to merge, which allows the quarks to move freely in a common "potential"[1].

---

[1]Note that the classical concept of a potential cannot be applied for hadrons formed by light quarks, as it is insufficient to describe the highly relativistic motion of the quarks and the presence of virtual particles. Nevertheless, it allows for an intuitive access to the generation of the QGP and can be used to some extend as an approximation for hadrons formed from quarks with high current mass.
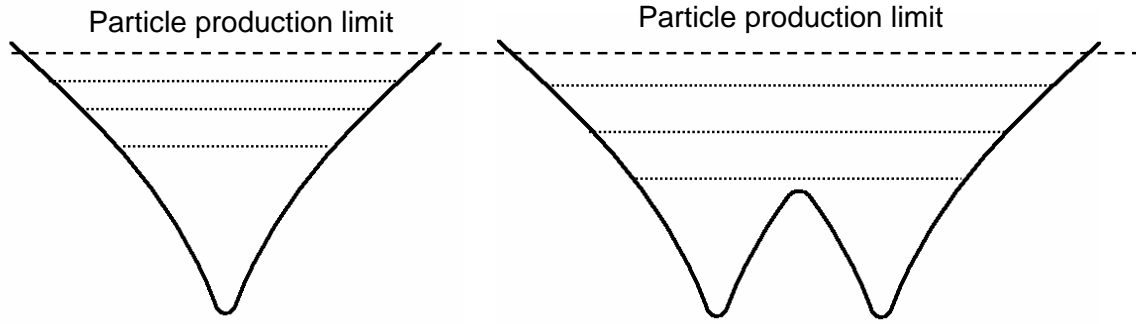
Figure 1.1.: *Illustration on confinement/deconfinement of quarks in a hadron (simplified). Typically, the common potential of the quarks allows for some excited states (left) but no quark can leave the common "potential" without producing a new quark-antiquark pair serving as partner (particle production limit). The situation in the deconfined hadronic matter is shown in the right plot. As the potentials of the different hadrons superpose, an individual quark may move almost freely within this matter. Note that this simplified picture is only valid for static quarks with very high current mass.*

This process is illustrated in figure 1.1, which provides a simplistic picture of the quantum states of a quark in the potential of an ordinary hadron (left). The number of excited states is limited as at some point it becomes energetically possible to create a new quark-antiquark-pair instead of further exciting the existing one. The energy level, at which this particle generation occurs is called *particle production limit*. As the particle production limit is generally below the energy level required to put a quark away from its partner, one cannot observe individual quarks in nature.

In the QGP, the distance between different hadrons becomes small either because of high compression or because of intense particle generation due to high temperature. At some point, the "potential" walls separating the hadrons fall below the particle production limit. As a consequence, quarks may now leave their partner and move towards neighboring hadrons. If the hadron density is sufficiently high, the quarks can be considered as quasi-free particles comparable to the conduction electrons in a metal. At this point, the matter has reached the state of QGP. In analogy to conducting electrons in a metal the deconfined quarks are free in their common potential but cannot leave it without finding the respective partner(s) to form a hadron.

Besides the formation of hadrons from QGP, a second phase transition in the early universe was important for the generation of nuclear matter; the transition from a chirally symmetric phase to a phase where this symmetry is spontaneously broken. This transition proceeded in two steps. The occurrence of a Higgs-field broke this symmetry explicitly and gave rise to the finite current mass of the quarks. In a later phase, when the temperature had dropped to around 200 $MeV$, the quarks and gluons formed spontaneously condensates. This particular ground state of QCD gives rise to the characteristic excitation spectrum of hadronic states with the bulk hadronic states having masses of 1 $GeV/c^2$ or above and only few Goldstone modes with masses well below 1 $GeV/c^2$.

It is considered that this process can be reproduced in the reaction zone of a relativistic heavy
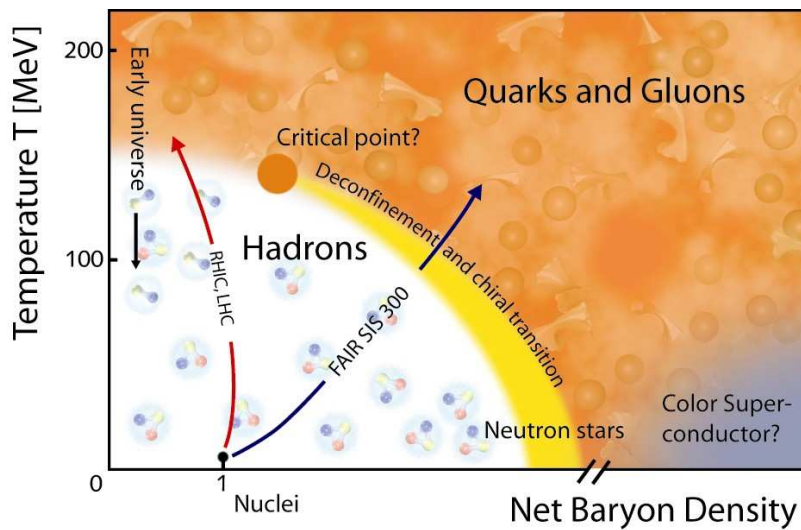
Figure 1.2.:
*The phase diagram of nuclear matter as a function of the temperature and the baryonic density.*

ion collision. It was shown in QCD-calculations on the lattice that the condensates start to melt once the temperature reaches values close to a critical temperature. Technically, already in nuclear matter in the ground state the condensate should be reduced substantially. According to model calculations, the expected value of the chiral condensate decreases linearly with increasing baryonic density. An observable consequence of such dependence is a change of the properties of some mesons. In a chirally symmetric state, the chiral partners of mesons should be degenerated.

### 1.1.2. The phase diagram of hadronic matter

Figure 1.2 illustrates the phase diagram of strongly interacting matter. It shows the phases as a function of the temperature and the net baryon density of the system. The regime of hadron gas is located at low temperatures and net baryon density, the QGP is predicted for high temperatures and densities. The details on the phase transition between both regimes are still under debate. Recent lattice QCD calculations predict a cross over between the phases occurs at high temperatures and low baryon densities. At higher densities, a first order phase transition is predicted. Both regimes are separated by a critical endpoint.

The phase transition to QGP has been addressed by several experiments at CERN-SPS and RHIC. These experiments focused on the region of high temperature and low net baryonic density. The CBM experiment is to complement the existing observations by addressing the region of high baryonic densities. Among the primary goals of the experiment is to find evidences for the existence of a first order phase transition and identifying the critical endpoint. Moreover, CBM aims to find evidences for the predicted restoration of chiral symmetry in the region of high net baryon densities and temperature.

### 1.1.3. Experimental access to the phase diagram

Relativistic heavy ion collisions are used to reach the temperatures and densities required for studying the phase transition to the QGP. The volume of hot and dense matter produced is usually called *fireball*. The fireball reaches the point of maximum density and temperature short after the first impact. After that it cools down by expansion. Although the exact evolution pathway of the fireball in the nuclear matter phase diagram is not directly accessible in experiment, model
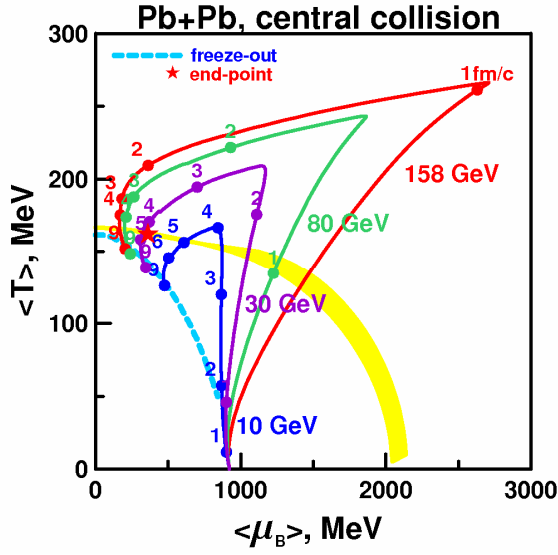
Figure 1.3.:
*Trajectories indicating the evolution of the central region of a heavy ion collision in the QCD phase diagram calculated by a 3-fluid hydrodynamics model. Trajectories for four different beam energies are shown (see labels). The numbers from 1 to 9 refer to time steps in units of $1 fm/c$. This model predicts a crossing of the phase boundary to a deconfined state of quarks and gluons (shown as shaded area) already for beam energies above $10 AGeV$, a regime easily accessible by the CBM experiment. Taken from [3].*

calculations can give some insight into the region of temperature and density reached by heavy ion collisions with a given beam energy and system size (see figure 1.3). Generally high beam energies produce higher temperatures in the fireball but the systems then stay in the region of high baryon density for comparatively shorter times.

The CBM experiment will be installed at the SIS300 accelerator of FAIR, which will provide ion beams with beam energies between 10 and 40 $AGeV$. While the highest energy is achieved for isospin symmetric ions, the heaviest beam, Uranium, will be accelerated to an energy of 25 $AGeV$ only. This energy coverage, in combination with high intensity beams, provides ideal conditions for studying nuclear matter at high baryonic densities and for exploring the phase transition line at finite baryo-chemical potential.

Experimentally, the exploration of the nuclear phase diagram is complicated by the fact that the fireballs formed in a given collision probe different regions of temperature and density simultaneously. However, more then twenty years of research in relativistic heavy ion collisions allowed establishing experimental observables being sensitive to different phases of the fireball evolution (see for example [4] and references herein). The evolution of the fireball and the observables sensitive to the different phases are briefly reviewed in the following.

At the first instant of a heavy ion collision, the constituents of the colliding nuclei undergo hard collisions with the highest center of mass energy through-out the reaction. At ultra-relativistic beam energies, the relevant degrees of freedom in these scattering processes are quarks and gluons. In the course of these collisions, the in-streaming matter is slowed down and an ultra-dense system with high energy density is formed. The collective beam energy is partly used for creating particle anti-particle states and also converted to heat in a rapid thermalization process. The fireball thus reaches in this phase its maximum values in density and temperature. It is commonly believed that this state is a strongly correlated system of quarks and gluons, the QGP. The quarks are deconfined and act as individual particles. Because of the expansion, temperature and density of the fireball shrink and fall below the values required for forming the QGP. At this point, the quarks bind again to hadrons. This process, which is inverse to the formation of the QGP by deconfinement, is called *hadronisation*.

After hadronisation, the fireball is composed of hadrons, which are frequently scattering elastically and inelastically. As long as the temperature of the fireball is sufficient to allow for inelastic scattering, the different particle species remain in chemical equilibrium. With further reducing

temperature, inelastic scattering processes start to cease and chemical equilibrium is broken. This chemical freeze-out point can be experimentally accessed by analyzing the experimentally observed particle abundances in terms of a statistical model assuming an instant freeze-out and taking into account the feeding of hadronic states by strong and weak decays of higher lying hadronic resonances and states.

At some later state also elastic collisions fade out and the particles finally decouple. This state, which marks the end of the fireballs lifetime, is called thermal freeze-out. The temperature of this transition is reflected in the characteristic phase space distribution of the particles observed in the detectors.

As a matter of fact, in a thermal expansion of the system practically all information from the early phase of the fireball evolution is lost at the freeze-out point. An exception are hadronic states which contain charm quarks, the latter not being abundantly produced in the thermal heat bath due to their high mass. Moreover, electromagnetic radiation can escape the fireball at any time due to the long mean free path of particles not undergoing strong interaction. Among this hard, respectively, penetrating probes are:

**Di-leptons:** The thermal equilibrium of the fireball relies on strong interactions. As leptons do not underlay this interaction, their properties remain mostly unchanged in the cooling process. This allows for an undistorted reconstruction of hadrons decaying into a lepton pair in the early stage of the collision, which makes dileptons an interesting probe [5] . In particular, it is possible to measure modifications of the mass of the mother particle, which are a predicted consequence of a partial restoration of the spontaneous chiral symmetry breaking in the medium.
A complication of this approach arises from the fact that those in medium modifications of the particle mass shrinks within the cooling process of the fireball. The signal observed superposes all phases of the collision, which complicates its interpretation. Moreover, the leptons generated from the fireball have to be distinguished from a substantial background caused by trivial processes.

**The $J/\psi$-meson :** This meson is formed by two charmed quarks and can decay into a lepton pair. The observable hence combines both aspects, penetrability and hardness, and can furthermore be reconstructed with good signal to background ratio from the invariant mass distribution of observed lepton pairs due to its narrow width.
A particular interest for studying the $J/\psi$ arises from the fact that the formation of this particle is substantially hindered in the presence of QGP [6]. As the two charmed quarks are deconfined by Debye screening in the QGP, they may instantaneously separate from each other. At FAIR energies, a generation of the particle in the hadronisation is unlike for combinatorial reasons. A substantial suppression of the production of $J/\psi$ is thus expected in the case of a formation of QGP. $J/\psi$ suppression compatible with the occurrence of QGP has indeed been observed [7]. Nevertheless, other scenarios than QGP were proposed to explain this observation [8].

**Open charm mesons :** All produced charm quark pairs not forming charmonium states finally hadronize as charmed hadrons. Studying open charm provides therefore important complementary information to the study of $J/\psi$. Observing a suppression of $J/\psi$ combined with a comparable increase of the open charm production would provide a strong evidence for a phase transition to QGP [9].
The measurement of open charm is difficult because of the short lifetime of the particles which
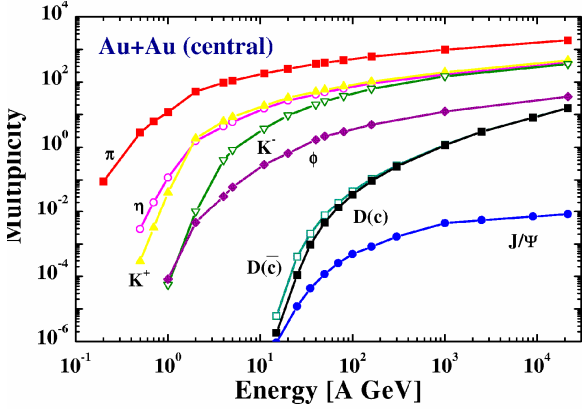
Figure 1.4.:
*The average number of mesons produced per central Au+Au collision (multiplicity) as a function of the incident beam energy. The calculation was performed with the HSD transport code. No in-medium mass modification was taken into account. One observes the multiplicity of open charm (D) to increase strongly as a function of beam energy in the energy range of FAIR. This makes this variable very sensitive to in medium mass modifications. Taken from [10].*

is typically in the order of $c\tau = \sim 100\ \mu m$. Moreover, the hadronic decay channels[2] used for the particle reconstruction suffer from an enormous background from uncorrelated particle pairs.

## 1.2. CBM, an experiment to explore the nuclear phase diagram

A first exploration of the energy range of FAIR has been done by experiments situated at the CERN-SPS and AGS. Nevertheless, because of constraints in beam intensity and detector technologies it was not possible to access rare probes like for example open charm.

The Compressed Baryonic Matter – experiment was proposed as a second generation fixed target experiment. It will be located at the Facility for Antiproton and Ion Research (FAIR) in Darmstadt/Germany. The beam will be delivered by the SIS300 accelerator of the FAIR facility. Some technical data of this accelerator is given in table 1.1. It will provide beams of up to 90 $GeV$ for protons and close to 35 $AGeV$ for fully stripped $U^{92+}$-ions. The beam will be extracted over periods of 10-100 seconds in a quasi-continuous mode. The maximum beam intensity in this mode is $10^9$ ions/s. Assuming an interaction rate of 1 %, this translates into $10^7$ nuclear collisions per second.

A particular strong point of the experiment is its detector technology. Driven by progresses in the field, CBM aims to measure for the first time simultaneously several hard probes like light vector mesons decaying into lepton pairs, $J/\psi$ decaying into lepton pairs and multi-strange particles . Moreover, for the first time open charm will be addressed in this energy range. This makes CBM detector an unprecedented tool for the study of the physics of QGP.

The global design of CBM expresses two main requirements on the experiments, which are the identification of open charm via its hadronic decay and the reconstruction of $J/\psi$ and light vector mesons via their decay into lepton pairs. Both, electron-positron pairs and dimuon pairs will be studied. An important background for both leptonic decay channels is due to a large number of pions. In order to suppress this background, excellent lepton identification abilities are mandatory.

The reconstruction of open charm is foreseen via their hadronic decays into pions and kaons. The background of these channels is formed by kaons and pions, which are produced in large numbers in the primary collision. To distinguish the signal from this combinatorial background, a reconstruction of the decay vertex of open charm particles is mandatory. Because of the relatively

---

[2]*D*-mesons have also been reconstructed by their semi-leptonic decay $D \rightarrow e+$ something. However, only the fast electrons are detected in this approach. They have to be distinguished from a substantial background of electrons having other origins, which causes substantial uncertainties on the multiplicity of the particles.

| | The SIS300 accelerator |
|---|---|
| Circumference | 1083.6 m |
| Bending power | 300 Tm |
| Magnetic field , Ramping | 6 T , 1 T/s |
| Particles/cycle ($U^{92+}$) | $1.3 \times 10^{10}$ |
| Particle Energy | 90 $AGeV$ for Protons, 34 $AGeV$ for $U^{92+}$ |
| Acceleration time | 8.2 s |
| Extraction time | 10 - 100 s |
| Ions/s ($U^{92+}$) (total) | $7.8 \times 10^{8}$ |
| Ions/s ($U^{92+}$) (extraction) | $1 \times 10^{9}$ |

Table 1.1.: *Technical data of the SIS300 accelerator. Compiled from [11].*

low lifetime of open charm, which is for example $c\tau = 123.0 \ \mu m$ for $D^0$ and $c\tau = 311.8 \ \mu m$ for $D^{\pm}$ [12], a vertex detector with excellent performances is required. This vertex detector has to assure a secondary vertex resolution of $\sim 50 \ \mu m$ [1]. The dominating background suppression abilities of this vertex detector will be complemented by a hadron identification system.

At the time being, the CBM experiment is planned to provide two different setups.

The first setup is dedicated to measurements based on electron/positron pairs and to open charm physics. This setup is shown in figure 1.5. It contains a Silicon Tracking System (STS) formed by a micro vertex detector based on silicon pixel detectors and by a tracker based on silicon strip detectors. The STS is located in the field of a dipole magnet with a bending power of roughly $\sim 1 \ Tm$. Together with a time of flight (TOF) hadron identification system, which is formed by a diamond start detector and resistive plate chambers (TOF-Wall), the STS serves for open charm measurements.

The very good electron identification abilities required for the reconstruction of hadrons decaying into electron/positron pairs is provided by a Ring Imaging CHerenkov detector (RICH) and additional Transition Radiation Detectors (TRD). The RICH is used to identify low and medium energy electrons and supports open charm measurements by identifying fast pions. The electron identification abilities of the RICH shrink with increasing electron energy. The system is thus complemented by TRDs, which provide an efficient identification of very fast electrons. The measurement chain for electron positron pairs is completed by an electro-magnetic calorimeter.

Besides those detectors, a forward calorimeter is foreseen in CBM (not shown). This calorimeter is intended to characterize the event centrality by measuring the energy taken away by spectator fragments, which did not participate in the collision.

The second setup aims for a reconstruction of hadrons decaying into dimuon pairs. This setup is formed by the STS (most probably without vertex detector) and a muon detector based on a sandwich of tracking detectors and metal layers, which are to stop electrons and hadrons. This detector replaces the RICH detector. Its use is not compatible with open charm reconstruction, as it stops hadrons before they are identified by the TOF-Wall.

Note that at the time being, the technical design of CBM is still under evolution. For an actual and detailed overview of the technical specifications of the different detector systems, the reader is therefore referred to the technical status reports of the experiment [3, 11].

## 1.3. The Silicon Tracking System (STS) of CBM

### 1.3.1. Requirements and running conditions

The physics program of open charm physics at CBM dominantly relies on $D$-mesons. The reconstruction of $\Lambda_c$-baryons is also discussed but this option will not be addressed in this work. The $D$-mesons will be reconstructed via their hadronic decay channels $D^0 \rightarrow K^- + \pi^+$ and $D^+ \rightarrow K^- + \pi^+ + \pi^+$. According to [12] the branching ratio of those channels is $3.83\% \pm 0.09\%$ and $9\% \pm 0.09\%$ respectively. The lifetime of the $D-$mesons is $c\tau = 123.0 \ \mu m$ for $D^0$ and $c\tau = 311.8 \ \mu m$ for $D^{\pm}$.

Among the $D$-mesons addressed, the $D^0$ is considered as most difficult to reconstruct because of its short lifetime. The design guidelines for the Micro Vertex Detector (MVD) and the STS of CBM are thus derived from the requirements set by this observable. Calculations based on the HSD model suggest a production multiplicity of $(1.2–1.8) \times 10^{-4}$ per central Au-Au collisions at $25 \ GeV$ beam energy for $D^0 + \bar{D}^0$ [73] . Taking into account the branching ratio, one can expect one $D^0 \rightarrow K + \pi$ decay per $\sim 2 \times 10^5$ central collisions.
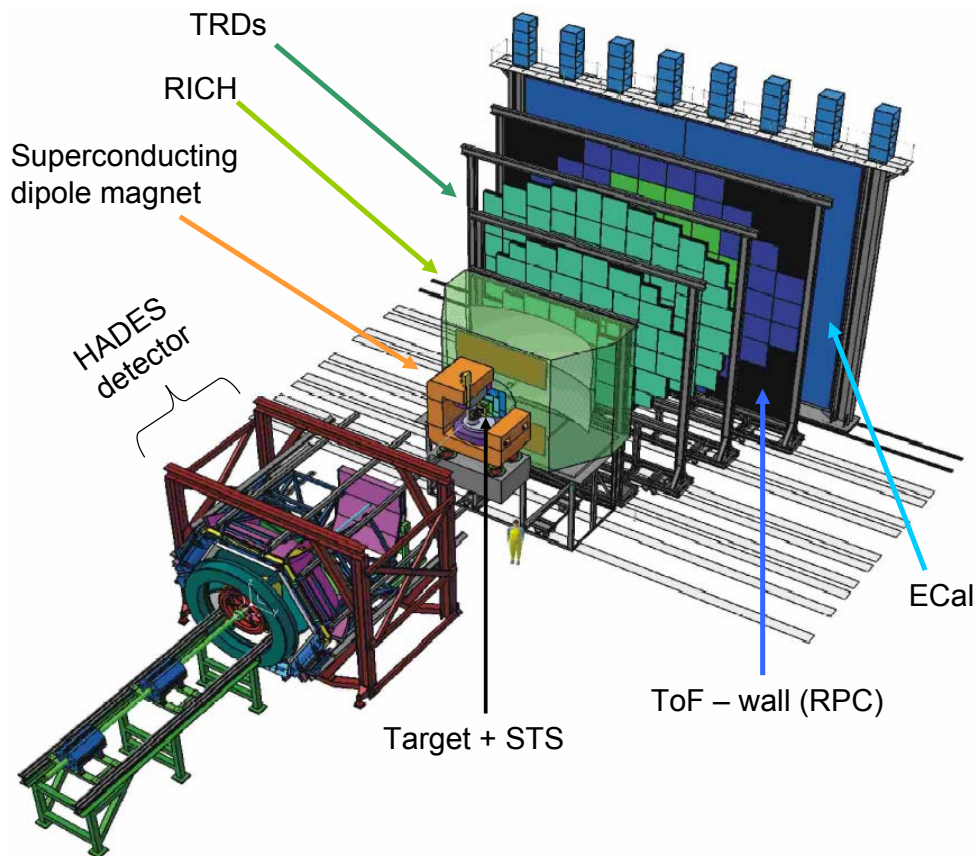
Figure 1.5.: *Schematic view of the CBM-detector. The picture shows the setup used for open charm and electron/positron measurements. In the di-muon setup, the RICH-detector is replaced by a muon detector (not shown). The existing HADES - experiment is located upstream to CBM at the same beam line. It will be used to explore the energy region below 8 AGeV.*

*1. The CBM experiment: Physics motivations and detector concept*
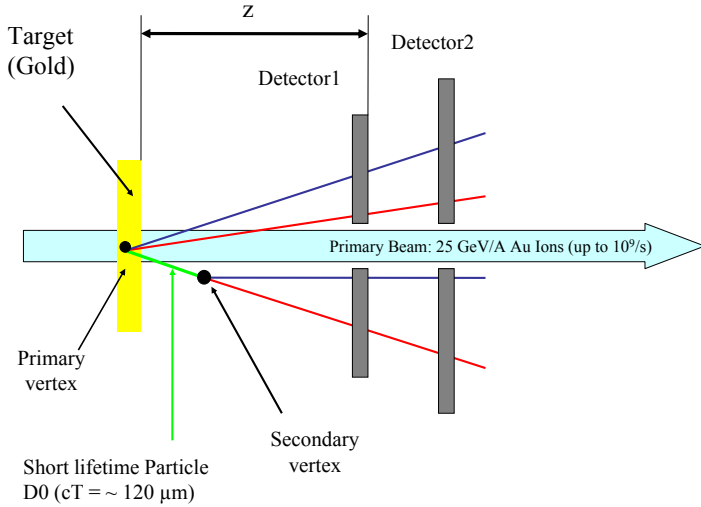


Figure 1.6.:
*The principle of the identification of short living particles with a vertex detector. As those particles decay into products, which are also produced in the primary interaction, one extrapolates the particle trajectories back. When finding two different intersections points (primary and secondary vertex) one can conclude on the presence of a particle with short lifetime.*

The background of the channel is formed from roughly $\sim 330\ \pi^+$, $\sim 370\ \pi^-$, 40 $K^+$ and 10 $K^-$ per central collision according to UrQMD calculations [3].

As the lifetime of open charm mesons does not allow them to reach the detector, they have to be reconstructed by detecting their daughter particles. If all daughter particles are correctly identified, the mass and momentum of the mother particle can be derived from their properties. The reconstruction process is schematically shown in figure 1.6 for the $D^0$-meson. The trajectories of the daughter particles of a $D^0$ are extrapolated back to its decay point, which is called secondary vertex. Identifying this secondary vertex allows to distinguish the true daughter particles from the *combinatorial background* formed by uncorrelated pairs, which are emitted from the nuclear collision point (primary vertex). It is commonly believed that a very good secondary vertex resolution of $\sim 50\ \mu m$ is required to reach a sufficiently background rejection. This benchmark sets the requirements on the spatial resolution and on the material budget of the vertex detector stations.

Additional requirements are set by the relatively low production multiplicity of open charm mesons. An intense beam is required for producing a sufficient amount of those particles in a reasonable amount of time. The collision rate foreseen at CBM is $\sim 10^7$ collisions per second. Roughly 10% of these collisions can be considered as central ones.

This intense beam generates a particle flow which may reach $\sim 3 \times 10^9$ charged particles per second and $cm^2$ for a vertex detector located 5 $cm$ from the target. The mean time between two collisions is as low as 100 $ns$. To account for this, the vertex detector has to feature a very good granularity, readout speed and time resolution.

Moreover, the intense particle flux sets severe constraints on the radiation hardness of the detectors. It is today commonly believed that the CBM experiment will have an effective beam time of roughly $5 \times 10^6\ s/year$ (about two months). Combining this information with the estimated particle flux, one finds that the detector will have to stand the radiation of more than $10^{15}$ particles per $cm^2$ and year at its most irradiated points. This value is at the limit of nowadays most radiation hard pixel detector technologies.

Concluding, the considerations mentioned above allow defining the unprecedented requirements for operating the vertex detector at the nominal collision rate of CBM:

- The vertex detector has to provide a secondary vertex resolution of $\sim 50\ \mu m$.
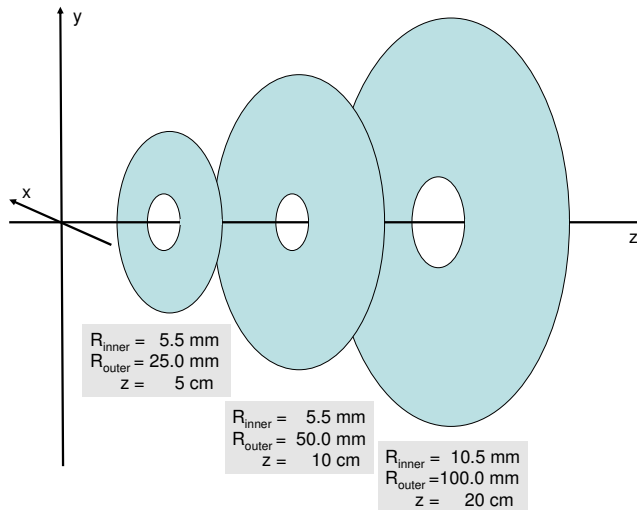
Figure 1.7.:
*The layout of the STS as it was initially proposed and used in the simulation. The detector stations (three of seven are shown) are modeled as silicon discs. A beam hole in the middle allows the primary beam to pass without interaction. The three first stations are surrounded by a vacuum vessel (not shown). The target will be placed in the origin of the coordinate system.*

- The granularity and readout speed of the detector have to be sufficient to sense a particle flux of up to $\sim 3 \times 10^9$ charged particles per $cm^2$ and second.

- To avoid event pile-up, the detector has to have a sufficient time resolution to separate the individual nuclear collisions, which appear after a mean time of 100 $ns$ at the nominal luminosity of FAIR.

- The detector has to resist to the radiation caused by a particle flux above $10^{15}$ particles per $cm^2$ and year at its most irradiated points.

Note that the numbers shown here are preliminary. It will be demonstrated later in this work that the goals of open charm physics at CBM will be most efficiently reached with reduced beam intensity. This substantially relaxes the requirements on radiation hardness and time resolution of the detectors.

## 1.3.2. The initial design proposal for the CBM silicon tracking system

In the early design proposal of CBM, the vertex detector and the tracker were commonly referred as silicon tracking system (STS). The design of the STS has consecutively been refined in the last years but the initial proposal will be shown here as it served as starting point of this work. The present status of the vertex detector will be developed in this work.

The original design of the STS [1] was composed of seven detector layers called stations. As illustrated in figure 1.7, those stations were proposed as thin silicon disks. A beam-hole in the middle of each of these disks was foreseen to allow for a passage of the beam. The surface of the seven silicon detector stations is 1.5 $m^2$. Their precise geometry is listed in table 1.2.

The use of silicon pixel detectors was planned for the first two detector stations. For the last four detector stations, the track density is sufficiently low to allow for the use of cheaper double-sided silicon strip detectors. The third station was composed of pixel detectors in the inner area and strip detectors in the outer area.

| Station | z | $R_{Inner}$ [mm] | $R_{Outer}$ [mm] | Technology |
|---------|------|------------------|------------------|------------|
| 1 | 5 cm | 5.5 | 25.0 | Pixel |
| 2 | 10 cm | 5.5 | 50.0 | Pixel |
| 3 | 20 cm | 10.5 | 100.0 | Combined |
| 4 | 40 cm | 20.5 | 200.0 | Strip |
| 5 | 60 cm | 30.5 | 300.0 | Strip |
| 6 | 80 cm | 40.5 | 400.0 | Strip |
| 7 | 100 cm | 50.5 | 500.0 | Strip |

Table 1.2.: *The initial proposal of the STS. The use of pixel detectors was foreseen for the first two stations as a consequence of the high particle density. The lower flux more downstream of the detector allowed for the use of strip detectors. The third station uses pixel detectors in the region of highest particle fluxes close to the beam axis.*

## 1.4. Questions on the pixel detector technology of the STS and the task of this work

The material budget and the spatial resolution of the pixel detectors were not addressed in the initial design proposal of the STS, as the requirements on these points were not yet worked out. They can be derived from the secondary vertex resolution needed. Both, the scattering of the particle in the matter of the detector and a low spatial resolution increase the uncertainties of the extrapolation of the trajectories towards the secondary vertex. Insufficient performances lead therefore to an insufficient secondary vertex resolution.

Preliminary requirements were derived with a back of envelop calculation, which is discussed in the appendix (see A.1). The outcome of the calculation is shown in figure 1.8 for the STS-geometry discussed in the previous section. The figure displays the secondary vertex resolution as a function of the material budget and the spatial resolution of the pixel detectors. One observes, that a material budget of only few 0.1% $X_0$ combined with a spatial resolution of $\lesssim 5~\mu m$ is required for achieving a secondary vertex resolution $\Delta z = 50~\mu m$. Moreover, it is considered that the matter required for a vacuum window would generate too much multiple scattering. The vertex detector has thus to operate in vacuum.

Hybrid pixel detectors as known from the CERN - LHC - experiments have been foreseen as technology for the vertex detector of CBM. Some features of those pixels are compared in table 1.3 with the preliminary requirements discussed above. One observes that the hybrid pixels combine a high radiation hardness, which may be sufficient to survive one year of operation at the nominal luminosity of FAIR, with an excellent time resolution (25 $ns$). On the other hand, they are relatively thick and show only a moderate spatial resolution, which leads to an insufficient performance in terms of secondary vertex resolution. One can thus state that hybrid pixel detectors are unlike to provide the precision required for discriminating the background from the decay channels of open charm.

Table 1.3 also contains data on competitive pixel detector technologies, the established CCD detectors and the novel Monolithic Active Pixel Sensors (MAPS). The CCD detectors can provide the material budget and spatial resolution needed but their poor radiation hardness is more than five orders of magnitude below the requirements. They are thus ruled out for a use in CBM.

MAPS provide a very good spatial resolution of 1.5 $\mu m$ to 2.5 $\mu m$ when being combined with analogue readout. Their thickness can potentially be reduced significantly below 0.1 % $X_0$. Both features allow MAPS to reach the secondary vertex resolution required. Moreover, there were first measurements suggesting [17] that the MAPS might reach a radiation tolerance, which is by orders

| | Required | Hybrid | CCD | MAPS [1] | MAPS [2] |
|---|---|---|---|---|---|
| Spat. resol. $[\mu m]$ | $\lesssim 5$ | $\sim 30$ [3] | $\sim 5$ [3] | $\sim 2$ [4] | $\sim 5$ [3] |
| Mat. budget $[X_0]$ | few 0.1% | $\sim 2\%$ [5] | $\sim 0.1\%$ [6] | $\sim 0.1\%$ [6] | few 0.1% [7] |
| Rad. hardn. $[n_{eq}/cm^2]$ | $> 10^{15}$/year | $\sim 10^{15}$ | $\sim 10^{10}$ | $\sim 10^{12}$ | $\sim 10^{13}$ |
| Time resolution | $\lesssim 100\ ns$ | $25\ ns$ | $\sim 50\ \mu s$ [8] | $\sim 200\ \mu s$ | $\sim 10\ \mu s$ |

Table 1.3.:
*Performances of different pixel detectors compared to the requirements for open charm meson reconstruction with full collision rate at CBM. The data on hybrid pixel detectors and CCDs was collected from [13, 14, 15, 16].*

Remarks:
[1]: *Established performances of MAPS.*
[2]: *MAPS design goal for CBM according to this work.*
[3]: *Derived from the typical pixel pitch assuming digital readout.*
[4]: *Analogue readout.*
[5]: *ATLAS pixel module.*
[6]: *ILC - design goal, air cooled.*
[7]: *Liquid cooled, vacuum compatible.*
[8]: *ILC - design goal.*
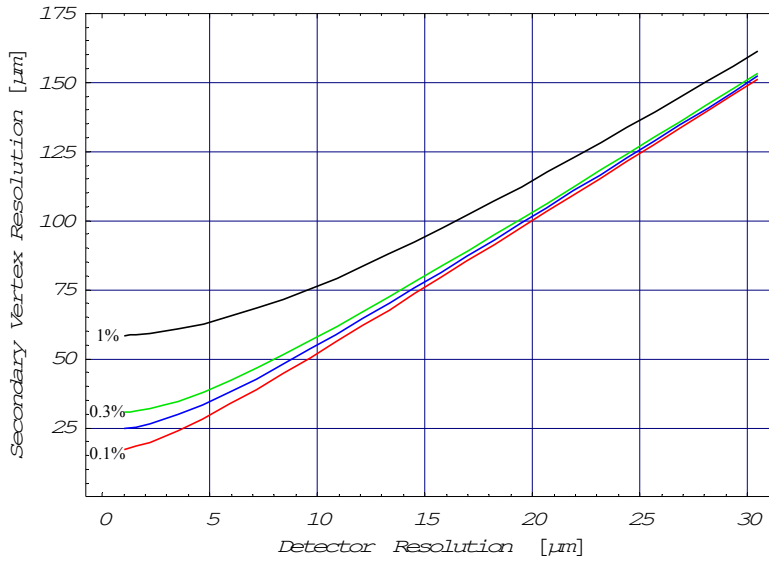
Figure 1.8.:
*The resolution of the STS according to an analytic calculation (see appendix A.1). The resolution is shown as a function of the spatial resolution of the detector stations and their material budget in radiation lengths.*

of magnitude above the one of established CCD detectors. Their flexible readout mechanism has the potential to reach a time resolution above the one of CCDs.

Even if they do not match the requirements in a straightforward way, MAPS are likely to represent the best technological compromise available today. They were therefore proposed as a detector technology for the CBM vertex detector. Nevertheless, comparing the requirements with the performances of MAPS detectors, two major critical parameters can be identified. Those are the time resolution and the radiation hardness of the MAPS detectors. Moreover, an estimate of the material budget, taking into account mechanical support and biasing structures for the MAPS, remained to be worked out.

MAPS form a novel technology. The prototypes available were successfully designed to prove the principle of the detectors. The first promising results on time resolution and radiation tolerance were reached despite they were not among the primary design goals of the early detector generations. Significant progresses in both fields were therefore expected from technology optimizations. Further room for optimization was provided by the fact that the concept of the CBM vertex detector was not optimized for MAPS. A revision of this concept was likely to relax the requirements.

The question to be answered in this work was if the optimization of the MAPS detectors combined with an optimization of the detection strategy allows for building a CBM vertex detector, which can reach the physics goals of CBM in terms of open charm physics.

## 1.5. Summary of this chapter

Within this chapter, the CBM experiment was introduced. The physics goals of the experiment, which are the exploration of the predicted phase transition between nuclear matter and the Quark Gluon Plasma, the search for the critical point of the nuclear phase diagram and the study of a potential chiral symmetry restoration, were addressed. It was shown that open charm mesons form an important probe for measuring the properties of the hot and dense hadronic matter. Their production multiplicity allows for probing the predicted variations of the effective mass

of the particles in the medium. Moreover, being combined with information on the production multiplicity of $J/\psi$, open charm may help to identify a phase transition to QGP.

The identification of open charm in a fixed target heavy ion experiment at a beam energy of $15 - 40$ $AGeV$ calls for unprecedented qualities of the vertex detector, which needs to provide a secondary vertex resolution of $\sigma_z \sim 50$ $\mu m$. It was shown, that such a good resolution demands for detectors, which combine a spatial resolution of $\sigma < 10$ $\mu m$ with a material budget of few $0.1\%$ $X_0$.

Moreover, because of the low production multiplicity of open charm, a high beam intensity is required, which might go up to $10^7$ nuclear collisions per second. The detector has thus to provide an excellent granularity and time resolution. The high particle flux generated by the intense collision rate also demands for high radiation hardness. A back-of-envelop calculation indicates that a tolerance to more than $10^{15}$ minimum ionizing particles per $cm^2$ is required for standing the nominal collision rate of CBM.

The hybrid pixel detectors proposed in the Conceptual Design Report [1] of CBM do not fulfill the requirements, as their material budget is too high and their spatial resolution is insufficient. Alternative technologies are thus required. One of them is formed by Monolithic Active Pixel Sensors, which provide the spatial resolution and low material budget required combined with advanced radiation hardness.

Studying the feasibility of their use as technology for the CBM vertex detector is the aim of this work.

# 2. Monolithic Active Pixel Sensors

Searching for alternative pixel detector technologies for CBM, Monolithic Active Pixel Sensors (MAPS, also referred as CMOS-sensors) [18, 19] were found as interesting candidates. Such pixels sensors were originally developed for optical imaging. Standing in competition with more classical optical pixel sensors like CCDs (Charge Coupled Device), they can be found nowadays in home entertainment electronics like digital cameras. The main advantage of MAPS in this field is their compatibility with standard CMOS-processes, which allows a fast development of these sensors with standard tools as much as a cheap mass production. On the other hand, being a depleted device, CCD sensors may deliver a slightly better signal quality in the field of optical imaging. In 1999, the idea came up to use MAPS for charged particle tracking. This development was driven by the requirements of the TESLA linear collider (today: International Linear Collider (ILC)) [20]. The vertex detector of this collider requires sensors providing the good spatial resolution and low thickness of CCDs. On the other hand, the requirements in terms of readout-speed and radiation hardness against neutrons seemed to be beyond the range of this established technology. In analogy to the situation in CBM, the more radiation hard hybrid pixels did not appear attractive due to their sizable material budget and their too poor spatial resolution. A detector compromising the strong points of both technologies was required and the hope was that the MAPS technology would provide this compromise.

The R&D-work on MAPS was started at the Institut de Recherches Subatomiques (IReS) in close collaboration with the Laboratoire Electronique et de Physique des Systémes Instrumentaux (LEPSI). First prototypes demonstrated the feasibility of MAPS-detectors for charged particle tracking as much as an excellent detection efficiency (well above 99 %) and spatial resolution ($\sim 1.5~\mu m$). Moreover, it was demonstrated that these sensors could be thinned to a thickness of $\sim 120~\mu m$ in a straightforward way and without loss in performance. First, preliminary studies demonstrated a radiation tolerance against neutrons, which was, several orders of magnitude higher than the one of CCDs.

This combination of spatial resolution, granularity, low material budget and radiation tolerance made MAPS an attractive candidate for the CBM vertex detector. On the other hand, a substantial amount of questions remained to be addressed. These concerned in particular readout speed / time resolution and radiation hardness of the MAPS. First results were available on the native abilities of the technology concerning both parameters, but no optimization was undertaken in both fields when this work was started in early 2003. Extensive studies were therefore required to conclude on the usefulness of such detectors in CBM.

These studies call for an understanding of the detector technology and of the specific strong and weak points of MAPS. In order to motivate these points, some basics of semiconductor physics will be reminded before discussing the design and working principles of MAPS detectors. The working principle of CCD and hybrid pixel detectors will also be briefly addressed for comparison. The description of the detector technology will be completed by a collection of the established performances of MAPS.

## 2.1. The detection principle of silicon detectors

### 2.1.1. A short introduction into semiconductors

A detailed knowledge on semiconductor physics is required to understand the operation principle of semiconductor detectors. However, the information required on the band model of semiconductors and the PN-junction is discussed in text bodies like [21],[22]. The description provided hereafter will therefore not go into many details, but restrict itself on some aspects, which are of importance for understanding the operation principle of MAPS.

#### 2.1.1.1. The band model

The band model was developed to describe the electrons located in a condensed material. In first order, it assumes the electrons of the material to form a Fermi gas of free electrons. However, by treating the regular potential of the atomic nuclei in the framework of quantum mechanics, one finds bands of dense quantum mechanical states. These bands are separated by so-called band gaps, energy where no quantum mechanical states are available for the electrons. Within this model, the conductivity of a material is determined by the location of the the Fermi energy of the material with respect to the band gaps.

Electrons have to move for contribution to conduction. This movement is only possible if they can change into a quantum state having a higher (kinetic) energy. This is not possible if the Fermi energy of the material is in the band gap, as (almost) no additional states for electrons are available. Consequently, in such materials there is in first order no conduction and the material is an isolator.

If the Fermi energy is located within a band or if two bands overlap without a real band gap[1] numerous states are available and the electrons can easily gain energy. This is the situation in metals, which are therefore excellent conductors.

Semiconductors are an exception in this picture. At the one hand, the Fermi energy is located within a band gap. On the other hand, this band gap is relatively small. Thermal excitation at room temperature is sufficient to transfer a moderate amount of electrons into the next band, where they can profit from a large amount of free states for their motion. Semiconductors therefore get conductive at a sufficient temperature.

This thermal excitation is not sufficient to transform the material in an outstanding conductor. However, it is not an isolator anymore. Therefore, the material is named semiconductor. It is a convention to name the band located above the Fermi energy *conduction band*. This is because the electrons have to reach this band if they want to participate in conduction. The band located below is named *valence band*.

Note that excited electrons leave empty states in the valence band behind them. Electrons bound in the valence band can use these states for their motion, which contributes to conduction. The free states arising from the absence of electrons are named holes. They are regularly modeled as a particle of a positive charge moving in the valence band. As every electron being excited to the conduction band generates a hole in the valence band, the amount of holes is equal to the amount of free electrons.

The density of charge carriers available per $cm^3$ of material is given by [23]

$$n_i = \sqrt{n_C n_V} \cdot e^{-\frac{E_g}{2 k_B T}}. \tag{2.1}$$

---

[1]The bands can still be defined in this case due to arguments arising from atomic physics. Moreover, this overlap usually exists only for electrons having a certain momentum.

Here, $E_g = 1.11 \ eV$ stands for the band gap of silicon, $T$ for the temperature in Kelvin, $k_B$ for the Boltzmann – constant. For silicon, the density of states in the conducting band and the valence band are given by $n_C = 3.22 \times 10^{19}/cm^2$ and $n_V = 1.83 \times 10^{19}/cm^2$ respectively. The conductivity relying on this thermal generation is called *intrinsic conductivity*.

### 2.1.1.2. Direct and indirect semiconductors

Besides the energy required to excite an electron from the valence band to the conduction band, one has also to care about momentum conservation. This becomes important when the energy available is sufficient for an excitation but the momentum of the electron does not fit to its final state.

This is particularly true in the case of silicon, as the highest states of its valence band and the lowest state of the conducting band have different momenta. Besides energy, a collision allowing for a transfer of momentum is required for passing the band gap. This is usually achieved by a collision with a phonon. Nevertheless, this constraint reduces the cross sections for an excitation of electrons even if the energy required is available.

Besides this indirect excitation, a direct excitation is possible in silicon. It however calls for a significantly higher energy than $E_g$. Semiconductors comparable to silicon are called *indirect semiconductors*. Semiconductors for which the lowest state conduction band and the highest state of the valence band show the same momentum, are called *direct semiconductors*.

As discussed in more detail later, this argument is of particular importance for MAPS, as it is also true for the recombination of the charge carriers. Since an adequate momentum transfer is required, a recombination calls for a free state in the valence band and for an additional collision partner. Consequently, the recombination cross-section of an indirect semiconductor is substantially lower than one would expect from a direct semiconductor like germanium. This leads to a relatively high life time of charge carriers in the conduction band.

### 2.1.1.3. Doping

The intrinsic conduction is neither strong nor very stable as it depends for example strongly on the temperature. Intrinsic semiconductors have therefore only few applications. A substantial improvement of the conductivity of semiconductors and its stability is reached by doping, which relies on the fact that small impurities in the material have strong impact on the material properties if they generate additional states in the band gap.

The materials used for doping are chosen such that the corresponding impurities in the band gap concentrate in a thin doping band, which is energetically close to the valence band or to the conduction band. Such defects can be produced by using elements which have five or three valence electrons instead of the four ones of silicon.

An atom with five valence electrons leads to the presence of an electron in the shell above the valence band. This electron is loosely bound and can easily escape to the conducting band. As this structure has tendency to deliver an electron to the conducting band it is called *donor*. As illustrated in figure 2.1 (left), in the band model it is represented by a filled electron state slightly below the conduction band. The doping with donors is called *N-doping*. In the case of atoms with three valence electrons, one electron is missing to form the standard atomic binding of the crystal lattice. The corresponding structure has thus tendency to absorb an additional free electron. It is therefore called *acceptor*. As illustrated in figure 2.1 (right), acceptors are represented by an empty electron state slightly above the valence band in the band model. The corresponding doping is called *P-doping*.
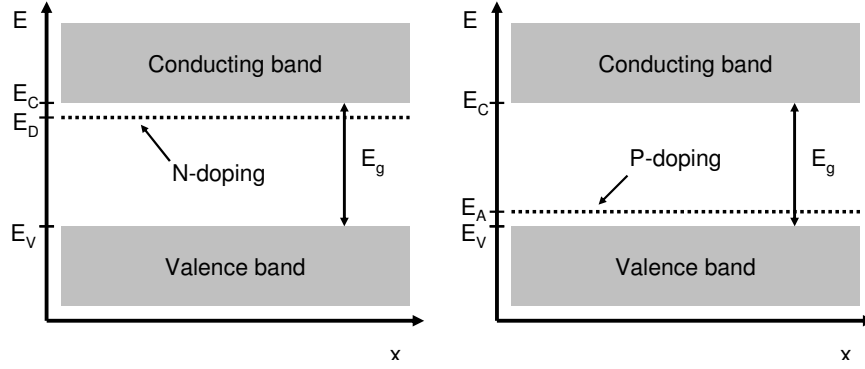
Figure 2.1.:
*Energy levels in N-doped (left) and P-doped silicon (right). At $T = 0$ K, the states of the N-doping are filled, the ones of the P-doping are empty.*

P-doping, for example, can be achieved with boron, which delivers an acceptor band at $E_A$–$E_V = 0.045$ $eV$, where $E_A$ stands for the energy level of the acceptor band and $E_V$ for the upper energy limit of the valence band. N-doping is done with phosphorous ($E_C$–$E_D = 0.0453$ $eV$) or arsenic ($E_C$–$E_D = 0.054$ $eV$). Here, $E_D$ stands for the donor band and $E_C$ represents the lowest energy level of the conducting band.

The additional states have a substantial impact on the conductivity of the material, as the excitation energy for producing charge carriers is substantially reduced. In the case of the N-doping, the doping band delivers additional electrons to the conducting band. In the case of the P-doping, the empty states of the doping band can be filled by electrons located in the valence band. This leads to the generation of additional holes.

At room temperature, the charge carriers from doping atoms dominate the ones generated by thermal excitation from the valence band. They are therefore named *majority charge carriers*. Nevertheless, thermal excitation also generates a small amount of opposite charge carriers, which are called *minority charge carriers*. These are for holes in a N-doped material or the conducting electrons in a P-doped material respectively.

Besides the generation of additional charge carriers, the Fermi-energy of the system is modified. As the doping band for N-doping is filled, the Fermi-edge is located between this band and the conduction band. Due to the empty band generated by the P-doping, it drops between this lower doping band and the valence band.

## 2.1.2. Particle detection with a silicon detector

Besides thermal excitation, electrons can also be excited by electro-magnetic interaction caused for example by photons with an energy above $E_g$. This is in particular the case for visible light. Moreover, such interactions can be caused by an incident fast charged particle.

The energy transferred to the bulk material by these particles is given by the Bethe-Bloch equation [2] :

$$-\frac{dE}{dx} = \frac{4\pi}{m_e c^2} \frac{nz^2}{\beta^2} \left(\frac{e^2}{4\pi\epsilon_0}\right)^2 \left[ln\left(\frac{2m_e c^2 \beta^2}{I \cdot (1 - \beta^2)}\right) - \beta^2\right] \qquad (2.2)$$

---

[2]The Bethe-Bloch equation is presented in different forms depending on the second order effects taken into account. As these effects are not of a particular importance for this discussion, the rather simple form presented by Povh [24] is shown here.

In this equation $E$ is the deposited energy,

$x$ is the path length,

$m_e$ is the electron mass,

$n$ is the electron density in the material,

$z$ is the charge of the impinging particle in units of $e$,

$e$ is the elementary charge,

$\beta = v/c$ is the velocity of the impinging particle,

$c$ is the speed of light,

$I \approx 16\ eV \cdot Z^{0.9}$ for $Z > 1$ is the effective ionization potential averaged over all electrons; a value of 173 $eV$ may be used for silicon.

Equation 2.2 describes the mean energy deposit per unit of path length. When interpreting this mean value, one has to take into account that the deposit proceeds through multiple individual interactions. Besides the electrons in the valence band, electrons bound in deeper shells participate to these processes. Moreover, direct and indirect excitations are possible. The mean energy required for exciting an electron to the conducting band is 3.6 $eV$ [25] and thus substantially higher than the band gap.

For minimum ionizing particles passing silicon, this leads to the excitation of roughly 80 electrons per micrometer of particle trajectory. Passing towards the conducting band, these electrons leaving an equal amount of holes behind. This is therefore referred to as the "generation of 80 electron hole pairs (e/h pairs) per micrometer silicon".

Besides the energy deposit due to charged particles it is worth to spend a word on the interaction of x-rays in silicon. These particles are typically absorbed by photo effect and excite a fast primary electron. This electron is slowed down exciting secondary electrons to the conduction band. The number of e/h pairs generated in this very local interaction is is again given by

$$N_{e^-} = \frac{E_{X-Ray}}{3.6\ eV} \qquad (2.3)$$

The free charge carriers generated by the radiation can be used to form an electric signal within a silicon particle detector. Assuming enough detector material, the amount of free charge carriers generated can reach a level which is sufficient to detect directly the corresponding current pulse. Indeed diamond detectors developed by CERN-RD42 demonstrate the feasibility of this approach. However, this approach is rarely used for silicon detectors because of the narrower band gap of this material. The latter eases the generation of a background of thermally excited minority charge carriers, which masks the weak signal.

### 2.1.3. The PN-Junction

Forming a well performing detector from a homogeneous block of silicon is difficult. This holds in particular, as unavoidable impurities originating from the production of the material further reduce the resistivity of the material. Reversed biased PN-junctions (diodes) are therefore usually used as particle detectors, as their depleted zone has a very high resistivity also in the presence of a modest amount of impurities.

In a simplified picture one may state than diodes are formed by a block of P-doped material which gets connected to a block of N-doped material[3]. At the junction of both materials, it is

---

[3] The picture of two blocks of material is used to ease the understanding of the processes taking place in a PN-junction. Real junctions are generated by a local inversion of the original doping within one block of silicon material. This can for example be done by ion implantation of doping atoms.

energetically preferable to move the electrons populating the donor states of the N-doped into the empty acceptor states of the P-doped material. This is illustrated in figure 2.2. As this process generates positively charged ions at the N-doped side and negatively charged ions at the P-doped side of the material, this leads to the generation of an electric field, which hampers the movement of the electrons. The process stops when the Fermi energies of both materials get equal. As the Fermi – energy of the N-doped silicon is close below the conduction band and the one of the P-doped silicon close to the valence band, the bands are locally deformed close to the PN-junction.
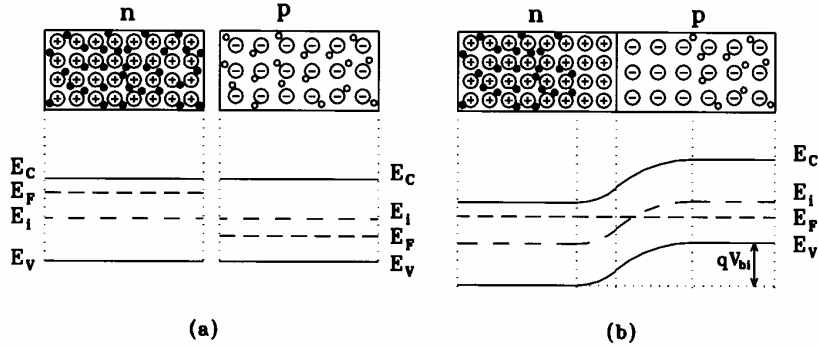


Figure 2.2.: *A P-N diode junction with its parts separated (a) and brought together (b). The Fermi energy ($E_F$), which is initially close to the conducting band in the N-doped silicon and close to the valence band in the P-doped silicon needs to get equal in both materials. This leads to a deformation of the potential in the material, which comes with electric fields. The potentials for electrons are shown in the figure. From [25].*

This diffusion of electrons has several consequences. The first and most desirable one is the appearance of a zone of limited thickness, which is depleted from all majority charge carriers. This is because the free electrons originating from the N-doping and the holes originating from the P-doping cancel out each other. As the arguments leading to this effect are universal, the statement holds also for defect states, which are the consequence of unwanted impurities. A small volume of non-perfect silicon can thus be manipulated to arrive close to the properties of the ideal ones.

The electrical field caused by the equalization of the Fermi energy generates a voltage between the P- and the N-doped side of the junction. The voltage, called *build-in voltage $V_{bi}$*, is defined by the deformation of the bands at the PN-junction. It is given by the expression:

$$V_{bi} = \frac{k_B T}{q} \ ln \left( \frac{N_A N_D}{n_i^2} \right) \tag{2.4}$$

In this equation, $N_A$ and $N_D$ represent the acceptor and donor concentration in the P(N)-silicon, respectively; $n_i$ is given by

$$n_i = \sqrt{N_C N_V} \ e^{-\frac{E_G}{2 k_B T}} \tag{2.5}$$

where $N_C = 2.8 \times 10^{19} \ cm^{-3}$ and $N_V = 1.04 \times 10^{19} \ cm^{-3}$ are the effective density of states in the conducting and in the valence bands, respectively.

The build-in voltage of the PN-junction stabilizes its depleted volume by electrostatically deflecting majority charge carriers from it. Because of this, the depleted zone has a very low

conductivity for these carriers. This statement however does not apply for the minority charge carriers, which are attracted by the voltage and thus form a current. As these electrons and holes have to be generated by thermal excitation, the current formed by them is called *generation current*. In thermal equilibrium, it is compensated by current of majority carriers, which recombine with each other in the depleted volume. This current is named *recombination current*.

The thermal equilibrium between generation and recombination current is distorted, if the PN-junction is connected with an external voltage. This voltage drives a DC-current through the device, which is given by:

$$J = J_S \left( e^{\frac{qV}{k_B T}} - 1 \right) \tag{2.6}$$

The current increases exponentially when a positive voltage is applied, as majority charge carriers are pumped into the depleted zone where they cancel each other out.

When applying a negative voltage, the negative current increases only up to the *reversed saturation current* $J_S$. This current is caused by the thermal generation of the charge carriers. Besides the temperature, the strength of this current depends on the details of the material [4].

A negative voltage is applied on the PN-junction in a particle detector. The corresponding negative current is called *leakage current*. This refers to the fact that this current would be zero under ideal conditions ($T = 0\ K$).

### 2.1.4. The PN-junction as detector for minimum ionizing particles

The diode delivers a zone with a very high resistivity for majority charge carriers. On the other hand, minority charge carriers may pass it being transported by the built in voltage. Consequently, the structure is an optimal device for detecting a small amount of minority charge carriers, as generated by an impinging particle.

However, even if an ordinary PN-junction is sufficient to detect visible light, the detection of minimum ionizing particles (MIP)[5] imposes specific complications as they deposit only $\sim 80\ e/h$-pairs per $\mu m$ trajectory into the semiconductor. The signal generated in the thin depleted area of a unbiased standard diode usually forms a signal, which is too weak to exceed the noise of an electronic amplification chain.

In order to increase the signal magnitude to a value sufficient for generating a satisfactory signal to noise ratio, the thickness of the sensitive area of the detector should be maximized. The standard method to achieve this goal is to in increasing the thickness of the depleted area by raising the reverse bias voltage. The thickness of the depleted zone is given by:

$$d = \sqrt{\frac{2\epsilon\epsilon_0(N_A + N_D)}{qN_AN_D}\ (V_{bi} - V)} \tag{2.7}$$

$V$ stands for the reverse bias voltage, which is applied from an external voltage source. This approach is successfully used in silicon strip and hybrid pixel detectors. They are equipped with diodes having a depleted zone which is typically $100 - 300\ \mu m$ thick. The corresponding signal of $\sim 10^4\ e^-$ is sufficient to drive dedicated low noise amplifiers.

---

[4] For more details, see [25], page 43ff.

[5] A minimum ionizing particle (MIP) is defined as a relativistic particle with charge $Z = \pm\ e$. According to the Bethe-Bloch equation 2.2, the minimal energy deposit occurs for a Lorentz factor of $\gamma \approx 3$, which defines the speed of this particle. The MIP is the charge particle, which is most difficult to detect when passing a sensor. It is therefore regularly used to benchmark detectors.

However, as the maximum reverse bias one can apply to a diode is limited[6]. To achieve a sufficient thickness, the doping concentration of the sensors must be orders of magnitude below the concentration used in CMOS processes, which is typically $N_A \approx 10^{15} \ cm^{-3}$ and $N_D \approx 10^{17} \ cm^{-3}$. Sensors based on PN-junctions with thick depletion are therefore incompatible with the CMOS processes used for building the circuits required for building amplification circuits.

### 2.1.5. The strategy of different pixel detectors

In principle one could envisage integrating the amplifiers into dedicated sensor material. However, this strategy becomes very unattractive when taking into account the practical constraints. The use of lowly doped silicon for microcircuit production is not of interest for commercial applications. A dedicated facility for microcircuit design is thus required for following this approach. This calls for investments out of reach of the small market for radiation detectors.

Different strategies were found in order to overcome the conflict between the need for a lowly doped detector material and a more highly doped material for the readout electronics. The most prominent approach is the use of separated microchips for sensing and amplification. In first order, this demands for a bonding between each individual sensitive element (pixels or strips) and the corresponding readout chain. This approach has been successfully used in systems like strip and hybrid-pixel detectors.
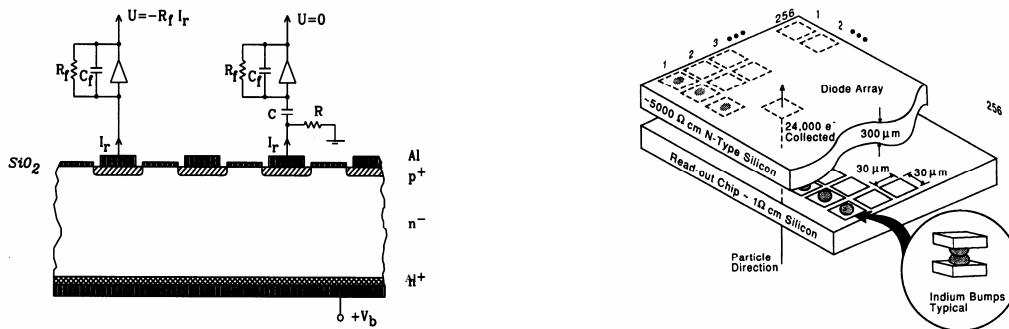


Figure 2.3.:
Left: *Schematic view of a silicon strip detector. The $n^-$ forms the sensitive medium. It is depleted by the junction to the $p^+$. A backside contact and a line contacting the individual strips bias the junction. An example of a direct (left) and capacitive coupled (right) readout is shown.*
Right: *Schematic view of a hybrid pixel detector. The detector is composed of a sensor chip (top) and a readout chip (bottom). The sensor contains diode structures comparable to ultra short strips which form the pixel. The readout of the pixels is obtained by ball bonding the sensor on a CMOS readout chip containing the amplifiers and readout logic. From [25].*

A cross section of a *silicon strip detector* is shown in figure 2.3 (left). These detectors are usually built on a lowly N-doped wafer $(n^-)$, which gets depleted and forms the sensitive layer. The electric voltage required is delivered by the backside contact (lowest layer) and by the aluminum strips $(Al)$. Highly doped contacts $n^+$ and $p^+$ are used to complete the diode. In the following, the strips have to be individually bonded to an amplifier outside of the sensor. The additional $n^+$

---

[6]A good description of the dependency of the break down voltage of a PN-junction and the thickness of the depleted zone on the doping concentrations can be found in [21].

implantation eases the operation of of irradiated sensors. As discussed in section 4.1, radiation may convert a $n^-$ material into an effective $p^-$ material. In the presence of the $n^+$, the diode however stays functional, as it converts from a $p^+$ - $n^-$ diode with $n^+$ contact to a $p^-$ - $n^+$ diode with $p^+$ contact.

The principle of strip detectors is also used by the *hybrid pixel detectors*, which are illustrated in the right panel of figure 2.3. In principle they can be regarded as strip sensors with strip length in the order of the strip width, hence the name pixel. In such devices, which are foreseen for the experiments of the CERN – LHC, each individual pixel sensor located on a sensor chip is connected by flip chip bonding to a readout cell located on a separate readout chip. This cell contains a full amplifying chain with integrated discrimination logic and data buffer. It can have a surface as small as $\sim 100~\mu m \times 100~\mu m$. This leads to a reliable detector with an excellent time resolution and good radiation hardness. However, the spatial resolution of the devices is still in the order of some 10 $\mu m$ and the presence of two chips plus the ball bonds lead to a substantial material budget and consequently to substantial multiple scattering.
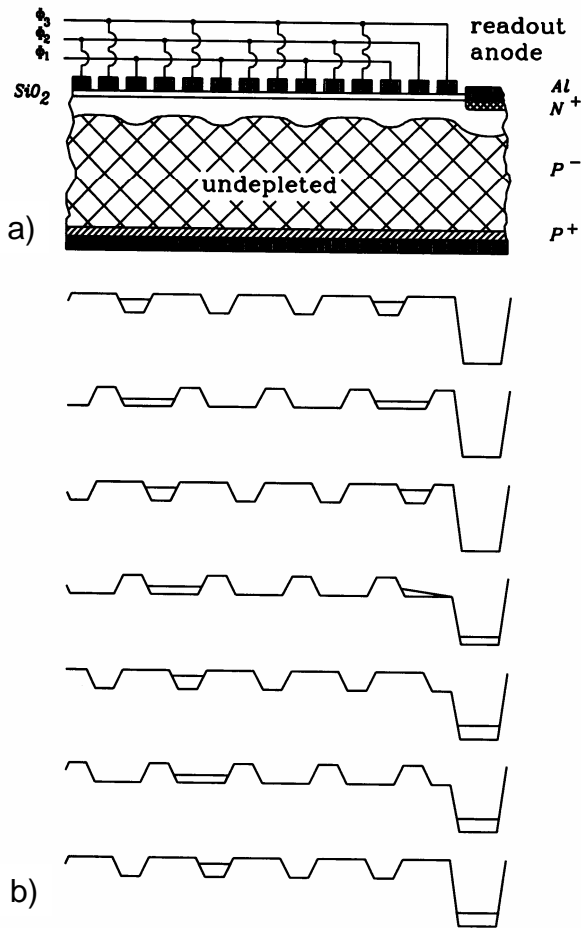


Figure 2.4.:
*Schematic view of a CCD (a). In the example, the sensitive medium of the detector is formed by a partially depleted $P^-$ layer. Contacts on its top generate potential minima in the silicon, which define the pixels. As shown in (b), a modulation of the fields transports the generated charge to the collecting diode ($N^+$). From [25].*

Another approach, which overcomes these two points, is followed by the *CCD (charged coupled devices)*. The working principle of this detector is shown in figure 2.4. CCDs collect their charge in local potential pockets in the $P^-$ layer (white), which are formed respectively shaped by electric fields. During the read-out process, this charge is transported towards the readout electronics by manipulating the position of the potential valley such, that it moves towards the readout anode. This anode is formed by a $N^+$ implantation, which, together with the $P^-$ of the bulk, again

realizes a diode. This technology can be modified in order to deplete fully the bulk.

The transport of the charge within the silicon has some important advantages. Only one readout chain is required to readout the full detector. This substantially reduces the complexity of the device, in particular the complexity of the pixel logic. The field plates required to generate the electric fields of a pixel can be integrated on a very small surface. A pixel pitch of $\sim 10\ \mu m$ gets thus possible. Moreover, the leakage current of these pixels is significantly lower than the ones of the hybrid pixel detectors. Consequently the noise of the pixel is reduced and the sensors can be operated with thinner sensor material, even at the price of smaller signals.

Over all, CCDs form extremely high granular detectors for charged particles, which can be thinned down to very low material budget. However, the charge transport in the silicon also restricts this technology. On the one hand, the transport process is relatively slow, which reduces the readout speed of the CCDs. On the other hand, this kind of readout works only, if the lifetime of the charge carriers in silicon is sufficiently high. This condition is fulfilled in high quality silicon but it gets an obstacle, if the quality of the material is reduced by radiation damage. CCDs are therefore also limited in terms of radiation hardness.

## 2.2. Building a Sensor in a CMOS process

### 2.2.1. Why CMOS pixels?

Conventional pixel detectors like CCDs and Hybrid Pixels have demonstrated their abilities to detect charged particles with good efficiencies. Nevertheless, both technologies show particular weak points. Because of the material needed for the second chip and the ball bonding, hybrid pixel detectors have typically a high material budget. Moreover, the minimum pixel pitch is constrained by the diameter of the balls used for bonding. CCDs are substantially thinner and may provide very small pixels. On the other hand, their radiation hardness is poor.

Moreover, both technologies require dedicated, lowly doped silicon material for reaching a sufficiently thick depleted zone. Specialized production facilities are required for a production of these sensors, as this material and the necessary structures are of modest interest for industrial applications. Maintaining such facilities causes high costs and they can usually not provide the low feature sizes allowing for an integration of efficient readout electronic circuits on the same substrate used for the sensor elements.

Sensors based on standard industrial CMOS processes, allow overcoming these complications, as sensor and readout electronics can be integrated on the same chip. Moreover, established and well understood industrial facilities providing low feature sizes can be used for their production. This dramatically reduces the costs, and allows the use of established simulation models for designing the microcircuits. This simplifies significantly the design of the detector system and allows for fast design iterations.

The price to be paid for the use of CMOS processes is reduced flexibility for some parameters, as the production processes are optimized for general electronics and cannot be changed by the users. A design has therefore to restrict itself to the predefined structures which are available in the process.

### 2.2.2. Structures in a typical CMOS process

A typical CMOS chip has three complementary functional layers, which are schematically shown in figure 2.5.
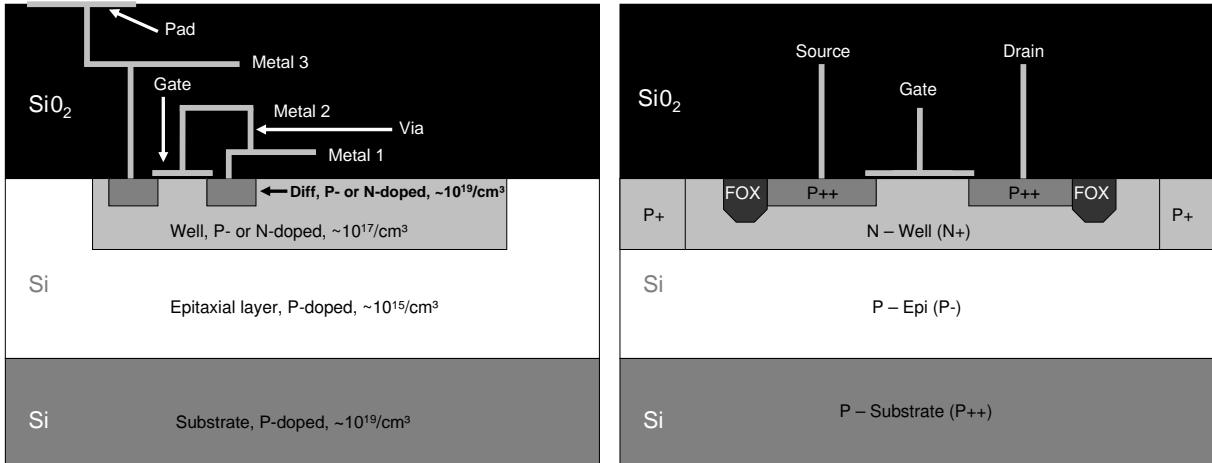
Figure 2.5.:
*A simplified picture of the most important structures available in a CMOS chip is given on the left side. The right side shows the typical integration diagram of an PMOS transistor into a CMOS process. Source and drain of the transistor are formed by P-diffusions (P++). The bulk of the transistor is an N-Well. The gate is formed by a metal or poly-silicon plate, which is separated from the conducting channel by a thin, so-called gate oxide. Field Oxide (FOX) typically made of $SiO_2$ are to insulate the transistor from potential other components (not shown).*

- The lowest layer is referred as wafer or substrate. It is made of highly doped, crystalline silicon and has a typical thickness of several $100~\mu m$. Within a microchip, it provides the mechanical stability and hosts all other structures. As this layer has no dedicated electric functionality, a moderate quality of the material in terms of crystal defects is sufficient. This simplifies the production of this material.

- A layer of epitaxial silicon is deposited on top of the substrate. This silicon has a higher quality than the one of the substrate; in particular, the amount of crystal defects is reduced. Moreover, the doping of this layer is typically some orders of magnitude lower than the one of the substrate. This increases the resistivity of the material and reduces parasitic currents. The active silicon components forming transistors and diodes are embedded into this epitaxial layer. In the processes used for this work, two different types of implantations with different properties are available.

- The so-called Well implantations are intended to serve as a bulk for Field Effect Transistors (FET). Their doping is higher than the one of the epitaxial layer. P- and N-doping can be chosen for this implantation, which allows for integrating PMOS and NMOS transistors into the microchip:

- The so-called Diff implantations are to form source and drain of the FETs. They have again a higher doping than the Well-implantations. As they are also thinner, they can be embedded into Wells, which is mandatory for constructing a transistor. Again, both types of doping can be chosen

- In order to connect the different silicon structures of the microchip, metal lines are used. These metal lines are typically made of aluminum and embedded into silicon oxide, which serves as an insulator. The processes used for building the detectors discussed in this work provide three to five layers of metal lines. Substantially more layers are provided by processes with lower feature sizes.

In general, parameters like the doping concentrations and the thickness of the different structures are predefined in the production process. Their position, surface layout and the type of doping can be chosen in the limits given by the production technology.

The doping levels of the different implantations are usually not published. For the epitaxial layer, a P-doping of roughly $10^{15}$ $cm^{-3}$ is considered as a realistic estimate. This value is by order of magnitudes above the doping level of the silicon, which is typically used for depleted detectors. The doping level of the Well implantations exceeds the one of the epitaxial layer by roughly two orders of magnitude. The doping of the Diff-implantations is itself by two orders of magnitude above that of the Well-implantations.

**Example: A transistor in the CMOS process** In order to illustrate the integration of electronic components into a CMOS process, the typical layout of an NMOS transistor is shown in figure 2.5. One sees the transistor bulk, which is formed by an N-Well implantation. The source and drain of the transistor is formed by a P-Diff implantation. A thin poly-silicon layer [7], which is isolated from the bulk with a thin gate oxide, forms the gate of the transistor.

It should be mentioned, that the thickness of this gate oxide amounts to only a few nanometers. This is to ease applying electric fields to the bulk of the transistor and stands in contrast to the substantially higher thickness of the standard oxide used for insulation. The latter is also partly implanted into the silicon, where it forms field oxide structures (FOX). This is to increase the conducting path between different silicon structures and thus to reduce the parasitic currents between them.

The different thickness of the thin gate oxide and the isolation oxide will be of importance for radiation hardness.

### 2.2.3. The sensor of a MAPS-detector

#### 2.2.3.1. Basic design

An essential design aspect for sensors manufactured in CMOS technology is the high doping, which reaching a sizable thickness of the depleted zone of a a reversed biased diode. A structure replacing this depleted volume has therefore to be found. The way out is a structure, which collects the charge carriers excited by radiation by means of thermal diffusion. This allows obtaining a sufficiently thick sensing volume without using strong electric fields. It exploits the relatively long lifetime of the charge carriers in silicon.

A sandwich of three differently P-doped silicon layers is used for guiding the intrinsically undirected diffusion of electrons towards the thin depleted volume of the collection diodes of the sensor, which are only weakly biased. This sandwich is shown in figure 2.6. Its moderately doped central layer of this sandwich ($P^-$) forms the active volume of the detector. The layers surrounding this area are highly doped ($P^+$).

The $P^+$ - $P^-$ junction produces a build-in-voltage, which is given by:

$$V_{bi} = \frac{k_B T}{q} \, ln \left( \frac{N_{P+}}{N_{P-}} \right) \tag{2.8}$$

where $N_{P+}$ and $N_{P-}$ represent the doping density of the $P^+$ and $P^-$ material respectively, $k_B$ is the Boltzmann-constant, $T$ the temperature and $q$ the elementary charge.

---

[7]In the early CMOS processes, this layer was made of aluminum. The use of conducting silicon is preferred nowadays, as it reduces the mechanical stress in the gate oxide.
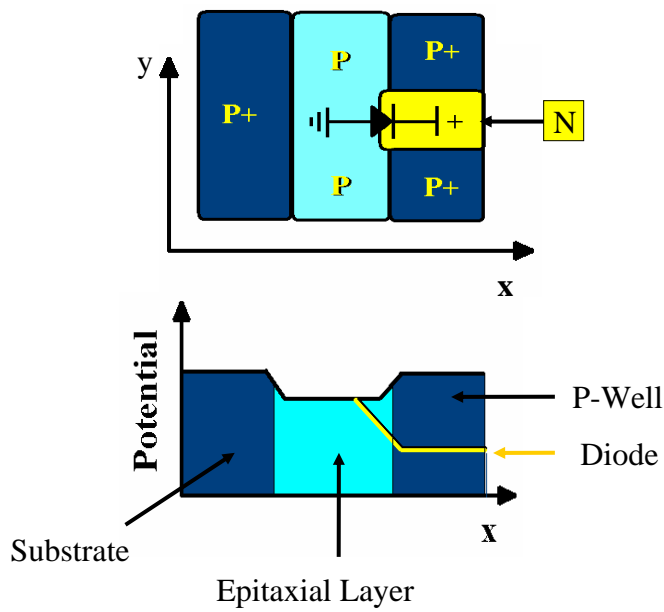
Figure 2.6.:
(Top):*A qualitative doping profile of a MAPS sensor. The geometry of the sensor is shown in the upper plot. P+ corresponds to areas with high doping; P corresponds to areas with moderate doping. The collecting diode (yellow) is highly doped.*
(Bottom): *A qualitative profile of the potential of the conduction band of the silicon, which is consequence of the structure shown above.*

The junctions generate a repulsive potential, which reflects the diffusing signal electrons. They can therefore diffuse freely within the central layer, but cannot leave it and are guided towards the collection diodes, which are formed by N-doped implantation breaking one of the highly P-doped layers. In this design, the thickness of the active area is given by the thickness of the central layer, which can be significantly thicker then the depleted zone of the diode.

### 2.2.3.2. Integration of the sensor into a CMOS process

In a CMOS process, the moderately doped epitaxial layer may serve as active volume of the sensor. The highly doped borders are formed by the substrate on the one side and by a P-Well implant on the other. The collecting diode realized by an N-well implantation.

This integration allows implementing the active volume of the sensor underneath the implantations used for building transistors. Consequently, almost the full set of structures delivered by a CMOS process can be integrated on the same surface together with the sensor. This allows the envisaged integration of the sensors together with control electronics, preamplifier, discriminator and further advanced analogue and digital microcircuits on the same substrate.

Nevertheless, there exists one important exception. As its integration would demand for an N-Well implantation comparable to the one forming the collection diode, PMOS transistors cannot share the same surface with the sensor. Their presence would lead to a competitive collection of the signal electrons and absorb the signal charge required for the sensing. Structures requiring PMOS transistors, like for example comparators, may be installed on the same chip but have to be put outside of the active area.

### 2.2.3.3. Thickness of the sensitive volume

As the thickness and doping of the epitaxial layer is a fixed feature of the individual CMOS production process, they can be varied only by choosing adapted processes. A typical thickness of the layer is in the order of 10 $\mu m$. It is therefore by more than one order of magnitude thinner than a standard microchip, as the thickness of such a chip is dominated by the thickness of the substrate.

The substrate of the chip has only one electrical functionality, which is the reflection of the diffusing electrons back towards the epitaxial layer. As this is a property of the interface between substrate and epitaxial layer, the substrate can be partly removed. This potentially allows for thinning the chip hosting the MAPS down to a thickness of few tens of micrometers. As thin sensors are preferred as they limit multiple scattering, this is considered as very favorable aspect.

On the other hand, the modest thickness of the active volume also limits the charge generation around 800 signal electrons. Moreover, because of the diffusion, this charge is distributed over several pixels. Very low noise amplifiers have to be added to the sensor in order to convert this little charge into a useful detector signal.

### 2.2.4. The on-pixel preamplifiers: Properties and signal encoding

Minimizing the input capacity of the first amplification stage is mandatory for this conversion. This requires building it closest to the source of the signal, which means integrating it into the pixel. No PMOS transistors can thus be used for the design. As additional requirement, the preamplifiers have to compensate the leakage current of the collecting diode. This current is usually only in the order $fA$, but its presence has sets important constraints on the design of the amplifiers.
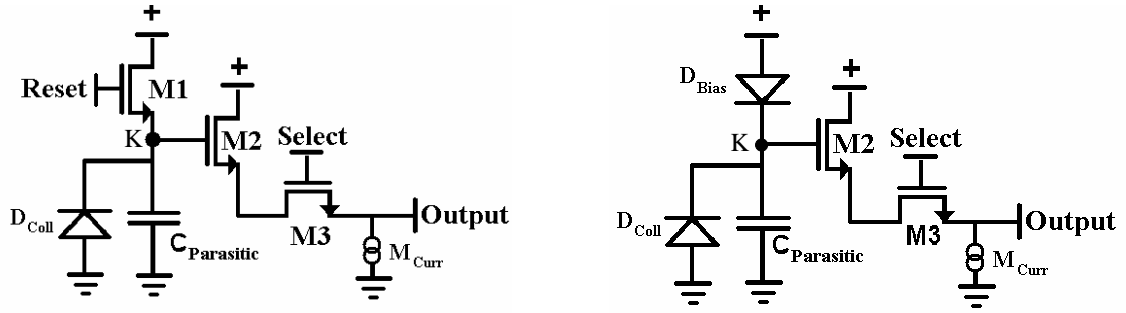
Figure 2.7.: *Diagram of the 3T-Pixel (left) and of the SB-pixel (right).*

Different preamplifiers have been developed in order to fulfill these requirements. Two of them are of particular importance for this work. They both follow the same amplification strategy but use different methods to compensate the leakage current. This either is done by restoring the charge in the capacitors of the pixel by means of a classical reset, using a reset switch, or by continues bias using a forward biased diode. The diagrams of both amplifiers is shown in figure 2.7. In the following, pixels containing an amplifier relying on a reset transistor will be referred as 3T-pixels. Pixels with biasing diode will be called self-bias (SB)-pixel.

### 2.2.4.1. The charge-to-voltage conversion

The amplification stage of both amplifiers relies on a small (parasitic) capacitor and on a source follower, which can be formed by an NMOS transistor connected to a current source located outside of the chip. The first step for the amplification is done with the help of the capacity $C$, which is dominantly formed by the capacity of the collecting diode. This capacity is initially charged positively to a potential $U_1$. This voltage is measured between the point $K$ and ground ($GND$) (see figure 2.7).

If the sensing diode collects charge carriers representing an amount of charge equal to $Q_{Col}$, they discharge the capacitor and thus deliver an additional voltage signal given by

$$U_{Col} = \frac{Q_{Col}}{C} = \frac{Q_2 - Q_1}{C}. \tag{2.9}$$

where $Q_1$ represents the charge initially present in the capacitor and $Q_2$ stands for the charge remaining after the collection process. As a consequence, the potential in the node $K$ drops to a new value

$$U_2 = U_1 - U_{Col} \tag{2.10}$$

which is transferred to the gate of the source follower transistor $M2$.

This source follower converts a constant potential on its input node towards a voltage source at its output, which has roughly the same potential as the input node. The signal at the output of the source follower is consequently given by

$$U_{Out_1} = g_S \cdot U_1 \qquad U_{Out_2} = g_S \cdot U_2 \tag{2.11}$$

where $g_S \lesssim 1$ represents the gain of the source follower. The voltages $U_{Out_1}$ and $U_{Out_2}$ are delivered to the output of the chip via additional buffers and can be measured.

### 2.2.4.2. Deriving the collected charge from measurements: The correlated double sampling

In order to derive $Q_{Col}$ from these output voltages, one has to subtract the voltages representing the charges present in the capacitor before and after the charge collection cycle:

$$\Delta U_{Out} = U_{Out_2} - U_{Out_1} = g_S \; (U_2 - U_1) = \frac{g_S}{C} \; (Q_2 - Q_1) = \frac{g_S}{C} \; Q_{Col} \tag{2.12}$$

For reasons discussed later in this section, it is not possible to measure the output voltage of each pixel of a MAPS detector continuously, as many pixels share one readout chain. The signal of the pixels is multiplexed on an individual line, which allows accessing the individual pixels in a regular period. Within this time period, the pixels integrate all impinging charge into their capacity without communicating with to the outside world. It is therefore named *integration time* $t_{Int} := t_2 - t_1$. [8]

Be $U_{Out_1}$ and $U_{Out_2}$ the output signal of the pixel at the time $t_1$ and $t_2$ respectively. Than it is justified to translate equation 2.12 to

$$U_{Out}(t_{1,2}) := U_{Out}(t_2) - U_{Out}(t_1) = \frac{g_S}{C} \; (Q(t_2) - Q(t_1)) = \frac{g_S}{C} \; Q_{Col}(t_{1,2}) \tag{2.13}$$

where

$$Q_{Col}(t_{1,2}) := \int_{t_1}^{t_2} I_C(t) \; dt \tag{2.14}$$

represents the charge integrated in the capacitor between the time $t_1$ and the time $t_2$. $I_C(t)$ stands for the current charging the capacitor of the pixel and $U_{Out}(t_{1,2})$ for the corresponding variation of the output voltage.

This way of deriving $Q_{Col}(t_{1,2})$ by subtraction is called *correlated double sampling (CDS)*, if $U_{Out}(t_1)$ and $U_{Out}(t_2)$ are obtained each by individual measurements. The advantage of using the subtraction is that the initial charge of the capacity $Q(t_1)$ may vary without influencing the result on $Q_{Col}(t_{1,2})$. As explained in the following, $Q(t_1)$ indeed encompasses important uncertainties in MAPS pixels, which are canceled out by $CDS$.

It is worth noticing, that $Q_{Col}(t_{1,2})$ is usually negative in this description, as the electrons collected reduce the charge loaded into the pixel capacity. This holds also for $U_{Out}(t_{1,2})$.

### 2.2.4.3. Currents in a MAPS pixel

The current $I_C(t)$ is made of three contributions. The obvious ones are the *leakage current* of the collection diode and the signal current reflecting the collection of signal charge. While the leakage current can be considered as constant, the signal current forms a short current pulse. This is because the charge collection process is usually fast with respect to the integration time. The third contribution comes from the a recharge current implemented to compensate the leakage current and to avoid a total discharge of the pixel capacity, which would drive the pixel into saturation.

Taking into account these contributions, one can write

$$I_{Col}(t) = I_{ReC}(t) - I_{Cur}(t) - I_{Phy}(t) \tag{2.15}$$

---

[8] In order to ease the understanding of the following calculations, the following symbols will be used:
Left hand side is equal to the right hand side is symboled by "=".
Left hand side is equal by definition to the right hand side is symboled by ":="
Left hand side has to be equal to the right hand side (condition) is symboled by " $\overset{!}{=}$ "

where $I_{ReC}$ represents the recharge current, $I_{Cur}$ represents the leakage current of the diode and $I_{Phy}$ the current caused by free electrons generated by an impinging particle in the sensor. The total integrated charge is given by

$$Q_{Col}(t_{1,2}) \quad = \quad \int_{t_1}^{t_2} I_{Col}(t) \ dt = \int_{t_1}^{t_2} (\ I_{ReC}(t) - I_{Cur}(t) - I_{Phy}(t)\ ) \ dt \tag{2.16}$$

$$\Rightarrow Q_{Col}(t_{1,2}) \quad = \quad Q_{ReC}(t_{1,2}) - Q_{Cur}(t_{1,2}) - Q_{Phy}(t_{1,2}) \tag{2.17}$$

with

$$Q_{ReC}(t_{1,2}) \quad := \quad \int_{t_1}^{t_2} I_{ReC}(t) \ dt \tag{2.18}$$

$$Q_{Cur}(t_{1,2}) \quad := \quad \int_{t_1}^{t_2} I_{Cur}(t) \ dt \tag{2.19}$$

$$Q_{Phy}(t_{1,2}) \quad := \quad \int_{t_1}^{t_2} I_{Phy}(t) \ dt \tag{2.20}$$

The charge contributions defined in equations 2.18 to 2.20 will used in the discussion of the algorithms allowing to identify particle hits.

### 2.2.4.4. The need for leakage current compensation

Besides converting the charge $Q_{Col}(t_{1,2})$ into a signal, which can be measured, the preamplifiers of the pixels have to ensure that the pixel capacitor is not fully discharged by the leakage current. A discharged capacitor would make the pixel insensitive to additional charge and thus blind to particles. The pixel has therefore to compensate the integrated charge. This is equivalent to fulfilling the condition

$$\int_{-\infty}^{\infty} I_{Col}(t) \ dt \overset{!}{=} 0 \tag{2.21}$$

despite of the presence of the leakage current ($I_{Cur} > 0$). Moreover, it must be possible to identify the signal charge in order to detect particles. It is therefore necessary to fulfill a second condition, which is

$$Q_{Col}(t_{1,2}) = \int_{t_1}^{t_2} I_{Col}(t) \ dt \overset{!}{=} -Q_{Phy}(t_{1,2}) + Q_{Const}(t_{1,2}). \tag{2.22}$$

It has to be pointed out that the presence of a constant integrated charge $Q_{Const}(t_{1,2})$ can be tolerated in equation 2.22, as long as it is known with sufficient accuracy.

### 2.2.4.5. Leakage current compensation in the 3T-pixel

The natural way for fulfilling simultaneously the condition exposed by the equations 2.21 and 2.22 in parallel consists in two alternating cycles in the pixel operation. This alternating cycle is used in the 3T-pixel, which is read out before and after the integration period, while the reset

transistor $M1$ is closed. No recharge current is thus within the integration time. Next, the reset transistor is opened and the capacitor is recharged again to the initial voltage (which corresponds to setting the pixel capacitor back to its initial charge). This corresponds to the period between $t_2$ and $t_3$.

In the first cycle, the recharge current is set to zero in the time slot from $t_1$ to $t_2$. It thus temporarily fulfills condition 2.22

$$Q_{Col}(t_{1,2}) = \int_{t_1}^{t_2} I_{Col}(t) \ dt = \int_{t_1}^{t_2} (\ 0 - I_{Cur}(t) - I_{Phy}(t) \ ) \ dt = -(Q_{Phy}(t_{1,2}) + Q_{Cur}(t_{1,2})) \quad (2.23)$$

as the leakage current $I_{Cur}(t)$ can be considered as constant. The recharge current in the period $t_{2,3}$ is (by definition) sufficient high to fulfill the condition:

$$Q_{Col}(t_2^3) = \int_{t_2}^{t_3} I_{ReC}(t) - I_{Cur}(t) - I_{Phy}(t) \ dt := -Q_{Col}(t_{1,2}) \quad (2.24)$$

This allows to fulfill condition 2.21, since

$$\int_{t_1}^{t_3} I_{Col}(t) \ dt = Q_{Col}(t_2^3) + Q_{Col}(t_{1,2}) = 0 \quad (2.25)$$

It should be mentioned, that within the reset process, the pixel is not sensitive to particles, as any signal charge is instantaneously canceled out. Moreover, the potential reached after the reset process is not perfectly reproduced. The use of $CDS$ is therefore mandatory for compensating this.

### 2.2.4.6. Leakage current compensation in the SB-pixel

The SB-pixel has been designed in order to overcome two disadvantages of the 3T-pixel. The first of them is the dead time consumed by the reset cycle. The traditional reset cycle, which needs to reset and hereafter to address each pixel to measure $U_{Out}(t_1)$, causes a dead time of slightly above 50%. The second weak point is the need to distinguish $Q_{Phy}(t_{1,2})$ from $Q_{Cur}(t_{1,2})$. For technical reasons, it is difficult to achieve this with an on-chip microcircuit outside of the pixel. A distinction executed in the pixel itself is the preferable solution.

In order to achieve it, the reset transistor is replaced by a forward biased diode ($D_{Bias}$ in figure 2.7). It provides a current, which is sufficient to compensate the charge lost through the leakage current. As long as the sensor is not hit by a particle, this corresponds to setting

$$I_{Eff}(t) := I_{ReC}(t) - I_{Cur}(t) = 0 \quad (if \ I_{Phy}(t) = 0). \quad (2.26)$$

In this equation, $I_{Eff}$ is the effective recharge current of the pixel capacitor. Condition 2.21 is obviously fulfilled, as the charge of the pixel capacitor remains constant.

Consider now, that the SB-pixel is hit by a particle at a time $t_{Hit}$. This time is in general not equal to the readout times $t_1$ and $t_2$ but lies in between ($t_1 < t_{Hit} < t_2$). At this time, it collects instantaneously a signal charge of $Q_{Phy}(t_{1,2})$ [9], which reduces the potential of the pixel according to 2.12 by

$$\Delta U_{Hit} = -\frac{g_S}{C} \ Q_{Phy}. \quad (2.27)$$

---

[9] We assume for simplification, that the pixel is hit only once in the period $t_{1,2}$.

This change of the potential at the node $K$ of the pixel increases the current passing the biasing diode $D_{Bias}$. Consequently, recharge current and leakage current are not in equilibrium anymore and an effective recharge starts current recharging the pixel capacity.

$$I_{Eff}(t > t_{Hit}) = I_{ReC}(t) - I_{Cur}(t) > 0 \tag{2.28}$$

Since the recharge process involves the interaction between two non-linear electronic components (the sensing and the biasing diode), a rather complex function was expected for the effective recharge current. However, it was empirically found, that the equation

$$I_{Eff}(t > t_{Hit}) = A_0 \cdot e^{-\frac{(t-t_{Hit})}{\tau}} \tag{2.29}$$

provides a satisfactory description. In this context, the constant $\tau$ is the decay constant of the recharge current and $A_0$ a normalization constant.

In order to fulfill condition 2.21, the collected charge has to be canceled out by the recharge process. In the optimal case of a low hit density, one can assume the pixel not to be hit a second time, before the charge of the first hit is completely removed. This leads to the following condition on the recharge process:

$$\int_{t_{Hit}}^{\infty} I_{Eff}(t) \, dt \overset{!}{=} Q_{Phy}(t_{1,2}) \tag{2.30}$$

The positive sign of $Q_{Phy}(t_{1,2})$ is required, as the initial signal charge contributes with negative sign to the total charge loaded in the capacitor. With

$$\int A_0 \cdot e^{-\frac{(t-t_{Hit})}{\tau}} \, dt = -A_0 \, \tau \cdot e^{-\frac{(t-t_{Hit})}{\tau}} \tag{2.31}$$

one finds this condition to be fulfilled, if

$$A_0 = \frac{Q_{Phy}(t_{1,2})}{\tau} \quad . \tag{2.32}$$

With this information, equation 2.29 becomes

$$I_{Eff}(t > t_{Hit}) = \frac{Q_{Phy}(t_{1,2})}{\tau} \cdot \exp\left(-\frac{t - t_{Hit}}{\tau}\right) \tag{2.33}$$

While this recharge current allows to bring the pixel back to its equilibrium, it also cancels out the signal charge $Q_{Phy}(t_{1,2})$ in the period between the hit and the second readout. Measuring this signal charge, and thus fulfilling condition 2.22, is only possible, if the recharge process is sufficiently slow, i.e.:

$$\int_{t_{Hit}}^{t_2} I_{eff}(t) \, dt = \frac{Q_{Phy}(t_{1,2})}{\tau} \cdot \exp\left(-\frac{t - t_{Hit}}{\tau}\right) \ll Q_{Phy}(t_{1,2}) \tag{2.34}$$

In this case,

$$Q_{Col}(t_{1,2}) = \int_{t_1}^{t_2} I_{Col}(t) \, dt = \int_{t_1}^{t_2} I_{Eff}(t) - I_{Phy}(t) \, dt \approx -Q_{Phy}(t_{1,2}) \quad . \tag{2.35}$$

*2. Monolithic Active Pixel Sensors*

The amount of charge, which has been canceled out by the recharge current is given by $Q_{Phy}(t_{1,2}) - Q_{Col}(t_{1,2})$. It can be estimated by approximating the effective recharge current short after the hit. One finds

$$I_{Eff}(t_{Hit}) = \frac{Q_{Phy}}{\tau} \quad . \tag{2.36}$$

In the period between the hit, which appears for instance at

$$t_{Hit} \approx \frac{t_2 + t_1}{2} \quad , \tag{2.37}$$

and the readout of the second sample $t_2$, $I_{Eff}$ removes a part of the signal. In a first order approximation, this part is given by

$$Q_{Phy}(t_{1,2}) - Q_{Col}(t_{1,2}) = \int\limits_{t_{Hit}}^{t_2} I_{Eff}(t) \, dt \approx I_{Eff}(t_{Hit}) \cdot \frac{t_2 + t_1}{2} = \frac{Q_{Phy}}{2} \cdot \frac{t_{1,2}}{\tau} \quad . \tag{2.38}$$

The pixel thus fulfills condition 2.22, if

$$Q_{Phy}(t_{1,2}) - Q_{Col}(t_{1,2}) \approx \frac{Q_{Phy}}{2} \cdot \frac{t_{1,2}}{\tau} \ll Q_{Phy} \quad , \tag{2.39}$$

which is fulfilled if $\tau \gg t_{1,2}$.

The fraction of signal $Q_{Lost}$, which was lost before the readout, is approximated with

$$\frac{Q_{Lost}}{Q_{Phy}} \approx \frac{1}{2} \frac{t_{1,2}}{\tau} \quad . \tag{2.40}$$

From equation 2.40 one learns, that the SB-Pixel can be used only with a fast readout. As $\tau$ is typically in the order of $10 - 100 \ ms$, an integration time $t_{1,2} \lesssim 1 \ ms$ or faster is recommended.

### The SB-Pixel at high particle rates

The assumption of a negligible hit rate does not fit to the situation in CBM. The case was therefore studied, where the sensor is exposed to a high hit rate. To study this situation one assumes the hits to impinge with a fixed frequency and to excite the same amount of charge carriers each time. In this situation, equilibrium can only be reached if the recharge process removes the signal of the first hit before the second one impinges. From the electronics point of view, the additional current required can easily be delivered, as the potential of the pixel node is reduced until the voltage on the biasing diode is sufficiently high.

In order to model this situation, one assumes $\tau$ to remain constant. Moreover, one assumes one particle to impinge within a period $t_{1,2\,Hit} = t_{2Hit} - t_{1Hit}$. Again, each of these particles deposes a signal charge $-Q_{Phy}$. One has then to replace the condition set in equation 2.30 by the following one:

$$\int\limits_{t_{1Hit}}^{t_{2Hit}} I_{Eff}(t) \, dt = \int\limits_{t_{1Hit}}^{t_{2Hit}} A_1 \cdot \exp\left(-\frac{t - t_{1Hit}}{\tau}\right) = \tau \, A_1 \left[1 - \exp\left(\frac{t_{1Hit} - t_{2Hit}}{\tau}\right)\right] := Q_{Phy} \tag{2.41}$$

In this calculation, $t_{Hit} := t_{1Hit}$ was set. This equation has to be solved to $A_1$:

$$A_1 = \frac{Q_{Phy}}{\tau \left[1 - \exp\left(\frac{t_{1Hit} - t_{2Hit}}{\tau}\right)\right]} = \frac{Q_{Phy}}{\tau \left[1 - \exp\left(-\frac{t_{1Hit}^2}{\tau}\right)\right]} \tag{2.42}$$

The effective recharge current then increases to

$$I_{Eff}(t, t_{1Hit}^2) \quad = \quad \frac{Q_{Phy}}{\tau \left[ 1 - \exp \left( -\frac{t_{1Hit}^2}{\tau} \right) \right]} \cdot \exp \left( -\frac{t - t_{1Hit}}{\tau} \right) \tag{2.43}$$

$$I_{Eff}(t, t_{1Hit}^2) \quad = \quad \frac{I_{Eff}(t)}{1 - \exp \left( -\frac{t_{1Hit}^2}{\tau} \right)} \tag{2.44}$$

Again, this result can be used in order to approximate the signal loss. One finds

$$Q_{Phy}(t_{1,2}) - Q_{Col}(t_{1,2}) \approx I_{Eff}(t_{1Hit}, t_{1Hit}^2) \cdot \frac{t_2 - t_1}{2} = \frac{t_{1,2}}{2\tau} \cdot \frac{Q_{Phy}}{1 - \exp \left( -\frac{t_{1Hit}^2}{\tau} \right)} \tag{2.45}$$

and consequently

$$\frac{Q_{Lost}}{Q_{Phy}} \approx \frac{t_{1,2}}{2\tau} \cdot \frac{1}{1 - \exp \left( -\frac{t_{1Hit}^2}{\tau} \right)} \tag{2.46}$$

If the relative amount of lost charge should not exceed a defined fraction of $Q_{Phy}$, the integration time has to be chosen like

$$t_{1,2} \lesssim 2\tau \cdot \frac{Q_{Lost}}{Q_{Phy}} \cdot \left[ 1 - \exp \left( -\frac{t_{1Hit}^2}{\tau} \right) \right] \tag{2.47}$$

A Taylor expansion in first order allows to obtaining:

$$t_{1,2} \lesssim 2 \, t_{1Hit}^2 \cdot \frac{Q_{Lost}}{Q_{Phy}} + O[(t_{1Hit}^2)^2] \qquad ( \, if \, (t_{1Hit}^2)^2 \ll \tau) \tag{2.48}$$

Some comments should be made concerning equation 2.48 and the SB-pixel:

- Provided a sufficiently long recharge constant $\tau$ and a sufficiently low integration time $t_{1,2}$, the SB-pixel works without dead time. This is because only a small fraction of newly impinging signal charge is lost because of the recharge process.

- The use of $CDS$ is nevertheless mandatory, as the actual charge of the pixel capacity varies substantially depending on the history of impinging hits. $CDS$ allows to compensate this variation.

- SB-pixels react to high occupancy by a faster recharge. They go therefore not in saturation.

- Unlike 3T-pixels, SB-pixels have an intrinsic limit for their occupancy. Exceeding this value, a substantial amount of the signal charge is canceled out before readout is possible.

### 2.2.4.7. Signal encoding

The different ways of encoding the signal into the output data stream of the different detectors is illustrated in figure 2.8.

The left panel addresses the 3T-pixel. The potential of this pixel in the node $K$ decreases linearly as long as the reset transistor is closed, as the capacity loses charge because of the constant leakage current. In this period of time, the pixel is twice connected with the readout system and the potential is measured by the ADC. The integration time of the pixel is started by the first sampling (point 1) and stopped by the second sampling (point 2).

After finishing the second measurement, the reset transistor is opened and the pixel is set to its initial potential. As the open reset transistor has a small, unwanted resistivity, this recharge
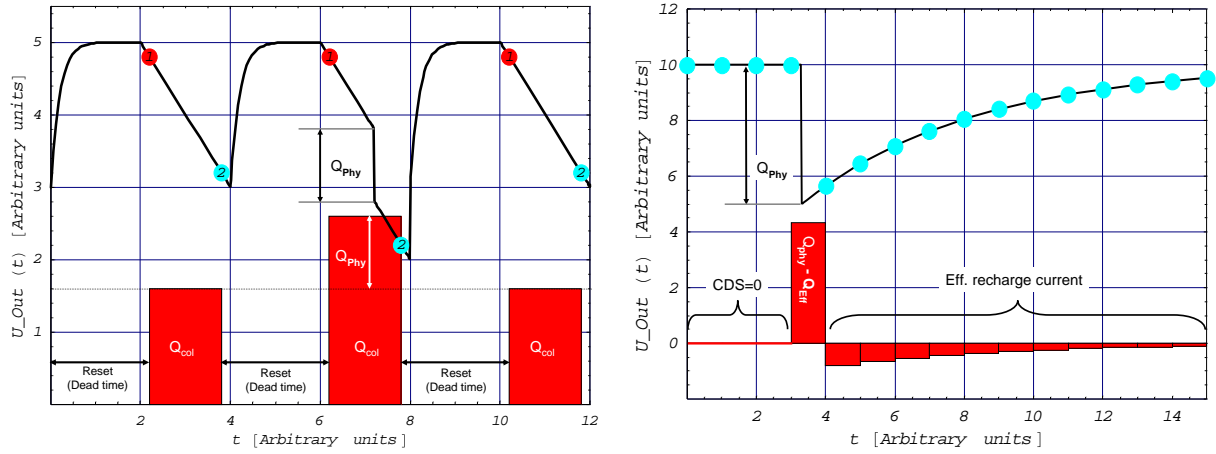
Figure 2.8.:
*The signal encoding for the 3T-pixel (left) and the SB-pixel (right). The potential of the node K is shown in the graph; the points represent the times, the ADC samples the corresponding output signal. The (inversed) signal after CDS is represented by the bar diagram.*

process is comparable to the recharge of an RC-element. The potential reached may thus slightly depend on the charge, which was already present in the capacitor before the reset-transistor was opened.

The dead time of the detector is defined by the time between the point 2 and point 1 of the next cycle. It is in general higher than the true time required for the reset process, as the sequential addressing and reading of the pixels of a chip requires a significant amount of time.

In the second cycle shown in the picture, a charge $Q_{Phy}$ is introduced by a particle. It leads to a faster decrease in the pixel potential and consequently to a higher value obtained after the CDS. The charge needs to be separated from the contribution of the leakage current. This can be done by comparing the cycle containing the signal with the charge, which is collected in other cycles.

The right panel illustrates the output signal of a SB-pixel. Because of the permanent recharge, the output signal after CDS of this pixel is usually zero. The readout points are equivalent as there is no dead time and CDS can be performed by subtracting two consecutive samples. A hit reduces the potential of the pixel, as the recharge process is slower than the charge collection. This leads to a positive signal indication after CDS.

Going into details, one finds that the potential present at the first readout consecutive to the hit is already reduced by the effective recharge current with respect to the true physics charge. The signal indicated by the CDS is therefore in general lower than the true physics charge.

In the readout cycles following to the hit, a negative signal is indicated. This corresponds to the charge integrated within the recharge process.

## 2.2.5. Readout of the pixel arrays

The individual pixels are arranged in to so-called *pixel matrices*, which are defined as the subset of pixels multiplexing their output signal to one common analogue data bus. A schema of such a readout system is shown in figure 2.9. The addressing of the pixels is done with two shift registers, where one of them sets the X-coordinate of the pixel addressed and the other one

defines the Y-coordinate. One of the shift registers opens the M3-Transistors of all pixels of a line and thus connects them to the data bussed leading towards the central amplifier. The other register addresses one of the $M_{Col}$-switches to connect one of these buses with the output. The
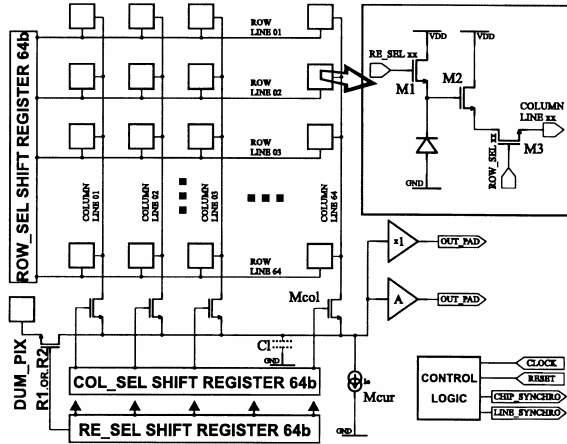


Figure 2.9.:
*Block diagram of a typical MAPS array. The pixels get addressed by two shift registers, which multiplex the output of an individual pixel to the output amplifier. See text.*

use of shift registers leads to a continuous readout of one pixel per clock cycle. If the registers come to the end of a frame, they generate a synchronization signal and start again with the first pixel. Unlike the pixel addressing, which is autonomously done by a logic on the chip, a reset of the system has to be forced from outside by a digital signal. If delivered, the reset transistors of the pixels get opened line by line, which brings the chip back to its original state. This process however consumes a non-negligible amount of time, which is roughly the amount of lines of the matrix in clock cycles.

Within this period, no pixel is connected with the current source $M_cur$. This leads to a problem, as the standard version of this source cannot be deactivated within the reset cycle. The capacity of the line towards the central amplifier, which is the only source of charge available, gets consequently discharged and the potential of the line drops.

Recharging the line before starting the next readout cycle came out to be to time consuming. The dummy pixel therefore was invented to overcome this point. This pixel, which is not meant to be sensing device, gets connected with the line within the reset cycle and delivers the charge required to hold the line potential on a good value.

The output signal of standard the pixel matrix is buffered by an output amplifier and sent to the outside world in form of a serial analogue signal.

## 2.3. Established performances of MAPS

MAPS show several advantages with respect to other detector technologies. One of them is that a pixel is formed by few components only. This allows the design of very small pixels with $< 10~\mu m$ pitch. However, in order to reduce the number of channels, bigger pixels with a typical pitch between $20~\mu m$ and $40~\mu m$ were usually built. All those pixels are sufficiently small to allow for charge sharing. Reading them out analogue (12-bit) readout, one can calculate the center of gravity of the charge spread about different pixels. The spatial resolution ($\sigma$) reached with this concept is plotted in figure 2.10 as a function of the pixel pitch $p$. It can be approximated with

$$\sigma \approx 0.075~p \qquad (2.49)$$
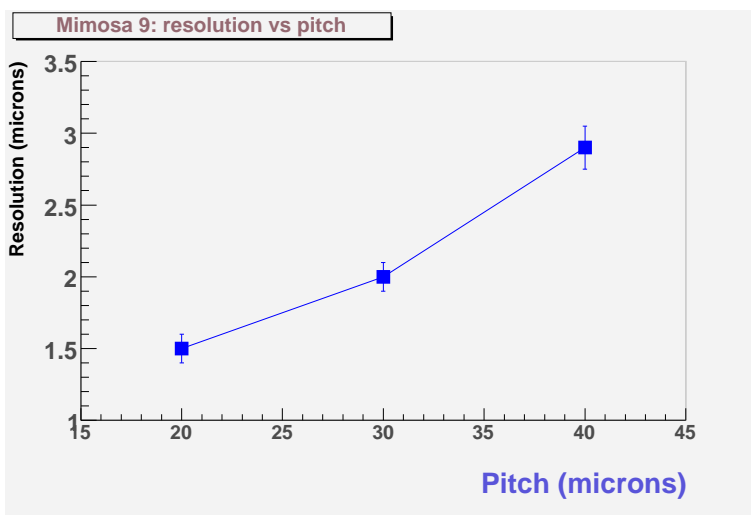
Figure 2.10.:
*The spatial resolution of MAPS (MIMOSA-9) as a function of the pixel pitch. From [26].*

For a pixel with a pitch of $p = 20\ \mu m$, this leads to a $\sigma = 1.5\ \mu m$ The advantage of an analogue readout becomes clear when comparing the resolution of MAPS with the one, one can typically expect from pixels (and strips) with digital readout. This resolution is given by

$$\sigma = \frac{p}{\sqrt{12}} = 0.289\ p \tag{2.50}$$

Simulations based on real data were undertaken in order to project the resolution measured with 12-bit readout to lower resolutions. It was shown, that a fully digital readout on 20 $\mu m$ leads to a resolution of $\approx 5\ \mu m$. This number is still better than the true digital resolution, as typically more than one pixel fires for one hit. The pattern generated allows regaining back a small part of the center of gravity information. For a readout with 3-bits, a spatial resolution slightly better then 3 $\mu m$ is predicted for MAPS with 20 $\mu m$ pitch.
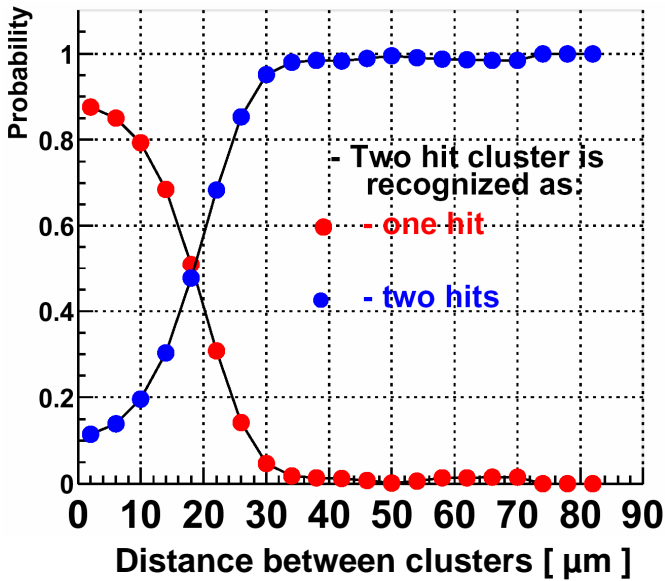


Figure 2.11.:
*The double hit separation capability of MAPS according to simulations on real data. Clusters generated by two true hits were placed close to each other in order to learn, when a merging is indicated. One observes a distance above 30 $\mu m$ to be sufficient to distinguish the two clusters in most cases.*

Another parameter to be taken into account is the double hit separation. The results of a simulation are shown in figure 2.11. One observes, that hits can be distinguished, if they are separated by more than 30 $\mu m$. This holds for a pixel pitch of 20 $\mu m$.

The minimal thickness of MAPS is dominated by the thickness of the epitaxial layer, which is used as sensor. This layer is extraordinary thin and does usually not exceed 20 $\mu m$. Chips with an epitaxial layer down to 4 $\mu m$ were found to deliver a sufficient signal for minimum ionizing particle detection. Roughly 10 $\mu m$ have to be added for the metal and isolating layers required to form the electric connections between the different silicon structures. This leads to a theoretical minimum thickness below 30 $\mu m$. The feasibility of thinning chips down to 120 $\mu m$ was already demonstrated prior to this work.

A thickness of less then 20 $\mu m$ for the sensor of the detector leads to a very low signal produced by every impinging particle. This signal is typically some 100 electrons in the seed pixel [10]. However, the noise of the pixels can be reduced to below 10 electrons equivalent [11]. A typical signal over noise ratio above 20 (most probable value) could thus be demonstrated for the detection

---

[10]As a hit spreads its charge over several pixels, only a part of the signal is seen by each individual one. The pixel with the strongest signal is called seed pixel.

[11]A noise of 10 electrons equivalent means, that the noise is comparable to the signal, which would be generated by 10 electrons.

of minimum ionizing particles. This is sufficient to guarantee a detection efficiency far above 99% combined with a negligible amount of wrong indications (fake hits), which is typically below $10^{-5}$ fake hits per scanned pixel.

The readout speed of MAPS is determined by the number of pixels being multiplexed to one readout line. A readout frequency of $10^7$ pixels per analogue readout line and second was regularly demonstrated with different prototypes. A readout with pixel frequencies up to $5 \times 10^7$ pixels per second and readout line was successfully tested. Combining this readout speed with the amount of pixels required for a sizable detector, a readout time of few milliseconds has to be expected.

The size of a detector chip is limited as a consequence of the CMOS production. As typical microchips like computers have a very limited surface, the maximum size of the masks for lithography is limited to a value below the size of a wafer. The surface of MAPS detectors based on such production cannot exceed the corresponding surface, which is roughly $4\ cm^2$ depending on the production process. The feasibility of using this surface with MAPS for detecting minimum ionizing particles has been demonstrated with the prototype MIMOSA-5.

Another point of interest is the radiation hardness of MAPS. As explained in more detail in chapter 4.1, one has to distinguish between types of interactions between silicon detectors and radiation. Ionizing radiation, which mainly damages the electronics, is produced by interactions between the radiation and the electrons of material. While the atoms remain at their place, the radiation may irreversibly destroy chemical bindings. Non-ionizing radiation dominantly interacts with the atoms of the material, kicking them out of their position in the crystal lattice.

The radiation hardness of MAPS against radiation was widely unknown with the beginning of this work. First measurements suggested a tolerance against $400\ kRad$ ionizing dose and $\sim 10^{12}\ n_{eq}/cm^2$ non-ionizing dose[12]. The latter corresponds to the damage, one can expect from $\sim 2 \times 10^{12}$ minimum ionizing particles impinging $1\ cm^2$ of detector surface.

## 2.4. CBM requirements versus MAPS abilities

The performances of the native MAPS discussed in chapter 2.3 partly fits the requirements of CBM as defined in chapter 1.3.1. In particular, the very good spatial resolution of MAPS and their low material budget are promising. The combination of both features allows fulfilling the requirements on the secondary vertex resolution in a straightforward way.

Questions were open concerning radiation hardness and time resolution. The abilities of the MAPS detectors available in 2003 were by orders of magnitude below the requirements of CBM in both fields. Nevertheless, both issues were not yet addressed in the R&D. Substantial improvements were therefore expected as an outcome of optimization. A feasibility study on $D^0$ detection relying on a MAPS vertex detector has to take into account these improvements. A clarification of the expected performances of optimized MAPS was therefore mandatory.

Besides the abilities of the sensors, the performance of a vertex detector depends on its geometry. This geometry is derived from the measurements envisaged as much as from the specific needs of the sensors for mechanical support and powering.

MAPS are very thin. The structures needed to host them are thus likely to dominate the material budget of the vertex detector. A realistic estimate on the material budget of a vertex detector therefore requires a study on the support structures required.

Over all, the ultimate time resolution of MAPS, their ultimate radiation hardness and their integration into a vertex detector system are identified as crucial questions. A realistic estimate

---

[12]For a detailed definition of the units, the reader is referred to chapter 4.1.

of the performances of future chips is required before simulating the feasibility of open charm detection. They will be covered in the following chapters:

Chapter 3 will discuss the strategies envisaged for improving the time resolution of MAPS. I a second part, a preliminary mechanical concept for system integration will be proposed.

Chapter 4-6 will summarize the outcome of the R&D program, which was to clarify the radiation hardness of MAPS.

# 3. Conceptiunal considerations for a vertex detector based on MAPS

As discussed in chapter 2.4, the material budget and the time resolution (i.e. readout speed) of MAPS were identified as crucial parameters for the feasibility of a MAPS based vertex detector for CBM. Since the request for good time resolution will also determine the geometry properties of the individual MAPS chips, this both aspects will be covered in this chapter.

In the first part, an overview on the design aspects determining the time resolution of MAPS will be given. It will be motivated that the time resolution of the detectors is equal to their frame readout time. The strategies for reducing this readout time by massive parallel readout will be introduced and the technical constraints will be discussed. Finally, the status of the corresponding R&D will be reported.

In the second part, a preliminary concept for a system integration of MAPS will be proposed. Besides the constraints obtained from the required good time resolution, the fact that the detector must be operated in vacuum will be taken into account. As vacuum operation excludes air-cooling, liquid cooling will be proposed and the dimensions of the cooling system will be estimated. The material budget of the proposed structures will be calculated as a function of the energy consumption of the individual detector chips.

## 3.1. A concept for fast MAPS

### 3.1.1. Fundamental considerations

The MAPS detectors developed in Strasbourg between 1999 and 2003 are read out in a serial analogue mode. The analogue output signal of up to $2.5 \times 10^5$ pixels was multiplexed onto a single output line. Digitization is done outside of the chip with a 12–bit ADC. Finally, cluster finding is performed on a PC.

While this approach allows exploiting substantial digital signal processing, the readout speed is limited to $f_P \approx 50~MHz$ for each analogue readout line. This corresponds to a readout time of $T_P = 20~ns$ for an individual pixel. The readout time $T_R$ of the chip is expressed as:

$$T_R = N/f_P \tag{3.1}$$

with N, the number of pixels connected with one readout line. For a sizable chip like MIMOSA-5, where up to $2.5 \times 10^5$ pixels are connected to one readout line, this leads to a readout time of $6~ms$ which is by orders of magnitude too slow for CBM.

**Time resolution of the pixel versus time resolution of the chip**  When discussing the time resolution achievable with MAPS, one has to distinguish the charge collection time of the individual pixel and the time required for the sequential readout of a pixel matrix. The latter forms the bottleneck for the time resolution of the system, as it is by orders of magnitude slower then the $\sim 100~ns$[27] required for charge collection. Improving the time resolution of MAPS has therefore

either to upspeed the readout procedure or to find ways for storing information about the time information of a hit until the corresponding pixel is read out.

The second option forms the classical approach of building pixel detectors with good time resolution. Nowadays hybrid pixels detectors integrate a discriminator and a hit memory into each pixel. By time stamping, the precise time information is stored and can be readout in a separate process. This concept is however not compatible with CMOS sensors since PMOS transistors in the pixel area are required for building an on-pixel discriminator. As motivated in section 2.2, the use of those transistors in the pixel area would lead to a parasitic collection of signal charge and thus dramatically disturb the sensor operation. The only choice is therefore to locate the discriminators beside the pixel matrix.

The approach chosen for MAPS detectors for CBM aims to minimize the time required to transport the pixel data towards those discriminators. This is done by replacing the conventional sequential readout pattern by a fully column parallel readout. By doing so, the number of readout buses used for data transport is upscaled by the number of columns of a pixel matrix. As this number is typically $\sim 1000$ the number of pixels multiplexed with one bus as much as the readout time required shrinks by this factor.

The time resolution remains equal to the readout time and may be computed with

$$t_R = N_C \cdot T_p \tag{3.2}$$

where $t_r$ stands for the time resolution of the detector, $N_C$ for the number of pixels in a column and $T_p$ for the time required to read one pixel. It should be mentioned that $T_p$ increases with respect to the classical sequential readout. This is because the column parallel readout requires for more precessing steps in the pixels. This fact, which will be discussed in more detail later on, leads to a typical readout time of one pixel of $T_p = \sim 100 \ ns$. Assuming that a column length of 3 $mm$ formed by 100 pixels with 30 $\mu m$ is acceptable, one derives an ultimate time resolution of $\gtrsim 10\mu s$ for a MAPS detector with column parallel readout. This value is considered as development goal for CBM.

**Data sparsification** Reading $\sim 10^{10}$ pixels per $cm^2$ and second would be required for reaching a readout time of $\sim 10 \ \mu s$ in a detector with a pixel pitch of 30 $\mu m$. The transfer of such an amount of data to a central DAQ is considered complicated. Moreover, it is questionable, if a central DAQ can treat the raw data stream delivered by a sizable vertex detector.

In order to reduce the data rate on the data lines between the chip and the outside world, a data sparsification on the chip is required. The strategy chosen for this relies on discriminating the pixel signal on the chip itself. Therefore, only the information of triggered pixels is processed further. The circuits required for discrimination and data sparsification can be installed at the border of the sensitive area, which is not affected by the limitations concerning the PMOS transistors.

The basic components of a fast MAPS for CBM can therefore be summarized as following:

- Sensing is done by an array of pixels, which is read out in a column parallel way.
- The signal of the pixels is send to one discriminator per column, which performs hit recognition.
- The hits recognized by the discriminators are send to a sparsification processor, which adds time stamps and coordinate information, before they are send to the outside world.

### 3.1.2. On-pixel functionalities required

In classical MAPS detectors, hit discrimination is done with powerful tools outside of the chip. In particular it is possible to define a discrimination threshold for each individual pixel. This is not the case for an on-chip hit discriminator, as the memory cells required would need too much surface on the chip. The on-chip discrimination can therefore not account for the properties of individual pixels.

Consequently it is necessary to develop pixels, which show very uniform output signals. The latter is not trivial as the components used for building them underlay substantial production tolerances. This affects in particular the leakage currents of the collecting diode. For standard 3T- or SB-pixels (see chapter 2.2.4), the distribution of pedestals is therefore typically higher than the signal generated by a hit. Using one discrimination level without compensating would lead to an important amount of hot or insensitive pixels.

The on-chip hit identification envisaged requires integrating parts of the functionalities used for offline hit discrimination into the chip. They have to take effect before the discrimination of the signal and must thus be located within the pixels or between the pixels and the discriminator.

The first functionality, which is leakage current compensation, is provided by the SB-pixel. This pixel showed good performance in the past. Nevertheless, as the potential at which the recharge currents and leakage currents of the SB-pixel reach equilibrium are unique to the individual pixel, a complementary CDS-processing is required. For CDS-processing, the information on the first pixel readout needs to be saved on the chip until the information on the second readout is available. As the capacitors required for analogue memory cells are big with respect to other structures used in CMOS circuits, the surface required is only available on the pixels.

### 3.1.3. Status of the R&D on readout speed

First trials to implement CDS relied on integrating two memory cells and a subtracting amplifier into each pixel [28]. This reduced the width of the distribution of the remaining pedestals by roughly one order of magnitude. Nevertheless, it became clear that the approach would require a high symmetry of the electronic circuits making up the two memory cells. The latter could finally not be reached because of the production tolerances already mentioned [29].

To overcome this problem, a structure was searched, which would be less sensitive to such production tolerances. This was done with a clamping structure, which was for a first time integrated into MIMOSA-8 [30]. The schematics of this pixel is shown in figure 3.1. Unlike the previous approach, only one readout line is used for each pixel. Its production tolerances contribute equally the signal of the first and second readout and the contribution cancels out in the CDS-processing. The latter is performed in two steps:

In the first step, AC-coupling (MOSCAP) removes the individual pedestal of the pixel. The preamplified AC-contribution of the pixel signal is modulated onto the potential defined by $Vr2$ via the Rst2-transistor. This potential is read out via a source follower to the RD-memory cell, which is located at the end of the column. After this, a reset is given to the pixel and the potential reached is loaded into the CALIB-memory cell. With this, the second CDS-step is prepared. Subtracting the potentials stored in the two memory cells performs this second CDS, which cancels out the tolerances of the Rst2-transistor and the source follower of the pixel. As the tolerances of the two memory cells and of the subtraction circuits is unique to the column, the pedestals of the pixels are fully removed.

Note that unlike to the conventional CDS, the signal taken after the integration time is readout first and sent to one of the memory cells. It is therefore assumed that the reset procedure is
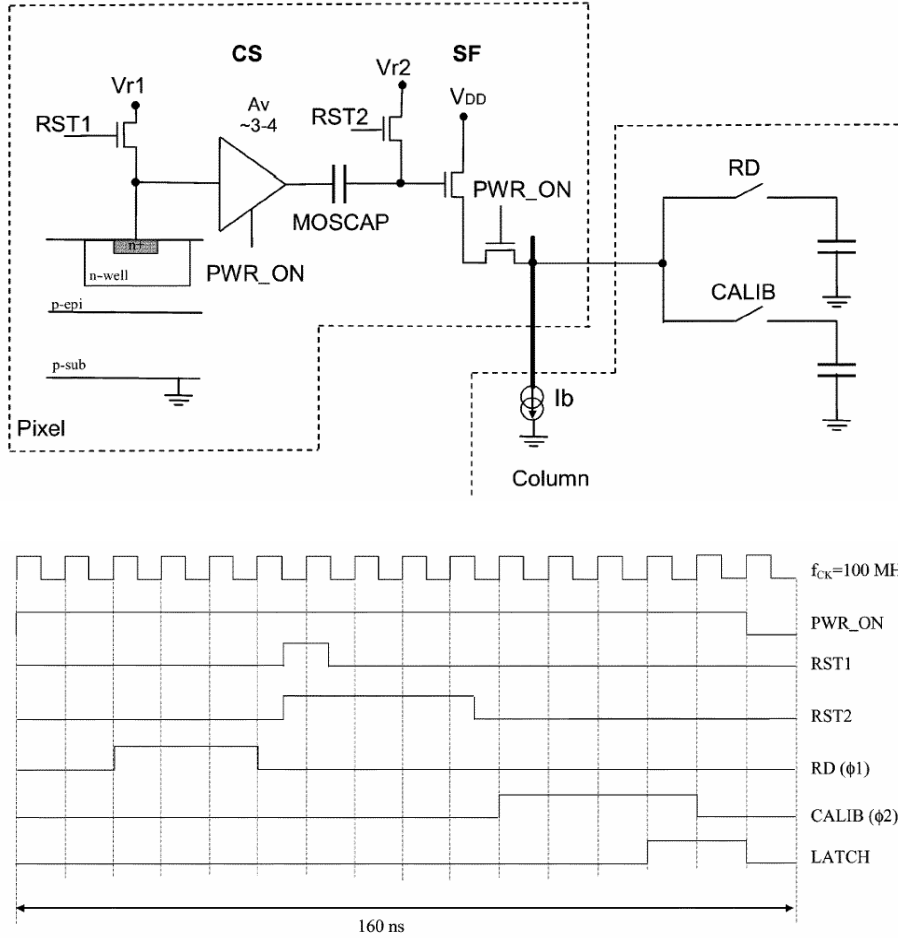
Figure 3.1.: *The diagram of MIMOSA-8 (DC-Coupled pixel) is illustrated in the left figure. The right figure illustrates the digital pattern required to drive the chip. From [30]*

reproducible with a sufficient precision.

Evaluations of MIMOSA-8 revealed low pixel intrinsic noise, which is 13–18 electrons equivalent depending on the details of the pixels. This remarkable value is only slightly above the one expected from conventional MAPS but within the limits one can expect from the digital TSMC 0.25 $\mu m$ process used for production. Moreover the pixel dispersion was found to be below 10 electrons equivalent, which allowed the use of an internal discriminator.

The full system including on pixel CDS pixel and on-chip discriminator was tested in an $\sim 5$ $GeV$ electron beam at DESY. A detection efficiency 99.3 % was reached at a fake hit rate of $\sim 0.1$ %. The average number of firing pixels per cluster was found to be $\sim 3.5$ (depending on the discrimination threshold).

Next steps in R&D will address the charge collection of the clamping pixels, which is still relatively low due to the very small diodes used, which were between $1.2 \times 1.2$ $\mu m^2$ and $2.4 \times 2.4$ $\mu m^2$.

### 3.1.4. Outlook: On-chip ADCs and data sparsification

So far it is not clear, if an analogue or a digital readout of the detector is preferable for CBM. The digital $(1 - bit)$ readout used in MIMOSA-8 is of a promising simplicity. However, the spatial

resolution in reach is given by $\sigma = p/\sqrt{12}$ with $p$ the pixel pitch. Assuming $p = 20\ \mu m$, this would lead to a spatial resolution of $\sim 6\ \mu m$. Charge weighting would allow for reaching a resolution of $\sim 2\ \mu m$.

Moreover, an ADC might indicate charge diffusing to the pixels surrounding the seed pixel of a cluster. A second discrimination on this charge might have a substantial benefit. Namely, it might reduce the effect of noisy pixels, which regularly pass their discrimination threshold. Taking into account both points, the analogue (4–bit) readout appears as preferable solution. Its advantages seem to dominate the complications introduced by the more complex circuits required.

Nevertheless, this conclusion has to be revisited taking into account the data rate produced by the chip. In case of using charge weighting, more information like analogue charge information of all pixels of a cluster, has sent from the chip to the DAQ. The complications induced by this higher data stream may dominate the benefit of analogue readout.

Even if this point remains to be clarified, the current working hypothesis for the design of a fast MAPS detector for CBM relies on the use of ADCs. This design might have the following components:

- A clamping pixel integrating leakage current compensation and CDS.
- An differential amplifier with two memory cells at the end of each line to perform pedestal correction.
- One fast ADC per column (most probably with 4-bit resolution)
- One fast and highly parallel digital signal processor per chip performing the first and second discriminator step (discrimination on the seed pixel signal and on the summed signal of the neighboring pixels).
- A serializer, which has to collect the hit information extracted by the signal processor. Pixel addresses and time stamps have to be added here.
- A digital output bus to send the data.

Even if the details of the on-chip processor remains to be clarified, an estimate of the performances and of the surface required is possible.

### 3.1.5. Expected performance and geometrical layout

A detector following the strategy discussed in the previous section will have unprecedented performances in compromising a good time resolution and a good spatial resolution. However, in terms of time resolution it cannot compete with dedicated detectors like the hybrid pixels. A pixel sensor with such high granularity and a time resolution of $25\ ns$ is not conceivable with nowadays technology. The time resolution of the detector will follow again equation 3.1. Because of the more complex functionalities implemented in the pixel, the individual pixel readout time will be higher than the one of the rather primitive 3T-pixel. A readout time of $100\ ns$ to $200\ ns$ per pixel is currently considered as a realistic estimate. Assuming that the column length should not be below 100 pixels, one comes to a maximum readout speed of $\sim 10\ \mu s$ for the full pixel matrix. The feasibility of a readout of a 128 pixel matrix within $\sim 20\ \mu s$ has been demonstrated with MIMOSA-8.

Concerning geometry, using such short column lengths leads to a rather aggressive design, as an additional non-sensitive surface has to be foreseen for the ADCs and the digital signal processors. This surface is currently estimated to be 2 to 3 $mm$ times the pixel pitch at the end of each column. Taking into account the pixel pitch of MAPS, which is typically between 20 $\mu m$ and 40 $\mu m$, one can conclude, that the sensitive area of such a chip is comparable to the non-sensitive one. A total size of $6 \times 20\ mm^2$ for the chips can be assumed as a realistic estimate.

Only a rough estimate is available concerning the power consumption of such a detector. An energy consumption of roughly 1 $W/cm^2$ is currently considered as realistic working hypothesis [31].

## 3.2. Material budget

An important design criterion of the pixel tracking stations is their material budget, i.e. the amount of material a particle has to traverse. Many design aspects as mechanical stability, read-out topology, power dissipation have to be taken into account.

### 3.2.1. Minimum thickness of the detector chips

MAPS have an outstanding potential for being thinned to very low material budget as the total thickness of their active volume and the full electronics is only $\sim 25$ $\mu m$. The thick substrate of the wafer is mostly not required. Only a few micrometer thick layer of this highly doped material is needed to reflect diffusing electrons back to the epitaxial layer.

Thinning CMOS chips by reducing their substrate is an established industrial process. However, the procedure is not trivial for very thin chips as the CMOS – processing introduces mechanical tensions into the bulk. The stability required to tolerate these tensions is provided by the substrate. Removing it may therefore lead to a mechanical destruction of the device.

First thinning experiments had already been done in 2003 with MIMOSA-5, which has been thinned down to 120 $\mu m$ without any loss of performance [32].

Important experiences could be obtained from a second study [33], which aimed to adapt MIMOSA-5 to the detection of $keV$ electrons. As electrons of this energy cannot deeply penetrate into silicon, the chip was thinned down to $\sim 15$ $\mu m$. This allows the electrons to directly access the sensitive volume without passing substrate or metal lines. Before thinning, the chip was mounted upside down on an additional support wafer. This wafer provides the mechanical stability required but comes with an additional material budget of more than 100 $\mu m$ silicon. This approach thus does not reduce the material budget of the chip but allowed for a first time to study the feasibility of operating a very thin MAPS detector.

The thinned detector performed well in laboratory tests. However, a substantial deteriorations of the charge collection efficiency was observed. This presumably as the full substrate and even a part of the epitaxial layer were removed by thinning. The electron reflection usually provided by the interface between substrate and epitaxial layer was therefore lost. The reduced charge collection efficiency also weakened the detection efficiency of the device for minimum ionizing particles. However, the thinned detector fulfilled its mission and successfully demonstrated the feasibility of detecting low energy electrons with MAPS.

In a next step, different companies were asked to thin MAPS down to $\sim 50$ $\mu m$. First test on MIMOSA-5 thinned down to $\sim 50$ $\mu m$ and $\sim 39$ $\mu m$ respectively suggest that this thickness can be achieved without substantial loss in performances [34]. The encouraging results obtained remain to be confirmed with beam tests.

Even if the studies on thinning are not yet finalized, it is reasonable to assume a thickness between 25 $\mu m$ and 50 $\mu m$ for the chips.

### 3.2.2. Material budget of the support structures

Realistic assumptions on the material budget of the detector station require detailed knowledge on their mechanical design, as the material of the mechanical structures tends to dominate the

one of the silicon. Due to the early state of CBM, this design was not yet available. A first rudimentary draft of the geometry has therefore been proposed, which may serve as guidelines for a more educated study. The proposal is not meant to provide a construction plan but should be interpreted as a preliminary collection of arguments, which is required to constrain the simulation model for the vertex detector of CBM.

### 3.2.2.1. Requirements on the support structures

The requirements on the support structures of the stations of the CBM vertex detector are assumed as follows:

- The structures have to induce a minimum material budget in the detector acceptance in order to ensure a good secondary vertex resolution.
- They have to be compatible to vacuum operation in all aspects.
- They have to support two layers of MAPS per STS-Station as only half of the surface of fast MAPS will be active.
- As air cooling is not possible in vacuum, the cooling of the MAPS chips has to be provided by the support. The heat production is assumed to be $\sim 2 \ W/cm^2$ for two layers of MAPS. A temperature of the chips well below $0 \ °C$ should be reached to reduce the effects of radiation damage on the chips.
- The support structures have to assure a mechanical stability of the detector chips comparable to their spatial resolution. This includes a sufficient suppression of potential vibrations.
- A possibility to install/uninstall quickly the full station is required. Besides allowing for maintenance of the stations outside of the potentially radioactive detector cave, this will allow for a quick replacement of the detector stations. The latter is probably necessary as the very high radiation doses expected will limit the lifetime of MAPS (see chapter 7).
- The support structures have to provide all supply and data lines required to operate the MAPS

### 3.2.2.2. Design guidelines

The design is guided by the cooling requirements. In vacuum, heat evacuation has therefore to be done by heat conductance or liquid cooling. The question, which of both options is preferable, is still under debate.

The current proposal relies on liquid cooling. It is proposed to provide it by means of a layer of micro-pipes embedded into the support of the MAPS chips. This approach eases the heat transfer from the chips to the cooling liquid. Moreover, the material budget of the stations is minimized, as the micro pipes also serve as mechanical support for the chips.

As illustrated in figure 3.2, the layout of a vertex detector station might then be formed from five functional layers:

- A layer of MAPS detector chips.
- A layer of carbon fiber material, which supports the MAPS. Moreover, it serves as wall of the "micro-pipes".
- A layer of "micro-pipes", which is mainly realized by cooling liquid and some intercepting walls. The latter are used to assure mechanical stability.
- A second layer of carbon fiber material.
- A second layer of MAPS which is required to cover the insensitive areas of the first one.
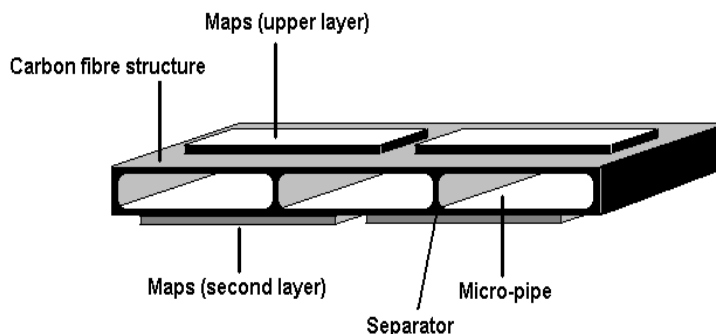
Figure 3.2.: *Cross section of the proposed vertex detector station. Only some MAPS chips are shown for clarity. In reality they are intended to matched as close as possible.*

In a passive cooling scenario, the layers 2-4 would have to be replaced by for example by a diamond support.

### 3.2.2.3. Mechanics

Sandwich structures of carbon fibers comparable to the proposed one are widely used in technological applications demanding for highest stiffness in combination with low weight. This is because of the high tensile strength of carbon fibers composite materials, which is about 2 $kN/mm^2$ to 3 $kN/mm^2$ and thus comparable to steel. On the other hand, the density of the material is as low as 1.7–2 $g/cm^2$ [35].
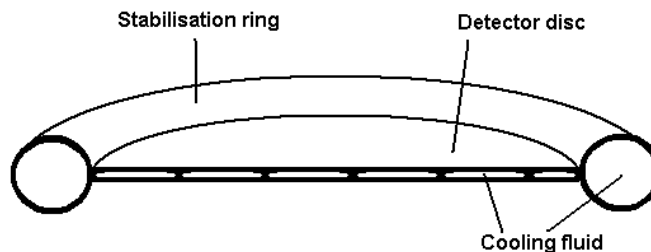


Figure 3.3.: *The drum-like geometry proposed (see text). The stabilization ring is also used to bias the micro-pipes with cooling liquid.*

Independently of the material used, thin structures providing very low material budget are unlike to stand harsh pressure or torsion. The static of the structures used within the detector acceptance should thus rely on tension forces, which can also be tolerated by a foil of flexible material. Compressive forces and torsions require a thicker material, which one might use outside of the acceptance.

In the design, a stable ring outside the acceptance of the detector is used to span the thin layers forming the detector. The design is very close to a drum, where the sandwich hosting the chips forms the drumheads. This structure is shown in figure 3.3. By using this geometry, any pressure difference between the cooling liquid and the vacuum outside the detector station is converted into tension forces, which can be absorbed by the thin support layers. The pipe separators provide additional stabilization.
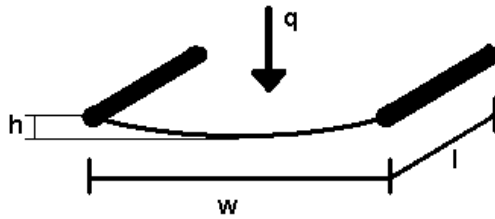
Figure 3.4.: *The ideal hanging membrane as used for the calculations. See text.*

In the following, a rough estimate of the material thickness required for the support structures will be made. This thickness is derived from the need to resist to the pressure of the cooling liquid. In order to evaluate it, one assumes a rectangular cross section of the pipes. This is more efficient in terms of cooling than the model used more below for estimating the heat evacuation abilities of the system. The height of this rectangle is undetermined while its width is assumed in the following with 5 $mm$.

This problem can be described with a hanging massless membrane, which has to carry an additional load density. This membrane is fixed at both borders. The additional load stretches the membrane with a force, which is [36]:

$$F = \frac{q \cdot w^2 \cdot l}{8h} \tag{3.3}$$

In this equation $q$ corresponds to the load of the membrane in $N/cm^2$, $l$ is the length and $w$ is the width of the pipe. The sag of the membrane is given by $h$. The model is illustrated in figure 3.2.2.3. The tensile strength of the membrane is sufficient to tolerate a force given by

$$F = t \cdot l \cdot \rho \tag{3.4}$$

where $t$ represents the thickness of the material and $\rho = 2.5 \ kN/mm^2$ is the maximum tension, the membrane can stand. By setting the load according to equation 3.3 equal to the strength of the material according to equation 3.4, one derives the material thickness required:

$$t = \frac{q \ w^2}{8 \ \rho \ h} \tag{3.5}$$

Assuming, that a sag of 10 $\mu m$ can be accepted, one concludes that a material thickness below 50 $\mu m$ is sufficient for the supporting layers.

However, the result of this calculation has to be taken with care, as equations and material constants are meant for macroscopic objects. They are thus not necessarily valid for a material thickness $\sim$ 10 $\mu m$ as discussed here. Moreover, it remains to be clarified, if carbon fiber material can be realized in a thickness of few tens of microns[1].

### 3.2.2.4. Heat evacuation

The power dissipation of MAPS for CBM is still unknown, as it depends on the final technology choices. The working hypothesis used in the following ($\sigma_{power} = 1 \ W/cm^2$ per layer of chips ) is considered only as a rough estimate.

---

[1]After finalizing the studies presented in this work, it became clear that the minimum thickness of nowadays carbon fiber materials is $\sim$ 150 $\mu m$. This triggered an iteration of the mechanical concept of the vertex detector stations, which is still ongoing.
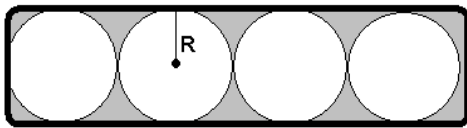
Figure 3.5.: *Calculation model for the micropipes. The cooling layer is assumed to be fully covered with pipes of a radius R*

The cooling power of the liquid cooling system depends on the thickness of the the micro-pipe layers. This thickness will be derived in the following in order to complete the estimate of the material budget of the system.

To obtain the thickness of the layer, one assumes that this layer is fully covered with straight pipes, having a round cross section each. This is illustrated in figure 3.5. The presence of the beam-hole is ignored for reasons of simplicity.

The length of the pipes is considered to be $l = 5\ cm$ for the first station and $l = 10\ cm$ for the second station, which corresponds to their diameter. For simplification, one assumes, that a surface of $A = w \cdot l$ has to be cooled with the pipes. We define the width with $w = 1\ cm$ to ease the understanding of the calculation. The final result will come out to be independent of this parameter. Moreover, we define that temperature of the cooling fluid is allowed to increase by $T_2 - T_1 = 10\ K$ and that its pressure may drop by $dp = 100\ hPa$ when passing the pipes. Light
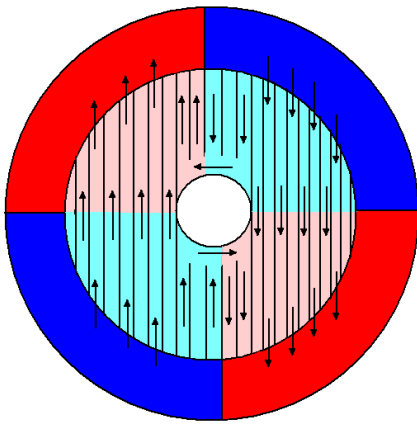


Figure 3.6.:
*A possible biasing diagram for biasing the micro-pipes. Cold liquid (blue) coming from the outer ring gets heated up on the disc. It gets collected again by the warm-liquid part of the ring (red). As the outer ring may be designed with a reasonably high inner diameter, it can be biased with macroscopic pipes. A vacuum compatible connector (not shown) should be used to connect them with a cooling system outside the vacuum vessel.*

oil (benzine/octane) is assumed as cooling fluid for all following calculations, as it combines a low freezing point with a low viscosity. The density of this oil is assumed to be $\rho = 0.75\ g/cm^3$, its heat capacity is roughly $c_p \approx 2\ Jg^{-1}K^{-1}$.

The power dissipated on the surface $A$ is given by

$$P = \sigma_{power} \cdot l \cdot w \tag{3.6}$$

The heat absorbed by a cooling fluid is given by

$$P = \frac{M}{t} \cdot c_p \cdot (T_2 – T_1) \tag{3.7}$$

where $P$ is the power absorbed and $M \cdot t^{-1}$ stands for the mass flux of cooling fluid in units of $kg/s$.

The necessary mass flux of the cooling liquid can be derived from equation 3.6 and equation 3.7:

$$\frac{M}{t} = \frac{\sigma_{power} \cdot l \cdot w}{c_p \cdot (T_2 - T_1)} \tag{3.8}$$

In our example the parameters are given by $\sigma_{power} = 2\ W/cm^2$ for two detector layers on a $l \cdot w = 5\ cm^2$ surface. From this one derives that $0.5\ g$ of cooling liquid have to be replaced in each second.

This flux of cooling liquid determines the necessary thickness of the cooling layer, which will be derived in the following. To do so, one assumes according to figure 3.5 is filled with round

micro pipes. The volume flux of a liquid through a round pipe is given by [37]

$$I = \frac{V}{t} = \frac{M}{\rho \cdot t} = \frac{\pi R^4 \cdot dp}{8 \, \eta \, l} \tag{3.9}$$

where $R$ is the radius of the pipe, $l$ is its length. A drop in pressure of $dp$ provides the force required to drive the cooling having a viscosity $\eta$ through the pipe.

Ignoring the separators, the amount of pipes passing the surface can be derived as $N = w/\,(2\,R)$. The total flux of cooling fluid in the surface is therefore given by:

$$I_{total} = \frac{M}{t} \frac{w}{2 \, R \, \rho \, t} = \frac{\pi R^4 \cdot dp}{8 \, \eta \, l} \tag{3.10}$$

Combining equation 3.8 and equation 3.10 one derives the diameter of the cooling pipe like:

$$R^3 = \frac{16 \, \eta \, l^2 \, \sigma_{power}}{\pi \, \rho \, c_p \, (T2 - T1) \cdot dp} \tag{3.11}$$

One finds $R \approx 0.11 \; mm$ assuming a density $\rho \approx 0.75 \; g/cm^3$ and a viscosity of roughly $\eta \approx 0.75 \times 10^{-3} \; Pa \cdot s$ for a light oil. For the longer pipes of the second station, this becomes $R \approx 0.172 \; mm$.

### 3.2.2.5. Vibrations and deformation

For the geometry proposed, there exist two obvious sources of vibrations, which need to be studied. The first of them is formed by potential turbulences of the cooling fluid in the micro-pipes. Turbulences are to be expected, if the Reynold-Number defined with

$$R_c = \rho \, v \, \frac{R}{\eta} \tag{3.12}$$

exceeds 2300 [37]. In this equation, $\rho$ is the density of the liquid, $\eta$ is the viscosity, $v$ the velocity of the liquid and $R$ the diameter of the pipe. For a micro-pipe as proposed for the first station, one calculates a Reynold-Number $\sim 5$, which lets a substantial security margin. No turbulences of the cooling fluid are thus expected.

The second source of vibration is a vibration of the full support structure. Resonances may be caused in the thin, drumhead like support layers. Studying the importance of this effect in detail is beyond the scope of this work. Nevertheless, two constructive elements dimming these vibrations should be mentioned:

- Even if the structure is very thin, the support layers combined with the separators of the pipes form a T-section. This geometry should at least partly absorb vibrations.
- The full structure stands under a substantial tension, which is caused by the pressure of the cooling liquid. This static load is probably high enough to allow for neglecting additional forces, which otherwise might generate vibrations.

A deformation of the surface of the support layers is expected in the case of liquid pressure fluctuations or when changing the gas pressure in the vacuum vessel. As carbon fibers are very inelastic and can get stretched less then 1% before breaking, no sizable deformations of the system are expected. The thin silicon detectors should be sufficiently flexible to tolerate the remaining deformations.

### 3.2.2.6. Vacuum aspects

As the cooling liquid and the vacuum are only separated by the thin support structure, a sizable diffusion of cooling liquid into the vacuum might appear. Removing the vapor generated from the beam-vacuum would require important pumping capacity.

In order to reduce the requirements on the vacuum pumps, a separation between the beam vacuum and the detector vacuum is proposed. The detector vacuum is by many orders of magnitude less demanding than the beam vacuum. One can thus establish it with rather simple technical means.

Despite of the sizable difference in gas pressure, the total forces on a separator between the two volumes are negligible. A remaining pressure of 1 $mBar$ in the detector volume would cause a load of 0.01 $N/cm^2$. Very thin material can therefore be used for separating the beam vacuum from the detector vacuum.

The low mechanical constraints suggest using the target foil as separator. This would allow suppressing the unwanted nuclear collisions, which otherwise would take place, when the primary beam passes the separator material.

### 3.2.2.7. Cables and connectors

Mylar flat band cables can be used for connecting the MAPS with their front-end electronics chips. The latter might be mounted on the carbon ring surrounding the detector. Radiation hard optical links should be installed on the ring. They are to transport the data with a reasonable amount of optical fibers to the outside world.

The electrical bias of the full station can probably be done with a very limited amount of cables concentrated in a flat band cable. Two to four vacuum resistant liquid plugs are required to bias the cooling system

Plugs allowing to quickly connect / disconnect the detector disk from the bias are required efficiently replace it.

### 3.2.3. Material budget of the full detector stations

| Object | Material | Thickness | 0.1 % $X_0$ |
|:---:|:---:|:---:|:---:|
| **MAPS (2 layers)** | Silicon | 25 $\mu m$ each | 0.53 |
| **Support (2 layers)** | Carbon | 50 $\mu m$ each | 0.53 |
| **Cooling liquid** | Octane | 220 $\mu m$ | 0.35 |
| **Cables (support)** | Mylar | 10 $\mu m$ | 0.04 |
| **Cables (conductor)** | Aluminum | 10 $\mu m$ | 0.13 |
| **SUM** | | | 1.45 |

Table 3.1.:
*Material budget of a potential MAPS support structure as described in the text. An aggressive scenario is assumed here. The radiation length ($X_0$) of the different materials is given. The cooling liquid is calculated for station 1 and slightly increases for the higher diameter of station 2. The material budget corresponds to 135 $\mu m$ silicon equivalent.*

An aggressive and a moderate scenario for the material budget of the detector stations proposed have been studied. In both cases, the material of the pipe-separators has been neglected, as it is

| Object | Material | Thickness | 0.1 % $X_0$ |
|:---:|:---:|:---:|:---:|
| **MAPS (2 layers)** | Silicon | 50 $\mu m$ each | 1.06 |
| **Support (2 layers)** | Carbon | 100 $\mu m$ each | 1.06 |
| **Cooling liquid** | Octane | 220 $\mu m$ | 0.35 |
| **Cables (support)** | Mylar | 50 $\mu m$ | 0.17 |
| **Cables (conductor)** | Aluminum | 20 $\mu m$ | 0.26 |
| **SUM** | | | 2.90 |

Table 3.2.: *Material budget of a potential MAPS support structure as described in the text. An more conservative scenario is assumed here. The radiation length ($X_0$) of the different materials is given. The cooling liquid is calculated for station 1 and slightly increases for the higher diameter of station 2. The material budget corresponds to 271 $\mu m$ silicon equivalent.*

only $\sim 200\ \mu m$ carbon at 1 % of the detector surface. The results of the study are given in table 3.1 for the aggressive model and in table 3.2 for the moderate model.

A material budget of 135 $\mu m$ and 271 $\mu m$ silicon equivalent is derived. These are excellent values as compared with nowadays solutions based on hybrid pixel detectors. In the ATLAS experiment, the full material budget (including support) of a layer of hybrid pixels is $\sim 1.3\%\ X_0$ [38]. This is equivalent to $\sim 1.2\ mm$ of silicon.

One should note that the material budget of the stations is function of the power dissipation of the MAPS. Additional power, as required for implementing a very fast readout, a very high granularity or a very complex on-chip signal processing, might therefore increase this thickness.

## 3.3. Summary and conclusion on readout speed and material budget

Within this chapter, questions of readout speed and material budget of a potential MAPS based vertex detector for CBM were addressed. It was motivated, that the readout speed and the time resolution of a MAPS detector are equal. This is as the sensor is not compatible with the structures required for integrating a discriminator into the pixel. The information of each pixel has therefore to be sent to discriminators located at the border of the sensing area. The time resolution is given by the time required for addressing twice an individual pixel, which corresponds to one full readout cycle of the pixel matrix.

Column parallel readout was identified as fastest readout mode compatible with MAPS in nowadays CMOS technology. In this approach, multiple pixels have to be connected with one discriminator having one single threshold. Intelligent pixels providing analogue CDS and uniform baselines are thus required.

The design of pixels with uniform properties is complicated by the substantial production tolerances of the components provided by the CMOS technologies used. The clamping pixels of MIMOSA-8, which came out to provide the functionalities and uniformity required, was introduced and its performances were discussed. It was concluded, that today's CMOS processes will allow for a production of MAPS with a time resolution of $\sim 10\ \mu s$. Short columns are required to enable this fast readout.

The short length of columns requires is expected to limit the length of the sensitive part of a chip to $\sim 3\ mm$ (assuming 30 $\mu m$ pixel pitch). An additional, non-sensitive surface of a comparable size has to be foreseen to host the digital electronics of each chip. Consequently, only $\sim 50$ % of

the surface of each chip can be considered as sensitive. In order to provide a fill factor of 100 % for each detector station, two layers of MAPS detectors are required. In this arrangement, the active surface of one chip has to cover the passive digital part of a second one.

A preliminary design of a MAPS detector station, which reflects these constraints and the need for vacuum operation, was presented. The material budget of the detector stations was studied as a function of the requirements on power of the liquid cooling system required. Depending on the detailed assumptions, a very low material budget of few 0.1% $X_0$ has been derived[2].

Because of the very high beam intensity envisaged for CBM, a pileup of up to 100 nuclear collisions in the vertex detector has to be expected. Recording the corresponding hits see,s feasible because of the very high granularity of the detectors. Nevertheless, track finding might be seriously complicated because of the very high track densities in the vertex detector.

A change in the track finding strategy has been proposed in order to ease this task. It is proposed to start track finding in the faster detectors located downstream of the MAPS stations. After a track seed is formed on the base of separated collisions, this seed can be extrapolated to the MAPS detectors. Assuming a reasonably low occupancy in the highly granular MAPS detectors, track matching should be possible. This would allow combining the very high spatial resolution of the MAPS with the good time resolution of the strip detectors.

Overall it was concluded, that MAPS fit the requirements in terms of material budget and vacuum operation. The compatibility of the time resolution of MAPS with the highest collision rates foreseen for CBM could not be clarified in this work and will be subject of further studies.

---

[2]Within the iteration process of the concept presented here, it became clear that nowadays minimum thickness of carbon fiber materials is $\sim 150~\mu m$. The consequences of this fact, which is not accounted for in this work, are presently under study. Today it seems likely that the thickness of the MAPS stations will be $\gtrsim 300~\mu m$.

3. *Conceptiunal considerations for a vertex detector based on MAPS*

# 4. Assessment of the radiation tolerance of MAPS

Radiation damage deteriorates the detection efficiency of silicon pixel detectors and increases their fake hit rate. At some point, track reconstruction becomes inefficient because of an increasing amount of missing or wrong hits. Misidentified tracks form an important source of background in particle physics and heavy ion physics experiments. To reduce it, one has to keep the number of fake hits and lost hits at a reasonably low level. Good radiation hardness is therefore mandatory for the detectors of CBM.

The micro vertex detector of CBM will be installed close to the interaction point. Among all detectors in the experiment, it will be exposed to most intense radiation levels. The expected yearly particle flux of up to $\sim 10^{15}$ minimum ionizing particles per $cm^2$ is extraordinary high. It reaches the limits of nowadays dedicated radiation hard pixel detectors (hybrid pixels), which demands for a careful technology choice.

As MAPS form a novel technology, their radiation hardness was widely unknown. Measuring and improving it was the central task of this work. The R&D on this topic could profit from first studies showing the native radiation tolerance of the technology [27, 39, 17]. For the sake of completeness, those early results will be shown and discussed in this work before introducing the progresses made.

The radiation hardness of MAPS will be covered in three chapters. In this chapter, established radiation effects on silicon devices will be shown. Hereafter, the methods used for assessing the effects of radiation damage in MAPS will be discussed. The results of the studies will be reported in the two following chapters separately for two main types of radiation damage, the ionizing and the non-ionizing radiation damage.

## 4.1. Radiation damage in silicon detectors

### 4.1.1. Fundamental radiation effects

Radiation hardness tests are done by aging the detector with intense radiation sources. This is to reach the dose expected for the lifetime of a detector after a reasonably low time. Testing the irradiated detector allows concluding, which performances the device will have at the end of its operation period. Potential problems can be identified and eliminated prior to the use of the detector in an experiment.

Testing vertex detectors is not straightforward because nowadays radiation sources cannot reproduce the complex radiation expected for the experiments. One has thus to simulate this complexity with a superposition of one or more intense sources. To do so, one notes that radiation damage originates from the energy deposit of the particles in the material. Provided, this energy deposit is correctly reproduced, the identity and energy of the particle causing it is of little interest.

Nevertheless, one has to distinguish two different interaction chains, which each lead to a qualitatively different response of the sensors. The so-called *ionizing* interaction refers to an

energy deposit into the electron gas of the material. This interaction has the potential to destroy chemical bindings but the atoms keep their position in the silicon crystals. An energy deposit to the atom cores of the material is referred as *non-ionizing* interaction. It may move atoms away from their position in the crystal lattice and cause irreversible crystal damage.

For semiconductor detectors, both interaction chains are of concern. Ionizing radiation does not harm pure silicon crystals, as ionized electrons can are be replaced by thermal electrons from the conduction band. Nevertheless, irreversible damage is generated at interfaces between structures formed from silicon and $SiO_2$. $SiO_2$, which is widely used as insulator in microcircuits, has another lattice constant than silicon. Numerous irregular bonds are thus formed at the interfaces between both materials. These irregular bonds are irreversibly broken by radiation, which changes the electric properties of the material. As the damage occurs dominantly at the interfaces between $Si$ and $SiO_2$, radiation damage caused by ionizing radiation is often referred as *surface damage.*

The crystal damage caused by non-ionizing interaction generates defect states in the band gap of the silicon structures. Comparably to impurities in the material, these defects may significantly deteriorate the properties of the bulk of the silicon. This is referred as *bulk damage.* Non-ionizing radiation has few impact on surfaces between silicon and $SiO_2$. Crystal imperfections caused by the different lattice constants of the materials dominate potential radiation effects.

In general, all particles contribute to both kinds of radiation damage. Nevertheless, neutral particles like neutrons have only a poor cross section for interactions with the electron cloud. They thus generate dominantly non-ionizing damage. Light particles, namely X-rays and slow electrons do not reach the momentum transfer required for displacing an atom. They contribute only to ionizing damage. This allows studying the effects of ionizing and non-ionizing radiation on the pixel detectors separately.

## 4.1.2. Effects of ionizing radiation doses on CMOS-devices

Ionizing radiation damage is caused by charged particles and by photons with quantum energy above UV-light. Dosimetry can be done with moderate effort as most radiation detectors rely on collecting electrons, which were separated from their atom by ionizing interactions. The SI-unit of ionizing radiation is Gray ($Gy = 1\ J/kg$). The former unit $1\ Rad = 10^{-2}\ Gy$ is still widely in use in detector physics and will therefore be used in this work.

Ionizing radiation takes effect at the strained and dangling bonds located at the interface between silicon and $SiO_2$ crystals. While manufacturing the material, the dangling bonds get saturated with hydrogen in order to neutralize their impact on the electronic properties of the material. Ionizing radiation can irreversibly damage the bindings and the neutralization of dangling bonds with hydrogen. This leads to a build up of permanent positive charge and to the generation of a substantial amount of generation/recombination centers at the interface region between both materials. While both effects are established on the macroscopic level, their microscopic origin is not yet full understood. For a deeper understanding, the reader is referred to literature [40, 41].

The explanation presented in those works assumes that radiation generates additional dangling bonds, which generate a wide spectrum of acceptor and donor like defect states in the band gap of the silicon. The amount of those states is limited by the number of precursors in the material to $D_{it} = (1-4) \times 10^{12} cm^{-2} eV^{-1}$. They ease the thermal generation of minority charge carriers. If located close to a collecting diode, the states may introduce a significant amount of additional leakage current, which forms a background to the current pulse caused by an impinging particle.

In thermal equilibrium, the charge of this kind of defects is neutral. This distinguishes them from a second group of defects, which causes the build up of positive charge mentioned above.

This second group of defects is probably caused by ionizing radiation impinging the $SiO_2$. Despite the relatively high band gap of this material (8.8 $eV$), ionizing particles can create electron/hole pairs in $SiO_2$. The mobility of the conducting electrons is substantially higher than the one of holes. If an electric field is applied to the material, the electrons can escape towards neighboring conducting structures. Because of a lack of thermal electrons in the conducting band, the holes cannot recombine and diffuse to the opposite border of the $SiO_2$. With a certain probability, they are trapped by defect states present in the transition zone between $SiO_2$ and $Si$ before they can accept an electron from the semiconductor. The number of trapped holes, which keep their positive charge at room temperature, is limited by the number of corresponding precursors to a surface density of $Q_{sat} \approx 3 \times 10^{12} cm^{-2}$ [25].

The effect of this charge build up is the generation of unwanted electric fields, which modify the energy of the valence and conducting band of the silicon comparably to the fields applied to a Field Effect Transistor (FET). Charge build up may thus modify the characteristic curve of those devices and cause a failure of circuits or individual transistors. For electronics build in standard sub micron processes, this problem is still present but considered as widely under control, if special radiation hard transistors and guard rings are used.
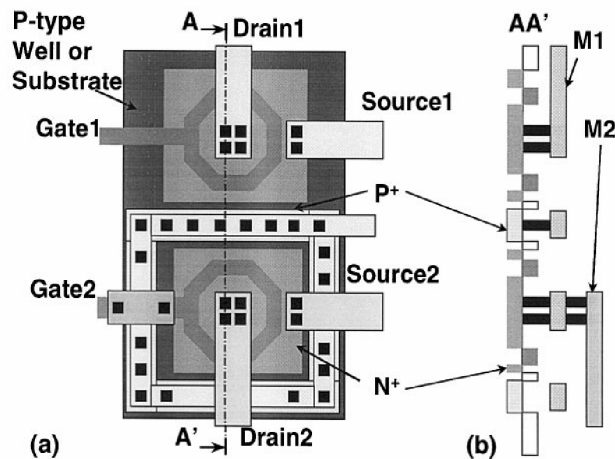


Figure 4.1.:
*Layout of an enclosed transistor. From [43].*

The concept of the transistors relies on the fact that the thin gate oxides used in deep sub micron processes allow for an annealing of the trapped holes by tunnel effect. Because of this annealing, the charge build up in the gate oxide can usually be neglected. Nevertheless, additional steps have to be undertaken as thicker oxide structures are located beside the gate. Charge build up in this thick oxide may open conducting channels between source and drain of the transistor and thus cause intolerable leakage currents. A solution was found by using the so-called *enclosed transistors* [42, 43], which are shown in figure 4.1. In this layout, either source or drain of the transistor are fully surrounded by thin and radiation tolerant gate oxide. This cuts potential conducting channels and the radiation hardness of the transistor is significantly above the one of standard transistors. P-Diff guard rings located around the NMOS transistors, which are to cut potential radiation induced conducting paths towards other implantations, enforce the structure.

The defects generated by ionizing radiation can be saturated again with hydrogen by an annealing process at a temperature of 450 °$C$. Unfortunately this temperature is too high to be applied to fully processed and bonded microchips. Also limited room temperature annealing has been observed [27].

### 4.1.3. Effects of non-ionizing radiation and the NIEL-model

**Dosimetry**   Unlike ionizing radiation, non-ionizing radiation has little impact on the surfaces between silicon and $SiO_2$. Due to the different lattice constants of the two materials, this area is full of lattice imperfections already by construction. Non-ionizing radiation damage takes thus dominantly effect in the bulk material of the sensor, which is damaged by displacements of atoms. One distinguishes *point defects* caused by an displacement of individual atoms and *defect clusters*. The latter are produced if the energy transferred to the first atom is sufficient to initiate a cascade of further displacements.

The energy threshold for removing an atom from its place in the lattice slightly depends on the direction of the recoil of the atomic core with respect to the crystal lattice. A mean threshold energy is $\sim 25~eV$ for silicon according to [25]. This threshold seems low, but the energy transfer has to be combined with a sufficient momentum transfer. As the mass of the nuclei and the impinging particle are very different, $\sim 190~eV$ kinetic particle energy are required to displace an atom with protons or neutrons. The minimum kinetic energy for electrons is $\sim 260~keV$ because of their lower rest mass. For generating defect clusters, a minimum energy of 15 $keV$ and 4.6 $MeV$ is required for protons/neutrons and electrons respectively.

Dosimetry is delicate for non-ionizing radiation, as the non-ionizing energy deposit in a detector is not necessarily proportional to the ionizing energy used for forming the signal. USilicon detectors comparable to the system under test can thus not measure the non-ionizing energy deposited. It is therefore derived in an indirect procedure based on on two steps. In the first step, one measures the number of particles impinging the detector under test with an independent detection system. In a second step, one evaluates the non-ionizing energy each of the particles typically deposit into silicon and combines both informations. The assumption made is that the radiation damage scales but with the energy deposit, no matter if point defects or defect clusters are generated. The semi empirical Non Ionizing Energy Loss (NIEL) model [44, 45] is used to evaluate the energy deposit. It bases on a simulation of the interaction between the particles and the detector material, taking into account all known interactions and cross sections. The resulting summed theoretical energy deposit depends on the type and energy of the impinging particles. In some cases, the theoretical studies are complemented by measurements. The results of those studies are summarized in tables quantifying the non-ionizing energy deposit over a wide energy range exist nowadays for the most frequent types of particles [46] (see figure 4.2).
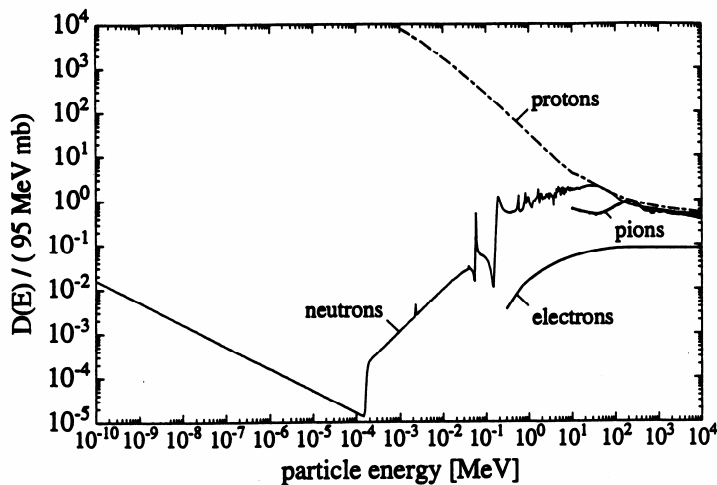


Figure 4.2.:
*The NIEL-Factors of different particles as a function of their energy. The factors are normalized with respect to a 1 MeV neutron. From [25].*

Within the NIEL-model, the energy deposit is usually not given in absolute units but nor-

malized with respect to the deposit of a reference particle, which is an 1 $MeV$ reactor neutron. According to this convention, non-ionizing doses will be given in units of $n_{eq}/cm^2$. This stands for the energy deposit equivalent to one of a neutron flux of one 1 $MeV$ neutron penetrating 1 $cm^2$ of detector surface.

The most prominent effect of non-ionizing doses is the generation of primary vacancies and interstitials in the crystal. Those introduce defect states into the band gap, which act as generation and recombination centers. This eases the thermal generation of minority charge carriers and increases the leakage currents of the collection diodes of silicon detectors. The additional current has to be absorbed by the preamplifiers of the readout electronics and may generate shot noise.

Moreover, the generation and recombination centers deteriorate the lifetime of the free signal electrons generated by impinging particles. The lifetime of free electrons before recombination is given in [25] as following:

$$\frac{1}{\tau_{t,n}} \approx \frac{1}{\tau_{t0,n}} + \gamma_n \Phi \tag{4.1}$$

Here, $\tau_{t,n}$ stands for the lifetime after irradiation, $\tau_{t0,n}$ for the lifetime before irradiation and $\Phi$ for the radiation dose in units of $n_{eq}/cm^2$. The factor $\gamma_n \approx 0.24 \times 10^{-6}$ $cm^2$ $s^{-1}$ is found empirically. If this lifetime decreases to the order of the charge collection time, a part of the signal gets lost, which further reduces the signal to noise ratio of the device.

Primary defects are not fixed in the material; they may diffuse within the detector material at room temperature. This diffusion has several wanted and unwanted consequences. As far as the diffusion of crystal defects leads to a regeneration of the crystal lattice, this is named *beneficial annealing*. This effect occurs if an interstitial atom fills a vacancy or moves to the border of the crystal. In both cases, the lattice defect is cured.

Besides beneficial annealing, the diffusion of primary defects may lead to an unwanted generation of defect complexes. Those complexes may be constituted for example from two vacancies or a vacancy and an oxygen atom, which are bound to each other. They may harm the detector more than the sum of the initial primary defects and remain stable at room temperature. As this process leads to additional damage in the detector, it is referred as *reverse annealing*.

Intense studies on annealing and reverse annealing were done by the CERN RD48 (ROSE) collaboration [47]. Those studies, which concentrate on high resistivity N-doped material, show that beneficial annealing dominates for newly irradiated detectors. Increasing the detector temperature, which simplifies the diffusion of the defects, can accelerate this annealing. However, after some time the reverse annealing gets dominant and the performances of the detector may drop below the values reached before the annealing process.

A side effect of the generation of defect complexes is the modification of the effective doping of silicon [25]. This can be caused by absorption of donors into defect complexes, which show different electric properties. Moreover, a sufficient number of defect states may act as doping bands.

Striking modifications of the effective doping have been observed in N-doped detector materials. The effective doping of these materials vanishes after a dose of roughly $10^{13}$ $n_{eq}/cm^2$ and an effective P-doping is observed. This effect is referred as *charge inversion*. With further increasing doses, the effective P-doping increases and may cause a breakdown of depleted silicon detectors, if the effective doping becomes too important and the sensor cannot be depleted anymore.

Special oxygen enriched materials were successfully tested in the last years (see for example [47]) to reduce the impact of radiation on the effective doping. Those materials show no charge inversion, presumably because the donors initially available in the material are replaced by the radiation-induced states [48]. This beneficial effect observed for pion and proton irradiation only,

neutron irradiated samples showed properties as expected from standard material. This observation, which questions the generality of the NIEL hypothesis, is discussed in [47].

Most studies on bulk damage at the high doses addressed were made for lowly N-doped silicon as this material is commonly used in silicon detectors. Transferring the existing results to the moderately P-doped sensor of MAPS is not straightforward as in particular the annealing and reverse annealing processes seem material dependent.

Nevertheless, one can state that charge inversion and modifications of effective doping is unlike to affect MAPS. This is because the sensor of MAPS is already undepleted and P-doped. Moreover, the doping concentration in N-doped structures of CMOS electronics is many orders of magnitude above the one of detector silicon, which makes them less vulnerable to absorption of doping atoms.

A particular danger for MAPS is the deterioration of the lifetime of the free signal electrons as the charge collection time of those detectors is relatively long ($\sim 50\ ns$). The expected increase of leakage current can be reduced by cooling.

## 4.2. Observables and precision goals

Despite of its complexity in detail, the assessment of the radiation tolerance of radiation detectors is guided by a simple procedure, which was also followed in this work. This guideline contains the following steps:

- First the performance parameters of interest are determined for the non-irradiated detector in order to gain a reference.
- Second, the detector is irradiated. As discussed in chapter 4.1, the type of radiation has to be chosen in a meaningful way in order to simulate the radiation dose the detector will have to face in a true experiment.
- Last the performance of the detector has to be measured again. The result has to be compared with the initial values as much as with the requirements. As far as the detector still fulfills the requirements, it has passed the test.
- If the detector did not reach the radiation tolerance required, one will try to identify the weak point of the system and to improve the design.

As this work focuses on the improvement of the radiation tolerance, the question how to localize the radiation damage of the detector was addressed. This cannot be done in a straightforward way, as the microcircuits of MAPS do in general not allow to access individual components of the detector. Moreover, the signal coming from the sensor is extremely weak. This hampers using external instruments.

The only remaining option was to extract information about potential malfunctions from the output signal of the detector itself. This limits the possibilities of the investigations. Namely, the identification of the position of a malfunction within the readout chain was of concern, as it was not possible to insulate the building blocks. Tests of the pixels were thus only possible if the internal amplifiers of the chip were working sufficiently well. The latter was fortunately fulfilled for the radiation doses addressed.

### 4.2.1. Observables

Within this work, the following observable were extracted from the output signal of the chips:

- The common gain of all amplifiers of the readout chain including the gain of the pixel.
- The charge collected within the individual pixels as much as of clusters defined by the added signal of several pixels. This parameter defines the signal of the detector.
- The noise of the pixels.
- The leakage current of the 3T-pixels.
- The recharge constant of the SB-Pixels

Isolating these parameters was difficult as their contributions are superposed. Moreover, the MAPS themselves as much as the electronics used for their readout were experimental and under continuous development. Instabilities in the transmission of the high frequency analogue data stream occurred repeatedly.

### 4.2.2. Precision goals

MAPS proved excellent detection efficiencies also in the presence of such instabilities. This indicates a good robustness of the technology against weak points in the analogue readout chain.

Nevertheless, instabilities of the readout chain put additional uncertainties on the measurement of parameters like leakage current, noise and charge collection.

The aim of this work is to decide about the radiation tolerance of MAPS and to identify the mechanisms leading to a failure of the system. To do so, measurements on a sizable amount of different detectors, each being equipped with an individual readout, were required. A pragmatic compromise had therefore to be found between the need for precise measurements and the investment required for improving it. This compromise was guided by the precision needed to clarify the mechanisms of radiation damage.

The limit of the radiation tolerance is defined by a partial failure of a MAPS chip after being irradiated. As this is very significant, identifying the underlying effects could be done by using robust methods, which are tolerating uncertainties of the detailed measurements up to some degree.

In this work, first order and second order effects will be thus distinguished. First order effects are considered as leading mechanisms of radiation damage, which question the save operation of the detector. Depending on the radiation doses, they are very significant and it was assured, that the corresponding observations were not caused by artifacts of the readout system and the algorithms used.

Visible effects are labeled to be of second order, if their unwanted impact on the detection abilities of MAPS remains negligible. The origin of these effects was not always addressed. This reflects that explaining small effects and modifications, which are compatible with the save operation of the detector, was not considered as the scope of this work.

## 4.3. The hardware setup

### 4.3.1. The external readout electronics

The hardware used for the readout of MAPS is described in [50]. It is composed from three different printed cards (PCBs).

The first one is the motherboard, on which the chip is bonded. This motherboard, which was called *MIMOSA-PCB*, contains two functionalities, which are a further buffering of the analogue output signal and the preparation of the input signals. This preparation is the termination of the lines, which deliver the high frequency signals like the clock from the outside world. Moreover, a noise filtering is done on the different reference voltages required for the operation of the MAPS-Chip. Finally, the current source of the chip matrices is realized with a simple resistance on this motherboard. Putting this current source outside the chip is not mandatory. However, it was chosen as reasonable and simple solution for the R&D phase, as it allows an adaptation of the current delivered to the chip within the tests by replacing the resistances.

The MIMOSA-PCB is connected per conventional flat band cable with a PCB called *AUX-board*. The latter contains a further buffering of the signal lines, which may also integrate a moderate amplification, as much as a transformation of the signal into a differential signal. The use of a differential signal allows driving the analogue output signal of the chip through very long lines (40 $m$), as required for beam tests. The reference voltages for the different buffers and amplifiers on the chip and on the motherboard are generated here using potentiometers and an external DC-voltage-source. The unipolar digital control signals like the clock are generated from a differential signal and delivered to the motherboard.

From the AUX-board, the signal is transferred via coaxial cables towards an *ADC-board*, which was also called *VME-board* or *USB-board* depending on the communication standard used. Besides

usually four 12-bit ADCs, this board contains a Xilinx-FPGA, which allows emulating hard-coded chips. This FPGA is programmed to generate the digital signals required to drive the MAPS-detector. Moreover, it controls the ADCs and brings the analogue output signals of the MAPS-detector into right order. 4 $MB$ RAM are available on the board, which is sufficient to store two signals of each pixel of the MAPS detectors with up to 1 $Mpixel$.

The data taken is stored into a 32-bit word per pixel and transferred either via VME-Bus and the corresponding processor and Ethernet, or via USB (depending on the version of the system) towards a PC. This PC stores the data taken on hard-drive. Moreover, it allows a real time monitoring of the data taken, which eases choosing good parameters for operating the chip.

Special software on the PC serves as user interface of the FPGA of the ADC board and of the VME-Processor. One can thus easily define parameters like the number of pixels of the dedicated MAPS-detector of the signal delay due to the different cable lengths. Besides this, it is to receive the data-stream delivered by the FPGA. The data gets stored on the local hard drive. The analysis is done offline using different codes written in Mathematica, Root or Labview.

### 4.3.2. The dark chamber and $^{55}$Fe-source

As MAPS are sensitive for visible light, a dark chamber was used in order to do measurements on the MAPS detectors. These measurements were used to asses the detection abilities of the chips before and after being irradiated. This was done by illuminating it with monochromatic X-rays and measuring the reaction of the chip on these photons.

The illumination was done with an $^{55}$Fe-Source, which had an intensity of 370 $MBeq$ in most cases. This source generates two monochromatic lines of X-rays [12], where the dominant (24.4 %) line with 5.9 $keV$ photons is of interest. Moreover, a smaller (2.9 %) number of 6.5 $keV$ photons is generated. The methods used for doing the measurement rely on the assumption of a perfectly monochromatic radiation; these additional photons are thus not helpful. However, because of their low number, their presence could be tolerated without provoking a relevant uncertainty.

The interest of illuminating the chips with monochromatic X-rays is because they allow injecting a well-defined amount of charge carriers into the sensitive medium of the sensors. As a mean value, 3.6 $eV$ are consumed for generating a free electron in silicon [25]. Consequently, $\sim$ 1640 electron hole pairs per 5.9 $keV$ photon are generated in the detector. Comparing the amount of these electron hole pairs with the amount of collected electrons allows determining the charge collection efficiency of the sensor.

It should be mentioned, that the initial geometrical shape of the cloud of free electrons caused by an X-ray can be considered a sphere of $\sim$ 1 $\mu m$ diameter.

Besides visible light, temperature fluctuations can have a significant influence on the parameters to be measured. This holds in particular for the leakage current of the collection diodes, which depends exponentially on the temperature. Temperature control was required in order to separate the influence of radiation from temperature effects.

A temperature control was therefore foreseen in the dark chamber. It was done by transferring cooling fluid to the chip support. The temperature of the liquid was precisely controlled by a cryostat, which allowed reproducing temperatures within a precision of few $K$.

While reproducing and stabilizing temperatures is well under control in the setup used, estimating the absolute temperature of the chips is subject of an systematic uncertainties. This is because the chip was dominantly cooled by heat conduction through its motherboard. As the chip dissipates power and the heat conductivity of printed cards is limited, temperature differences of up to 10 $°C$ between the cooling fluid and the chip has to be expected. It was not possible to

calibrate the temperature of the chip against the temperature of the cooling support, as the the small size and fragility of the microchips did not allow for the mechanical contact required for temperature measurements. As, however, the temperature of the microchip remains proportional to the temperature of the cooling support and the temperature can be reproduced, a lack of knowledge on the absolute numbers can be accepted. This is because it remains possible to separate temperature effects and radiation effects from each other. Moreover, the information available is sufficient to study the correlation between radiation effects and temperature in a systematic way.

The temperatures shown in this work correspond either to the temperature of the support structure or to the almost identical temperature of the cooling liquid.

## 4.4. Algorithms for interpreting the output signal of 3T-Pixel and the SB-pixel.

### 4.4.1. Definitions

As already mentioned, assessing the different observables of the MAPS had to be done by extracting their contribution from the analogue data stream of the detector. This will be explained for the 3T-pixel, as the methods used were developed for this kind of detector. The consequences of applying them for SB-pixels will be discussed at the end of this section.

A precise understanding of the functionality of the pixels is mandatory in the following. The reader is encouraged to read the corresponding introduction in section 2.2.4 before continuing, as the definitions and relations introduced there will be used in the following.

It is reminded, that three major currents, the recharge current $I_{ReC}(t)$, the leakage current of the collection diode $I_{Cur}(t)$ and the signal current $I_{Phy}(t)$ contribute to the output of MAPS. Their sum is defined with:

$$I_{Col}(t) = I_{ReC}(t) - I_{Cur}(t) - I_{Phy}(t) \tag{4.2}$$

where $I_{Col}(t)$ represents the current charging the pixel capacitor. Integrating $I_{Col}(t)$ over a period $t_1^2$, which starts at $t_1$ and ends at $t_2$, one obtains the integrated charge loaded into the capacitor of the pixel. It is given by

$$Q_{Col}(t_1^2) = Q_{ReC}(t_1^2) - Q_{Cur}(t_1^2) - Q_{Phy}(t_1^2) \tag{4.3}$$

Using the charge to voltage conversion properties of the on-pixel preamplifiers, this charge is translated to an output signal according to

$$\Delta U(t_1^2) = \frac{g}{C} \, Q_{Col}(t_1^2) \quad . \tag{4.4}$$

Here, $g$ represents the gain of the preamplifier and $C$ for the capacitor of the pixel. For simplicity, we will not distinguish between the gain of the preamplifier and the gain of all amplifiers in the readout chain in the following. As only consequence of the generalized definition, the gain differ from $g \approx 1$, which is the gain of the source follower of the pixel.

### 4.4.2. The noise of MAPS

#### 4.4.2.1. Units

For reasons of clarity, the noise of MAPS was neglected so far. As the signal charge generated by impinging particles is very low, this simplification cannot be applied to methods used for doing measurements.

When introducing the noise, it is important to be aware that the signal of the sensor is converted from currents to charges and further to voltages within the readout chain. Hereafter, a conversion from voltage to digital is done by the ADC. Sources of noise are located at all points of the readout chain. Contributions to the noise can therefore have the units of currents, charges, voltages and AD-units. As they are converted together with the signal, different contributions add up independently of their initial units.

The algorithms and methods shown rely on the information delivered by the ADC. They work therefore internally in AD-units. Nevertheless, as the observables of interest are (signal) charges, the description will be done on the level of charges in order to ease the identification with the underlying processes in the sensor. In order to make the different contributions compatible with this description, it is common to convert them into an equivalent charge. Be for example $V_n(t_1^2)$ a noise contribution in units of Volt, $I_n(t)$ a contribution in units of Ampere and $Q_n(t_1^2)$ a contribution in units of Coulomb. The charge equivalent of the sum of those contributions is then given by

$$Q_{Eq}(t_1^2) = \frac{C}{g}V_n \ \oplus \ Q_n(t_1^2) \ \oplus \ \int\limits_{t_1}^{t^2} I_n(t) \ dt \tag{4.5}$$

and $Q_{Eq}$ is called the noise equivalent charge, which is usually given in units of electrons. This work will follow to this convention.

### 4.4.2.2. Sources of noise

A detailed discussion of the noise present in a MAPS detector is discussed in [27] from the microelectronic point of view. What concerns the noise of the full readout chain, which is of importance for this work, one has to be aware such different contributions like:

- The thermal noise, which follows a Gaussian distribution and which has a high frequency with respect to the integration time.
- The shot noise, which follows from the leakage current. It is caused by the fluctuations in the collection of individual leakage current electrons. These fluctuations are correctly modeled with the Poisson statistics but a Gaussian approximation is sufficient for our purposes. Assuming $n_e$ electrons to be collected within a certain integration time, the statistical uncertainty on this value is given by $\sqrt{n_e}$. This uncertainty manifests itself as an additional random noise in the detector signal.
- The common mode noise. Unlike the two noise sources above, the common mode is not considered a noise of the individual pixel. It is most probably dominated by the pickup from sources outside of the chip, which has a sufficiently low frequency to influence the readout of numerous pixels in the analogue data stream.
- The discretization error of the ADC.

When analyzing the noise, one finds that it is worth to distinguish correlated noise and random noise. This classification is independent of the source of noise. It is motivated by the fact, that correlated noise can be filtered to some extend by digital filters in the data analysis. Random noise can only be dimmed by optimizing the electronics and the operation conditions of the chip but not by using digital filters.

### 4.4.3. Categories distinguished by the analysis software

Only the output signal of the readout chain is available in order to assess different properties of the MAPS. One has therefore to insulate the different effects contributing to this output signal

in order to come to meaningful results. In particular one has to separate the best possible the signal charge $Q_{Phy}(t_1^2)$ from all other contributions.

The reconstruction of the different sources from a superposed signal is a limited instrument. The different categories insulated are therefore not identical to the contributions physics sources. Nevertheless, the differences are usually sufficiently negligible or not of practical interest, which allows for useful measurements.

The following categories were defined in the analysis software:

- The signal $Q_{Phy}^p(t_1^2)$, which directly corresponds to the signal charge collected from the sensing volume. In this category, the identification between the physics effect and the software picture is fully valid. The index $p$ refers the pixel address. Moreover, putting the index intendeds to distinguish the software picture from the true signal charge.

- The leakage current $Q_{Cur}^p(t_1^2)$. This category contains *any* DC component of the current charging the pixel capacitor, independently whether it is caused by the leakage current of the diode or not. Unlike the physics leakage current, which underlies statistical fluctuations, a strict constancy is postulated in this category.
  As in the 3T-pixel other contributions are usually negligible, this category corresponds to the true leakage current but ignores its fluctuations. In few cases, other contributions were observed. Where required, this will be mentioned as exception.
  The leakage current is property of the individual pixel.

- The common mode noise $Q_{CM}^p(t_1^2)$ addresses contributions, which are correlated over the pixel index but not over time. It represents with a certain precision low frequency pick up, which moves the zero level of all pixels but changes before the next frame is readout. The common mode noise is a property of the individual event. Its mean value over the time is postulated to be rigorously zero.

- The random noise (noise) $Q_{Rnd}^p(t_1^2)$. This category contains all uncorrelated noise independently of its source. In particular, the fluctuations of the physical leakage current are modeled in this category.
  It is postulated that the noise follows approximately a Gaussian distribution with a mean value of rigorously zero, no matter if the distribution was build as a function of $t$ or as a function of $p$. The postulate of a mean value equal to zero is justified, as any contribution on the mean value is interpreted either as leakage current or common mode in this parameterization.
  The random noise describes the remaining noise, which one cannot filter. It has to be sufficiently small to allow distinguishing the signal charge from it.

### 4.4.4. Algorithms used for assessing the 3T-pixel

The data analysis used for separating the different categories starts with equation 4.3. This equation is expanded in order to include the random and common mode noise. As for the 3T-pixel no recharge current is present in the integrating phase, this recharge current can be ignored.

By doing these modifications, the equation is translated to

$$Q_{Col}^p(t_1^2) = -Q_{Cur}^p(t_1^2) - Q_{Phy}^p(t_1^2) - Q_{CM}^p(t_1^2) - Q_{Rnd}^p(t_1^2) \quad . \tag{4.6}$$

One property of this modified equation is that a true physics signal is shown as negative. For simplification, it worth to multiply it with $-1$ and to define

$$Q_{Out}^p(t_1^2) := -Q_{Col}^p(t_1^2) \quad . \tag{4.7}$$

This leads to

$$Q^p_{Out}(t^2_1) = Q^p_{Cur}(t^2_1) + Q^p_{Phy}(t^2_1) + Q^p_{CM}(t^2_1) + Q^p_{Rnd}(t^2_1) \quad . \tag{4.8}$$

For the event number $n$, which is defined as the time interval $t^n_{n-1}$, this turns into the basic equation used in the analysis software:

$$Q^p_{Out}(t^n_{n-1}) = Q^p_{Cur}(t^n_{n-1}) + Q^p_{Phy}(t^n_{n-1}) + Q^p_{CM}(t^n_{n-1}) + Q^p_{Rnd}(t^n_{n-1}) \tag{4.9}$$

Note that for the sake of simplicity, the dead time caused by the reset process is ignored in this equation. Doing so has no impact on the result.

In order to rigorously insulate the categories of random noise, common mode noise and leakage current, one has to assume the absence of signal charge $Q^p_{Phy}(t^n_{n-1})$ from the output signal. This contrasts the intension of a particle detector, which is to measure this charge. Nevertheless, insulating the signal charge requires knowledge on the other contributions.

Good approximations were found to insulate the contributions also in the presence of particle hits. However, in order to ease the understanding of the methods used, the ideal case $Q^p_{Phy}(t^n_{n-1}) = 0$ will be assumed at this point. The methods will be expanded to the general case more below.

### 4.4.4.1. Insulating the leakage current in the absence of a hit

In order to insulate the leakage current of a pixel, it is necessary to read a chain of events, where each of these events is composed by taking the signal of all pixels of an array and apply CDS. For the individual pixel with index $p$, this chain is then given by a serial of $N$ values $Q^p_{Out}$ taken at time intervals $t^1_0$ to $t^N_{N-1}$.

It is now worth to calculate the mean value $\bar{Q}^p_{Out}$ of the different values $Q^p_{Out}(t^n_{n-1})$:

$$\bar{Q}^p_{Out} = \frac{1}{N} \sum_{n=1}^{N} Q^p_{Out}(t^n_{n-1}) \tag{4.10}$$

$$= \frac{1}{N} \left( \sum_{n=1}^{N} Q^p_{Cur}(t^n_{n-1}) + \sum_{n=1}^{N} Q^p_{CM}(t^n_{n-1}) + \sum_{n=1}^{N} Q^p_{Rnd}(t^n_{n-1}) \right) \tag{4.11}$$

The assumption $Q^p_{Phy}(t^n_{n-1}) := 0$ was used to derive equation 4.11. According to their definition, the mean value of the common mode noise and of the random noise over the time are always zero. One finds therefore:

$$\frac{1}{N} \sum_{n=1}^{N} Q^p_{CM}(t^n_{n-1}) = \bar{Q}^p_{CM} := 0 \tag{4.12}$$

$$\frac{1}{N} \sum_{n=1}^{N} Q^p_{Rnd}(t^n_{n-1}) = \bar{Q}^p_{Rnd} := 0 \tag{4.13}$$

The remaining contribution is given by:

$$\bar{Q}^p_{Out} = \frac{1}{N} \sum_{n=1}^{N} Q^p_{Out}(t^n_{n-1}) = \frac{1}{N} \sum_{n=1}^{N} Q^p_{Cur}(t^n_{n-1}) = \bar{Q}^p_{Cur} \tag{4.14}$$

$$\Rightarrow \bar{Q}^p_{Cur} = \frac{1}{N} \sum_{n=1}^{N} Q^p_{Out}(t^n_{n-1}) \tag{4.15}$$

## 4. Assessment of the radiation tolerance of MAPS

As the leakage current is by definition constant, one can conclude

$$Q^p_{Cur}(t^n_{n-1}) := \bar{Q}^p_{Cur} = \frac{1}{N}\sum_{n=1}^{N} Q^p_{Out}(t^n_{n-1}) \qquad (if\ Q^p_{Phy} = 0) \qquad (4.16)$$

### 4.4.4.2. Insulating the common mode in the absence of a hit

Knowing the leakage current and in the absence of signal charge, equation 4.9 becomes

$$Q^p_{Out}(t^n_{n-1}) = \bar{Q}^p_{Cur} + Q^p_{CM}(t^n_{n-1}) + Q^p_{Rnd}(t^n_{n-1}) \qquad (4.17)$$

In order to insulate the common mode, one has the reduce the known value $\bar{Q}^p_{Cur}$ from $Q^p_{Out}(t^n_{n-1})$ and hereafter to calculate the mean value over the pixels:

$$\frac{1}{P}\sum_{p=1}^{P}(Q^p_{Out}(t^n_{n-1}) - \bar{Q}^p_{Cur}) = \frac{1}{P}\sum_{p=1}^{P}(Q^p_{CM}(t^n_{n-1}) + Q^p_{Rnd}(t^n_{n-1})) \qquad (4.18)$$

Because of

$$\frac{1}{P}\sum_{p=1}^{P} Q^p_{Rnd}(t^n_{n-1}) = \bar{Q}^p_{Rnd} := 0 \qquad (4.19)$$

this becomes

$$\frac{1}{P}\sum_{p=1}^{P}(Q^p_{Out}(t^n_{n-1}) - \bar{Q}^p_{Cur}) = \frac{1}{P}\sum_{p=1}^{P} Q^p_{CM}(t^n_{n-1}) =: \bar{Q}_{CM}(t^n_{n-1}) \quad . \qquad (4.20)$$

When assuming, that the impact of the common mode is approximately the same for all pixels, one can model it like:

$$Q^p_{CM}(t^n_{n-1}) \approx \bar{Q}_{CM}(t^n_{n-1}) = \frac{1}{P}\sum_{p=1}^{P}(Q^p_{Out}(t^n_{n-1}) - \bar{Q}^p_{Cur}) \qquad (if\ Q^p_{Phy} = 0) \qquad (4.21)$$

It should be mentioned, that better approximations for the common mode can be found when approximating it as a serial of mean values each describing a subset of pixels. This can for example be done by approximating the common mode for the pixels of a line of pixel matrix, which was the method of choice in the data analysis made for this work.

### 4.4.4.3. Estimating the noise in the absence of a hit

Knowing the leakage current and the common mode, equation 4.9 becomes:

$$Q^p_{Out}(t^n_{n-1}) = \bar{Q}^p_{Cur} + \bar{Q}_{CM} + Q^p_{Rnd}(t^n_{n-1}) \qquad (4.22)$$

Again the absence of signal charge was assumed.

The remaining contribution, which is $Q^p_{Rnd}(t^n_{n-1})$, cannot be predicted as it is a random number. Nevertheless, the equation allows to estimate the standard deviation of the noise distribution $\sigma(Q^p_{Rnd})$:

$$Q^p_{Rnd}(t^n_{n-1}) = Q^p_{Out}(t^n_{n-1}) - \bar{Q}^p_{Cur} - \bar{Q}_{CM} \qquad (4.23)$$

$$\sigma(Q^p_{Rnd}) = \sigma(Q^p_{Out}(t^n_{n-1}) - \bar{Q}^p_{Cur} - \bar{Q}_{CM}) \qquad (4.24)$$

$$\sigma(Q^p_{Rnd}) = \sqrt{\frac{1}{N}\sum_{n=1}^{N} Q^p_{Out}(t^n_{n-1}) - \bar{Q}^p_{Cur} - \bar{Q}_{CM}} \qquad (if\ Q^p_{Phy} = 0) \qquad (4.25)$$

### 4.4.4.4. Estimating the signal charge and hit detection

After knowing $\bar{Q}_{Cur}^{p}$, $\bar{Q}_{CM}$ and $\sigma(Q_{Rnd}^{p})$ one gives up the simplification $Q_{Phy}^{p} = 0$ and assumes that at the time $t_{n-1}^{n}$ the individual pixel $p$ contains signal charge. The modification of our assumption is allowed, as knowledge on $\bar{Q}_{Cur}^{p}$, $\bar{Q}_{CM}$ and $\sigma(Q_{Rnd}^{p})$ may also be obtained in the presence of signal charge in individual pixels. This will be discussed more below.

Our goal is now, to measure the physics charge $Q_{Phy}^{p}$ and to decide, if it is significant. To do so, we use the constants $\bar{Q}_{Cur}^{p}$, $\bar{Q}_{CM}$ and $\sigma(Q_{Rnd}^{p})$ to predict the contributions of leakage current, common mode and noise to $Q_{Out}^{p}(t_{n-1}^{n})$. Equation 4.9 becomes:

$$Q_{Out}^{p}(t_{n-1}^{n}) = Q_{Phy}^{p}(t_{n-1}^{n}) + \bar{Q}_{Cur}^{p} + \bar{Q}_{CM} \pm \sigma(Q_{Rnd}^{p}) \tag{4.26}$$

From this, one can derive the signal charge like following:

$$Q_{Phy}^{p}(t_{n-1}^{n}) = Q_{Out}^{p}(t_{n-1}^{n}) - \bar{Q}_{Cur}^{p} - \bar{Q}_{CM} \pm \sigma(Q_{Rnd}^{p}) \tag{4.27}$$

Note, that the noise is now interpreted as uncertainty of the measurement of $Q_{Phy}^{p}(t_{n-1}^{n})$. The presence of a physics charge indicating an impinging particle can be assumed, if the indicated signal charge is significantly above the noise level. This is fulfilled if

$$Q_{Phy}^{p}(t_{n-1}^{n}) > C_{Threshold} \cdot \sigma(Q_{Rnd}^{p}) \tag{4.28}$$

### 4.4.4.5. Clusterisation

The charge of an impinging hit is spread over several neighboring pixels. To evaluate the total signal charge, a pixel cluster formed by the significant pixel and the first and second crown of pixels surrounding the significant pixel was defined. The calculated signal charge and noise of all pixels in this cluster was stored. As far as more than one significant pixel was found in one cluster, the pixel with highest charge was chosen as central pixel of the cluster.

Summing the charge of one cluster and comparing it with the squared sum of the noise of the participating pixels allows to some extend for a discrimination of hit candidates caused by irregular noise present in individual pixels. Moreover, it allows to estimate the charge collection efficiency of a group of pixels.

### 4.4.4.6. Estimating leakage current, noise and common mode in the presence of hits

So far, the absence of signal charge has been assumed for estimating leakage current, noise and common mode. For precision measurements of these parameters, this was indeed realized by removing the particle source. However, this is obviously not a good approach for operating a particle detector.

To dissolve the contradiction between the need for measuring the signal of particles and excluding it from the leakage current and noise estimates, different software models were used. They aim to remove hit candidates from the the sums used for estimating leakage current, noise and common mode. The models have different qualities depending on the information already available. They were used in an iterative process.

- *Model 1: Brute candidate rejection*
  This model rejects the 20% of $Q_{Out}^{p}(t_{n-1}^{n})$ showing the highest value from the sums. This rate is chosen arbitrary and very high in order to reliably remove all signal charge. One therefore accepts a relevant bias for both, $\bar{Q}_{Cur}^{p}$ and $\sigma(Q_{Rnd}^{p})$ towards lower values. Nevertheless, this method allows obtaining a first estimate on both, which can be refined hereafter by more precise algorithms. This model does not derive $\bar{Q}_{CM}$ but approximates it with zero.

- *Model 2: Seed pixel rejection*
  This model was used in order to refine the results obtained with Model 1. based on on the preliminary estimate of $\bar{Q}_{Cur}^p$ and $\sigma(Q_{Rnd}^p)$, all $Q_{Phy}^p(t_{n-1}^n) > 5\ \sigma(Q_{Rnd}^p)$ were rejected from the sums. These pixels were also rejected from the estimate of $\bar{Q}_{CM}(t_{n-1}^n)$. As non-significant signal charge is accepted, the bias for given for $\bar{Q}_{Cur}^p$ and $\sigma(Q_{Rnd}^p)$ by this algorithm is towards higher values. The noise obtained is typically 20% higher than the one of Model 1.
- *Model 3: Cluster rejection*
  While the to precedent models were used in order to obtain $\bar{Q}_{Cur}^p$ and $\sigma(Q_{Rnd}^p)$ before starting to scan a run for particle hits, a refined approach could be used within the scanning process. As the detailed hit information are available in this process (including the position of the pixels in the cluster), one can exclude all pixels of the cluster. This excludes all pixels potentially carrying signal charge as far as at least one pixel of the cluster is significant.

An example of the noise distributions obtained with the different models are compared in figure 4.3. One observes that the indicated "noise" of a MAPS detector significantly depends on the algorithm used for measuring it. Model 1 underestimates the noise by $\sim 15$ %. Model 2 and Model 3 overestimate the mean noise by $\sim 30$ % and $\sim 7$ %.

The choice of this algorithm is to some extend a question of taste, as all of them have disadvantages. Measuring the noise without the presence of impinging particles is most precise but can only be done under ideal conditions. Model 3 represents the best noise estimate for a system detecting particles, but the underlying common mode estimate can be biased by intense recharge currents as present in irradiated SB-pixels. This bias is not of concern for Model 1, which provides most comparable noise estimates for SB-pixels. However, it remains intrinsically biased.

With increasing understanding of their advantages and limits, different algorithms were preferred. Today, the absence of a particle source is considered as the preferable solution. Nevertheless, the data required was not taken in early measurements. In order to reach the precision goal of this work (reliable trends), special care was undertaken to compare only noise measured with identical algorithms. This is in general fulfilled when comparing noise from the same chip.

### 4.4.4.7. Update of leakage current and noise estimate

So far, $\bar{Q}_{Cur}^p$ and $\sigma(Q_{Rnd}^p)$ were considered as rigorously constant. This is justified in the time scale of seconds. Nevertheless, in particular changes in temperature influence both values. An update was therefore foreseen in the algorithm scanning runs for particle hits. This was done by using:

$$\bar{Q}_{Cur,2}^p = \frac{1}{M}\left[(M-1)\bar{Q}_{Cur,1}^p + Q_{Out}^p(t_{n-1}^n)\right] \tag{4.29}$$

$$\sigma_2(Q_{Rnd}^p) = \sqrt{\frac{1}{M}\left[(M-1)[\sigma_1(Q_{Rnd}^p)]^2 + (Q_1^p(t_{n-1}^n) - \bar{Q}_{Cur,1}^p - \bar{Q}_{CM}(t_{n-1}^n))^2\right]} \tag{4.30}$$

The constant $M$ has to be chosen in order to retard the speed of the adaptation to a reasonable value. Normally $M = 20$ was used.

No correction for the common mode has been done in equation 4.29 as doing so would allow for a unwanted divergence of $\bar{Q}_{Cur}^p$. This divergence would bias the measurements of the leakage currents.
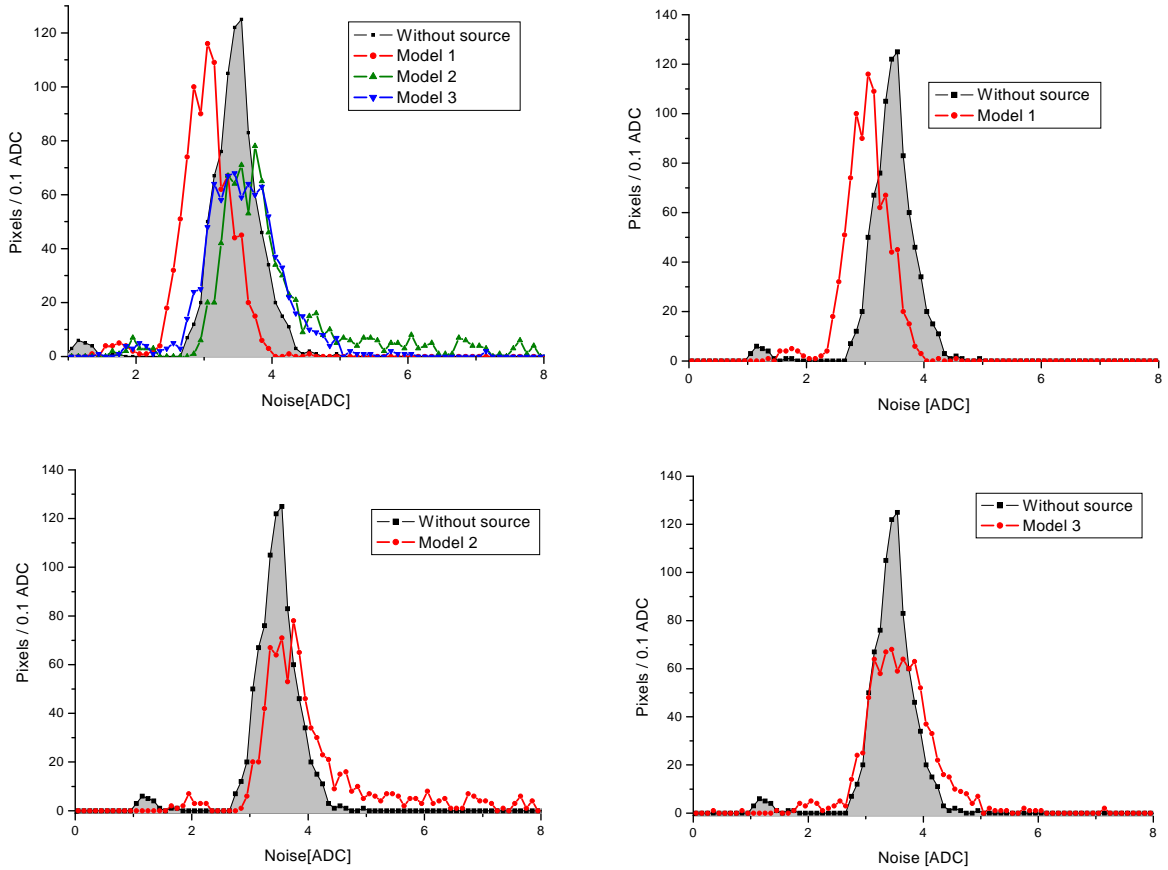
Figure 4.3.:

(Upper left panel): *Example of noise distributions as derived by the different measuring methods (see text).*

(Upper right panel): *Comparison between the noise measured without source and the noise approximation according to model 1 (brute candidate rejection). As this model rejects a part of the noise, the indicated mean noise is $\sim 15$ % below the true value.*

(Lower left panel): *Comparison between the noise measured without source and the noise approximation according to model 2 (seed pixel rejection). As this model rejects only significant pixels, charge from the border of clusters is taken into account in the measurement. This leads to a over estimation of the noise of the pixels, which can become very high in some cases. The indicated mean noise is $\sim 30$ % above the true value, the bias for individual pixels may be as high as factors.*

(Lower right panel): *Comparison between the noise measured without source and the noise approximation according to model 3 (cluster rejection). As this model rejects all clusters around significant pixels, which cures a part of the disadvantages of model 2. Nevertheless, charge of hits, which were not recognized, is still taken into account. The indicated mean noise is $\sim 7$ % above the true value.*

## 4.4.5. Limits of the algorithm when being applied to data from SB-pixels

In principle, the algorithm used can be applied to the data produced by SB-pixels in a straightforward way. However, one has to be aware that one of the basic assumptions, which is the absence of a recharge current, is not fulfilled anymore. This has several consequences, which have to be taken into account.

One of these consequences is the removal of a part of the signal charge. As discussed in detail in chapter 2.2.4.6, this is because parts of the signal is canceled out between the moment the hit occurs and the next readout of the pixel. This leads to an indicated reduction of the signal charge, which depends on the time constant of the recharge current $\tau$, the initial signal and the time between the hit and the following readout. Under bad circumstances it can reach some 10% of the initial signal.

Another consequence is a systematic bias of the estimate of the leakage current and of the noise. As the recharge current of a SB-pixel is neither constant nor fully uncorrelated, it influences both categories without fitting into one of them.

In order to illustrate this problem, an ideal output signal of a MAPS detector was generated using a random generator, which generated a serial of samples according to $\bar{Q}^p_{Cur,1} = 0$ and $\sigma(Q^p_{Rnd}) = 10 \ e^-$. This reflects a SB-pixel having with its intrinsic leakage current compensation and a noise of $10 \ e^-$ with a sufficient degree of realism.
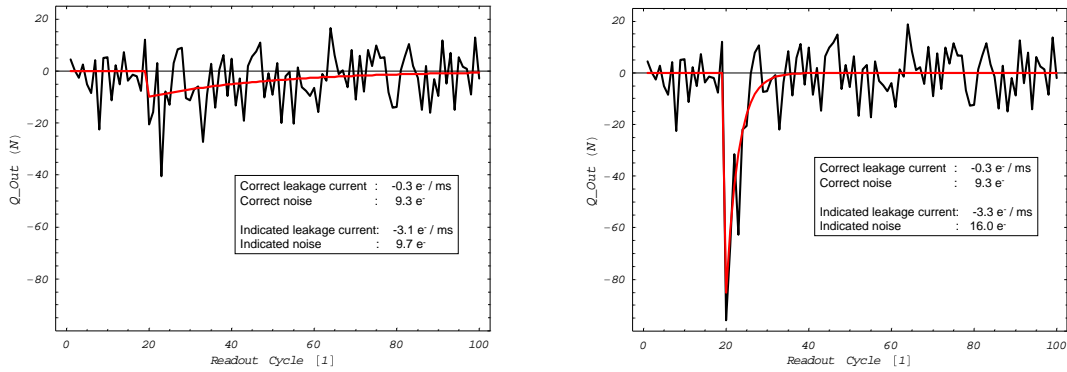


Figure 4.4.: *Data sample with a hit as seen by the algorithm used for estimating the noise of a SB-pixel. The hit arrives in sample number 20 (where the time between two samples was assumed with 1 ms). Its charge gets recognized and removed from the sum. The recharge currents remain and bias the estimate of leakage current and noise depending on $\tau$. In the left panel $\tau = 30$ ms was simulated, which corresponds to a non-irradiated chip. In the right panel, the same situation is shown for $\tau = 3$ ms, which corresponds to an irradiated chip. One observes, that the noise estimate is heavily biased in this case.*

Hereafter, the random noise and leakage current of the sample was calculated according to Model 2, which removes the charge of the hit. For the given sample, this led to an indication of $\sigma(Q^p_{Rnd}) = 9.3e^-$ and $\bar{Q}^p_{Cur,1} = 0.3 \ e^-$. The difference to the ideal value is because of the limited amount of samples (N=100).

In a next step, the recharge current caused by a particle hit with $Q^p_{Phy}(t^n_{n-1}) = 300 \ e^-$ was simulated using equation 2.33. The integration time was assumed with $t^n_{n-1} = 1 \ ms$ and a recharge

constant of $\tau = 30\ ms$ and $\tau = 3\ ms$ was chosen in order to simulate a detector with high and low time constant. Both, the initial distribution and the recharge current were superposed.

As in the following the indication for leakage current and noise had to be simulated, the charge of the hit was removed according to Model 2. The resulting data sets are illustrated in figure 4.4 (left) for $\tau = 30\ ms$ and in figure 4.4 (right) for $\tau = 3\ ms$.

Hereafter, the leakage current and noise were recalculated for both modified data samples, which simulates the reaction of the analysis software to the presence of the recharge current of a particle hit. In the case of the sample with $\tau = 30\ ms$, the indicated leakage current dropped to $\bar{Q}^p_{Cur,1} = -3.1\ e^-/ms$, which represents now the mean recharge current. The indicated noise increased by 4 % to $\sigma(Q^p_{Rnd}) = 9.7 e^-$.

In the case of the sample with $\tau = 3\ ms$, the indicated leakage current dropped again to moderate $\bar{Q}^p_{Cur,1} = -3.3\ e^-/ms$. The indicated noise on the other hand increased by 72 % to $\sigma(Q^p_{Rnd}) = 16.0\ e^-$ even if the true random noise was not changed. This scenario can be considered as a problem when estimating the random noise of irradiated SB-pixels. This is in particular true as a comparable effect has also to be expected in the beam tests, which were used for estimating the detection efficiency of the irradiated detectors.

So far, there are no reliable strategies to overcome this overestimation of noise. In principle, one could predict the recharge current on the base of a recognized particle hit. Nevertheless, this approach is so far not feasible, as the test systems used for driving the chips show a relevant dead time. The hits leading to the presence of the recharge currents are therefore usually not visible in the data.

Another strategy would be to measure the noise of the pixels in the absence of a particle source and to use this information hereafter without modifying it. This is problematic, as the noise estimate does not follow anymore potential changes in the true noise, as they can be caused by changes in temperature.

As a positive aspect it should be mentioned, that the problem discussed above leads to an underestimation of the performances of the chip and thus also to an underestimation of its radiation tolerance. Any radiation tolerance results shown in this work remains therefore valid but might be improved when using an adapted algorithm for analyzing the data obtained from irradiated SB-pixels. Moreover, the impact of this effect to noise measurements depends on the occupancy of the detector, which was assumed with 1 % in this calculation. Lower occupancies were typically chosen in particular in beam tests, which reduces the bias.

## 4.5. Procedures for measuring the electronic properties of MAPS

### 4.5.1. Gain and charge collection efficiency

#### 4.5.1.1. The charge collection distribution

The gain and charge collection efficiency of MAPS was measured by building the distribution of the charge collected from hits of a monochromatic X-ray source ($^{55}Fe$). Obtaining this distribution called *charge collection distribution* hereafter is done by illuminating the detector with photons from the source and detecting the hits with the MAPS to be examined.

When interacting with the silicon of the detector, these photons are converted into electron/hole pairs. The mean energy required for such a conversion is given with 3.6 $eV$ [25]. One expects therefore the generation of about 1640 free electrons from a photon originating from the dominant 5.9 $keV$ line of the source.

*4. Assessment of the radiation tolerance of MAPS*

The charge collection distribution is a histogram of the number of free electrons collected from an interacting photon. Therefore, it contains information on the process of charge collection.

### 4.5.1.2. Impact of the charge collection process on the distribution for X-rays

This information can be compared with the current hypothesizes on the collection process. As explained in chapter 2.2, the charge generated in the sensitive medium of a MAPS is not attracted by electric fields but has to reach the collecting diodes by means of thermal diffusion. This fact has important consequences:

- Due to the statistical character of the charge collection (random walk), the charge generated by a particle is usually spread over several pixels. In order to judge the total amount of charge collected, one has therefore to sum the signal of several neighboring pixels.
  One should mention, that this spread of charge allows substantially improving the spatial resolution of the MAPS by calculating the center of gravity of the charge distribution on the pixels of one cluster. Moreover, wrong indications caused by irregular noise in individual pixels can be distinguished from the signal of minimum ionizing particles by also requiring a charge indication in the neighbor pixels.
  On the other hand, a higher signal over noise ratio of the detector would be reached by concentrating all signal charge into only one pixel.

- There always remains a probability, that a part of the charge carriers recombine before reaching the collecting diodes. This probability depends on the distance between the hit and the diodes and thus on the position of the particle impact with respect to the collection diode. As the charge collection efficiency is thus not homogeneous in the detection volume, MAPS are not suited for a use as a spectroscopic instrument.

### 4.5.1.3. Classes of interactions between X-rays and the detector

Besides the impact of the diffusion process, one has to be aware of different classes of interactions between the photons and the silicon detector. These classes depend on, in which part of the detector the interaction occurs. Besides the ordinary interactions in the epitaxial layer, two additional cases have to be mentioned:

Interactions occur frequently outside but close to the epitaxial layer of the detector. In this case, a part of the charge diffuses into the epitaxial layer where it gets collected. Another part gets lost outside of the sensitive medium. Only a part of the charge generated is thus accessible for the detector from the beginning and the photon is useless for estimating the charge collection efficiency. The signal generated by these interactions is expected to have a broad distribution, which goes down to the noise level.

The second particular case corresponds to an interaction of a photon in the depleted zone of the collecting diodes. Even if the probability of such an interaction is low, this case is of a particular interest, as the local electric field of this volume concentrates the signal electrons into one individual pixel. As the amount of these electrons is relatively well known, this concentration allows getting an estimate on the gain of the detector.

### 4.5.1.4. Charge collection distributions for groups of pixels

As the charge is spread over many pixels, it is of importance, which pixels have been taken into account when discussing the charge collection efficiency. Most ($\sim 40\,\%$) of the charge is collected
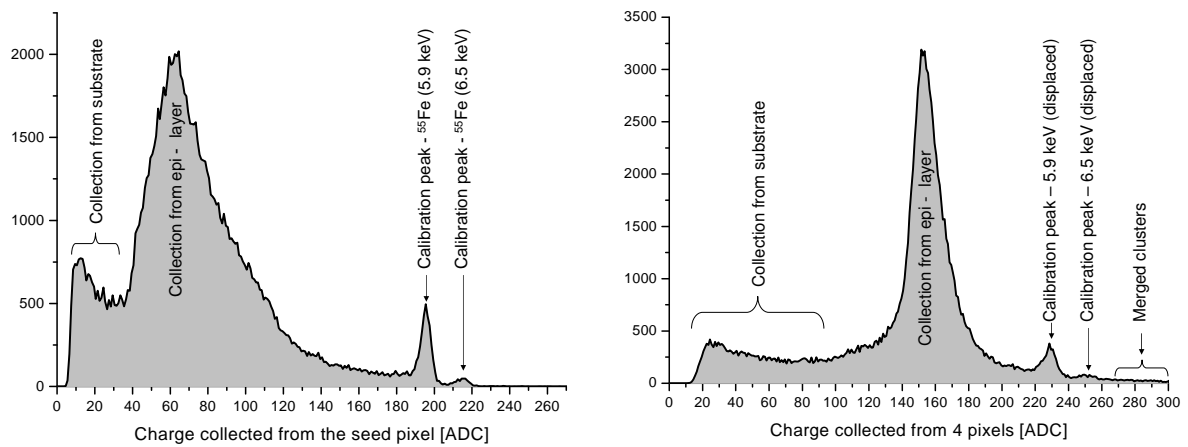
Figure 4.5.: *Typical distributions of a MAPS-detector illuminated with a $^{55}Fe$-source. The distribution of the seed pixel is shown in the left panel. The right panel shows the one obtained by summing the charge of the four pixels with highest signal in the cluster. See text.*

by the seed pixel. The eight pixels forming the first crown in common receive $\sim 55$ % of the charge. A smaller amount of charge can also found in the second crown ($\sim 5$ %) [1].

Because of this charge sharing, the charge collection distributions vary depending on the amount of pixels taken into account. In order to build the distributions, a cluster of $5 \times 5$ pixels was formed around each seed pixel. The $i$ pixels with the highest signal within this cluster were summed in order to gain the collected charge distribution of $i$ pixels. One should note that this way of choosing the pixels to be summed does not set a requirement on the position of these pixels with respect to the seed pixel.

### 4.5.1.5. Peaks in the charge collection distribution

Today, there is no simulation available, which would quantitatively predict the shape of a charge collection distribution as shown in figure 4.5. This is because simulating more than individual interactions by the means of a semiconductor simulator requires an unrealistic amount of computing power. However, there exists a widely accepted qualitative explanation, which is sufficiently precise for interpreting the information of the distribution.

According to this explication, the small Gaussian peaks labeled *calibration peak* corresponds to a hit into the depleted zone of the collecting diode. As in this case the charge of a photon is concentrated into one individual pixel, this peak is most precise in the single pixel distribution. The naming is inspired by the fact that the position of this peak combined with the knowledge on the energy of an impinging X-ray photon allows calibrating the gain of the readout chain. This will be explained in detail more below.

A measurement with a sufficiently high statistics shows a smaller second peak at a signal level slightly above the calibration peak. This peak corresponds to the interaction of the photons of the weaker 6.5 $keV$ - line of the $^{55}Fe$ source. In principle, this peak can also be used for doing a calibration. This was usually not done because of the high statistics required. Nevertheless, this option provides a useful crosscheck of our understanding of the origin of these peaks.

The dominant peak in the distribution originates from the charge collected from hits occurring inside the epitaxial layer but outside of the depleted zone of the collecting diode. As its position allows estimating the charge collection efficiency of the detector, it is called *charge-collection peak*. Because of the charge spread, the position of this peak depends on the amount of pixels summed. A comparison between two of these peaks is therefore only meaningful, if an identical number of pixels is summed in both distributions.

The background below the two peaks is usually interpreted as result of the hits outside the epitaxial layer. This interpretation is probably incomplete, as noise and hits in the epitaxial layer close to a collection diode are likely to contribute to its low energy and the high-energy part respectively. However, it is sufficient, as the detailed composition of the background is not of practical importance for this work.

### 4.5.1.6. The calibration peak in single and multi pixel distribution: A side remark.

Comparing the position of the calibration peak in figure 4.5 (left) and figure 4.5 (right), one finds the peak at a $\sim 40$ $ADC$ higher value. Smaller effects of this type can be caused by shaping the noise when sorting the pixels to be summed with respect to their charge. Nevertheless, in the particular case, another effect was responsible for this effect.

---

[1]It should be mentioned, that the numbers presented depend on the details of the sensor and are therefore not of universal use. Nevertheless, they provide an instructive example.
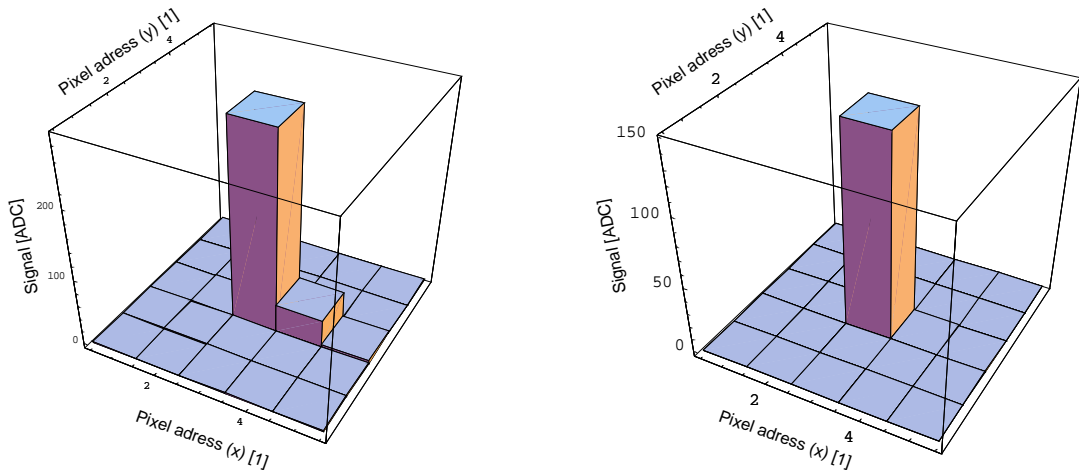
Figure 4.6.: *The left panel shows the mean value of the charge deposited into each pixel of pixel clusters originating from the calibration peak of the distribution shown in figure 4.5. Even if the theory predicts no charge deposit outside of the central pixel, a charge indication can be found in the pixel readout next. The origin of this observation made on MIMOSA-9 remains to be clarified. A good candidate for an explanation is problem in the readout chain specific to this chip. Having a comparable chip design but a slightly different readout chain, MIMOSA-4 did not show this problem (right panel).*

This is illustrated in figure 4.6, which shows the mean value of the charge collected from all pixels of the clusters participating in the calibration peak. According to the theory, only the central pixel of the cluster should contain charge. Nevertheless, a charge indication is found in the neighboring pixel right of the central pixel, which corresponds to the pixel being readout next to the central one.

The cause of this observation, which was made with MIMOSA-9 remains to be clarified. It is likely not to represent properties of the chip itself but to point on a weak point of the readout chain. This is covered by the results of MIMOSA-4 shown in the right panel of figure 4.6. Being equipped with comparable pixels but a slightly different readout chain, this elder chip produces a cluster shape, which corresponds to the theory.

From this observation, one can learn that it is important to choose always the seed pixel distribution when deriving the gain of the readout chain, as this allows excluding parasitic effects. Moreover, it highlights the need for a conservative interpretation of the data obtained from different measurements. Effects like the one shown are sometimes difficult to identify and may mislead for example when directly comparing charge measurements of the two chips relying on purely statistical error estimates.

It should also be mentioned, that despite of the problem shown, MIMOSA-9 showed comparable detection performances and a better spatial resolution than MIMOSA-4. This demonstrates a certain robustness of MAPS against smaller analogue problems.

### 4.5.1.7. Estimating gain and charge collection efficiency

The gain of the readout chain is derived by comparing the position of the calibration peak with the corresponding amount of electrons. As this peak corresponds to a full collection of all electrons generated by a photon with well-defined energy, the amount of collected electrons is well known. Assuming a linear response of the readout chain (what is justified for the 3T-pixel and can be considered as sufficient approximation for the SB-pixel) one can translate the output signal, which is usually given in AD-counts of the 12-bit ADC, into electrons. The position of the calibration peak was always measured from the distribution of the seed pixel of the cluster.

In a next step, the position of the charge collection peak was compared with the one of the calibration peak. Assuming again linearity, this allows judging the efficiency of charge collection from the epitaxial layer. Because of the charge spread, this value depends on the number of pixels grouped in the charge collection distribution. A group of four summed pixels was used by default. This choice was originally motivated by the need to compare the distributions of pixel arrays mounted on MIMOSA-2, which were arranged partly hexagonally and partly quadratic. Nevertheless, this choice demonstrated in most cases a good compromise between collecting most charge and reducing the amount of pixels. The latter is advantageous as every pixel taken into account also contributes some noise.

No fit models motivated by physics are available to fit the calibration peak and the charge collection peak. Namely, a gauss shape is not necessarily to be expected as the width of these peaks does not only reflect the noise of the measurement but also the geometry of the sensitive volume. For instance, the distance between the impact position and the next collecting diode is of importance.

In order to obtain a good fit results, several empirical fit expressions were tested for the peaks and the background respectively. The fit of the background was performed first using functions as different as polynomials, exponentials and the shoulder of a cosine. The points obviously belonging to peaks were removed from this fit. The result of the fit function was hereafter subtracted from the data.

Next, the peaks were approximated with a Gauss- and a Lorenz-peak in the region of interest. Both peak models were combined with all models describing the background.

The uncertainty of the peak position was derived conservatively from the uncertainties of the fit and the difference between the highest and the lowest indication of the peak position provided by the different fit models. It was found to be typically below $\sim 1$ %, which can be considered as negligible with respect to the systematic uncertainties of the measurements.

Given, $U_{Calib}$ represents the position of the calibration peak and $U_{Charge}$ the position of the charge collection peak in ADC-units respectively. The gain of the readout chain (which is because of external amplification *not* in general the gain of the chip) is then given by

$$G = \frac{C}{g} = \frac{1640e^-}{U_{Calib}} \tag{4.31}$$

where the $1640e^-$ represent the amount of electron/hole pairs generated by the 5.9 $keV$ photon of the $^{55}Fe$ source.

The charge collected with $N_P$ summed pixels can be calculated like

$$Q_{Epi}(N_P) = U_{Charge}(N_P) \cdot G. \tag{4.32}$$

Some comments should be made on the uncertainty of the measurements done for obtaining the charge collection and the gain:

- In principle, the method shown is able to measure the gain of each individual pixel by generating the collected charge distribution of the hits impinging into it. For the detectors discussed in this work, such an individual calibration was not mandatory, as the gain of the pixels is sufficiently uniform. This is was cross checked by analyzing the width of the calibration peak, as it is formed by events collected from all pixels of a sub matrix. Substantial non-uniformity in the gain of the individual pixels would contribute to the width of this peak. This was not observed, the width measured can be explained with pure counting fluctuations.

- Besides the fitting error, the measurement of $G$ underlies a systematic uncertainty of few percent according to the production tolerances of the electronic components used in the readout chain. Namely, the resistors used to define the gain of the different amplifiers are of concern. This effect is relevant when comparing two different chips of the same type but can be ignored when comparing the two measurements done on the same chip.

- A slight (few percent) systematic underestimation in the measurement of charge collection can be caused by assuming no signal charge when calculating the common mode in the analysis algorithms. This effect is of importance for the measurement of the absolute values of charge collection but should widely cancel out when comparing the results of two chips (also of different identity), as far as they were operated modest occupancy.

- As illustrated in figure 4.6, the limitations of the readout chain may provide an additional bias. In the illustrated case, this bias was $\sim 15\%$. This systematic bias concerns absolute measurements but should be canceled out when comparing different measurements done with the same chip and readout chain.

## 4.5.2. Leakage currents

The measurements of the leakage currents and the noise of MAPS based on the estimate made with the analysis software on $\bar{Q}^p_{Cur}$. The measurements of the leakage current were usually made without particle source and $\bar{Q}^p_{Cur}$ was identified with the leakage current.

It should be mentioned, that a higher integration time than the usual one was used in order to derive the leakage current. This was done by replacing the usual readout cycle based on on two readouts after one reset by another one, which was usually eight readouts after one reset cycle. CDS was done between the first and the last frame of the cycle, which multiplies the integration time by a factor of seven. This measurement of $\bar{Q}^p_{Cur}(t_1^8)$ instead of $\bar{Q}^p_{Cur}(t_1^2)$ significantly improved the sensitivity of the method.

The leakage current is a property of the individual pixel, as production tolerances play an important role. The values shown indicate the mean value of the leakage current over all pixels over the same type. The error bars usually indicate the standard deviation of the pixel-to-pixel dispersion as far as the distribution was sufficiently Gaussian. This dispersion is more important as the uncertainties of the measurements performed on the individual pixels. In few cases, important systematic non-uniformities in the leakage current were observed, which led to others than Gaussian distributions for the leakage current. This will be discussed separately.

Over all, the measurement of the leakage current was possible with a reasonable precision down to currents of $\sim fA$.

The leakage current was translated to physics units by:

$$I^p = \frac{\bar{Q}^p_{Cur}}{t_{Int}} = G \cdot \frac{\bar{Q}^p_{Cur}[ADC]}{t_{Int}} \tag{4.33}$$

In this equation, $G$ stands for the gain as derived in equation 4.31, $\bar{Q}^p_{Cur}[ADC]$ for the leakage current indicated by the analysis software, which is in AD-units and $t_{Int}$ for the integration time.

### 4.5.3. Noise

The noise of the detectors was derived based on on $\sigma(Q^p_{Rnd})$ given by the analysis software (see chapter 4.4.4).

Initially, the measurements of noise were partially based on on the run also used for building the charge collection distribution. In this case, $\sigma(Q^p_{Rnd})$ was derived using the signal rejection models. Noise values obtained from beam tests also rely on this approach. With increasing understanding of the limits of this method, this was changed and dedicated runs without source were done. Again, a train of readout cycles was taken after each reset, which allowed deriving the noise as a function of the integration time.

Comparable to the leakage current, the noise of MAPS is a property of the individual pixel and follows roughly a Gaussian distribution with poorly populated additional tail towards higher values. The mean value of this distribution is usually given and the error bars represents the standard deviation of the noise distribution (which is again more important then the uncertainties of the measurement).

According to the principle of measurement, the noise shown includes also the noise of the external readout chain. This noise depended on details of the readout chain like the length of the cables between the AUX-board and the ADCs, which was $\sim 1\ m$ in the laboratory-setup but $\sim 40\ m$ in the setup used for beam test. Moreover, a dependence of the noise of the system on the gain of the buffers installed on the motherboard was found. This influenced the noise by $\sim 20\%$.

Because of the numerous systematic problems in the noise estimate, only noise measurements obtained with the same type of chip and the same readout chain and the same algorithm are considered as comparable. In this case, the systematic problems are expected to cancel out and the precision of the noise measurement used for studying trends is represented by the statistical errors given.

In contrast, the results on the absolute number of noise may contain systematic errors in the order some tens of percent under bad circumstances.

### 4.5.4. The time constant of the recharge current ($\tau$)

The time constant of the recharge current of the SB-pixel $\tau$ (see chapter 2.2.4.6) is defined as the time the pixel needs to remove a signal charge from its capacity. This time must be high with respect to the integration time of the pixel in order to avoid the signal to be removed before it is read out.

A measurement of this time constant requires for the presence of a signal charge in the pixel capacity. Its decay can then be observed by a chain of consecutive readout processes. To do the measurement, the following procedure was used:

- The detector under test was installed in a temperature controlled dark chamber and illuminated with photons of the $^{55}Fe$ source to generate the signal charge required.
- A special readout scheme based on on a train of 128 consecutive readouts (without reset and dead time) was used to readout the chip. This special scheme was required in order to avoid the dead times of the standard readout based on on two frames, which is caused by the time required for transferring the data towards its storage.

- Within the trains of 128 frames, hits of $^{55}Fe$ were searched with an simplified algorithm based on on a high fixed signal threshold. This algorithm intentionally recognizes only the hits with highest signal charge, as they provide the clearest signal for measuring $\tau$. Within the limits of the underlying first order description of the recharge process, the time constant can be considered as independent of the signal charge.

- Once a hit was recognized, the signal (after CDS) obtained from the 32 readout cycles after the hit were stored. This signal shows the effective current $I_{Eff}$ charging the pixel transistor.

- Typically several hundreds of these 32 readout cycles long samples were obtained in each measurement. The mean value of all values for a i-th readout after the hit respectively was computed in order to remove thermal noise from the results. The corresponding standard deviation was used as indicator for the uncertainties.

- An exponential function was fitted to the curve generated from the mean values.

The procedure allows to measure $\tau$ in the range between few $ms$ and some tens of $ms$. This range is determined by the relative length of $\tau$ with respect to the integration time of the chip. If $\tau$ becomes too high, the observed curve becomes compatible with a straight line. This leads to significant uncertainties in the fitting procedure. If $\tau$ becomes comparable to the integration time of the chip, the time between the readout cycles becomes too long to observe the fast recharge process.

Two major sources of systematic uncertainties are to be mentioned for this measuring method. The first one concerns the measurement of the time in which the hits arrive. This precision of this measurement is limited to the integration time, as no access to the pixel is possible between two readouts. The second point concerns the initial amplitude of the signal. This amplitude was typically set to very high (and constant) values. Because of the low population of this area in the collected charge distribution, only relatively few entries with a substantial spread are available. The spread tolerated was typically in the order of few 10 %.

A subtly additional aspect comes into the game, if $\tau$ is not significantly higher than the integration time. Because of the instating signal decay, identical hits occurring "long" before the readout provide a lower remaining signal than the ones occurring short before the readout. A hit with sufficient signal charge for detection may thus be accepted if it occurred short before the readout while it is rejected if it occurs "long" before the readout. This biases both, the mean amplitude and the mean time information.

Taking the mean value of the different 32 readout cycles long samples reduces the effect of both uncertainties. The use of the standard deviation as indicator for the uncertainties provides a basic measure of their impact on the result, which is sufficient for the purpose of this work. Nevertheless, it is too simplistic to represent the complexity of the systematic uncertainties discussed. This limits the use of the method described for precision measurements.

For measurements demanding for a very good resolution for $\tau$, observing the decay of the signal of a short, synchronized light pulse is recommended. This has the advantage that time and amplitude of the signal can be precisely reproduced which substantially reduces uncertainties discussed. Nevertheless, unlike the solution chosen, this approach requires modifications on the existing setup.

It should be mentioned, that in most Plots $-I_{Eff}$ is shown. This was done, as one interprets the signal of a particle intuitively as positive peak and this current has a negative sign with respect to the one causing the signal.

*4. Assessment of the radiation tolerance of MAPS*

# 5. Ionizing radiation tolerance of MAPS

## 5.1. Introduction

The radiation tolerance of MAPS has already been studied prior to the start of this PhD, mainly in order to establish their use as sensors for optical imaging in radioactive environments like space. The main outcome of these studies was a radiation-induced increase of the dark current of the pixels, combined with increasing shot noise. Moreover, total failures of chips after some tens of $kRad$ were reported. An overview over these activities are given in [49].

The latter reports about a first trial to build MAPS in a deep sub micron process $(0.35\mu m)$, which is intrinsically more radiation hard than the processes used before. Moreover, the use of this process was for a first time combined with the use of radiation hard design rules (namely enclosed transistors, see section 4.1.2). The MAPS detectors were irradiated with a $^{60}Co$-source up to doses of 30 $MRad$ (Si). Again, a strong increase of leakage current was reported, but the device remained operational up to the highest dose applied. The leakage current was observed to go into saturation after some $MRad$. It was concluded that MAPS can be built, which tolerate up to 30 $MRad$.

Being valid for MAPS used in optical imaging, this statement cannot be straightforwardly translated for applications in nuclear and particle physics. One the one hand, the radiation doses in nuclear and particle physics experiments are substantially higher than the ones in space. The radiation doses of interest were thus rarely covered by the earlier studies. On the other hand, the requirements for a sensor for optical imaging are slightly different from the ones for a sensor used in charged particle detection.

The differences concern in particular the sensitivity of the pixel, which is given by its signal to noise ratio (S/N). In optical imaging, a high S/N is welcome but not mandatory as, to some extend, the intensity of the impinging light can be enforced by the optics of the camera. This is not possible in charged particle detection since each particle generates only a very limited amount of charge carriers in the pixel. A sufficient S/N, allowing distinguishing unambiguously this modest charge from the noise, is thus mandatory.

On the other hand, MAPS used in optical imaging run with relatively long integration times. This makes the devices very sensitive to increased leakage current. The integration times used in charged particle detection are typically orders of magnitude shorter in order to contribute to the time resolution of the experiments. Consequently, substantially higher leakage currents can be tolerated.

Since the studies on MAPS for optical imaging do not reflect the requirements for charged particle tracking, the existing literature on radiation tolerance of MAPS was insufficient for a feasibility study of CBM. Dedicated radiation tolerance tests were thus required to judge if MAPS could resist the high radiation doses expected for this experiment.

The radiation tolerance studies for CBM were guided by first results obtained at the IPHC in the context of the International Linear Collider (ILC) [27], [39]. As the observations made during these studies guided the work for CBM, they will be intensely discussed before motivating the different optimization steps performed to improve the radiation tolerance of MAPS.

Within the studies, it was found that the radiation tolerance of MAPS partly depends on undocumented features specific to the processes used for their fabrication. This was initially not accounted for, which led to wrong or incomplete interpretations of the observations made within the studies. radiation tolerance studies from ten different prototypes, each featuring several pixel structures, were required to reach a preliminary understanding of the radiation effects in MAPS.

Within this chapter, the results of the study of selected pixels from eight prototypes will be presented and discussed. The presentation of the results and intermediate conclusions will be done in chronological order. This seems best suited to motivate direction of the studies, which had to be reconsidered repeatedly because of unexpected results and increasing understanding.

The presentation will be split in two parts. In the first one, the results obtained with native MAPS, not optimized for radiation tolerance, will be shown. The weak points of these chips and strategies for improvements will be discussed.

In the second part, chips hosting the optimized structures will be introduced and the effects of the optimizations will be shown. Finally, the preliminary conclusions of this ongoing work and the consequences for CBM will be discussed.

## 5.2. Native radiation tolerance of MAPS against ionizing radiation damage

### 5.2.1. Early studies on the 3T-pixel

#### 5.2.1.1. MIMOSA-1

| MIMOSA-1 (1999), AMS 0.6 µm | |
|---|---|
| Epitaxial layer: ~ 14 µm, 3 Metal layers | |
| 64 x 64  3T-Pixels | 64 x 64  3T-Pixels |
| 20 µm pixel pitch | 20 µm pixel pitch |
| 1 Diode/Pixel | 4 Diodes/Pixel |
| Diode size: 3.1 x 3.1 µm² | Diode size: 3.1 x 3.1 µm² |
| Not discussed | Not discussed |

Figure 5.1.:
*Selected technical data of MIMOSA-1. Only pixel matrices of interest for this work are shown. The electronics of the chip was designed with radiation soft standard transistors.*

MIMOSA-1 was the first prototype designed to study the feasibility of charged particle tracking with MAPS detectors. It was intended to provide a reliable estimate of parameters like noise and gain of the detector. Moreover, the signal collected from an impinging minimum ionizing particle, the detection efficiency and the spatial resolution were addressed.

A design without unnecessary complexity was required to conclude reliably on the fundamental questions addressed. MIMOSA-1 was thus not optimized for radiation tolerance or high readout speed and known radiation soft structures were tolerated in the chip. In particular, conventional

transistors were used instead of the more radiation hard enclosed transistors, as their electrical properties are well established. As moreover the production process chosen had a relatively sizable feature size (AMS 0.6 $\mu m$), substantial leakage current in NMOS transistors was expected already after a rather moderate radiation dose.

Nevertheless, some exploratory measurements of the tolerance of MIMOSA sensors to ionizing radiation were performed by irradiating MIMOSA-1 with an IRD of 200 $kRad$ using a $\sim 10 \ keV$ X-ray source[1] [27] . This moderate dose was chosen according to the requirements of the ILC.

Despite of the known weak points in the chip design, only slight radiation effects were observed. Small (some percent) deteriorations of gain and charge collection were found for some pixel geometries. These have a minor incidence and are at the limit of the sensitivity of the measurements. It was thus concluded that the readout chain of the chips (including NMOS-transistors) tolerated the IRD expected for ILC. On the other hand, a strong effect of the radiation on the collecting diodes of the pixels was observed: after irradiation, their leakage current increased by roughly one order of magnitude. A potential influence of the irradiation on the noise was not addressed in these early measurements.

### 5.2.1.2. MIMOSA-2

| MIMOSA-2 (2000), MIETEC 0.35 µm | |
|---|---|
| Epitaxial layer: ~ 4 µm, 5 Metal layers | |
| 64 x 64  3T-Pixels<br>20 µm pixel pitch<br>Squared geometry<br>1 Diode/Pixel<br>Diode size: 1.7 x 1.7 µm² | 64 x 64  3T-Pixels<br>20 µm pixel pitch<br>Hexagonal geometry<br>2 Diodes/Pixel<br>Diode size: 1.7 x 1.7 µm² |
| 64 x 64  3T-Pixels<br>20 µm pixel pitch<br>Hexagonal geometry<br>1 Diode/Pixel<br>Diode size: 1.7 x 1.7 µm² | Not discussed |

Figure 5.2.:
*Selected technical data of MIMOSA-2. Only pixel matrices of interest for this work are shown. Radiation hard transistors were used in the analogue electronics of MIMOSA-2.*

**Chip design and radiation doses:**   Because of the radiation soft design of the chip, the radiation tolerance studies on MIMOSA-1 were not continued with higher radiation doses. A next generation chip, MIMOSA-2, was designed. The chip was manufactured in a process with a smaller feature size than MIMOSA-1 (AMI/MIETEC 0.35 $\mu m$). Moreover, radiation hard transistors were used in the sensitive analogue part of the chip, while the more robust digital electronics still relied on standard transistors. Because of the modifications, MIMOSA-2 was expected to withstand substantially higher radiation doses than MIMOSA-1.

---

[1]In parallel to this work, the dosimetry of the X-ray source has been revised. The dose used in earlier publications came out to be underestimated by roughly a factor of two. Whenever required, the doses of elder studies cited in this work are corrected by this factor.

According to the results of MIMOSA-1, only light degradations of the chip performances were expected after a dose of a few hundreds of $kRad$. Irradiations were thus done with IRDs of 400 $kRad$ and 800 $kRad$ of soft X-rays [39].

**Observations:** Like MIMOSA-1, MIMOSA-2 showed a significant increase of leakage current after irradiation. This increase was as high as a factor of 10. Nevertheless, as the initial leakage current of the MIMOSA-2 pixel was rather modest, it could easily be compensated by pedestal correction while processing the signal.

Tests of the chip irradiated with 800 $kRad$ showed a systematic dependence of the leakage current on the position of the pixels. This effect was first considered as being a consequence of an inhomogeneous irradiation of the pixel matrix. Meanwhile, temperature gradients on the chip, which may be due to high local power consumption of individual components of the circuit, appeared as a more credible explanation.

A moderate increase of the noise was observed, compatible with the shot noise expected from the additional leakage current. At a temperature of $10°C$, this increase was of the order of a few percent after a dose of 400 $kRad$ and reached almost 20% after a dose of 800 $kRad$. As the noise remained below 15 $e^-$, it was not considered to be a problem.

Charge collection distributions[2] of MIMOSA-2, measured before and after irradiating the chip with a dose of 400 $kRad$, are shown in figure 5.3. The upper plot illustrates the charge collected in the seed pixel of the cluster; the lower plot displays the charge collected within a group of four pixels. The calibration peak indicating the gain of the readout chain is visible in the upper plot at a position of $\sim 320$ $ADC$-units. Its position remained unchanged for all doses applied to MIMOSA-2. The gain of the readout chain did thus remain stable and one can conclude that the readout chain including the transistors of the pixel tolerated the radiation.

In contrast to the predictions and to the results of MIMOSA-1, a strong loss in charge collection was observed already on the MIMOSA-2 sensor irradiated with 400 $kRad$. This is illustrated in the lower plot of figure 5.3. One observes the position of the big peak representing the charge collection from the sensitive epitaxial layer to move from $\sim 200$ $ADC$-units before irradiation to $\sim 100$ $ADC$-units after irradiation.

According to the shift of the peak, the remaining charge collection of a group of four pixels after irradiation is $\lesssim 50\%$ of the initial value. The value is likely to be biased towards higher values, since hits generating a low signal (fluctuation) are likely to disappear from the distribution because of the discrimination threshold of the cluster reconstruction. Consequently, the analysis performs a pre-selection of the signals, which tends to bias the results towards a higher charge collection.

**Discussion of the results:** The observed increase of leakage current and the corresponding shot noise were known from literature and were observed on MIMOSA-1 before. They are interpreted as a consequence of radiation damage in the interfaces between $Si$ and $SiO_2$ in the vicinity of the collecting diode. This radiation damage generates defects, which ease the thermal generation of charge. A part of this charge is collected by the collection diode, which causes the additional leakage current.

As noise and leakage current remained tolerable, the deterioration in charge collection was identified as the dominating problem of the irradiated MIMOSA-2. This observation was remarkable as it contrasts with the results obtained with MIMOSA-1. In order to explain the effect and to improve the detector design, the origin of the charge loss had to be traced back. This

---

[2]See chapter 4.5.1 for a detailed discussion of charge collection distributions.
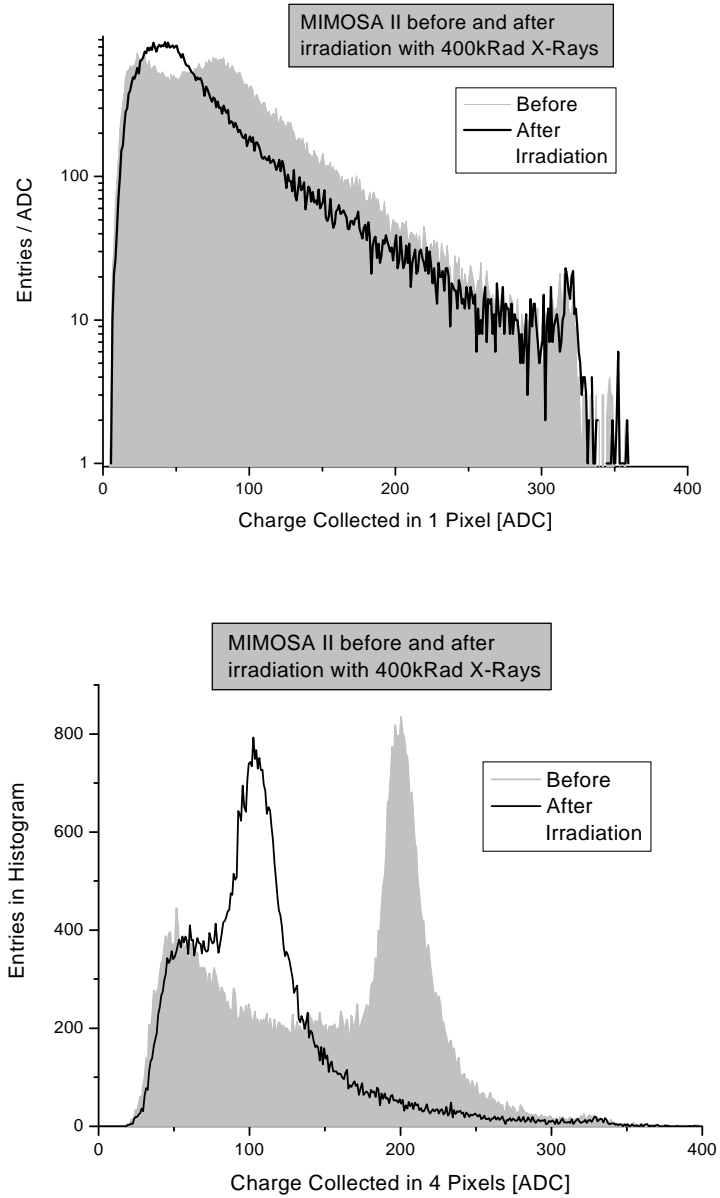
Figure 5.3.: *Distribution of the signal charge collected from hits of $^{55}Fe$ photons in MIMOSA-2 before and after an irradiation with $\sim 400$ kRad X-rays. The top plot displays the charge collected with the seed pixel of a cluster only, the bottom plot refers to the charge collected with a group of four pixels.*

was simplified by the observation that the calibration peak did not change significantly for all radiation doses applied.

The calibration peak is produced by hits impinging the depleted area of the collection diode of a pixel. As the radiation had no significant impact on the properties of the peak, one concludes the charge created in this depleted area to be correctly collected and translated into a signal. This is only possible if the depleted area of the collecting diode and all electronic components between the collecting diode and the ADC remain within their specification despite the radiation damage. One can thus conclude that these components do not contribute to the observed loss of signal. Consequently, any effect absorbing the signal has to take place before the diffusing charge has reached the depleted area of the sensing diode.

This conclusion seems conflicting with the theory of radiation tolerance, as this diffusion takes place in the epitaxial layer of the detector. As explained in chapter 4.1, soft X-rays have a too low energy to generate bulk damage in this material. Moreover, ionizing damage is reversible in silicon, as the presence of thermal electrons in the conduction band allows for a fast annealing of broken bindings. Soft X-Rays should thus not affect the epitaxial layer or the diffusion process of electrons in this volume. As the epitaxial layer is surrounded by P-Wells and substrate layers, all made of silicon, no surface damage as these known from interfaces between $Si$ and $SiO_2$ is to be expected.

Additional information obtained with other chips was required to explain the observation made on MIMOSA-2. This will be discussed in the following.

## 5.2.2. First studies on the SB-Pixel (MIMOSA-4)

| MIMOSA-4 (2001), AMS 0.35 µm | |
|---|---|
| Epitaxial layer: None, 3 Metal layers | |
| 64 x 64  3T-Pixels<br><br>20 µm pixel pitch<br><br>Squared geometry<br><br>1 Diode/Pixel<br><br>Diode size: 2 x 2 µm² | 64 x 64  3T-Pixels (modified)<br><br>20 µm pixel pitch<br><br>Squared geometry<br><br>1 Diodes/Pixel<br><br>Diode size: 2 x 2 µm² |
| 64 x 64  SB-Pixels<br><br>20 µm pixel pitch<br><br>Squared geometry<br><br>1 Diode/Pixel<br><br>Diode size: 4.3 x 3.4 µm² | 64 x 64  3T-Pixels<br><br>20 µm pixel pitch<br><br>Squared geometry<br><br>3 Diodes/Pixel<br><br>Diode size: 2 x 2 µm² |

Figure 5.4.:
*Selected technical data of MIMOSA-4. Only pixel matrices of interest for this work are shown. Radiation hard transistors were used in the full electronics chain of MIMOSA-4. The 3T-pixels showed poor charge collection efficiency.*

**Chip design and radiation doses:**  Observations made on the chip MIMOSA-4 allowed for establishing a first hypothesis on the deterioration in charge collection observed on MIMOSA-2. The chip was produced with the AMS 0.35 $\mu m$ process, which featured a moderately doped substrate instead of an epitaxial layer. This feature was undocumented in the specification of the process but

allowed to study whether this new variety of CMOS processes could be used for MAPS design[3].
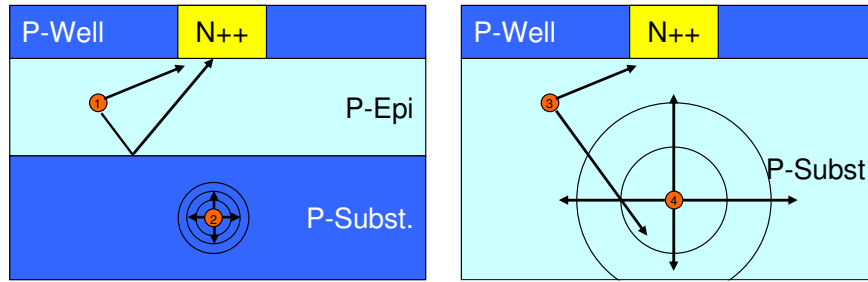


Figure 5.5.: *Simplified picture of the different effects to be expected in a MAPS detector with and without epitaxial layer when being hit by an $^{55}Fe$-photon. In the case of an detector with epitaxial layer (left), free electrons are reflected back to the epitaxial layer. Electrons occurring in the substrate are suppressed. This suppression does not exist in the lowly doped substrate of a chip without epitaxial layer (right). A charge collection from the deep substrate is thus possible. On the other hand, electrons diffusing away from the collecting diode get lost.*

The doping of the substrate of this AMS 0.35 $\mu m$-process is actually quite close to the one of epitaxial layers. The substrate can thus be used as active medium. Nevertheless, the absence of an epitaxial layer has an important impact on the charge collection properties of the chip, which needs to be briefly discussed.

Some aspects of the charge collection from hits of $^{55}Fe$-photons in detectors with and without epitaxial layer are illustrated in figure 5.5. The left figure illustrates the situation in a standard detector with epitaxial layer. For a hit within the epitaxial layer (hit 1), the charge may diffuse directly to the collecting diode (N++). Moreover, if the charge diffuses towards the substrate, it gets reflected at the interface between the P-Epi and the P-Substrate and may subsequently be collected by a sensing diode.

Electrons diffusing in the substrate have a significantly lower lifetime with respect to the ones diffusing in the epitaxial layer. This is because the presence of the doping atoms favors recombination. Electrons produced by a hit in the substrate (hit 2) are thus often absorbed within this medium. Consequently, the charge collection distribution dominantly shows hits of photons interacting within (or close to) the epitaxial layer. This leads to the generation of the big peak in the charge collection distribution (see bottom of figure 5.3).

As illustrated in figure 5.5 (right), the interface between the P-Epi and the P-Substrate is not present in chips without epitaxial layer. Electrons diffusing away from the collection diode are thus not reflected back and get lost (see hit 3). On the other hand, electrons produced in the deep substrate (hit 4) have now a lifetime comparable to the ones produced in a standard epitaxial layer. The collection of charges originating from the deep substrate is thus possible.

For MIP detection, it was hoped that the charge collection from the deep substrate would compensate the fraction of charge which escapes towards it. This came out to be fulfilled for the non-irradiated chips and the detector exhibited a very good performances. Nevertheless,

---

[3]At the time being, a trend to replace epitaxial layers by this kind of substrate was observed in industry. This questioned the future availability of processes suited to MAPS production. MIMOSA-4 allowed to proof that MAPS are also compatible with processes based on on a high resistivity substrate. Meanwhile, the success of commercial MAPS motivated industry to develop so called *opto processes*, which are optimized for their production. This provides a long time perspective for the technology.
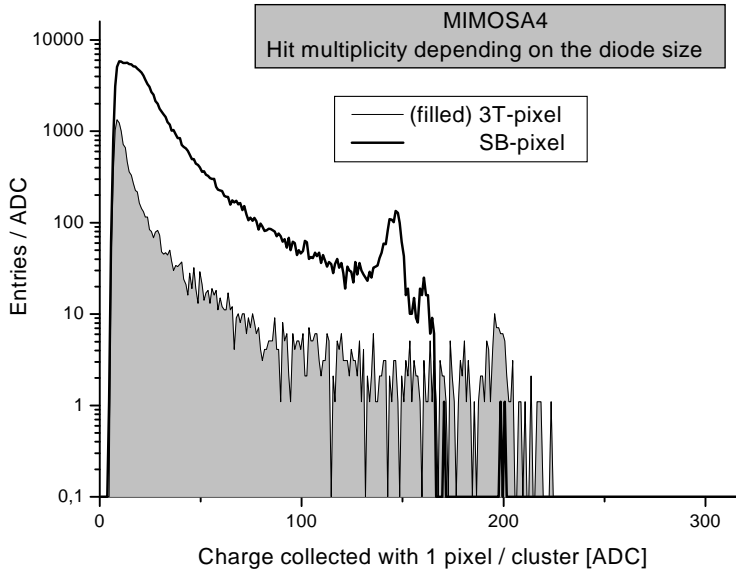
Figure 5.6.:
*The charge collection distribution of the SB-pixel and the 3T-pixel of MIMOSA-4 at a temperature of 10 °C. The integration time was 3.3 ms.*

significant consequences were observed on the shape of the collected charge distribution for $^{55}Fe$ photons. The generation of a charge collection peak in the charge collection distribution requires an (approximatively) constant charge collection efficiency (CCE) in the sensitive volume. This is not fulfilled in MAPS detectors without epitaxial layer, as of the sensitive volume is more than one order of magnitude thicker than the standard epitaxial layer. Since a part of the electrons recombine on their path, the CCE depends on the depth at which the hit occurred. This leads to a smearing of the charge collection peak, which cannot be insulated anymore. Unlike chips with epitaxial layer, a measurement of the CCE with $^{55}Fe$ is thus impossible for MAPS without epitaxial layer.

A second peculiarity of MIMOSA-4 was due to the on-pixel amplifiers used. Besides different 3T-Pixels, an array with SB-pixels (see chapter 2.2.4) was integrated into this chip. As discussed more extensively below, these pixels showed good performances. Nevertheless, their presence generated an additional complication for the measurements. The standard method for assessing the leakage current of the collection diodes of the pixels relies on measuring the charge removed by this current from the capacities of the on-pixel amplifiers. As the current is compensated by the biasing diode in the SB-pixel, this method cannot be applied in this case. Direct measurements were not possible, as the design of MIMOSA-4 did not allow insulating the power source of the pixels from the one of other components. No leakage current measurements are thus available for the SB-pixels.

**Observations:** A first important observation on MIMOSA-4 was that the SB-pixels of this detector worked efficiently, while the established 3T-pixels showed very poor detection efficiency. This is illustrated in figure 5.6, which shows the collected charge distribution of the seed pixel for the 3T-pixel and for the SB-pixel. One observes the amount of hits detected with the SB-pixel to be close to one order of magnitude above the value found with the 3T-pixel. On the other hand, a calibration peak is visible for both pixels. As the sensitivity of the 3T-pixels was very poor, their measurements were abandoned and the investigations concentrated on the SB-Pixel.

As MIMOSA-4 provided the first opportunity to study SB-pixels, the radiation tolerance of this detector was studied extensively. The radiation effects came out to differ from the ones known from 3T-pixels. Within the study, MIMOSA-4 was irradiated with 400 *kRad* X-rays and
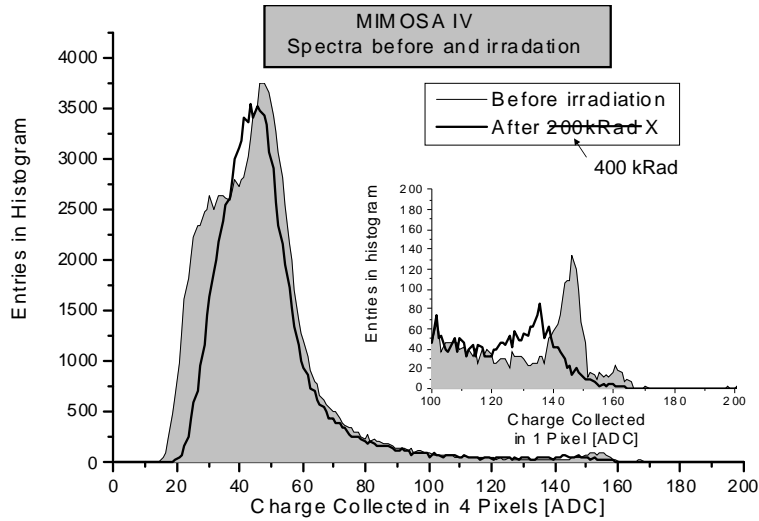
Figure 5.7.:

*The collected charge distribution of the SB-pixel of MIMOSA-4 at a temperature of 10 °C measured before and after irradiation with ~ 400 kRad X-rays. The charge collected by a group of four pixels from a hit of $^{55}Fe$ photons is shown in the main diagram. The zoom shows the charge collected by the seed pixel in the region around the the calibration peak.*
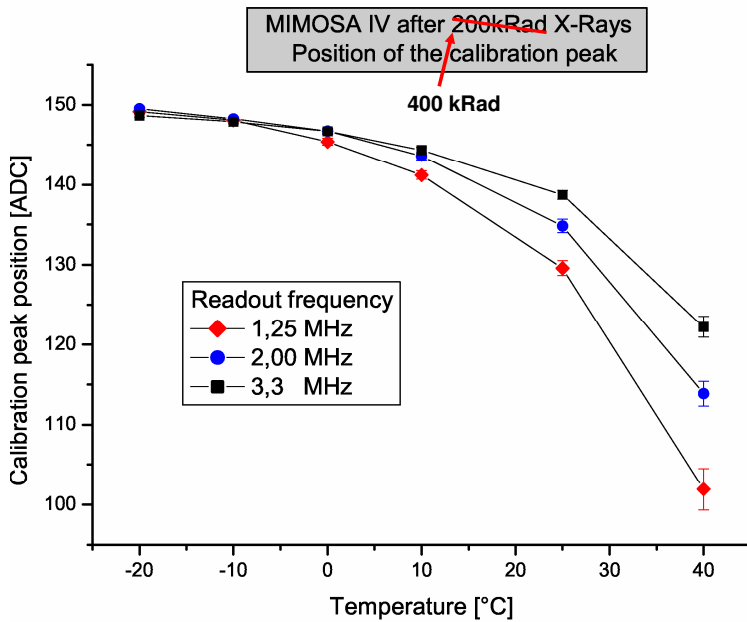


Figure 5.8.:
*The position of the calibration peak of the MIMOSA-4 SB-pixel as a function of the integration time and the temperature of the coolant. The cross over of the lines at temperatures below 0 °C is considered as an artifact of the measurement procedure.*
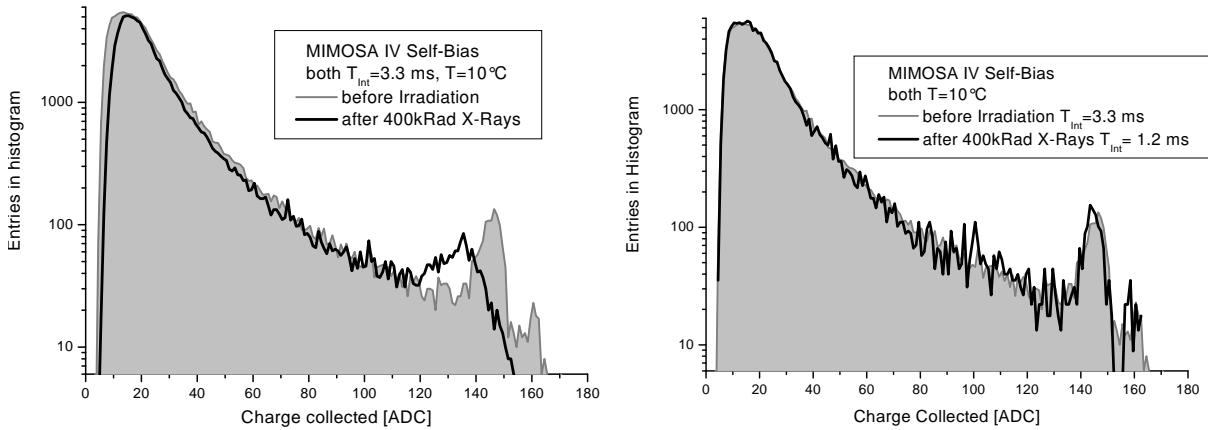
Figure 5.9.:
*Left: The charge collection distribution of the SB-pixel of MIMOSA-4 at a temperature of* 10 °*C taken before and after irradiation with* ∼ 400 *kRad X-rays.*
*Right: A reduction of the of the integration time from* 3.3 *ms to* 1.2 *ms allows compensating the radiation effects.*

its properties were compared with the ones of a second, non-irradiated, chip.

The collected charge distributions obtained at a temperature of 10 °$C$ with the non-irradiated and the irradiated MIMOSA-4 sensor are shown in figure 5.7. The peak at 50 $ADC$-units in the distribution for four pixels should not be confused with the charge collection peak; as already stressed earlier, the concept of a charge collection peak cannot be applied to a MAPS detector collecting the signal charge from the substrate. An interesting observation was made on the positions of the calibration peak. As shown in the zoom of figure 5.7, the position of this peak changes and its width increases after irradiation. This contrasts with the observations on 3T-pixels, where the peak remains unaffected.

The shift of the calibration peak was studied systematically as a function of the temperature and the integration time. As illustrated in figure 5.8, a strong correlation between the peak position and these two parameters was observed. The cross-over of the three lines occurring at temperatures below $\lesssim -10°C$ is not considered as significant. A slight (few percent) gain drop of the readout chain has been observed regularly when increasing the readout frequency.

The measurement suggests that parts of the radiation effects of MIMOSA-4 can be recovered by reducing the integration time of the chip or its temperature.

In the following, the issue is addressed whether if choosing a sufficiently short integration time or temperature may allow removing the radiation induced modifications of the charge collection distribution. The outcome of this study is illustrated in figure 5.9. The left figure shows the radiation induced distortion of the charge collection distribution for chips running under identical conditions (top). In the right figure, the distribution obtained with a non-irradiated chip was compared with the one of an irradiated chip running under more favorable condition (1.2 *ms* integration time instead of 3.3 *ms*). One observes that the reduced integration time is sufficient to restore the shape of the distribution. Similar results were achieved by keeping the integration time constant and reducing the temperature of the irradiated chip to −10 °$C$ (not shown). From this it was concluded, that cooling or reducing the integration time could reduce the effects of radiation damage.
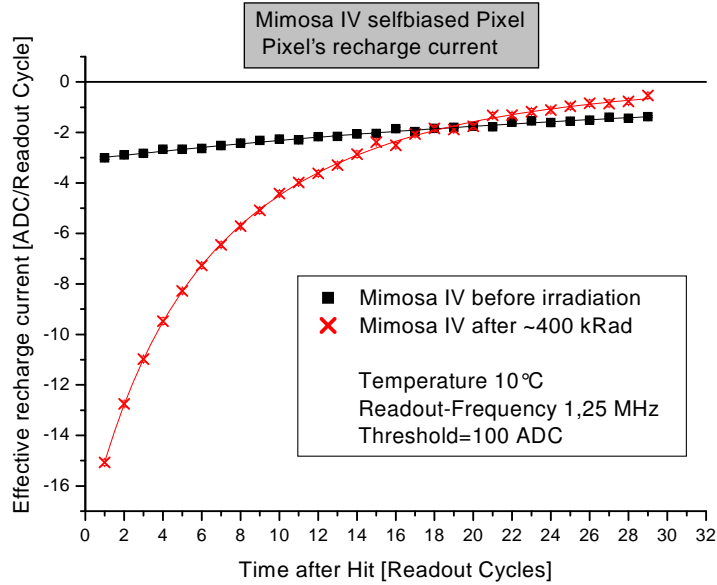
Figure 5.10.:
*The effective recharge current of MIMOSA-4 before and after irradiation with $\sim 400\ kRad$ X-rays, at a temperature of $10\ ^\circ C$. The integration time was $3.3\ ms$, the unit of the current is $\sim 0.55\ fA = 1\ ADC - unit/cycle$ in this plot. Only statistical uncertainties were accounted for.*
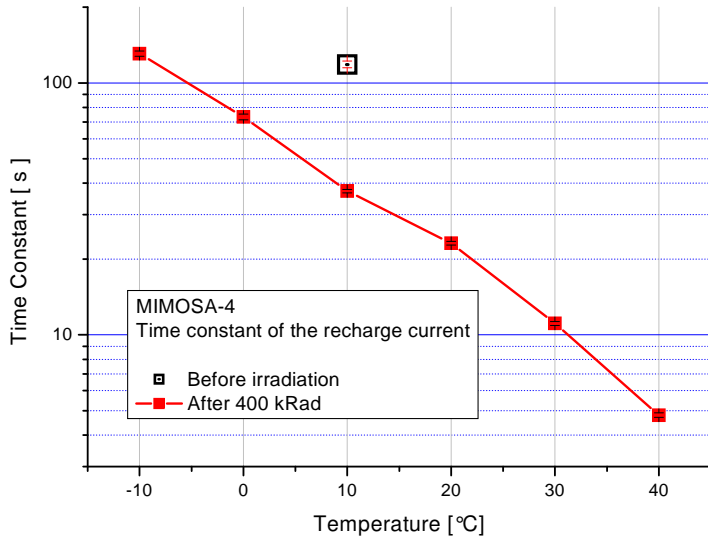


Figure 5.11.:
*The time constant of the effective recharge current of MIMOSA-4 after $\sim 400\ kRad$ X-rays, as a function of the temperature. Only statistical uncertainties were accounted for.*

One hypothesis explaining why reduced temperature and integration time have a positive effect, based on the influence of both parameters on the time constant of the recharge current, $\tau$ (see section 2.2.4.6). It was suggested that this constant drops because of radiation damage, which would lead to a recharge of the pixels before the signal can be readout. This hypothesis would explain the distortions observed on the collected charge distribution.

The time constant was measured for the SB-pixels of MIMOSA-4. As discussed in section 4.5.4, this was done by observing the decay of the signal generated by $^{55}Fe$ photons. This is illustrated in figure 5.10, which shows the effective recharge current of the pixel as a function of the delay after the hit for the non-irradiated and the irradiated chips. One observes that this current is higher for the irradiated chip in case of short delays. An exponential function was fitted to the samples illustrated in figure 5.10 in order to obtain an estimate of $\tau$.

The measurement was repeated with the irradiated chip for six different temperatures, ranging from $-10\ ^\circ C$ to $+40\ ^\circ C$. The outcome of the study is illustrated in figure 5.11, which displays the extracted values of $\tau$ as a function of the temperature. One observes that radiation effects significantly reduce the time constant. Moreover, the decrease was found to follow roughly an
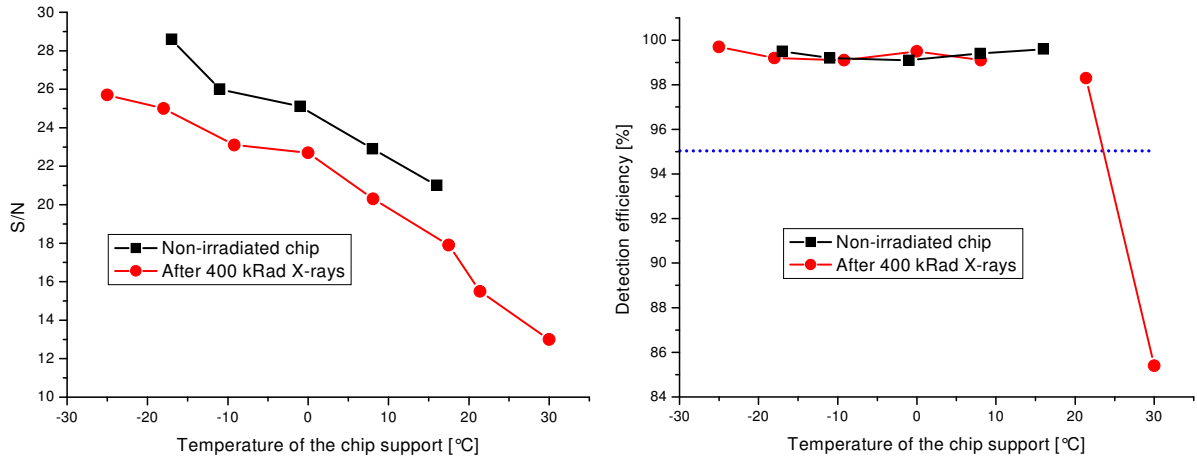
Figure 5.12.:
*Left: The S/N of MIMOSA-4 before and after being irradiated with $400\ kRad$ X-rays as a function of the temperature.*
*Right: The detection efficiency of MIMOSA-4. A badly measured point at $T = 17\ °C$ was removed. From [51].*

exponentially dependence on the temperature.

It should be mentioned that the measurement procedure for $\tau$ is exposed to (sometimes) significant and complex systematic uncertainties, which were only partially taken into account in the uncertainties displayed in figure 5.10 and 5.11. This concerns in particular the limited control over the amplitude of the initial signal and the precise moment of its generation with respect to the readout time. The measurements are however informative enough on the radiation and temperature effects on $\tau$, to fit the requirements for the purpose of this work. Nevertheless, a bias cannot be excluded and safety margins should be foreseen for applications, which depend crucially on $\tau$. This point is discussed in more detail in chapter 4.5.4, which also suggests methods to reduce the systematic uncertainties.

MIMOSA-4 was the first chip irradiated with ionizing radiation to be qualified with a particle beam. To do so, it was exposed to a $\sim 120 GeV$ pion beam of the CERN-SPS. The measurement results are shown in figure 5.12, which displays the observed distributions of the S/N (left) and the detection efficiency (right). One observes a fast decrease of the S/N as the temperature increases for both, the irradiated and the non-irradiated chip. Moreover, the S/N drops by slightly more than 10 % after irradiation. The drop is clearly significant, when compared to the typical uncertainty affecting the S/N measurement, which amounts for a few percent. Whether the effect is due to a noise increase or to a signal reduction was not clarified, as the corresponding measurements are ambiguous for SB-pixels.

As illustrated in figure 5.12 (right), the S/N of the detector was sufficient to provide a detection efficiency above 99 % for all temperatures applied to the non-irradiated chip. For the irradiated chip, a strong reduction of the detection efficiency appears for temperatures $\gtrsim 20\ °C$. This reflects the S/N decrease below the minimum value ($\sim 13 - 14$) required for ensuring a satisfactory detection efficiency[4].

This effect is presumably not restricted to the irradiated chip. As the S/N decreases also

---

[4]The uncertainty on the detection efficiencies is typically in the order of a few 0.1 %.

for the non-irradiated chip, a similar effect is expected also for this device, but at much higher temperature.

Despite the limitations in the operation temperature, MIMOSA-4 was the first chip demonstrating a satisfactory radiation tolerance against 400 $kRad$ integrated dose. Even if the latter was still not sufficient for CBM, the observation was considered as a breakthrough as it showed the path to follow for further improvements.

**Discussion:** The results obtained with MIMOSA-4 highlight the differences between the classical 3T-pixel and the SB-pixel. Both kinds of pixels show a very different macroscopic reaction to ionizing radiation doses, which is a consequence of different concepts of the preamplifier.

Despite of their diversity, all radiation effects observed on the SB-Pixels of MIMOSA-4 can be explained with a radiation-induced increase of the leakage current of the collection diode. In order to motivate this argument, the scheme of the SB-pixel (see figure 2.7) should be reminded. In this scheme, one finds the collection diode ($D_{Coll}$) and the biasing diode ($D_{Bias}$). As discussed in chapter 2.2.4, the current passing $D_{Bias}$ is equal to the leakage current of $D_{Coll}$ if the system is in equilibrium. If this equilibrium gets disturbed by the presence of a signal charge, an additional current is delivered by $D_{Bias}$. This additional, so-called *effective recharge current* ($I_{eff}$), recharges the pixel capacity and thus removes the signal charge. As illustrated in figure 5.13, the amplitude
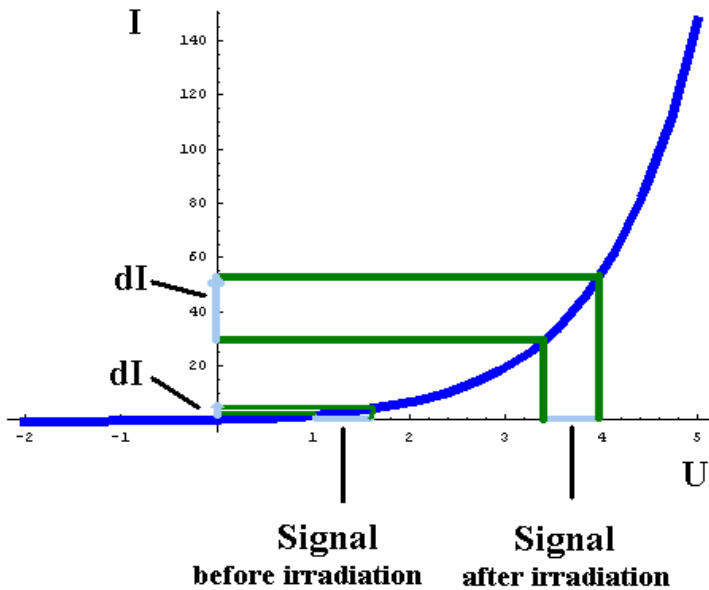


Figure 5.13.:
*The characteristic curve (current versus voltage) of the biasing diode of the SB-pixel is shown. Because of the non-linear characteristics of the diode, the effect of an additional signal voltage depends on the initial current flow, which is equal to the leakage current. If this current is higher because of radiation damage, the effective recharge current (dI) increases significantly, which leads to a faster recharge of the pixel capacity.*

of $I_{eff}(= dI)$ depends on the initial current transversing the diode. Provided this current is low, as before irradiation, the diode is in the regime of low resistivity ($R = \Delta I / \Delta U$). A small signal thus generates modest additional current and the recharge of the capacity is slow. Consequently, the time constant $\tau$ is long.

If the leakage current of the $D_{Coll}$ increases after irradiation, a higher voltage drop at $D_{Bias}$ is required for compensation. This leads to a decrease of the resistivity of the diode and the signal triggers a higher additional current flow. This leads to the observed reduction of $\tau$ after irradiation. Moreover, the temperature dependence of $\tau$ can be explained in a natural way, as the leakage current increases with temperature.

A straightforward consequence of the shortening of $\tau$ is the fact that the recharge current removes an increasing part of the signal charge, before the readout occurs. This effect can explain
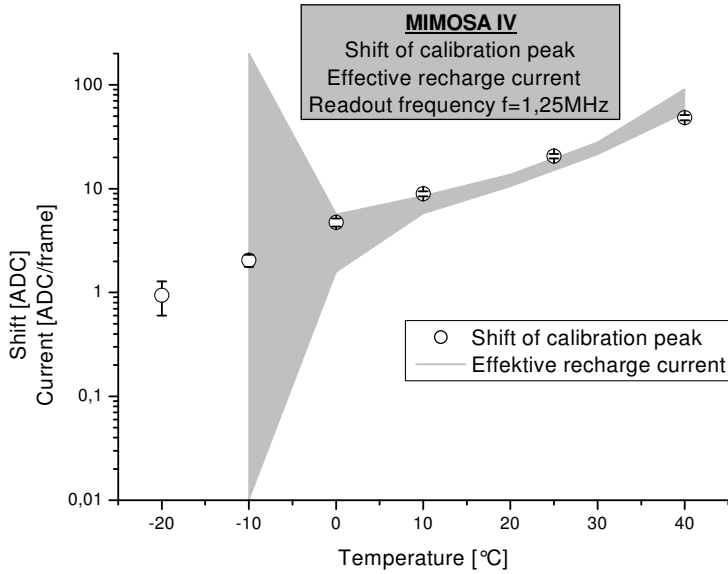
Figure 5.14.:

*The correlation between the shift of the calibration peak and the maximal effective recharge current. The gray area is spanned by the measured value of $I_{eff} \pm \Delta I_{eff}$, where $\Delta I_{eff}$ stands for the uncertainty of the measurement. Only statistical uncertainties were computed.*

the shift of the small calibration peak in the collected charge distribution. If so, a correlation between the amplitude of $I_{eff}$ and the shift should be visible. This was experimentally checked by comparing the shift of the calibration peak with the mean signal loss expected from the recharge current (see figure 5.14). One observes a clear correlation[5] between both parameters.

The key conclusion of the study was that unlike MIMOSA-2, MIMOSA-4 showed no sign of degradation in the CCE. A direct measurement of this parameter was however not possible because of the design of the chip. Nevertheless, the conclusion is indirectly proven by the results of the beam test and the observation that reducing the temperature or the integration time was sufficient to suppress the radiation-induced distortion of the charge collection distribution. Both modifications in the running conditions dominantly dim the effects of radiation induced leakage current increase and shortening of $\tau$ induced by irradiation.

It seems unlikely that the modifications of both parameters (temperature and read-out time) could influence a single common source absorbing diffusing charge. While postulating a temperature dependence of potential trapping or recombination mechanisms can still be justified, a correlation between these effects and the integration time is ruled out. This is supported by the fact that a reduced integration time was observed to be beneficial. An opposite consequence would be expected if the beneficial effect was caused be a delayed arrival of charge carriers, which were trapped and re-emitted on their way to the collecting diode.

### 5.2.3. Discussion of the results for native detectors

The radiation tolerance studies on MIMOSA-2 and MIMOSA-4 led to unexpected and contradictory results. It was not clear why, in contrast to the theory, the charge collection dropped after a given ionizing dose in MIMOSA-2, while it did not change in the SB-pixels of MIMOSA-4. Moreover, the failure of the 3T-pixels of MIMOSA-4 was in contradiction with the fact that these pixels worked perfectly in MIMOSA-1 and MIMOSA-2.

---

[5]The details of this rather complex analysis underlying figure 5.14 is of little interest for the questions addressed in this work. They are discussed in [39]. Summarizing, one should remind that the systematic uncertainties on the hit amplitude and the impact time biases both parameters. The results obtained are thus not considered as sufficiently reliable for a more quantitative analysis.

Combining all information, one can claim that the observations on the SB-pixel were widely understood, while the 3T-pixels showed unexpected reactions. Searching for explanations, the focus went to the obvious difference between both pixels, which is the presence, or absence respectively, of the reset transistor. A scenario was developed, which had the potential to explain all effects observed.

It is assumed that, the reset transistor exhibits a weak point concerning the insulation between the N-Diff implantations used for fabricating it and the epitaxial layer forming the sensitive volume[6].
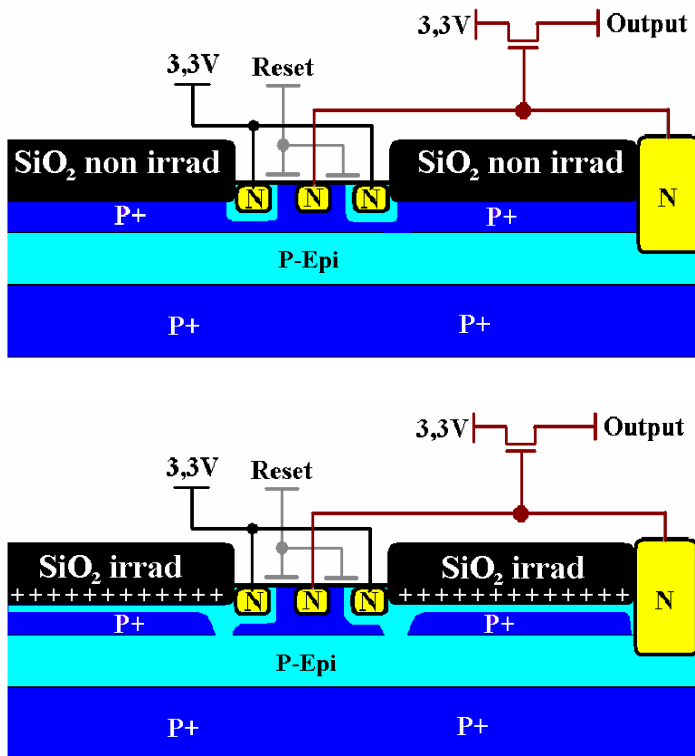


Figure 5.15.:
*Schematic cross-section through the non-irradiated (top) and the irradiated (bottom) pixel of MIMOSA-2. The circular reset-transistor is shown in the middle of the cross-section. The N-implantation on the right hand side represents the collecting diode. The hypothetical punch-trough between the N-Diff implantations of the reset transistor and the epitaxial layer (P-Epi) is illustrated for the irradiated chip. See chapter 2.2.2 for a description of the implantations used in CMOS-Processes.*

This is illustrated in figure 5.15 (top), which shows a cross-section through the non-irradiated 3T-pixel. One can see the collecting diode (right N-Well implantation) and the enclosed[7] reset transistor. In MIMOSA-2 and MIMOSA-4, this circular transistor is connected with the voltage source at its outer ring. The ring is thus set to a voltage of 3.3 $V$. The PN-junction together with this (for microchips) high voltage depletes a part of the thin P-Well layer, supposed to separate the transistor from the epitaxial layer.

The situation after irradiation is shown in figure 5.15 (bottom). Here, a positive charge is expected to build up at the interface between the thick $SiO_2$ and the P-Well. It generates additional fields, which may suffice to deplete fully the P-Well. In this case, the potential barrier between the epitaxial layer and the reset transistor is destroyed and the outer ring of the reset transistor starts to collect free electrons in competition with the collecting diode.

As the electrons collected by the transistor move towards the voltage source without touching the readout circuits of the chip, they do not contribute to the signal. The charge gets lost before reaching the collection diode, which fits to the observation made with MIMOSA-2. The failure of the MIMOSA-4 3T-pixels was interpreted as a consequence of a possibly thinner P-Well in the

---

[6]A description of the different implantation in CMOS-processes can be found in chapter 2.2.2

[7]A description of enclosed transistors can be found in chapter 4.1.2.

AMS 0.35 $\mu m$ process. Unlike the situation in MIMOSA-2, its initial thickness might have already been insufficient to insulate the readout electronics from the epitaxial layer.

As discussed in the following, the hypothesis considered here came out to be partly wrong, because the failure of the 3T-pixels of MIMOSA-4 came out to have other origins. Nevertheless, investigating the question, guided by this hypothesis, allowed to find out the true origin of the problem encountered.

## 5.3. Design improvements for enhanced ionizing radiation tolerance

### 5.3.1. Strategies to identify the weak points of the early pixel designs

Confirming the existence of a punch through between the epitaxial layer and the reset transistor was not possible with the existing chips. New pixel designs, supposed to avoid or to tolerate a potential break down of the insulating layer, were therefore developed. Their design also aimed to test the hypothesis of a punch through the P-Well, as discussed above.

Two different approaches were followed to overcome a potential punch through. One approach consisted in reducing the voltage on the outer ring of the reset transistor. This was achieved by inverting the source and drain of the reset-transistor. As a consequence of this modification,
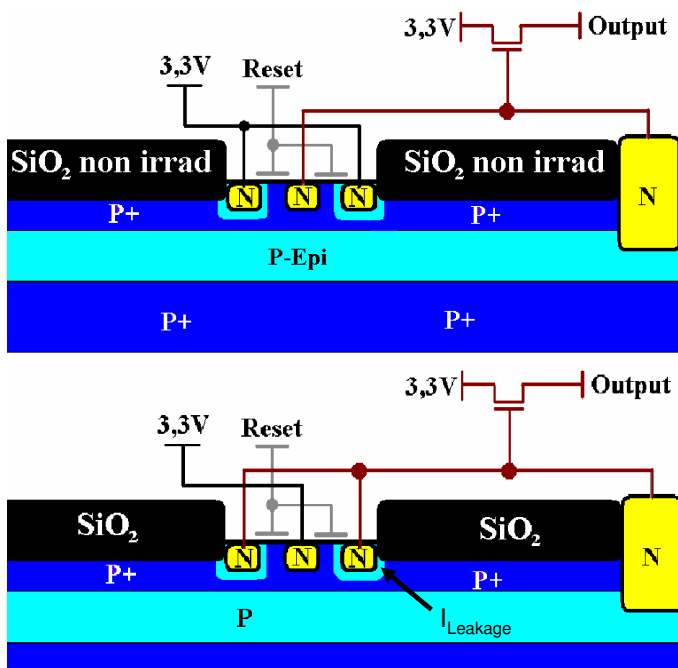


Figure 5.16.:
*The design of the conventional reset transistor as implemented in MIMOSA-2 (top) and the inversed reset transistor as used in the chips SUCCESSOR-1,-2 and MIMOSA-9 (bottom). The arrow marks the additional source of leakage current of the inversed reset transistor, which was identified with MIMOSA-15 (see chapter 5.3.4.3).*

the outer ring of the transistor was disconnected from the voltage source and connected to the lower potential of the collecting diode. This is illustrated in figure 5.16. The expected effect was a reduction of the electrical field applied to the P-well. It was hoped that one could sufficiently dim the field to avoid the conjectured punch trough. The price to pay for this modification was an increase of the pixel capacity, as the larger outer ring of the transistor was now connected with the sensing diode. Applying the same modification to the source follower transistor and the select transistor was not required, as these devices were by chance correctly designed from the beginning.

The second positive effect of the modification was not anticipated. The outer ring of the modified transistor being connected with the collecting diode, any charge collected by this ring

is charged in the capacity of the pixel, and the former parasitic charge collection of the reset transistor becomes a complementary one.

The chips hosting the modified pixels were designed in the context of the SUCIMA collaboration, which studied biomedical applications of silicon detectors [52]. They were named SUCCESSOR-1 and SUCCESSOR-2.

## 5.3.2. Identification of the weak point of the 3T-pixels of MIMOSA-4

### SUCCESSOR-2

| SUCCESSOR-2 (2003), AMS 0.35 µm | |
|---|---|
| Epitaxial layer: None, 3 Metal layers | |
| 32 x 16 3T-Pixels<br>40 µm pixel pitch<br>Diode size: 2 x 2 µm² | 32 x 16 SB-Pixels<br>40 µm pixel pitch<br>Diode size: 4.3 x 3.4 µm² |
| 32 x 16 3T-Pixels<br>40 µm pixel pitch<br>Diode size: 4.3 x 3.4 µm² | 32 x 16 3T-Pixels<br>40 µm pixel pitch<br>Diode size: 6 x 6 µm² |
| PhotoFET 1 | PhotoFET 2 |

Figure 5.17.:
*Selected technical data of SUCCESSOR-2. Only pixel matrices of interest for this work are shown. Radiation hard transistors were used in the full electronics chain of SUCCESSOR-2, source and drain of the reset transistors of the 3T-pixels were inverted.*

Due to a problem in the production of SUCCESSOR-1, SUCCESSOR-2 was the first chip under study. Even if the main application of this chip was dosimetry, it had a 100 % fill factor and was thus compatible with its use in a vertex detector. From its technical aspects, the chip was the direct successor of MIMOSA-4 and based on the same production process (AMS 0.35 $\mu m$). Here too, the substrate of the chip was used as a sensitive medium.

SUCCESSOR-2 was equipped with eight different types of pixels arranged in matrices with a 40 $\mu m$ pitch. This larger pitch was chosen because of the modest spatial resolution required for dosimetry. The lower pixel density was expected to ease the design of a cost effective and robust readout system, as required for a device to be used in medical applications.

On the pixel level, the detector was equipped with two types of 3T-pixels and two types of SB-pixels. The other four arrays were filled with PhotoFET-pixels [53], which will not be discussed in this work.

Two interesting features are integrated into the 3T-pixels of SUCCESSOR-2: Source and drain of the reset transistor are inverted in order to reduce the electrical fields in the P-Well of the detector. Moreover, one of the two arrays equipped with 3T-pixels featured sensing diodes of $2.0 \times 2.0 \ \mu m^2$, while the other 3T-pixel array was hosting diodes of $4.3 \times 3.4 \ \mu m^2$. This was to study the impact of the diode size on the charge collection.

The SB-pixels were also equipped with different diode sizes. Due to the additional implantation required for forming the biasing diode, these diodes needed to be in general slightly bigger than the ones used for 3T-pixels. Sizes of $4.3 \times 3.4 \ \mu m^2$ and $6 \times 6 \ \mu m^2$ were retained.
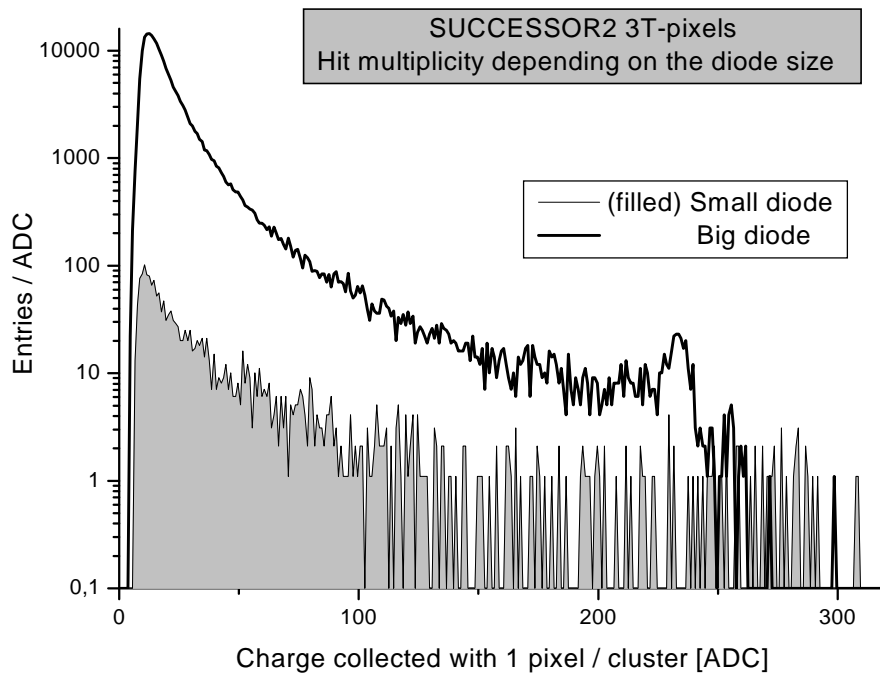
Figure 5.18.: *The collected charge distributions for the two 3T-pixel arrays of SUCCESSOR-2 being illuminated with a $^{55}Fe$-source. The pixels with "small" diode were equipped with a collecting diode of $2.0 \times 2.0 \ \mu m^2$, the "big" diode was $4.3 \times 3.4 \ \mu m^2$.*

Beam tests with SUCCESSOR-2 demonstrated the 40 $\mu m$ pixels to have excellent detection efficiencies for all but one sub-arrays. The exception was the 3T-pixel hosting the small $(2.0 \times 2.0 \ \mu m^2)$ collection diode. The charge collection distribution of this diode, as obtained from a test with the $^{55}Fe$-source, is shown in figure 5.18. The distribution of the 3T-pixel with the bigger diode is put for comparison. One observes an dramatically poor sensitivity of the pixel with the small diode, which reminds the effect observed on the 3T-pixels in MIMOSA-4 (see figure 5.6). Comparing the charge collection distributions of the 3T-matrices of both chips, the effect was even stronger in the case of SUCCESSOR-2.

This observation could not be explained with a lack of insulation between the reset transistor and the sensitive volume of the pixels, as both pixels were equipped with the same transistor design. The only (known) difference between both pixels concerned the size of the sensing diode.

The CCE of the 3T-pixels with the big diode was found close to the one of the SB-Pixel with the same diode size. This parameter was thus concluded to be of unexpectedly strong importance for the CCE of the pixel. A diode significantly larger than the minimum size[8] of an N-well implantation seems to be required to achieve a well working N-well/P-epi – diode in the AMS 0.35 $\mu m$ process[9].

As small diodes lead to a smaller capacitance of the pixel and thus to a higher gain, the diodes of the pixels were so far designed with the minimal size possible. Consequently, even smaller diodes $(1.7 \times 1.7 \ \mu m^2)$ had been chosen for MIMOSA-2. As MIMOSA-2 demonstrated good performances, the size of the $2.0 \times 2.0 \ \mu m^2$ diodes used in the 3T-pixels of MIMOSA-4 had not been considered as a possible explanation for the poor performances of this chip.

Once taken into account, the size of the different diodes allowed explaining the observations made on MIMOSA-4 independently from the punch through hypothesis. In MIMOSA-4 both, the collecting diodes of the 3T-pixel and the SB-pixel, were design with the minimum surface possible. For the N-Well implantation forming the collecting diode of the 3T-pixel, this surface was $2.0 \times 2.0 \ \mu m^2$ and thus equal to the one of the ineffective pixel of SUCCESSOR-2. The N-Well implantation of the SB-pixel contributes simultaneously to the collection and the biasing diode of the pixel. This requires an additional P-diffusion, which increases the minimum size of the structure to $4.3 \times 3.4 \ \mu m^2$ corresponding to one of the effective 3T-pixel of SUCCESSOR-2. After the experience accumulated with SUCCESSOR-2, the observations made on MIMOSA-4 were not anymore surprising.

At first sight, the results obtained with SUCCESSOR-2 and MIMOSA-2 seem contradictory as the $1.7 \times 1.7 \ \mu m^2$ diodes of MIMOSA-2 worked but the $2.0 \times 2.0 \ \mu m^2$ diodes of SUCCESSOR-2 did not. These different behaviors reflect actually the fact that the chips were produced in different production processes and factories. Production tolerances and microscopic differences between the components (e.g. doping profile) of the processes are expected, which could easily generate the different behaviors observed.

### 5.3.3. Identification of the weak point of the 3T-pixel of MIMOSA-2

#### SUCCESSOR-1

**Detector design:** SUCCESSOR-2 was already equipped with a reset transistor with inversed geometry. Nevertheless, the chip could not be used to test the hypothesis of a potential punch

---

[8]The minimum size of an object as defined by the design rules of the production process.

[9]This was reproduced later on with a more complex pixel in the AMS 0.35 Opto process. A potential explanation assumes that N-Well structures with a minimum size do not penetrate the P-Well deep enough to reach the epitaxial layer.

| SUCCESSOR-1 (2003), MIETEC 0.35 µm | | | |
|---|---|---|---|
| Epitaxial layer: ~4 µm, 5 Metal layers | | | |
| 32 x 16 3T-Pixels<br>Alternating pixel pitch<br>Diode size: 3.2 x 3.2 µm²<br>No N-Well guard ring | 32 x 16 3T-Pixels<br>Alternating pitch<br>Diode size: 3.2 x 3.2 µm²<br>N-Well guard ring | % *Not discussed* | % |
| 32 x 16 SB-Pixels<br>Alternating pixel pitch<br>Diode size: 1.7 x 1.7 µm²<br>No N-Well guard ring | 32 x 16 3T-Pixels<br>40µm pixel pitch<br>Diode size: 1.7 x 1.7 µm²<br>N-Well guard ring | % | % |

Figure 5.19.:
*Selected technical data of SUCCESSOR-1. Only pixel matrices of interest for this work are shown. Radiation hard transistors were used only in the pixels of SUCCESSOR-1. Source and drain of the reset transistors of the 3T-pixels were inverted. The pixel pitch was alternating (see figure 5.20).*

through between this transistor and the sensitive volume. This was because the sensor had no epitaxial layer. No charge collection efficiency could therefore be assessed. Unlike SUCCESSOR-2, SUCCESSOR-1 was designed with the AMI/MIETEC 0.35 $\mu m$ process, which had already been used for MIMOSA-2. As this process features an epitaxial layer, measuring the charge collection efficiency with the [55]Fe source was possible.

The chip was hosting eight matrices made of $32 \times 32$ 3T-pixels with different layouts. As it was optimized for dosimetry, only a part of the pixels had the high sensitivity and fill factor required for sensing minimum ionizing particles.
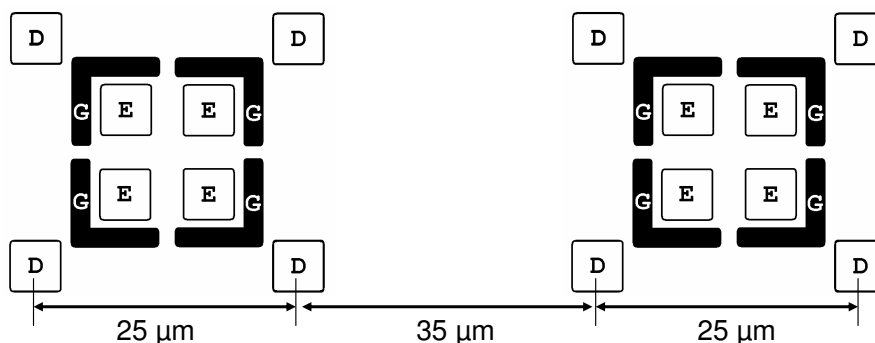


Figure 5.20.: *Schematic top view of the SUCCESSOR-1 super pixel geometry. Four pixels, composed of their diode (D) and their transistors (E) are grouped and surrounded in some cases by a N-Well guard ring (G). Note the different distances between the diodes ( 25 $\mu m$ versus 35 $\mu m$).*

Two of the eight different types of pixels were of particular interest for equipping a vertex detector. They are usually referred as pixel 3 and pixel 4.

Pixel 3 featured a 3.2 $\mu m \times$ 3.2 $\mu m$ diode. The dimensions of the diode of pixel 4 were 1.7 $\mu m \times$ 1.7 $\mu m$, which corresponds to the minimum diode size of the process. For both reset transistors, source and drain were swapped to avoid a potential depletion of the P-well insulation.

To optimism the geometry of the pixels for dosimetry, groups of four pixels were arranged in so-called super-pixels. Because of this arrangement, which is illustrated in figure 5.20, the pixel pitch was alternating between 25 $\mu m$ between neighbor pixels forming a super-pixel and 35 $\mu m$ between neighbor pixels belonging to two different super-pixels. The pitch of the super-pixels thus

became 60 $\mu m$.

It should be mentioned that only the pixels and the output buffers of SUCCESSOR-1 were designed with radiation hard transistors. The digital logic was made with standard transistors for reasons of simplicity. As it was separated from the pixels, this logic could be shielded while irradiating the sensor.

**Testing procedures:** The tests of SUCCESSOR-1 were done in a common project with the SUCIMA collaboration. The results of the study are summarized below, additional details can be found in [54].
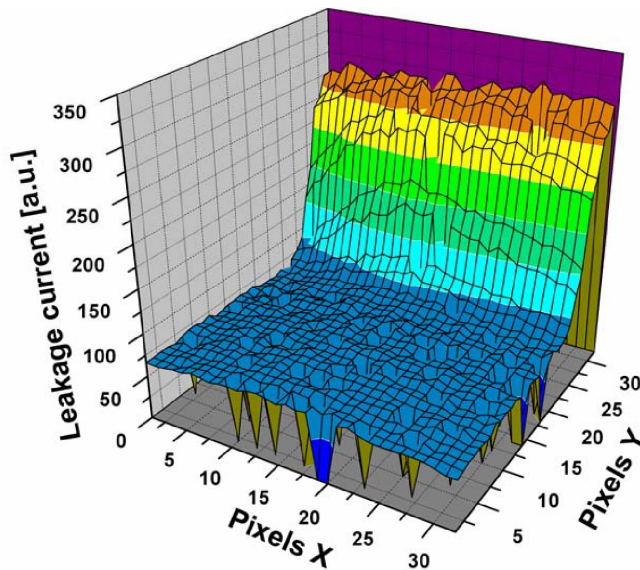


Figure 5.21.:
*The leakage current of pixel 3 of SUCCESSOR-1 as a function of the pixel position after an ionizing dose of 500 kRad at a temperature of 20 °C. Plot by H. Bol and L. Jungermann.*

The specific design of SUCCESSOR-1 imposed several complications for testing. The alternating pixel pitch was one of them. This geometry breaks the uniformity of the pixels, which complicates the interpretation of the collected charge distribution. This is in particular the case for the distributions for clusters of four pixels. Depending on the impact position of the particle detected, the four pixels surrounding the impact point may form a square of 25 $\mu m \times$ 25 $\mu m$, a square of 35 $\mu m \times$ 35 $\mu m$ or a rectangle of 25 $\mu m \times$ 35 $\mu m$. As the charge collection efficiency depends on the length of the diffusion paths, different CCEs are expected for each of these geometries. This hampers a straightforward use of the charge collection distribution for measuring the CCE.

Clusters of nine combined pixels were used in the test of SUCCESSOR-1, as they always cover the same surface. Moreover, radiation effects were searched by visually comparing the shape of the full charge collection distribution. This approach does not provide absolute numbers on the CCE. Nevertheless, it is very sensitive to losses in charge collection and unwanted effects caused by the geometry of the pixels are canceled out.

The second complication occurring within the tests of SUCCESSOR-1 is probably related to the heat generated in the output buffers of the chip. These buffers were located close to the pixel matrices and presumably induced a significant temperature gradient into the pixel matrices. As illustrated in figure 5.21, this led to a strong correlation between the leakage current of the pixels and their position. As the difference in leakage currents of identical pixels reached up to a factor of four, it was not possible to unambiguously determine the typical current of a type of pixels. The values shown in the following are mean values and are not corrected for this effect.
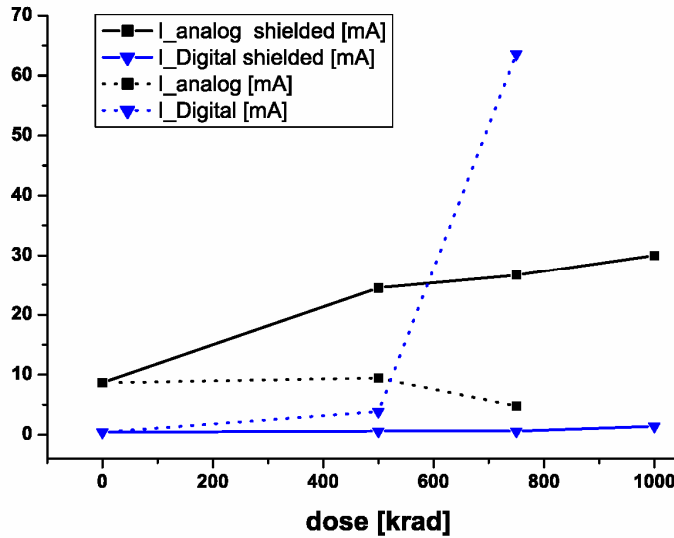
Figure 5.22.:
*The power consumption of the analogue and digital part of SUCCESSOR-1 as a function of the ionizing dose. The analogue and digital current consumption of chips irradiated with and without shielding of the digital part is shown. Taken from [54].*

Because of these complications, the accuracy of the measurements in terms of absolute values was substantially reduced and only few quantitative data could be obtained from measuring the chip. On the other hand, in some qualitative observations made by a direct comparison of irradiated and non-irradiated chips helped clarifying open questions as well as guiding further improvements of the detector design.

**Observations on SUCCESSOR-1:** SUCCESSOR-1 was irradiated to doses up to 2 $MRad$ of $\sim 10~keV$ X-Rays. The radiation soft digital logic of the chip was shielded with a 3 $mm$ copper plate within the irradiation process.

One detector was accidentally irradiated without shielding, which allowed getting an idea on the intrinsic radiation tolerance of the process. Up to a dose of 500 $kRad$, this detector showed radiation damage effects comparable to the ones observed on shielded chips. Nevertheless, as illustrated in figure 5.22, the power consumption of the analogue and the digital electronics of the two chips was found to differ significantly. In further irradiation steps, the power consumption of the digital logic of the chip increased dramatically, which led to a breakdown of the chip after a dose of 1 $MRad$. This breakdown recovered after few weeks of room temperature annealing.

The charge collection distributions of pixel 3 and pixel 4 are given as a function of the radiation dose in figure 5.23 for doses of up to 1 $MRad$. In contrast to the situation on MIMOSA-2, one observes no significant degradation in the charge collection efficiency. This holds also for a dose of 2 $MRad$ (not shown). In the case of SUCCESSOR-1, the charge collection efficiency was thus not of concern.

On the other hand, an important increase of leakage current was observed. This is in particular true for pixel 3. The mean leakage current of this pixel increased by almost three orders of magnitude after an irradiation of 2 $MRad$. At the first order, this statement holds for any temperature in the range of interest. The increase of the mean leakage current of pixel 4 was substantially less important, i.e. in the order of a factor of 20. Extreme care has to be taken when comparing the increase of the leakage currents of pixel 3 and pixel 4. As the matrix hosting pixel 3 was located closer to the output buffers than pixel 4, its leakage current is stronger affected by the heat emission of this component. This heat emission can depend on the radiation dose, as radiation damage is known to vary the currents passing transistors.

The noise of pixel 3 is shown in figure 5.24. It increases above 30 $e^-$ after an irradiation with a
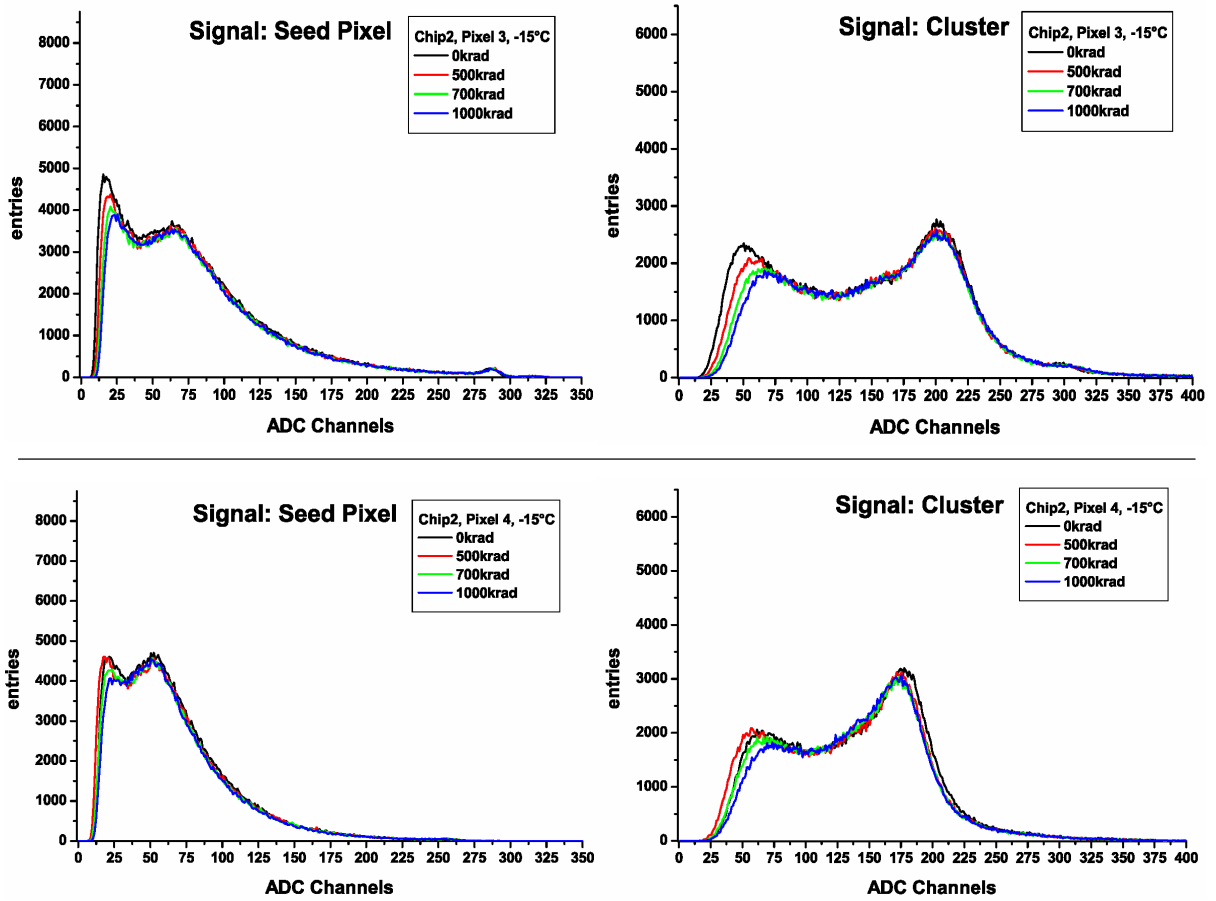
Figure 5.23.: *The charge collection distributions of SUCCESSOR-1 as a function of the ionizing dose for pixel 3 (upper plots) and pixel 4 (lower plots). The spectrum of the seed pixel and of clusters of $3 \times 3$ pixels at a temperature of $-15\ ^{\circ}C$ and an integration time of $0.8\ ms$ is shown. Taken from [54].*
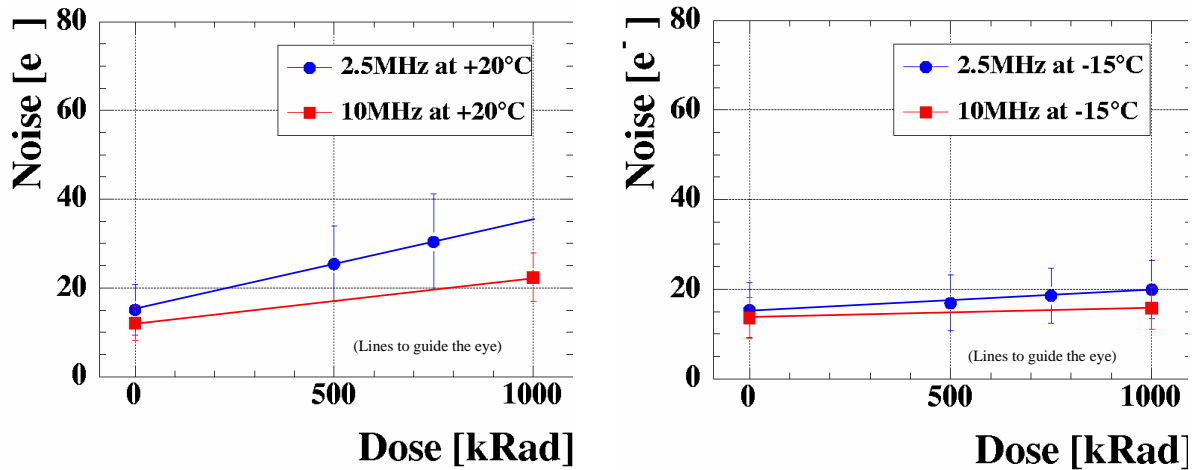
Figure 5.24.:
*The noise of SUCCESSOR-1 pixel 3 as a function of the ionizing dose and the integration time at a temperature of* 20 °C *(left figure) and* −15 °C *(right figure). The integration times are given with* 0.4 ms ⇔ 2.5 MHz *and* 0.1 ms ⇔ 10 MHz

dose of 1 *MRad* at a temperature of $T = 25$ °C and an integration time of 0.4 *ms*. This effect is likely to lead to a significant reduction of the detection efficiency of the chip. However, reducing the temperature and the integration time can dim this additional noise. This suggests that the increase is like to originate from shot noise.

**Discussion:** Despite of the low absolute precision of the measurements, the results of SUCCESSOR-1 were of substantial importance, as it allowed clarify the observations made on MIMOSA-2. They gave for the first time direct evidence that the absorption of signal charge observed in MIMOSA-2 was related to the design of the reset transistor. This became clear, as this effect was not observed at the pixels with modified reset transistor installed at SUCCESSOR-1.

Moreover, the results of SUCCESSOR-1 also allowed ruling out alternative explanations:

- Potential effects caused by the combination of a too small diode and additional radiation damage could be ruled out because pixel 4 (having diodes with minimum size allowed) worked before and after irradiation.
- Some field plates installed on pixel 4 were ruled out to play a role, as the CCE remained also stable for the very standard pixel 3.
- The digital electronics of MIMOSA-2 was designed with radiation soft transistors. Nevertheless, it was not considered to be substantially damaged for radiation doses up of to 400 *kRad*. This indirect conclusion is backed up by the irradiation of the radiation soft digital electronic of SUCCESSOR-1, which withstood doses of up to ∼ 500 *kRad*. Moreover, it was proven that the effects of a failure of the digital electronics could be clearly distinguished from the effects seen with MIMOSA-2.

Therefore, it was concluded that the punch through hypothesis correctly described the failure of MIMOSA-2. Moreover, it was shown that a swap of source and drain of the reset-transistor was sufficient to overcome this point.

This second conclusion is valid only, if the production process used for MIMOSA-2 and SUCCESSOR-1 were identical. This was fulfilled according to the documentations available.

Nevertheless, non-documented changes in the production process like the use of a slightly thicker P-Well may lead to comparable results. In this case, the progress observed on SUCCESSOR-1 would be independent of the new design of the reset transistor.

Nevertheless, it is justified to state, that the design iteration done on the 3T-pixel was successful and that the problem of the absorption of signal charge was solved. The signal reduction was not a worry anymore but the radiation tolerance of SUCCESSOR-1 was limited by another effect. This was the strong increase and dispersion of the leakage currents of the pixels. Besides generating important shot noise, this also caused problems for reading out the chips.

In the readout pattern used, the baseline of the pixels is modified by leakage current already in the time between the pixel reset and the first readout. Because of the strong dispersion of the leakage currents of the pixels, their baselines became very inhomogeneous. At some point, the dynamical range of the ADC of the readout-system was not sufficient anymore to read all pixels of a matrix.

Intense cooling and the use of short integration times were required to dim this effect. Using them allowed operating SUCCESSOR-1 after an irradiation with 2 $MRad$ X-rays.

## 5.3.4. Design improvements to reduce the leakage current

### 5.3.4.1. MIMOSA-9

| Mimosa-9 (2004), AMS 0.35 µm Opto | |
|---|---|
| Epitaxial layer: ~11 µm, 4 Metal layers | |
| 64 x 32  SB-Pixels<br>20 µm pixel pitch<br>Diode size: 3.4 x 4.3 µm² | 32 x 16  3T-Pixels<br>40 µm pixel pitch<br>Radiation hard diode |
| 64 x 32  SB-Pixels<br>20 µm pixel pitch<br>Diode size: 6 x 6 µm² | 32 x 16  3T-Pixels<br>40 µm pixel pitch<br>Radiation soft diode |
| 32 x 16  SB-Pixels<br>30 µm pixel pitch<br>Diode size: 3.4 x 4.3 µm² | 32 x 16  SB-Pixels<br>40 µm pixel pitch<br>Diode size: 3.4 x 4.3 µm² |
| 32 x 16  SB-Pixels<br>30 µm pixel pitch<br>Diode size: 5 x 5 µm² | 32 x 16  SB-Pixels<br>40 µm pixel pitch<br>Diode size: 6 x 6 µm² |

Figure 5.25.:
*Selected technical data of MIMOSA-9. Only pixel matrices of interest for this work are shown. Radiation hard transistors were used in the full electronics chain of MIMOSA-9, source and drain of the reset transistors of the 3T-pixels were inverted.*

The results of SUCCESSOR-1 represented a breakthrough in the search for more radiation hard MAPS detectors. As the problem of charge collection was solved, new studies were undertaken to dim the effect of the new limiting factor, which was the radiation induced increase of the leakage current.

Early structures to reduce the increase of leakage currents were already implemented into SUCCESSOR-1. Unfortunately, the wide spread of leakage currents over the pixel matrices prevented meaningful tests. The first chip allowing for a systematic study of structures limiting the leakage currents was actually MIMOSA-9.

MIMOSA-9 was the first chip produced with the new AMS 0.35 $\mu m$ Opto process. The latter is dedicated to the production of MAPS for visible light detection. The production process was in

particular optimized for reduced the leakage currents of the collection diodes. It was hoped that this intrinsic feature of the process would help to dim the leakage currents also after irradiation.

The chip contained eight different pixel matrices. Six of them were composed of SB-pixels. They are of little interest for this discussion. The two others were based on two different types of 3T-pixels, which were arranged in a matrix with 40 $\mu m$ pitch. While one of the 3T-pixels had
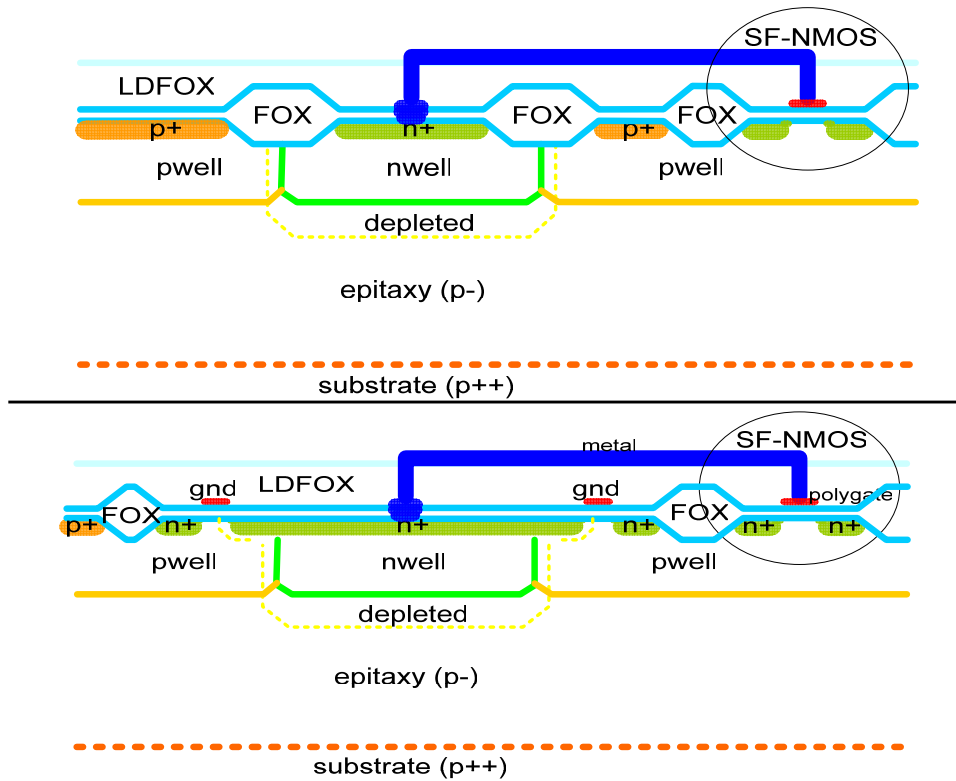


Figure 5.26.: *Structure of the radiation hard and radiation soft pixel of MIMOSA-9. The thick (SiO$_2$) field oxide (FOX) of the radiation soft geometry (top) was replaced by a pseudo gate on GND and a widened n-Diff implantation (bottom)*

the standard design with inversed reset transistor, the other one was equipped in addition with a modified layout of the collection diode. These modifications were intended to separate structures made of thick oxide from the collecting diode.

The classical and the modified designs of the collecting diode are shown in figure 5.26. In the classical design, the collecting diode is surrounded by thick oxide (FOX). In the modified design, this FOX is replaced by a transistor-like structure formed by n-Diff implantations and a pseudo-gate. As a consequence of this modification, the collecting diode is now surrounded by thin gate oxide.

The aim of the modification was to reduce the amount of radiation induced surface defects close to the collecting diode. Ionizing radiation generates such defects in particular at the interface between thick oxide and silicon[10]. At the interfaces with the thin gate oxide, defects are also generated but they get annealed by tunnel effect in a large extend. This makes thin gate oxide

---

[10]See section 4.1.2.
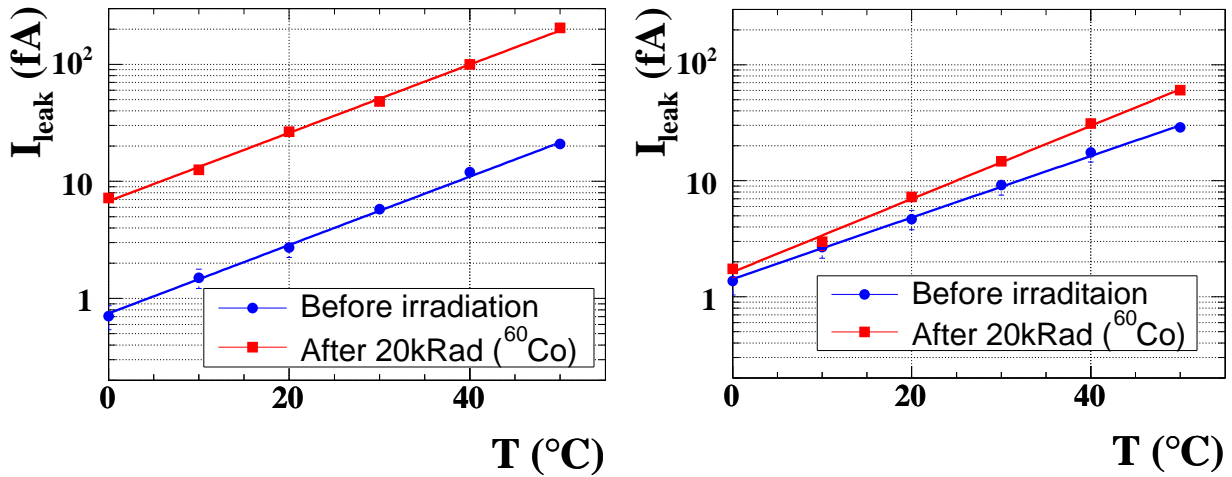
Figure 5.27.: *Leakage current on the radiation soft (left) and the radiation hard (right) 3T-pixel of MIMOSA-9 before and after an irradiation with $\sim 20~kRad~\gamma$ - rays from a $^{60}Co$ - source.*

radiation hard with respect to the thick structures. As the defects ease the thermal generation of charge carriers, reducing their number was hoped to dim the leakage currents picked up by the collection diode.

Experiences with SUCCESSOR-1 had shown that structures comparable to the pseudo-gate inject substantial noise to the chip if being connected with an external voltage source. To avoid this, the gate was connected with the $GND$ of the chip instead.

MIMOSA-9 was irradiated with $\sim 20~kRad$ of $^{60}Co$ gamma rays in order to verify the effect of the new structures. The results of these tests are shown in figure 5.27. One observes the leakage current of the standard pixel to increase by a factor of 10 after this dose. For the radiation hard pixel, the increase of leakage current was reduced to a factor below 3 (depending on the temperature)[11].

On the other hand, the modified pixel shows a slightly higher initial leakage current. This is presumably the consequence of removing the FOX. In chips not designed to be radiation tolerant, the FOX serves to suppress leakage currents between different components. This functionality is not available in the modified pixel. The advantage of higher radiation tolerance had thus to be paid with a slightly higher initial leakage current.

This demonstrated that separating the collecting diode from thick silicon structures can improve the radiation tolerance of MAPS.

| Mimosa-11 (2005), AMS 0.35 μm Opto | |
|---|---|
| Epitaxial layer: ~11 μm, 4 Metal layers | |
| 42 x 21  SB-Pixels (Pixel 1)<br>30 μm pixel pitch<br>Diode size: 3.4 x 4.3 μm²<br>Metal guard ring | Not discussed |
| 42 x 21  SB-Pixels<br>30 μm pixel pitch<br>Diode size: 3.4 x 4.3 μm²<br>Standard diode | Not discussed |
| 42 x 21  SB-Pixels (Pixel 2)<br>30 μm pixel pitch<br>Diode size: 3.4 x 4.3 μm²<br>Metal + P-Diff guard ring | Not discussed |
| Not discussed | Not discussed |

Figure 5.28.:
*Selected technical data of MIMOSA-11. Only pixel matrices of interest for this work are shown. Radiation hard transistors were used in the full electronics chain of MIMOSA-11.*

### 5.3.4.2. MIMOSA-11

**Chip design:**  The aim of MIMOSA-11 was to optimize further the properties of the radiation hard pixel design of MIMOSA-9. The chip was designed again in the AMS-0.35 Opto process. It contained eight different types of SB-pixels with a pitch of 30 $\mu m$. The pixel designs combined different approaches to reduce the capacity and the leakage current of the radiation hard pixel of MIMOSA-9. In particular, the effect of different combinations of guard rings was investigated.

The discussion in this work will restrict itself to three selected pixel designs, which illustrate best the outcome of the study. The size of the collection diode of these pixels is 4.3 $\mu m \times 3.4$ $\mu m$.

- The pixel named "standard pixel" [12] in the following is comparable to the standard pixels of MIMOSA-4 and MIMOSA-9. It is not equipped with dedicated radiation hard structures and serves as a reference.
- The pixel named "pixel 1" [13] in the following is comparable to the radiation hard pixel of MIMOSA-9 (see figure 5.26.
- The pixel named "pixel 2" [14] in the following follows the spirit of pixel 1 but contains an additional guard ring of metal and p-Diff[15] implantations, which generate a structure comparable to an enclosed transistor.

Figure 5.29 illustrates the detailed structures of the pixels. The standard pixel, which is illustrated with the upper drawing, has thick $SiO_2$ surrounding the collecting diode. This oxide is part of the intrinsically radiation soft production process, and is meant to electrically insulate

---

[11]As discussed later (in section 5.3.4.3) in detail, the leakage current observed with MIMOSA-9 contains a non-negligible contribution generated in the reset transistor. This was not accounted for in the studies on MIMOSA-9, as this effect was discovered subsequently with MIMOSA-15. As the pixel of MIMOSA-9 has an inverted reset transistor layout comparable to SUCCESSOR-1, the contribution of the reset transistor is likely to dominate the leakage current of the irradiated radiation hard pixel. The positive effect of the modified diode is thus probably much higher than suggested by figure 5.27.

[12]Also referred as MIMOSA-11 A0S2

[13]Also referred as MIMOSA-11 A0S1

[14]Also referred as MIMOSA-11 A3S1

[15]The same structure has also been implemented with an N-Diff guard ring. This structure had performances below the ones of the two radiation hard pixels shown here.
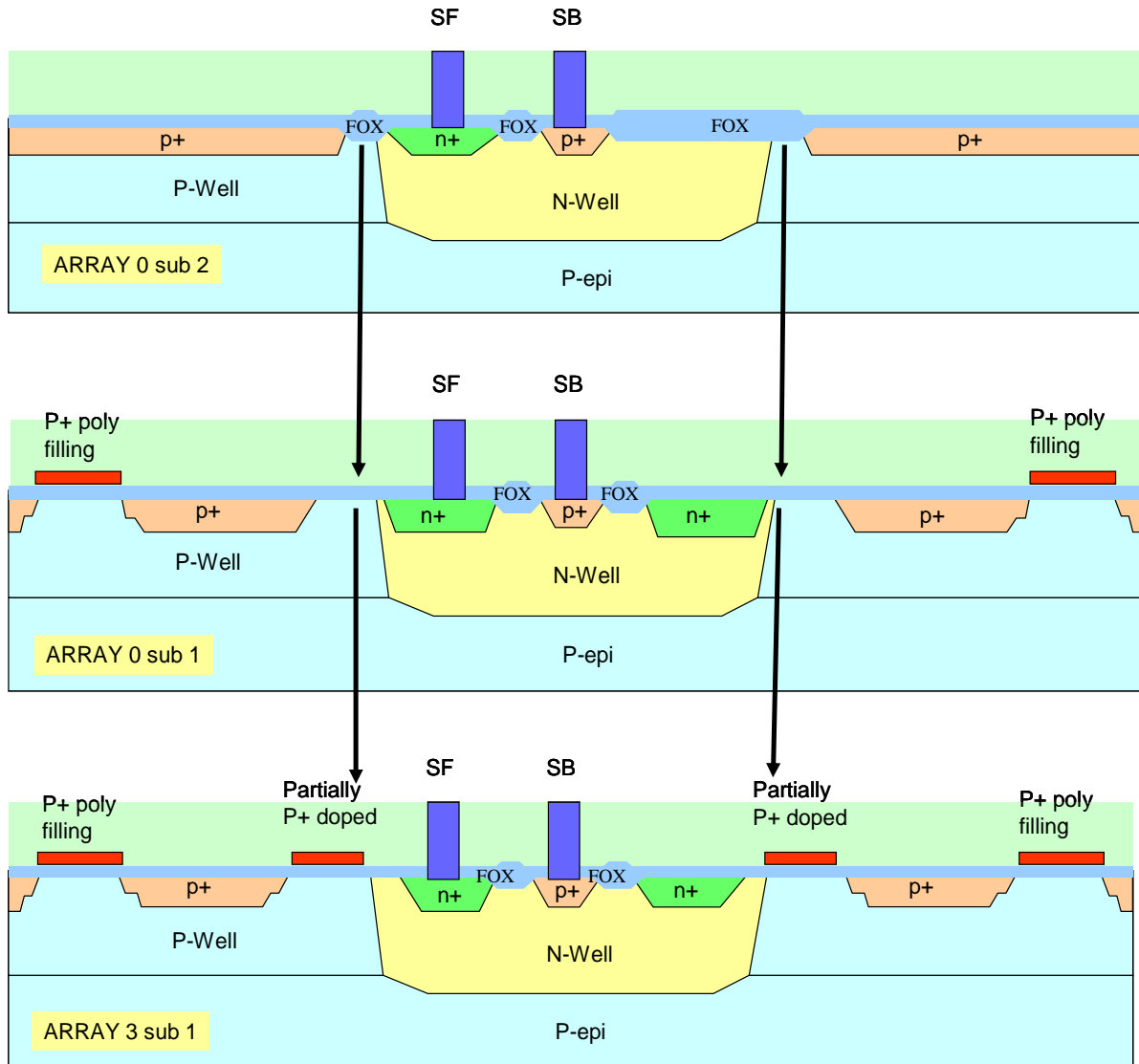
Figure 5.29.:
*The structures of the pixel types of interest of MIMOSA-11. The standard pixel is shown on the top. In this pixel, the collecting diode is surrounded by thick oxide (labeled FOX).*
*Without adding new structures, this oxide has been removed in pixel 1 (middle).*
*In pixel 2, a new insulating structure was introduced by adding a pseudo-gate and a p-Diff (P+) guard ring (bottom).*

the different components from each other. In pixel 1 the thick oxide has been removed without adding further structures. This approach violates the design rules of the production process, as the insulation foreseen gets lost and the properties of the new structure are therefore not guaranteed. However, fabricating the structure is possible.

Pixel 2 avoids the violation of the design rules by adding a poly guard ring and a P++ (P-Diff) guard ring. The structure is comparable to a radiation hard, enclosed, transistor where the P-Diff defines the outer ring. Unlike such transistors however, the inner and the outer rings have opposite doping. The poly-implantation acts like a transistor gate and forces the use of thin oxide. Moreover, the gate is connected to ground and sets the potential of the thin silicon to a well-defined potential. The P++ guard ring cuts possible conducting channels between the collecting diode and the outside world.

MIMOSA-11 was irradiated with doses of up to 3.5 $MRad$ and tested consecutively with the $^{55}Fe$-source.

**Test results**   Comparably to the radiation hard pixel of MIMOSA-9, the modifications made to improve the radiation tolerance of pixel 1 and pixel 2 are accompanied by slight drawbacks in the pixel performance. As long as the pixels are not irradiated, the gain of the standard pixel is $\sim 10$ % higher than the one of pixel 1 and $\sim 15$ % higher than the one of pixel 2. In terms of charge collection efficiency from the epitaxial layer, the performances of the radiation hard pixels lie by 10 % below the one of the standard pixel. Also in terms of noise and of the time constant of the recharge current, the standard pixel appears as the favored choice. This observation is of interest for a deeper understanding the pixel design. From the user point of view, all three pixels show a fully satisfactory S/N and detection efficiency. Moreover, as we will see in the following, the advantages of the standard pixel vanishes after irradiating it with few 100 $kRad$ of $\sim 10$ $keV$ X-rays.

In order to evaluate the properties of the pixels after irradiation, their noise was measured as a function of the radiation dose and of the temperature of the chip support. An integration time of 0.7 $ms$ was chosen and the measurements were done without illuminating the sensors. The gain used for translating the noise from AD-units to electrons was measured under the most favorable conditions ($T = -25$ $°C$ $t_{Int} = 0.18$ $ms$, non-irradiated chip) reachable. Hereafter, the same value was used for all combination of temperature, readout frequency and radiation doses. This was done in order to minimize the bias caused by the radiation-induced movement of the calibration peak, which is a known feature of irradiated SB-pixels (see section 5.2.2).

The results of the measurements are shown in figure 5.30. One observes the noise of the standard pixel to be the lowest before irradiation. Since the noise of this pixel raises fast with increasing radiation dose, the radiation hard pixels show a lower noise after a few hundreds of $kRad$. At moderate temperatures, the two radiation hard pixels exhibit similar performances but at a temperature of $+40$ $°C$ pixel 2 performs significantly better the one of pixel 1. The observed noise of pixel 2 lies $\sim 5 - 10$ $e^-$ $ENC$ below the one of pixel 1. Pixel 2 was therefore concluded to show best noise performances after irradiation.

In particular after irradiation, the integration time is likely to have a significant impact on the noise of the pixel. This is because the shot noise increases with the number of electrons, which are collected within the integration time. The impact of integration time on the noise of the standard pixel and the best performing radiation hard pixel (pixel 2) was studied as a function of the radiation doses and temperature. For this purpose, MIMOSA-11 detectors previously exposed to different radiation doses were operated without illumination by the $^{55}Fe$-source in a dark chamber.
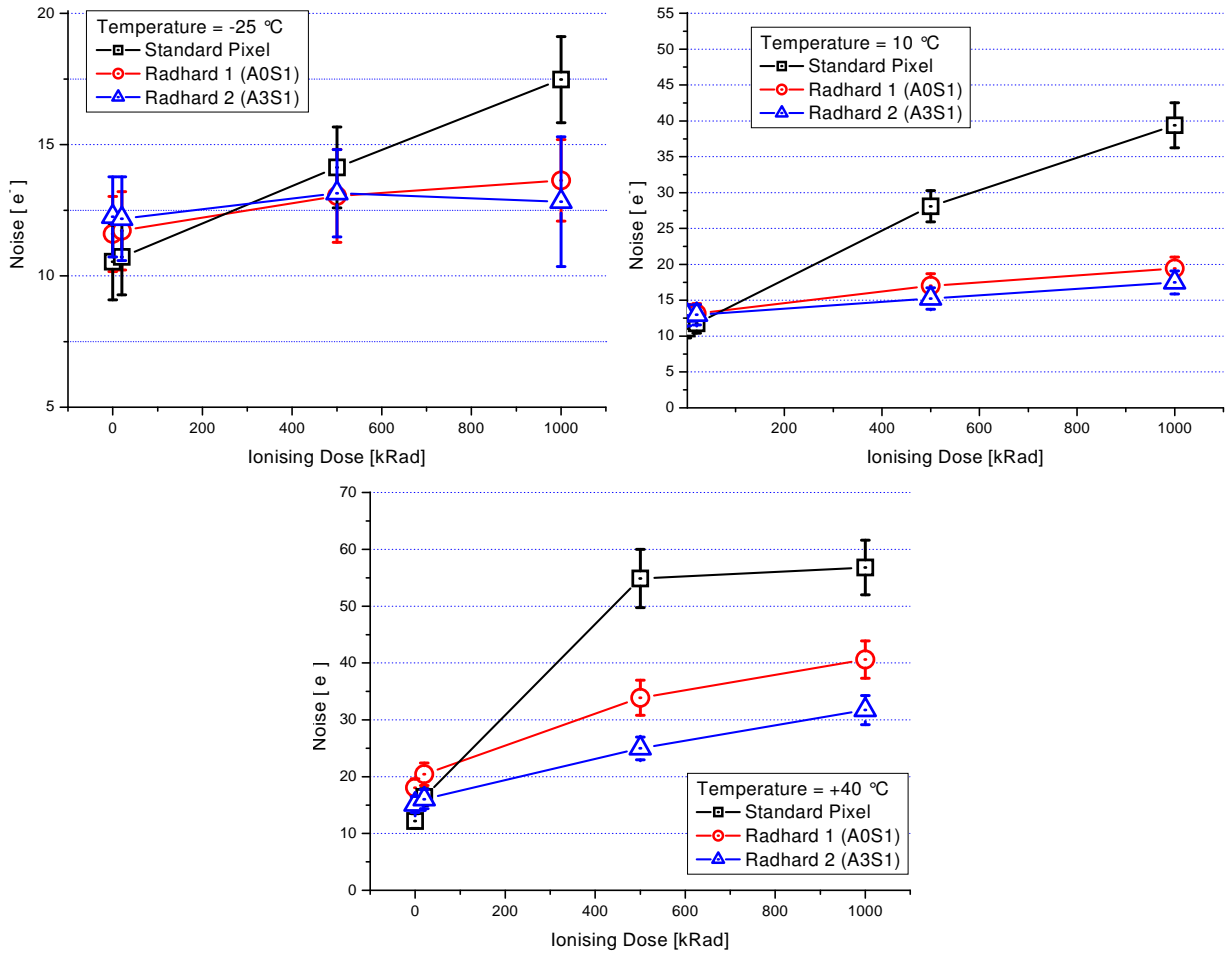
Figure 5.30.:
*The noise of the different pixels of MIMOSA-11 as a function of the temperature and the ionizing radiation dose. The measurements were done without source. The integration time was 0.7 ms. The error bars stand for the pixel-to-pixel dispersion of the noise, which dominates the measurement uncertainties on the noise of the individual pixels.*
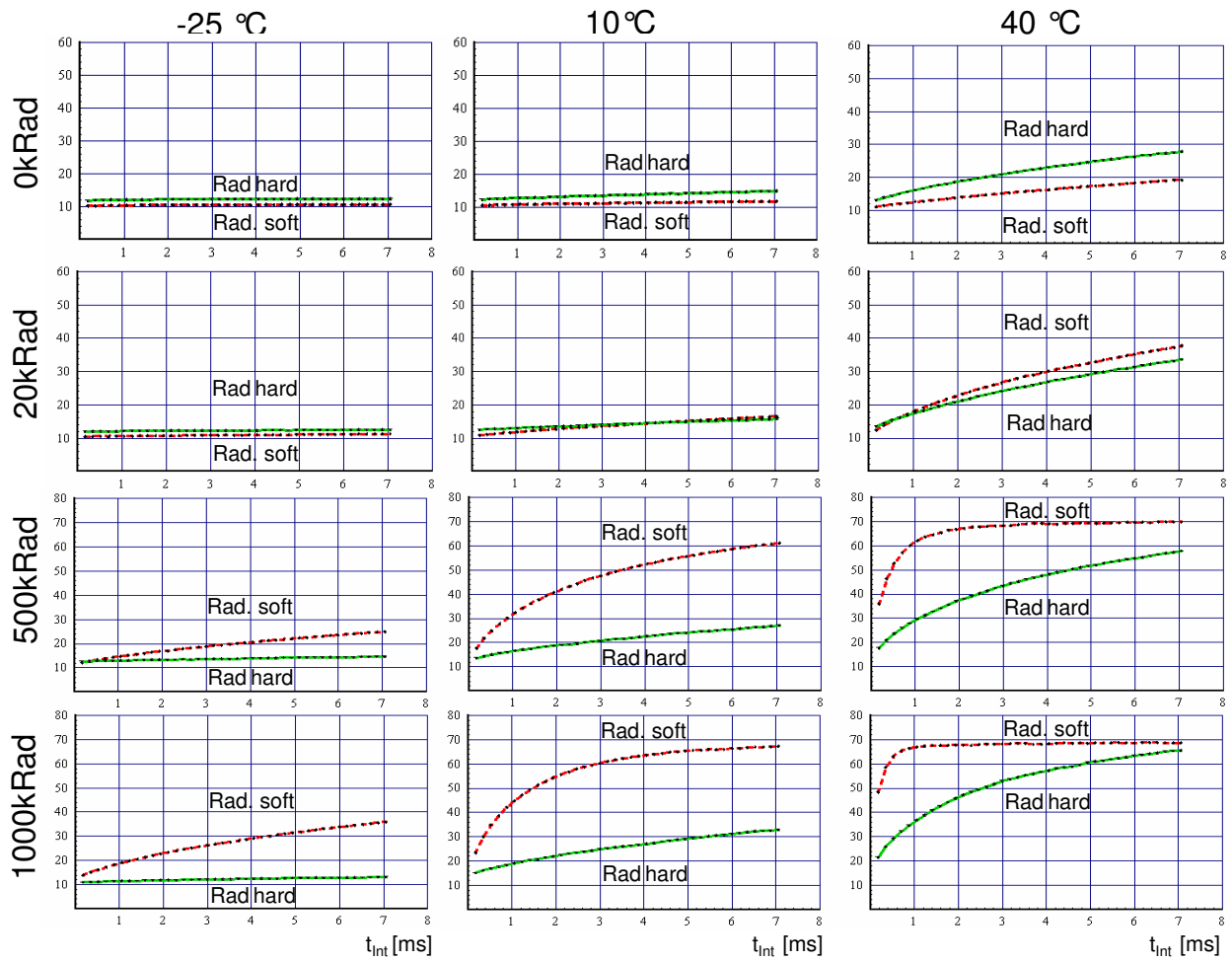
Figure 5.31.: *Noise of pixel 2 (Rad. hard, green) and of the standard pixel (Rad. soft, red) of MIMOSA-11 as a function of 10 keV X-ray doses (0, 20, 500, and 1000 kRad) temperature (−25 °C,+10 °C, +40 °C) and integration time (0.2–7 ms).*

In order to measure the noise of the detector above its native integration time[16], one profits from the fact that the readout of the SB-pixel does in good approximation not influence its integration process. This allows for reading out a train of $N$ consecutive frames. By performing CDS between the frame one and the frame $N$, an integration time of $t_{Int} = (N-1) \cdot t_F$ is reached ($t_F$ stands for the time required to read one frame). This procedure is equivalent to a true measurement with an integration time of $t_{Int}$. Reading the intermediate frames serves only for generating the delay required for the final readout and the corresponding data is ignored.
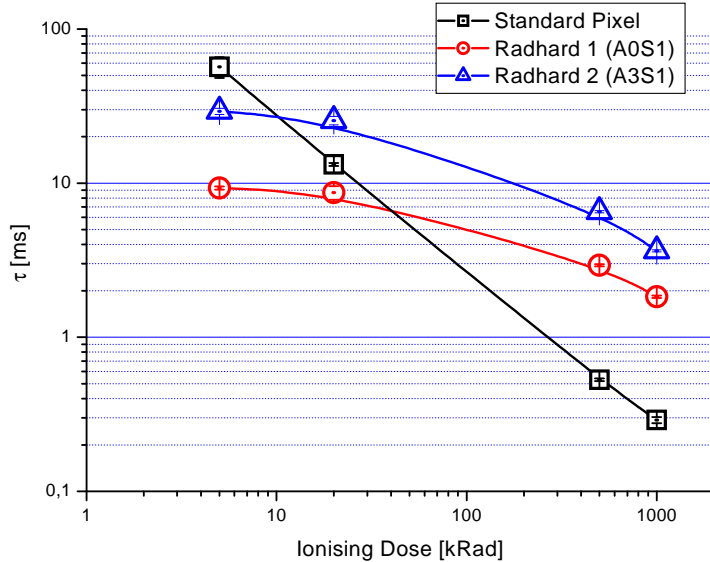


Figure 5.32.:
*The time constant of the recharge current of the different pixels of MIMOSA-11. Only data for a temperature of $T = 40\ °C$ is shown because of the limitations of the measurement procedure. The non-irradiated pixels are represented at $5\ kRad$ for the sake of clarity. The lines are to guide the eye.*

This procedure was used to measure the noise for integration times between $0.18\ ms$ (corresponding to the time between two readouts at a frequency of $10\ MHz$) and $\sim 7\ ms$. Results are shown in figure 5.31. One observes the performances of the radiation hard pixel to exceed the performances of the standard one a dose roughly $20\ kRad$ and above. By increasing the dose and the temperature, the tendency becomes more and more pronounced. Under bad conditions, the noise of the standard pixel reaches a saturation level which is located at near $70\ e^-\ ENC$. This observation departs from the standard expectation for shot noise, which should to increase with the square root of the integration time. The reason for this effect is not clarified so far. Nevertheless, it is worth mentioning that the theory ignores distortions in the integration process of the leakage current, as those generated by the biasing current of the SB-pixel. The theory might thus be insufficient to describe the irradiated SB-pixel.

The time constant of the recharge current is displayed as a function of the radiation dose in figure 5.32. Results are provided for a temperature of $40\ °C$ only. For lower temperatures, the recharge process of the non-irradiated pixels was too slow to allow for reliable measurements. Nevertheless, the qualitative results can be considered as representative also for other temperatures. As for the noise measurements, one observes the standard pixel to show the best performances (longest recharge time) before irradiation. This advantage vanishes after irradiation and, after a few $100\ kRad$, the time constant drops below $1\ ms$. For the integration times chosen, this corresponds to a breakdown of the chip, as most of the charge collected is canceled out between the instants of hit and of the readout.

For the radiation hard pixels, the degradation of the constant is substantially slower than for

---

[16]Given by the number of pixels of the structure combined with the minimum clock frequency provided by the readout system.
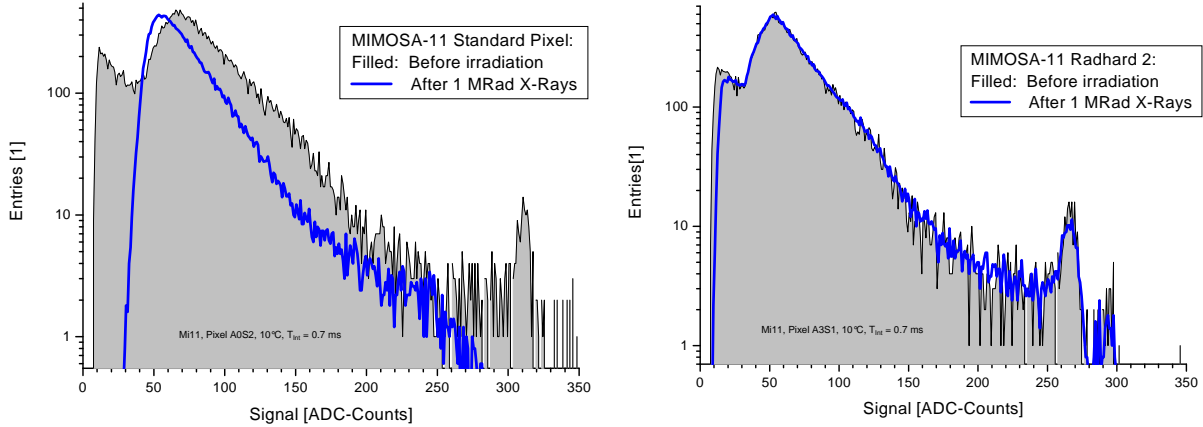
Figure 5.33.:
*The charge collection distribution for the seed pixel of MIMOSA-11 before and after 1 MRad X-rays. The distributions for the standard pixel (left) and pixel 2 (right) were measured at $T = 10\ °C$ with an integration time of 0.7 ms. From [55].*

the standard pixels. This makes them the best choice for radiation doses above $\sim 100\ kRad$. Here again, pixel 2 exhibits better performances than pixel 1.

Besides the noise, charge collection distributions of the standard pixel and of pixel 2 were recorded. They confirm the qualities of the modified structure, as the CCE of the irradiated pixel was clearly improved by the modifications. This is illustrated in figure 5.33, which displays the measurements for the standard pixel and pixel 2 before and after an IRD of 1 $MRad$. The distributions were recorded with an integration time of 0.7 $ms$ and a temperature of $T = 10\ °C$. They were chosen as an example extracted from a more general study to illustrate the contrast between the performances of the radiation hard and radiation soft pixel for high radiation doses.

Figure 5.33 (left) compares the charge collection distribution of the irradiated and the non-irradiated standard pixel. One observes the typical symptoms of a SB-pixel damaged by ionizing radiation[17], which are an increase of the signal discrimination threshold and a harsh shift of the calibration peak (which gets almost completely diluted after irradiation). The time constant of the recharge current is sufficiently reduced to displace significantly the large peak due to the charge collected from the epitaxial layer.

On the contrary, the charge collection of the radiation hard pixel 2 (see figure 5.33, right) remains almost unaffected after irradiation. Only a slight increase of the threshold can be observed, as a consequence of an increased noise.

**Summary and Conclusion:** MIMOSA-11 was designed to test several approaches for radiation hard collection diodes. The results obtained from the three most representative pixels hosted on this chip were discussed in detail. It was shown, that the radiation soft standard pixel provides slightly better initial performances than the radiation hard structures. However, this bonus disappears already after a radiation dose of a few tens of $kRad$ as the radiation tolerance of the pixel is insufficient.

The best performing radiation hard pixel (pixel 2) relies on a pseudo-transistor structure formed by a metal and an P-Diff guard ring surrounding its collection diode. After radiation

---

[17]As known from MIMOSA-4, see section 5.2.2.

doses above some tens of $kRad$, this pixel exhibits best performances in terms of noise, gain, CCE and recharge time. This statement holds for all temperatures and integration times considered in the study. The benefit of the radiation hard structure increases if the running conditions get more severe (high temperature and integration time).

### 5.3.4.3. MIMOSA-15

| Mimosa-15 (2005), AMS 0.35 µm Opto | |
|---|---|
| Epitaxial layer: ~11 µm, 4 Metal layers | |
| 42 x 21  3T-Pixels<br>30 µm pixel pitch<br>Standard reset transistor<br>Metal + P-Diff guard ring | Not discussed |
| 42 x 21  3T-Pixels<br>30 µm pixel pitch<br>Inversed reset transistor<br>Metal + P-Diff guard ring | Not discussed |
| 42 x 21  SB-Pixels (Pixel 1)<br>30 µm pixel pitch<br>Diode size: 3.4 x 4.3 µm²<br>Metal + P-Diff guard ring | Not discussed |
| Not discussed | Not discussed |

Figure 5.34.:
*Selected technical data of MIMOSA-15. Only pixel matrices of interest for this work are mentioned. Radiation hard transistors were used in the full electronics chain of MIMOSA-15.*

**Chip design:**    MIMOSA-15 was equipped with two different kinds of 3T-pixels. The latter were designed to answer two questions, which could not be clarified with the former detector generations. The first question concerned the leakage current of the radiation hard collecting diodes (MIMOSA-11, pixel 2). A significant reduction of the radiation-induced leakage current was suspected for this pixel by indirect observation. However, since the pixels of MIMOSA-11 had a SB-design, no quantitative and direct measurement of the leakage current was achievable.

The second point, which was never addressed before, was the direct comparison between the standard and the inversed reset transistor of the 3T-pixel. Comparing the results of MIMOSA-2 and SUCCESSOR-1 had demonstrated that pixels with inversed reset transistor feature a significant better CCE after irradiation (see section 5.3.3). However, this observation was made on two different detector generations optimized for different applications, which complicates its interpretation. A direct comparison of both designs being implemented on the same chip was intended to allow concluding on the hypothesis of a parasitic charge collection (see chapter 5.2.3).

In order to address these questions, two sub-arrays of 3T-pixels were integrated into MIMOSA-15.    Both sub-arrays were equipped with radiation hard collection diodes of 3.4 $\mu m \times 4.3 \mu m$ similar to pixel 2 in MIMOSA-11. In one matrix, this diode was connected with the inner ring of the enclosed reset transistor, which leads to a design comparable to MIMOSA-2 (see figure 5.16). This pixel will thus be named Mi2-pixel in the following. In the other 3T-matrix, the collection diode was connected with the outer ring of the enclosed reset transistor. This corresponds to the pixel design implemented into SUCCESSOR-1. The pixel will thus be named Su1-pixel. The pitch of the 3T-pixels was 20 $\mu m$.

Besides the 3T-pixels, a SB-pixel comparable to pixel 2 of MIMOSA-11 was implemented into MIMOSA-15. Minor improvements were applied in order to reduce the capacity of the diode. The pitch of the SB-pixels was 30 $\mu m$.

In order to study their radiation tolerance, the pixels were irradiated with 1 $MRad$ of $\sim$ 10 $keV$ X-rays. The effect of the irradiation on the charge collection characteristics, leakage current and noise of the pixels is described hereafter.

**Results of the laboratory tests:** The CCE of MIMOSA-15 was measured before and after irradiation. No reduction in CCE was observed for both, the Mi2- and the Su1-pixel. This observation stands in contrast to the observations made with MIMOSA-2, which suggested a significant reduction of the CCE for the Mi2-pixel (see chapter 5.2.1.2).

On the other hand, a strong dependence of the gain, leakage current and noise on the IRD and on the pixel design was observed. These observations are summarized in table 5.1. One finds the Mi2-pixel to provide a better gain (6.4 $e^-/ADC - unit$) than the Su1-pixel (9.1 $e^-/ADC - unit$). Both fain values remained constant after irradiation. The difference in gain between both designs can be explained by the higher capacity of the outer ring of the transistor, which was connected to the diode in the case of the Su1-pixel.

Strong differences between both pixels were found concerning their noise and leakage currents. At a temperature of 10 $°C$ and an integration time of 0.7 $ms$, the initial noise of the Su1-pixel was found to be 20 $e^-$ $ENC$ and thus higher than the one of the Mi2-pixel (17 $e^-$ $ENC$). This can partly be explained with the difference in the gain of the pixels, partly by the significantly higher leakage current of the Su1-pixel (4.68 $\pm$ 0.05 $fA$ against 3.65 $\pm$ 0.03 $fA$).

Both the noise and the leakage current of the pixels increase after irradiation. At a temperature of $T = 10$ $°C$, the Mi2-pixel showed a noise of 21 $e^-$ $ENC$, which corresponds to a noise increase of a factor of $\sim$ 1.2. The leakage current raised by a factor of $\sim$ 8.6, reaching 31.6 $\pm$ 0.2 $fA$.

The Su1-pixel was substantially more affected by the irradiation: Its noise increased by a factor of $\sim$ 2 to 40 $e^-$ $ENC$ equivalent, driven by an increase of the leakage current by a factor of $\sim$ 61, which resulted in a current of 286.9 $\pm$ 1.7 $fA$ after irradiation. It thus widely reproduced the very high leakage currents observed in SUCCESSOR-1.

**Discussion of the laboratory tests:** The measurements of the leakage current hint to the presence of a contribution, which was not taken into account so far. This contribution is presumably due to the implantation forming the reset transistor source. To understand this point, one has to be aware that the N-Diff implantation forming this structure, combined with the enclosing P-well, forms a reversed bias diode comparable to the collecting diode. Like any diode, this diode delivers a small leakage current, which can usually be neglected in standard microcircuit designs.

The differences between the leakage currents and the noise of MIMOSA-15 suggest that this simplification does not apply to MAPS. As the collection diodes are identical for both pixels, the reset transistor must generate the differences in the leakage current. The decisive difference

| Pixel | IRD | Gain | Noise | $I_{Leak}/Diode$ |
|---|---|---|---|---|
| Mi2-Pixel | 0 | 6.4 $e^-/ACD$ | 17 $e^-$ | 3.6 $fA$ |
| Su1-Pixel | 0 | 9.1 $e^-/ACD$ | 20 $e^-$ | 4.6 $fA$ |
| Mi2-Pixel | 1 $MRad$ | 6.4 $e^-/ACD$ | 21 $e^-$ | 31 $fA$ |
| Su1-Pixel | 1 $MRad$ | 9.1 $e^-/ACD$ | 40 $e^-$ | 180 $fA$ |

Table 5.1.:
*Comparison of the performances of the Mi2-Pixel and Su1-Pixel of MIMOSA-15. The data was taken at a temperature of 10 $°C$ with an integration time of 0.7 ms.*

between the Mi2-pixel and the Su1-pixel stems from whether the inner or the outer ring of the reset transistor is connected with the pixel capacity. As the surface of the outer ring is larger, a higher leakage current is expected for the Su1-pixel already before irradiation.

Besides the different surface of the two rings, another element has to be taken into account for the irradiated chip: The outer ring is surrounded by thick oxide, just like the standard diode; the inner ring is surrounded by thin oxide, just like the radiation hard diode. In analogy to the diodes, an important increase of leakage current after irradiation is therefore expected for the outer ring while the inner ring is less affected.

The precise contribution of the transistor to the leakage current of the pixel remains unknown, as it is not possible to distinguish it from the leakage current of the diode. Nevertheless, an order of magnitude can be obtained for the Su1-pixel by deriving the difference between the leakage current of the two pixels after irradiation. This difference is $\sim 140\ fA$. Comparing this value with the leakage current of the Mi2-pixel ($31\ fA$), it is justified to state that the reset transistor is the dominating source of leakage current for the Su1-pixel. This is probably also true for SUCCESSOR-1 and the radiation hard pixel of MIMOSA-9.

Overall, the observations suggest the Mi2-like pixel to be the best choice in the case of the AMS 0.35 $\mu$m (opto) technology. It exhibits a higher gain, lower noise and lower leakage current than the Su1-like pixel. Moreover, unlike the true pixel of MIMOSA-2, no degradation in charge collection was observed up to a dose of 1 $MRad$. This might be a consequence of a slightly higher thickness of the P-well layer of the AMS 0.35 $\mu$m (opto) technology as compared to the one used in the MIETEC 0.35 $\mu$m technology in which MIMOSA-2 was fabricated. This statement remains however to be checked confirmed.

**Beam test with the MIMOSA-15 SB-pixel**   Laboratory tests showed that the radiation hard pixel designs provide a substantially higher radiation tolerance than the conventional pixels. However, this observation had not yet been confirmed with beam tests. It remained therefore to be shown that the improvements observed with the $^{55}Fe$-source would also apply for minimum ionizing particles.

To do this, a MIMOSA-15 was irradiated with an IRD of 1 $MRad$ of 10 $keV$ X-rays. The radiation hard SB-pixel of this chip, which is similar to pixel 2 of MIMOSA-11 was tested hereafter on a $\sim 5\ GeV$ electron beam at DESY. The limited beam time allowed for one run, which was taken at a temperature of $-25$ °$C$ and with an integration time of $\sim 0.17\ ms$. The chip was observed to provide a satisfactory signal over noise ratio of $19.4 \pm 0.2$ (most probable value). This allowed for an excellent detection efficiency above 99.9 %. From these measurements one can conclude that MAPS are resistant to ionizing doses of 1 $MRad$.

## 5.4. Summary and conclusion on the ionizing radiation tolerance of MAPS

### 5.4.1. Radiation damage effects observed

The radiation tolerance of MAPS against ionizing radiation was explored by developing and testing eight consecutive chip generations, each hosting several different types of pixels. Those pixels were subdivided into two groups, which are distinguished by their compensation of the dark currents. The classical 3T-pixels do this by means of a reset switch while the so-called SB-pixels use a high resistivity forward bias diode for a continuous leakage current compensation.

## 5. Ionizing radiation tolerance of MAPS

Measurements on early prototypes showed performance losses already after an integrated radiation dose (IRD) of $10 - 100$ $kRad$ of 10 $keV$ X-rays, which is well below the radiation tolerance required. The losses concerned in particular an increase of leakage current and noise and a deterioration of the signal. The analogue and digital readout chain of the pixels demonstrated a radiation tolerance, which was far above the one of the sensing elements.

The origin of the different performance drops of the sensors was systematically studied by designing dedicated pixel structures in different production processes. This allowed for distinguishing unwanted effects, which are due to the particular production process, from the ones originating from the sensor layout. It was concluded that the signal losses observed in the 3T-pixels originate from specific weak points in the production processes. This concerns in particular MAPS build in the MIETEC 0.35 $\mu m$-process, which show after irradiation a parasitic signal charge collection caused by the reset-transistor. This effect is not observed for example in the AMS 0.35 $\mu m$-process. It was shown that one could overcome this signal loss by fine-tuning the layout of the reset transistor (e.g. swapping source and train of this transistor) with drawbacks in terms of reduced gain and excessive increases of leakage current after irradiation.

Signal losses observed on the SB-pixels are specific to their inherent recharge procedure, which is to remove a particle signal after readout without creating a dead time. It was shown that the time constant of this process decreases substantially because of radiation damage. If it reaches the order of the integration time, a fraction of the signal charge is already removed before the readout of the pixel occurs. It was demonstrated that the decrease of the time constant originates from the increase of leakage current of the pixel, which is generally observed after irradiation. Cooling irradiated chips to temperatures of ($\sim$ –20 °C) partially restored the initially low leakage currents and the long time constant of the pixel.

A second option to reduce the increase of leakage currents after irradiation is a fine-tuning the layout of the pixel diode. Best results were achieved by adding a guard ring formed from thin gate oxide and a p-Diff implantation around each collection diode. Again the benefits translated also into a lower time constant of the SB-pixels and the reduced shot noise of all pixels. The success of the design modifications came out to be of particular importance if irradiated pixels are operated at high temperatures and with high integration times.

The modifications made on the pixels as much as the choice of good running conditions (small integration time, low operation temperature) reduced substantially the effects of radiation damage. While the early prototypes broke down already after few 100 $kRad$, a beam test on the newest detector generation showed a fully satisfactory detection efficiency for minimum ionizing particles after a IRD of 1 $MRad$. This number is not considered as hard limit for the radiation tolerance of MAPS. It is likely that further cooling and the use of the short integration times foreseen in CBM will allow for substantial progresses in the radiation tolerance even of nowadays prototypes. Moreover, building MAPS in production processes with smaller feature sizes will presumably allow overcoming the problems observed in the readout chain of one individual sensor, which was irradiated to an IRD of 3.5 $MRad$.

From the studies performed it is concluded that MAPS will tolerate radiation doses of at least 1 $MRad$. As further improvements are likely to be reached in the mid-term timescale, the ionizing radiation tolerance of MAPS is not considered as crucial drawback for using them in the vertex detector of CBM. Nevertheless, an efficient cooling to temperatures of $\lesssim$ 20 °C seems mandatory to control the leakage currents of the pixels.

The tolerance of MAPS against ionizing radiation seems also of modest concern, as their lifetime in the CBM experiment will be limited by their tolerance against non-ionizing doses. The latter is discussed in the following chapter.

# 6. Non-ionizing radiation tolerance of MAPS

The studies shown in the last chapter suggest that the radiation tolerance of MAPS against ionizing doses can reach reasonably high values. This holds as long as moderate cooling controls the high leakage currents of the irradiated MAPS. Moreover, the very small integration times foreseen in the CBM vertex detector have a beneficial effect.

Compensating the effects of non-ionizing radiation appeared more difficult. The bulk damage caused by this radiation degrades in particular the sensor material. Known effects like modifications in the effective doping of the material, charge inversion and a deterioration of the lifetime of signal electrons endanger the detection efficiency of irradiated sensors. As MAPS collect the signal charge by the relatively slow thermal diffusion, they were considered as being particularly sensitive to deteriorations in the lifetime of signal electrons. At which point this effect becomes important, and in how far design modifications within the limits of commercial CMOS processes could compensate for this, was not clear.

Besides identifying the native radiation hardness of MAPS, the first studies aimed for identifying accessible parameters, which could potentially influence the radiation tolerance of the detectors. The thickness of the sensitive layer and the density of collection diodes were expected to provide a handle, as both vary the diffusion paths, the signal electrons have to pass before being collected. While a higher diode density was considered as beneficial in any case, the thickness of the sensitive layer demands for optimization. Reduced thickness was expected to shorten the diffusion paths and therefore to increases the charge collection efficiency. On the other hand, a thin sensitive layer provides only a poor initial signal for minimum ionizing particles, as the number of signal electrons generated scales with the length of the particle trajectory in the sensor.

Despite the early prototypes MIMOSA-1 and MIMOSA-2 were not designed for addressing these questions, the study performed with them provided valuable information on the impact of both parameters on the radiation tolerance of MAPS. This will be discussed in the following before showing the results from detector generations, which were optimized for radiation tolerance. At the end of this chapter, the information obtained on the tolerance of MAPS against non-ionizing radiation will be summarized and the consequences for CBM will be discussed.

## 6.1. Influence of the epitaxial layer thickness and number of diodes per pixel

### 6.1.1. Motivation of the measurements

The hardness against non-ionizing radiation was addressed with the first prototypes MIMOSA-1 and MIMOSA-2. These exploratory measurements were oriented to obtain a first understanding of the radiation damage to be expected.

From the today's perspective, the measurements are of particular interest, as the chips provide some features which were not available anymore on newer pixels. One of these features was the very different thickness of the epitaxial layer of the chips. MIMOSA-1 based on an $AMS$ 0.6 $\mu m$
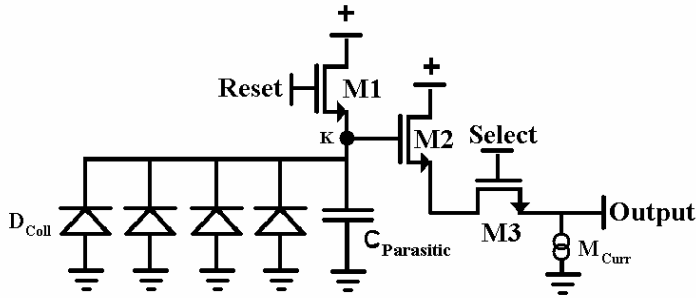
Figure 6.1.:
*Schema of a pixel hosting multiple diodes. The parasitic capacity gets increased in this layout, as the diodes substantially contribute to it.*

process with a $\sim 14~\mu m$ epitaxial layer. MIMOSA-2 was produced in $MIETEC/AMIS$ 0.35 $\mu m$, which provided an epitaxial layer of $\sim 4~\mu m$.

Moreover, both chips are equipped with pixels containing more than one collecting diode each. MIMOSA-1 has pixels with one and four collecting diodes respectively. One matrix of MIMOSA-2 is equipped with pixels having two collecting diodes each. As illustrated in figure 6.1, these diodes are connected in parallel. This leads to shorter diffusion paths for the signal electrons and was therefore expected to increase the charge collection efficiency. On the other hand, the higher amount of diodes per pixel increases the summed capacity of the diodes. This was likely to reduce the gain of the pixels and also to lead to additional noise. The leakage currents from the additional diodes was supposed to contribute to the shot noise of the pixels.

The aim of this study was to learn, which thickness of the epitaxial layer and which amount of diodes in a pixel was the preferable one.

### 6.1.2. Irradiation procedure and measurements

MIMOSA-1 and MIMOSA-2 were irradiated with $\sim 1~MeV$ reactor neutrons up to integrated radiation doses (IRD) of $10^{12}~n_{eq}/cm^2$ and $10^{13}~n_{eq}/cm^2$ respectively. Within this procedure, a negligible parasitic ionizing radiation dose ($< 1~kRad$) was applied to the chips. Bonding the chips to their motherboard was done after irradiation as unlike to the chips, the motherboards become radioactive within the irradiation procedure.

Because of the irradiation procedure, it was not possible to test the chips before irradiation. The results had to be obtained by comparing the properties of irradiated chips with the ones of another, new chip. This procedure introduced a small systematic uncertainty (few %) in the comparison, reflecting the dispersion between the genuine characteristics of the individual chips and of the front-end readout cards, on which the chips were mounted.

After mounting the chips, their charge collection efficiency, noise, leakage current and gain of the pixels were measured at a temperature of 10 $^\circ C$. The integration time was 3.3 $ms$.

### 6.1.3. Results for gain, leakage current and noise

Within the studies of MIMOSA-1 and MIMOSA-2, no change of the position of the calibration peak was found within the accuracy of the measurements ($<$ 2 %). This holds for the full range of fluencies considered. From this, one concludes that the efficiency of charge collection from the depleted area of the collection diode has not significantly changed. Moreover, the gain of the readout chain (including the on-chip amplifiers) remained constant.

The leakage current of the 1-diode and 2-diode pixels of MIMOSA-2 is shown as a function of the temperature with and without irradiation on figure 6.2. The IRD considered here amounts
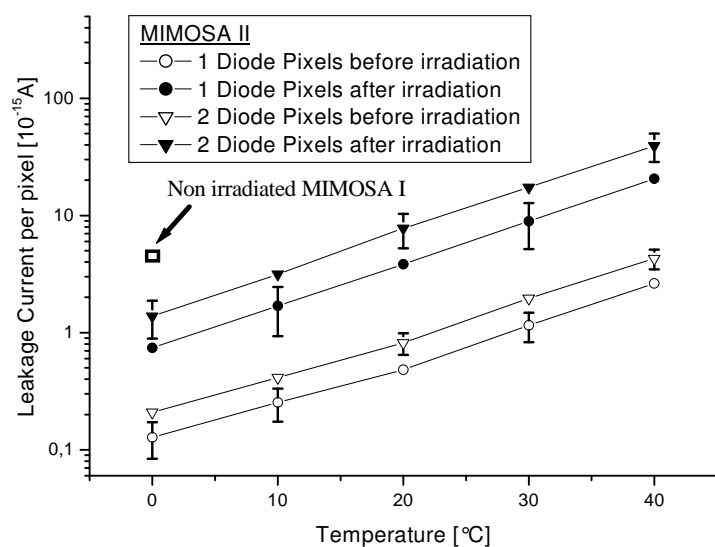
Figure 6.2.:

*Leakage current of MIMOSA-2 before and after irradiation with $10^{13} n_{eq}/cm^2$ as a function of temperature. The leakage currents measured at $0\,°C$ on non-irradiated MIMOSA-1 chips is included for comparison. Error bars represent the pixel-to-pixel leakage current dispersions. Some of them were removed for clarity.*
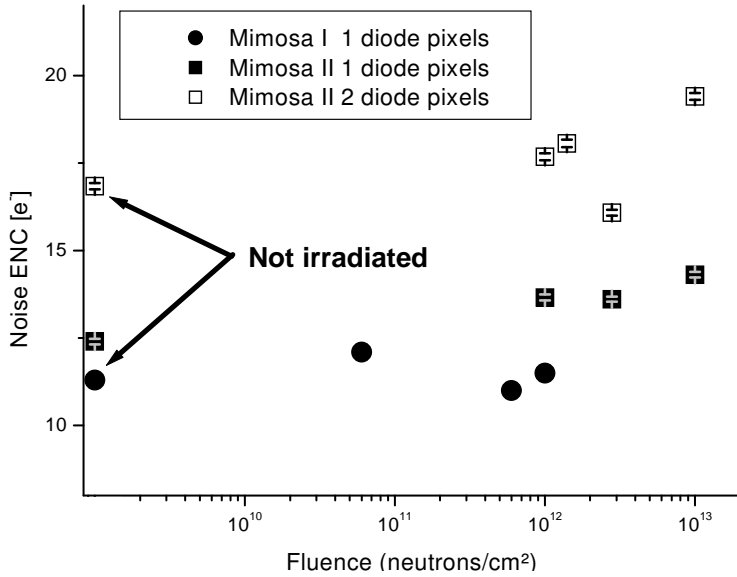
Figure 6.3.:
*Noise of MIMOSA-1 and -2 as a function of IRD. Error bars represent the statistical uncertainties of the measurement (not available for MIMOSA-1). Because of the additional scattering of the data points, it was concluded that the measurement shows no significant trend within its accuracy.*

to $10^{13}$ $n_{eq}/cm^2$. The leakage current was observed to increase by an order of magnitude for both, the pixels with one and two collection diodes. This statement holds at all temperatures considered.

The temperature dependence of the leakage current was observed not to change after irradiation.

An increase of leakage current as being observed on MIMOSA-2 is compatible with the theory. It is likely to be caused by bulk damage, which generates additional generation and recombination centers providing additional thermal generated leakage current. As the absolute leakage current at the temperature of 10 °$C$ is moderate, its influence was not considered as harmful.

In contrast to the results obtained with MIMOSA-2, no significant increase of the leakage current has been observed for MIMOSA-1. It is likely that this was caused by the limits of the measurement methods available for testing this first prototype.

The impact of radiation on the noise was verified experimentally. The results are shown in figure 6.3, which displays the noise measured after CDS as a function of the IRD. The data shown for MIMOSA-1 was taken from [27]. One observes that despite of the small statistical errors of the individual points, the noise varies in an irregular way. This variation is more important than the contribution of the additional shot noise caused by the increase of leakage current. The latter was calculated to cause an increase of noise $\sim$ 10 % for a IRD of $10^{13}$ $n_{eq}/cm^2$.

The irregular dependence of noise as a function of the IRD is so far not understood. It was observed only for 3T-pixels while SB-pixels show different properties. As independently of the IRD both, the measured and calculated noise is sufficiently small not to endanger the operation of the chip, this scattering was treated as second order effect. For the time being it is thus concluded that the noise does not change significantly within the accuracy of the measurement. Nevertheless, this accuracy is considered as reduced with respect to the statistic estimates of the error.

## 6.1.4. Results for the charge collection efficiency and signal over noise

For MIMOSA-1 and MIMOSA-2, no beam test data is available for irradiated chips. In order to obtain an estimate on the dependency of both parameters on the IRD, data from beam tests done with non-irradiated chips were combined with data collected on irradiated chips with the
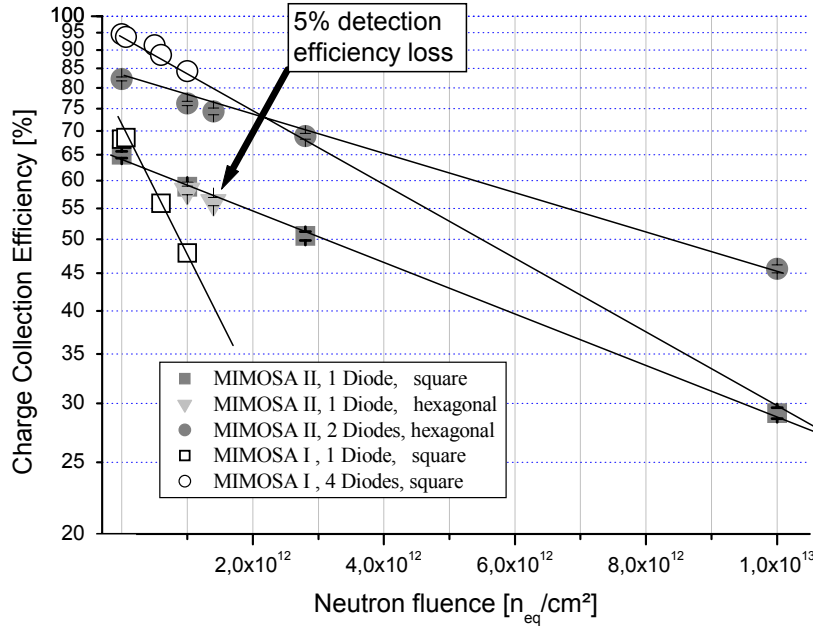
Figure 6.4.:
*Charge collection efficiency of MIMOSA-1 and -2 as a function of the neutron fluence. The data was measured for groups of four pixels detecting the charge generated with the photons of a $^{55}Fe$-source. Straight lines were added to guide the eye. For the questions discussed in this work, the hexagonal and the square pixels can be considered as equivalent.*

$^{55}Fe$ source. This procedure, which will be described in the following, allowed to extrapolate the charge collection efficiency (CCE) obtained with irradiated chips on the source to a S/N(IRD), provided that the increase of shot noise is negligible.

### 6.1.4.1. The charge collection efficiency of irradiated MAPS

The sensitivity of the charge collection efficiency (CCE) of the chips with respect to the IRD is displayed on figure 6.4 for MIMOSA-1 and MIMOSA-2. The figure represents the CCE of groups of 4 pixels in a cluster. It was measured by comparing the charge collected by the diodes with the charge generated with the photons of a $^{55}Fe$ source. Despite of the complexity of the processes involved in the charge collection, the results suggest a simple exponential dependence between the IRD and the CCE:

$$P_{CCE}(d) = P_{CCE}(0) \ e^{-Ad} \tag{6.1}$$

where $d$ represents the radiation dose in units of $n_{eq}/cm^2$, $P_{CCE}(d = 0)$ and $P_{CCE}(d)$ the CCE before and after irradiation respectively.

In the plot one observes a clear hierarchy on the slope $A$, which indicates the deterioration of the CCE as a consequence of the irradiation. The fastest decrease can be observed for MIMOSA-1 with standard pixels followed by the MIMOSA-1 pixels hosting four diodes each. The MIMOSA-2 pixel with two diodes shows the lowest degradation.

This observation can be explained with a radiation induced shortening of the charge carrier's lifetime, which is a known consequence of bulk damage. At a given point, the lifetime reaches a level where a significant fraction of the signal charges recombines before reaching the collection diodes of the pixel.

The mean time required for reaching them increases with reduction of the density of collection diodes. Moreover, the diffusion paths are prolongated because of a higher thickness of the epitaxial layer. The most important degradation can thus be expected for detectors with thick epitaxial layer and low diode densities. In the experiment, this is represented by MIMOSA-1 with one diode per pixel. MIMOSA-2 with two diodes per pixel combines a high diode density with a thin

epitaxial layer. A low deterioration of the CCE is thus to be expected. Both predictions are compatible with the observations.

For the non-irradiated pixels, the lifetime of the charge carriers is very long with respect to the collecting time. The differences observed in the native CCEs of the detectors are thus not dominantly determined by this factor. In order to understand the values obtained from the measurements, one has to be aware that the size of the clusters is bigger than the four pixels taken into account. Only a fraction of the charge generated is thus collected in the four pixels observed. This fraction increases for pixels with more than one diode, as the four pixels represent more collection diodes. Moreover, the probability to collect charge carriers already in the four central pixels increases with a higher surface of the collection diodes. As the collection diodes of the chips are slightly different ($3.1 \times 3.1 \ \mu m^2$ for MIMOSA-1 but only $1.7 \times 1.7 \ \mu m^2$ for MIMOSA-2), the indicated CCE is expected to be slightly better for MIMOSA-1 with the same diode density [1].

From the data shown in figure 6.4 one learns that a detector with thin epitaxial layer and high diode density minimizes the deterioration of the CCE(IRD). Nevertheless, there are draw backs against this solution:

i) For the detection of minimum ionizing particles (MIPs) the signal charge generated depends linearly on the thickness of the sensitive volume. A reduction of the thickness of the epitaxial layer thus improves the CCE(IRD) but reduces the amount of charge carriers available for the charge collection. The effect of a reduced thickness of the epitaxial layer on the total number of electrons collected is thus not necessarily positive.

ii) Pixels hosting more than one collection diode show a higher noise than conventional pixels. This is because of their higher capacity and leakage currents. Despite of their better performance in terms of charge collection, the S/N of these pixels may thus be lower than the one of single diode pixels.

An estimate of the signal charge and the S/N reached in MIP detection is required to judge, in how far the draw backs change the picture.

### 6.1.4.2. The expected signal of minimum ionizing particles (MIP) in irradiated MAPS

Because of the different charge generation processes, the signal caused by a MIP in the irradiated detectors cannot be estimated in an straight forward way with measurements done with an $^{55}Fe$-source. Data from beam tests is required in order to obtain the correct results. Because of the complexity of beam tests, the latter is only available for non-irradiated MIMOSA-1 and 2 [56].

In order to estimate the signal to be expected from a MIP impinging an irradiated detector, the signal observed for a group of four pixels

$$S\left(d\right) = Q_0 \cdot P_{CCE}\left(d\right) \tag{6.2}$$

was scaled with the CCE ($P_{CCE}\left(d\right)$) observed after irradiation according to figure 6.4. In equation 6.2, $d$ stands for the IRD and $Q_0$ stands for the charge generated by the impinging particle in its sensitive medium.

The signal expected from the irradiated detector can be derived from the native one according to:

$$S\left(d\right) = Q_0 \cdot P_{CCE}\left(d\right) = S(0) \frac{P_{CCE}\left(d\right)}{P_{CCE}\left(0\right)} \tag{6.3}$$
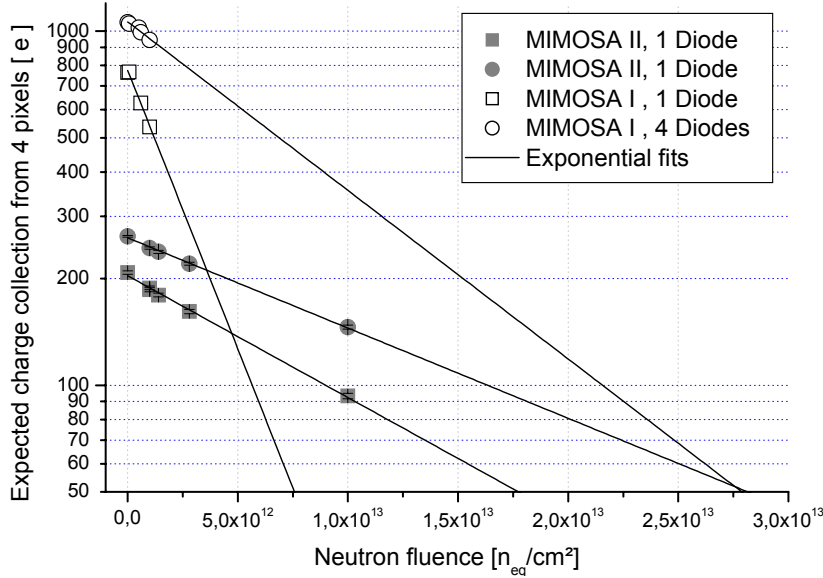
Figure 6.5.:
*Expected signal of MIMOSA-1 and -2 for minimum ionizing particles as a function of the neutron fluence. The CCE from figure 6.4 was combined with the signal measured in beam tests for the non-irradiated detectors after [56]. The lines represent fits of the data.*

This is plotted in figure 6.5 for the irradiated MIMOSA-1 and 2.

One observes that even if the CCE of the pixels of MIMOSA-1 deteriorates faster than the ones of MIMOSA-2, they show a substantially better signal for the radiation doses applied (up to $10^{12}$ $n_{eq}/cm^2$). A straight forward extrapolation of the fits of the data was done in order to obtain an estimate on the behavior of the detectors for very high radiation doses. These extrapolations are represented in the figure by straight lines.

Using them allows estimating when the higher initial signal of detectors with a bigger epitaxial layer is canceled out by the lower stability of the device. One finds this point to strongly depend on the diode density. The single diode pixels of MIMOSA-1 falls behind the ones of MIMOSA-2 after few $10^{12}$ $n_{eq}/cm^2$. The four diode pixels of MIMOSA-1 seem to keep their advantage in pure charge collection up to a dose of roughly $2.5 \times 10^{13} - 3 \times 10^{13}$ $n_{eq}/cm^2$.

### 6.1.4.3. The expected signal over noise ratio for MIPs in irradiated MAPS:

The charge collection as shown in figure 6.5 still needs to be completed by introducing the noise of the different pixels. The latter is mandatory to obtain the decisive parameter for the detector performance, which is its S/N.

To do so, the signal was scaled with the noise of the pixels according to [56]. These noise values were preferred with respect to the ones measured in the source tests (see figure 6.3) because they were taken under the same conditions as the signal. The slight increase of noise as a function of the IRD was ignored, as it is weak and the numbers available are ambiguous.

In order to estimate the minimum S/N required for a reasonable detector operation, data from one individual beam test result was used. This result was obtained with a MIMOSA-2 detector irradiated with neutrons, which was tested in a $\sim 120$ $GeV$ pion beam of the CERN – STS. The test demonstrated that this detector delivers a sufficient ($> 95$ %) detection efficiency for MIPs after an IRD of $10^{12}$ $n_{eq}/cm^2$. The S/N of this chip (according to the analysis method used in this chapter) was used to define the minimum S/N required for obtaining a sufficient

---

[1]The effect of the different size of the collection diodes in the radiation tolerance has been studied systematically with the chip MIMOSA-9. As discussed more below, it was found significant but small, which allows for neglecting it in the following.

detection efficiency. By doing so one assumes the detection efficiency of the detectors to depend on anything but on their mean S/N. This is not generally fulfilled but may serve as valid first order approximation.
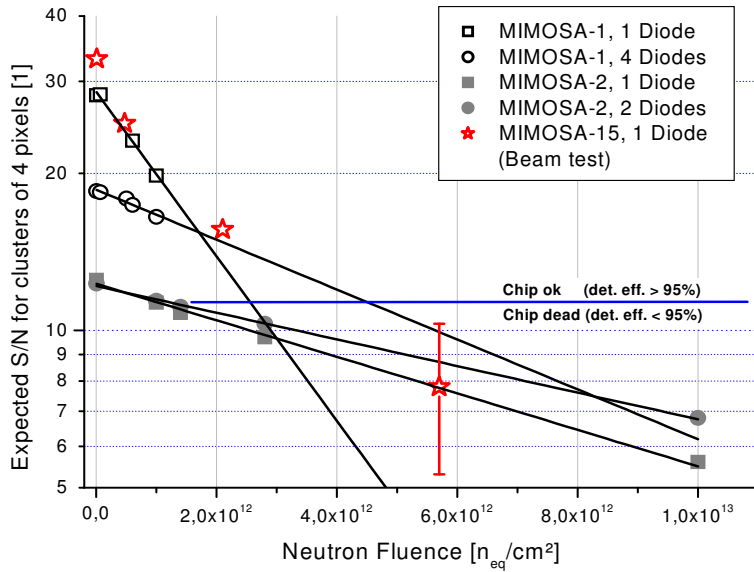


Figure 6.6.:
*The expected S/N of MIMOSA-1 and -2 for minimum ionizing particles as a function of the neutron fluence. Results of a true beam test with MIMOSA-15 (comparable to MIMOSA-1, 1 diode per pixel) are shown for comparison.*
*An individual beam test on an irradiated MIMOSA-2 allowed to estimating the S/N required to reach a detection efficiency of 95 %. which is considered as minimum requirement for tracking applications.*

The results of the scaling are shown in figure 6.6, which shows also the estimated requirement for the S/N. One observes that the four diode pixel of MIMOSA-1 to remains the best option and may provide a radiation tolerance against some $10^{12}$ $n_{eq}/cm^2$. However, because of its relatively high noise, the initial S/N of this pixels is lower than the one of the corresponding single diode pixel.

The conclusions taken from figure 6.6 are weakened by the fact, that the results were generated from various independent measurements made under slightly different conditions. The uncertainties of the results might therefore be substantial. In order to estimate them, the results were compared with the results of a beam test done with MIMOSA-15. The pixel tested from this chip has a geometry comparable with the one of MIMOSA-1 (single diode). The outcome of the test, which will be discussed in more detail in a dedicated section more below, is plotted into the figure. One observes that the beam test fits reasonably well to the predictions made on the base of the plot, which justifies the approach.

Three closing remarks should be done concerning figure 6.6

- The point of MIMOSA-15 at an IRD of $5.8 \times 10^{12}$ $n_{eq}$ is biased because of the reduced detection efficiency of the chip after this irradiation. As hits with very low S/N were not recognized anymore, the bias is towards higher values.
- This bias is not to be expected for the data of MIMOSA-2 at $10^{13}$ $n_{eq}/cm^2$ as the $^{55}Fe$ source was used in order to measure this point. This source generates a signal roughly six times above the one expected from a minimum ionizing particle. The S/N was thus sufficient to reliably detect the photons.
- Independently from the two points raised before, the S/N of the beam tests do not show the clear exponential dependence on the IRD, which one expects from the tests with the $^{55}Fe$ source. This difference is only weak but it has also been observed for other beam test with different chips. The reason for this difference is still under discussion.

### 6.1.5. Summary and Conclusion

The exploratory measurements made with MIMOSA-1 and MIMOSA-2 concentrated on getting a first impression on the tolerance of MAPS against non-ionizing radiation. This tolerance was estimated as a function of the density of the collecting diodes and the thickness of the epitaxial layer. The chips were irradiated with IRDs of up to $10^{13}$ $n_{eq}/cm^2$. Consecutively, their performances were compared with the ones of non-irradiated chips.

An increase of the leakage currents by roughly one order of magnitude was observed for MIMOSA-2 irradiated to $10^{13}$ $n_{eq}/cm^2$. By itself, this additional leakage current can be tolerated. Nevertheless, an increase of noise of $\sim 10\%$ is to be expected because of shot noise at a temperature of 10 $^\circ C$ and an integration time of 3.3 $ms$.

The direct measurements of the noise of the irradiated MIMOSA-2 led to ambiguous results. A significant scattering of the data points was observed. This suggests the existence of further effect on the noise, which has so far not been identified. Until the sources of the observations are identified, this scattering has to be handled as additional ($\sim 10\%$) uncertainty of the measurements. Hereafter, no significant variation of the radiation dose on the noise can be observed at a temperature of 10 $^\circ C$ and an integration time of 3.3 $ms$.

The dominant effect of non-ionizing radiation is caused by the drop of the charge carriers' lifetime, which is a known consequence of bulk damage. If this lifetime deteriorates to the order of the time required for charge collection, a part of the signal charge is lost by recombination. It was expected, that shortening the mean diffusion path of the charge carriers might alleviate this effect. As the thickness of the epitaxial layer and the density of collecting diodes influences the length of the drift paths, the CCE, the total number of collected charge carriers and the S/N were studied as a function of both geometrical parameters and the IRD.

Within this study, the density of the collecting diodes was varied by choosing pixels with the same pitch but a different amount of collecting diodes per pixel. This approach leads to a better CCE with draw backs because of the lower noise performance of the pixels hosting multiple collecting diodes.

According to what was expected, the highest tolerance against non-ionizing radiation in terms of CCE was observed for MAPS with thin epitaxial layer and high diode density. For the S/N(IRD), a thicker epitaxial layer seems preferable as the amount of charge carriers generated by a MIP scales linearly with the thickness of the sensitive volume. The higher amount of charge carriers produced in this volume over compensates the faster deterioration of the CCE for all IRDs of interest for tracking applications.

Despite of their higher noise, multi diode pixels provide a better S/N than single diode pixels. This statement holds under the assumption that the expected radiation induced increase of shot noise is negligible. This condition not generally fulfilled. It can considered as realistic for the vertex detector of CBM, as the chips will run at low temperatures with very low integration times, which dims the shot noise. For applications running the chips under less beneficial conditions, the noise generated by the additional diodes of the pixel has to be balanced against the higher CCE provided by them.

Over all from the measurements of MIMOSA-1 and MIMOSA-2 one can state, that a high diode density combined with a high thickness of the epitaxial layer provides the highest radiation tolerance. A beam test with MIMOSA-2 demonstrated a radiation tolerance against $\sim 10^{12}$ $n_{eq}/cm^2$.

## 6.2. Radiation tolerance of MAPS collecting from the substrate (MIMOSA-4)

The functionality losses of MIMOSA-1 and -2 are dominantly caused by a radiation induced reduction of the charge carriers' lifetime. There is no trivial way to overcome this fundamental effect. Nevertheless, it was hoped that an improvement of the initial signal would allow for obtaining a S/N that is substantially above the one needed for an efficient MIP detection. In this case, one may tolerate losses in S/N as long as the requirements remain fulfilled. The aim of the following studies was to improve the "reserves" of the chip in terms of S/N.

A chip of particular interest in this context is MIMOSA-4. This chip was build on a wafer without epitaxial layer. A substrate with a doping comparable to this layer was used instead as sensitive medium. In a simplified picture, this solution can be interpreted as a sensor with an epitaxial layer of infinite (several 100 $\mu m$) thickness.

The obvious advantage of this solution is the high signal charge generated by MIPS in the sensitive volume, which is by more than one order of magnitude above the one of conventional epitaxial layers. On the other hand, a poor CCE had to be expected as the diffusion paths of the charge carriers become extremely long. A substantial part of the charge was thus expected to recombine before being collected. The latter is particularly true for electrons, which diffuse away from the collecting diodes. In the case of an epitaxial layer with moderate thickness, these electrons are reflected back at the interface between the layer and the substrate. Despite of initially diffusing into the wrong direction, they therefore reach the collecting diodes after diffusing some tens of $\mu m$. As this interface is missing in the wafer used for producing MIMOSA-4 and the fraction of charge carriers diffusing into the wrong direction gets lost. Nevertheless it was hoped that the higher signal of the sensor would compensate the reduced CCE.
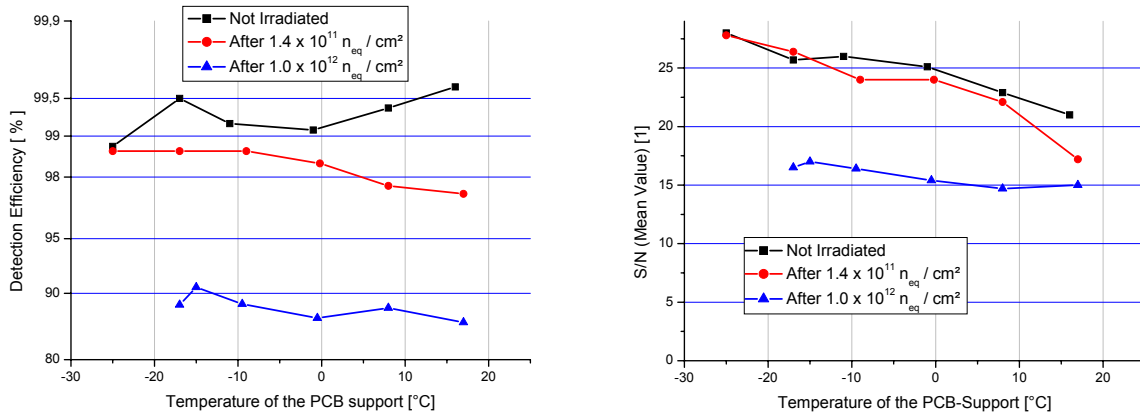


Figure 6.7.: **Top:** *The detection efficiency of MIMOSA-4 as a function of the temperature and the IRD. The variations of the detection efficiency as a function of temperature is not considered as significant for the non-irradiated chip.*
**Bottom:** *The S/N (mean value) of MIMOSA-4 as a function of the IRD. The S/N is slightly temperature dependent and decreases with increasing temperatures. The values obtained at $1.0 \times 10^{12}$ $n_{eq}/cm^2$ are biased as because of the reduced detection efficiency only a part of the distribution was recorded. From [51].*

The tests of MIMOSA-4 was particularly difficult as the methods usually used for testing chips cannot be easily applied to this chip. This complication is discussed in detail in chapter 5.2.2.

It came out to aggravate in particular the measurement of the CCE, which is one of the most important parameters for judging the non-ionizing radiation tolerance of a chip in laboratory test. The few useful results, which are summarized in figure 6.7, were thus dominantly obtained in a series of beam tests.

In this figure, one observes that MIMOSA-4 shows a good S/N and a good detection efficiency for radiation doses of up to $\sim 1.4 \times 10^{11}$ $n_{eq}/cm^2$. At a dose of $\sim 1 \times 10^{12}$ $n_{eq}/cm^2$, significant deteriorations of the S/N are observed. This led to a drop of the detection efficiency to values of $\lesssim 90$ %. The performances of the chip was thus found to be below the ones of MIMOSA-2 at this dose.

The measurements of the temperature dependence of S/N and the detection efficiency provides few information. The variation of the detection efficiency over temperature for the non-irradiated chip are certainly below the uncertainties of the experiment[2]. Moreover, the S/N(T) of the most irradiated chip is biased. Because of the reduced detection efficiency, only fraction of the distribution was taken into account for computing it. From the remaining measurements one can carefully state that an increase in temperature leads to slightly reduced detection performances. This reflects the superposed effects of noise, charge collection and the time constant of the recharge current of the SB-pixel. As the contributions are difficult to isolate, the temperature dependence was not analyzed a systematic way.

The measurements done on MIMOSA-4 show clearly, that the radiation tolerance of a detector with "infinite" epitaxial layer is below the one observed for sensors with an $\sim 10$ $\mu m$ epitaxial layer. This is presumably because of the high diffusion paths required to collect signal charge generated deep in the substrate. If the life time of the charge carriers is reduced after irradiation, only the part located close to the collecting diodes contributes to the signal while the charge generated in the deep substrate is lost by recombination. This leads to an effective thickness of the sensitive volume, which shrinks with increasing IRD. At a relatively moderate IRD, the number of charge carriers generated within this effective thickness becomes comparable to the one generated in a conventional epitaxial layer. In this case, the absence of the electron reflection at the interface between epitaxial layer and substrate is not compensated anymore by additional charge and the reduced CCE is of the sensor of MIMOSA-4 takes its full effect.

One can therefore conclude that there is an optimal thickness of the sensitive volume, which is above the $\sim 4$ $\mu m$ tested in MIMOSA-2 and below the several 100 $\mu m$ tested in MIMOSA-4. An unreflected increase of the thickness of the epitaxial layer is thus not a mean to improve the radiation tolerance of MAPS against non-ionizing radiation.

## 6.3. Dependence on the pixel size (MIMOSA-9)

**Chip design:** MIMOSA-9 is the first sensor, which was engineered in the AMS 0.35 $\mu m$ OPTO process. This process is optimized for building MAPS for visible light detection. The thickness of the epitaxial layer was announced to have a 20 $\mu m$. Even if the true value came out to be $\sim 11$ $\mu m$, a high initial signal for MIPs was observed. A good charge collection was thus also expected after a radiation induced reduction of the CCE. This made the detector a good candidate for reaching high radiation tolerance against non-ionizing radiation.

The chip contained eight different pixel matrices. Six of these matrices were equipped with SB-pixels (see chapter 2.2.4) with a pitch of 20 $\mu m$, 30 $\mu m$ and 40 $\mu m$ combined with two differently big collection diodes respectively. The size of the small collection diode was $3.4 \times 4.3$ $\mu m^2$, the one of the big diode was $6.0 \times 6.0$ $\mu m^2$ for the pixels with 20 $\mu m$ and 40 $\mu m$ pitch. For the pixels

---

[2]Note the scale of the Y-axis!

with 30 $\mu m$ pitch, a diode size of $5.0 \times 5.0$ $\mu m^2$ was chosen for the big diodes. Moreover, two different types of 3T-pixels were arranged in a matrix with 40 $\mu m$ pitch. The latter are discussed in the context of ionizing radiation tolerance studies.

The design of MIMOSA-9 was of interest for studying the variation of the S/N and the detection efficiency as a function of the IRD and the density of the collecting diodes. In the earlier studies done on MIMOSA-1 and -2, this density was varied by hosting more than one diode in a pixel. As this also leads to a higher pixel capacity and a higher pixel noise, the effect of the diode density was not fully isolated. Arranging identical pixels with different pitch in MIMOSA-9 allowed to overcome this point.
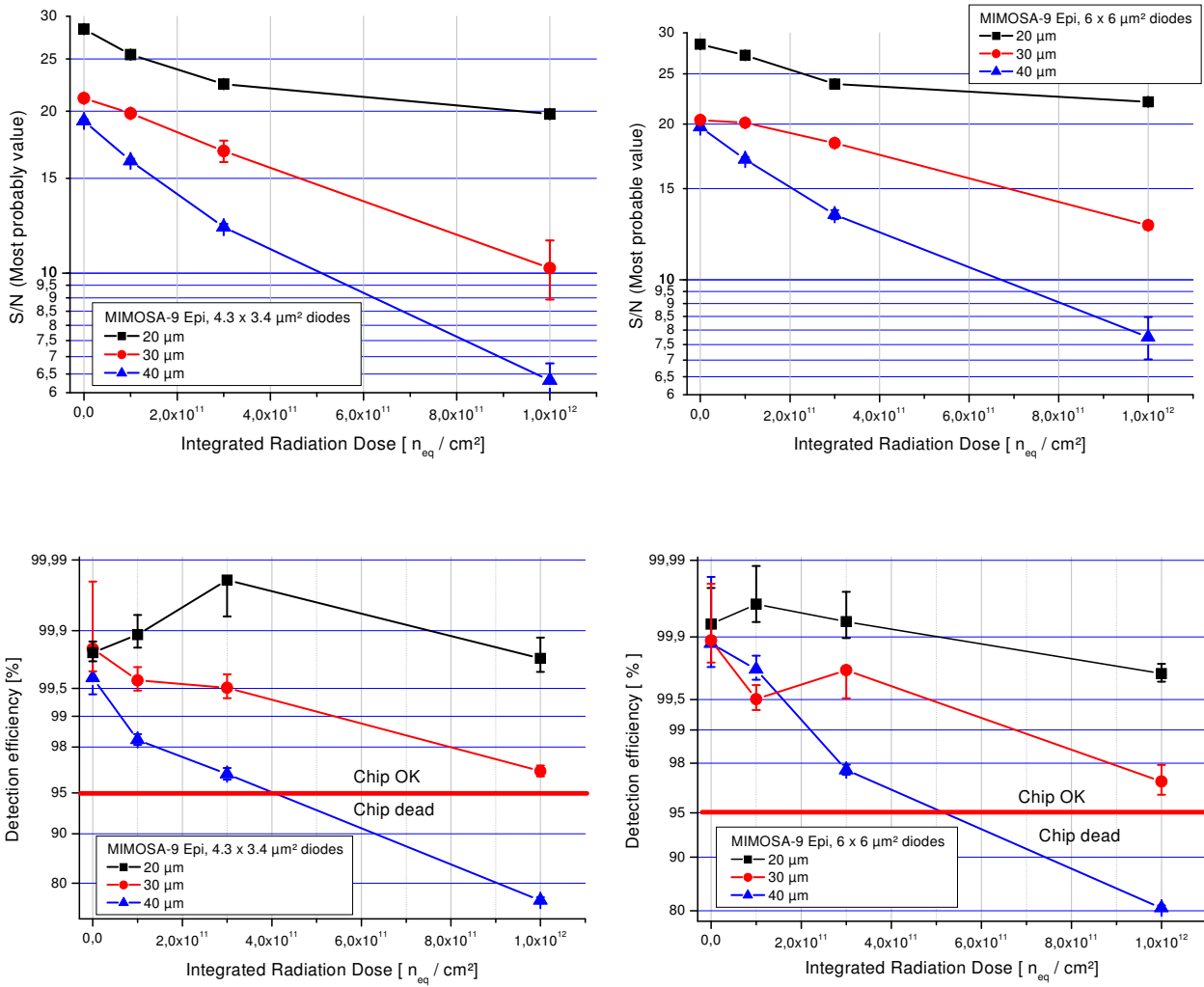


Figure 6.8.: *Signal over noise ratio and detection efficiency of MIMOSA-9 as a function of the radiation dose, the pixel pitch and the diode size. Note that the diode size of the big pixel with 30 $\mu m$ pitch was $5.0 \times 5.0$ $\mu m^2$. The data was taken at a temperature of $T = -20$ $°C$ and $f_{clk} = 2.5$ $MHz$.*
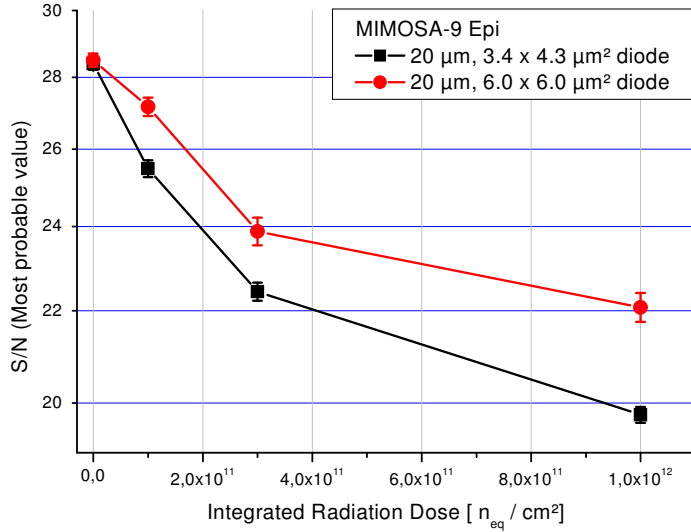
Figure 6.9.:
*S/N of MIMOSA-9 irradiated with neutrons as a function of the diode size and the IRD. Note the logarithmic Y-axis. The data was taken at $T = -20\ ^\circ C$.*

**Test results:** The measurements shown in the following were done with a beam test on a $\sim 5\ GeV$ electron beam at DESY (Hamburg). According to the experiences obtained from MIMOSA-2 and MIMOSA-4, MIMOSA-9 was irradiated with IRDs of up to $10^{12}\ n_{eq}/cm^2$ and the S/N and the detection efficiency were measured in the beam tests. The S/N as a function of the IRD are shown in the upper plots of figure 6.8. The corresponding detection efficiencies can be found in the lower plots for the big and the small pixels respectively. It has to be pointed out that the most probable value of the signal over noise ratio is shown in the plots. As the S/N follows a Landau distribution, this leads to values systematically below the mean values shown earlier for MIMOSA-4.

The signal over noise ratio clearly depends on the pixel pitch, which is the expected consequence of the radiation-induced reduction of the lifetime of the charge carriers. One observes the ratios not to trivially follow the exponential decent, which was observed in the laboratory measurements with MIMOSA-1 and MIMOSA-2 (see equation 6.1).

A closer look at the detection efficiency of the different pixel geometries shows the influence of the pixel pitch on the radiation tolerance. One observes the pixels with 40 $\mu m$ pitch to exhibit already a loss in detection efficiency for a dose of $3 \times 10^{11}\ n_{eq}/cm^2$. The pixels with 30 $\mu m$ show a similar deterioration for a dose of $10^{12}\ n_{eq}/cm^2$. In both cases, the pixels still work, i.e. their detection efficiency amounts to $\sim 98\%$, but they clearly exhausted their reserves in terms of S/N.

Unlike for the large pitches, the 20 $\mu m$ pixels show an excellent detection efficiency for the highest doses accumulated. The remaining reserves in S/N indicate the pixels to also tolerate doses above $10^{12}\ n_{eq}/cm^2$. Extrapolations give an indication that the ultimate radiation tolerance of the pixels is $\sim 3 \times 10^{12}\ n_{eq}/cm^2$. This was not confirmed directly with MIMOSA-9 but the question was addressed with MIMOSA-15 in the following serial of measurements.

An interesting point is the direct comparison between the pixels with big and with small diodes. This is shown in figure 6.9. In spite of their lower gain provoking a slightly higher noise, these pixels show a significantly higher signal over noise ratio after irradiation. This can be interpreted as a consequence of the higher cross section for a diffusing electron reaching a big collecting diode.

A direct comparison was made between the S/N(IRD) of pixels with small and the big diode. Comparable to multi diode pixels, the latter were expected to provide a slightly higher CCE combined with higher noise, which is caused by enlarged pixel capacity and leakage current. It was to be clarified, if the better CCE or the higher noise would dominate. The results of the measurement are illustrated in figure 6.9. One observes the S/N to be slightly higher for the

pixels with big diode. This difference becomes more important after irradiation and reaches the order of 10 %. One can thus conclude that the gain in CCE slightly dominates the disadvantages of the big pixels. This is in particular true for irradiated chips. Nevertheless, the effect is rather small and will probably shrink further at higher temperatures, which provoke relevant shot noise.

A second aspect, which is clearly visible in figure 6.9, is the fact that the S/N does not follow the simple exponential dependence on the IRD, which was observed in the CCE measurements done on MIMOSA-1 and -2. The reasons for this are so far not clarified. One aspect might be the different geometries of the charge deposit of the different particles. The X-rays used for the CCE measurements depose their charge in a spherical volume of $\sim 1~\mu m$ diameter while the MIPs used for the S/N measurement is spread along the particle trajectory, e.g. over the full thickness of the epitaxial layer. Assuming the CCE not to be uniform over the depth of the epitaxial layer, different charge collection distributions are to be expected.

**Discussion:** The measurements on MIMOSA-9 allowed to estimate the effect of different pixel pitches and the diode size on the radiation tolerance. It was shown that a reduction of the pixel pitch leads to a substantial increase of the radiation tolerance. The increase reached by a reduction of the pixel pitch from 40 $\mu m$ to 20 $\mu m$ is roughly one order of magnitude (see also the measurements done with MIMOSA-15). A positive influence of bigger collection diodes was also observed. This effect is significant but too weak to be of practical use.

Over all, the measurements on MIMOSA-9 show the chip to provide better radiation tolerance against non-ionizing doses than MIMOSA-2 and MIMOSA-4.

## 6.4. The state of the art (MIMOSA-15)

The design of MIMOSA-15 was made again in the AMS 0.35 $\mu$m opto process. It hosted several matrices of SB-pixels with 30 $\mu m$ and 3T-pixels with 20 $\mu m$ pitch. Unlike the pixels of MIMOSA-9, the pixels of MIMOSA-15 were optimized for ionizing radiation tolerance (see also chapter 5.3.4.3 and 5.3.4.2).

The studies on MIMOSA-15 are ongoing. Nevertheless, two results should be mentioned in order to complete the picture obtained with the previous measurements. One of them was obtained with a beam tests of detectors irradiated to IRDs above $10^{12}~n_{eq}/cm^2$. Moreover, comparing the dependence of the noise on the IRD is of interest, as for a first time SB-pixels and 3T-pixels can be directly compared.

Figure 6.10 shows the S/N and the detection efficiency as obtained from a beam test, which was done at a temperature of $-20~°C$ and an integration time of 0.7 $ms$. One observes a reasonably high detection efficiency (above 99 %) after an IRD of $2.1 \times 10^{12}~n_{eq}/cm^2$. At an IRD of $5.8 \times 10^{12}~n_{eq}/cm^2$, this detection efficiency drops to a value of $\sim 80$ %. At this point, the detector cannot be considered as correctly working device. Nevertheless, this result underlines that MAPS detectors may keep a part of their detection efficiency even after being irradiated with IRDs substantially above their nominal limit.

The noise of MIMOSA-15 is shown in figure 6.11 for a temperature of $T = -20~°C$ (left) and $T = +20~°C$ (right). One observes the noise to significantly increase after neutron irradiation. This stands in contrast to the observations made on MIMOSA-2. The noise of the 3T-pixel at a temperature of $T = +20~°C$ shows again the irregular behavior already observed at MIMOSA-2. As this behavior is not reproduced by the SB-pixel it is likely that this is caused by a particularity of the 3T-pixel. Nevertheless, it was so far not possible to clarify this point.
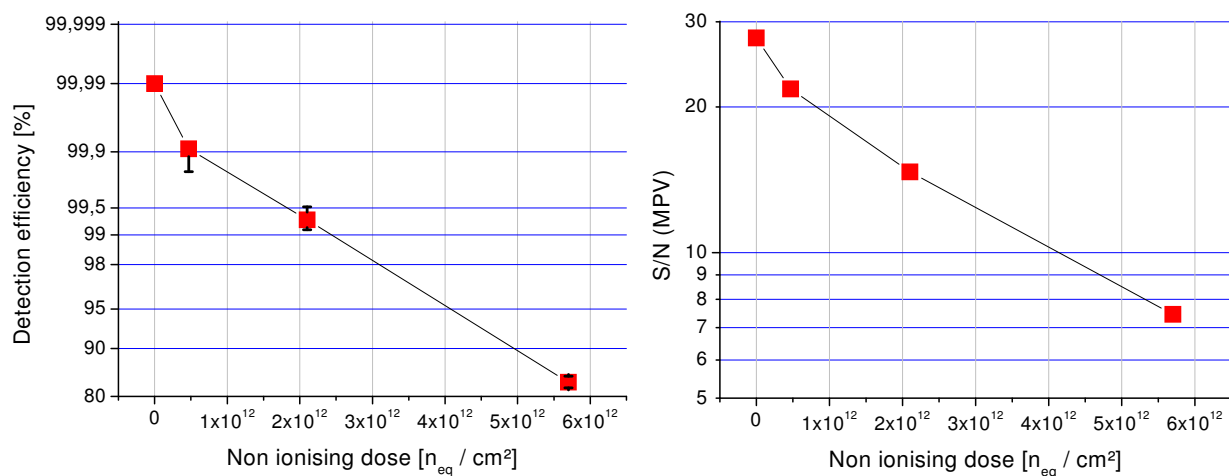
Figure 6.10.: *Signal over noise ratio and detection efficiency of MIMOSA-15 as a function of the radiation dose. The data was taken at a temperature of $-20\ °C$ in order to reduce shot noise. The integration time was $0.7\ ms$.*
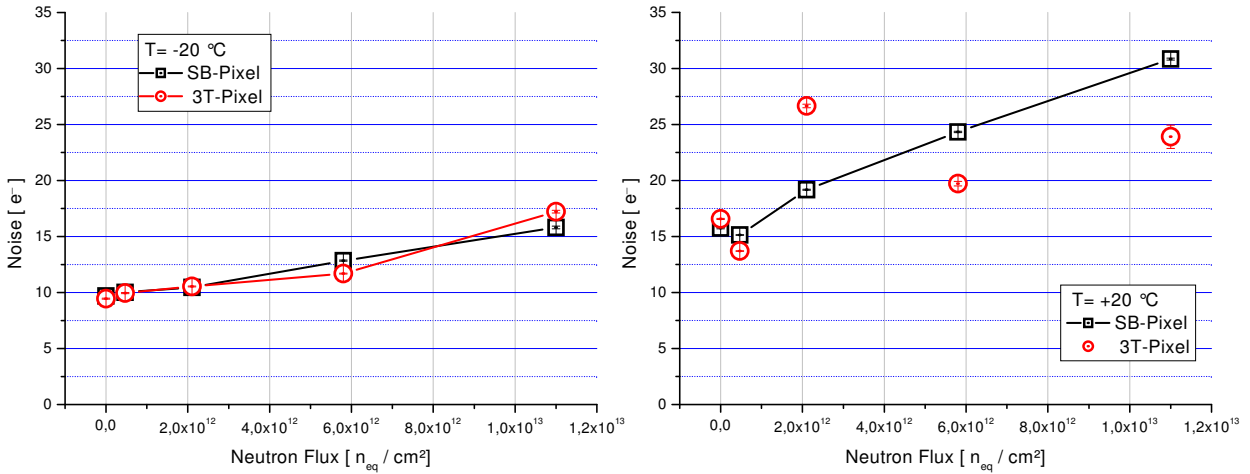
Figure 6.11.: *Noise of MIMOSA-15 as a function of the radiation dose at a temperature of $-20$ °C (left) and $+20$ °C (right). Unlike MIMOSA-2 on observes a substantial increase of noise after irradiation. At a temperature of $+20$ °C, the noise of the 3T-pixel shows the irregular behavior already observed at MIMOSA-2.*

From the measurements done on MIMOSA-15 one concludes that a significant increase of noise (up to a factor 2) has to be expected after irradiation with $1.1 \times 10^{13}$ $n_{eq}/cm^2$. The difference with respect to the observations made on MIMOSA-2 may be caused by the higher leakage current of MIMOSA-15. According to preliminary measurements, this current is more than one order of magnitude higher for MIMOSA-15 than for MIMOSA-2. Refined measurements are still required to stabilize this result.

Nevertheless, MIMOSA-15 has demonstrated a radiation tolerance against an IRD of $2.1 \times 10^{12}$ $n_{eq}/cm^2$.

## 6.5. Random Telegraph Signal

### 6.5.1. Random Telegraph Signal in MAPS

Random Telegraph Signal (RTS) is usually known as a modulation of the leakage current of a transistor [25]. The current is alternating between two (or more) well-defined "quantum states". As the time required to change the current is negligible with respect to the time the system remains in one state, plotting the leakage current over time provides a picture comparable to a (meaningless) Morse code, which probably motivated the name of the effect.

According to literature, RTS is explained by the modifications of the field applied to a field effect transistor. This modification is caused by the additional field generated by an individual crystal defect, which changes its charge state by electron/hole capture and emission processes. Despite of being small, the modification of the field in the transistor is sufficient to change slightly its resistivity, which leads to a current modulated by a change of an individual quantum state in the material.

A comparable effect was observed on MIMOSA-2 irradiated with $10^{13}$ $n_{eq}/cm^2$. According to the aim of this work, the studies of RTS on MAPS restricted themselves to aspects, which

endanger the operation of the CBM vertex detector. For additional information about RTS on MAPS, the reader is referred to literature [57], which was helpful to interpret the observations described in this section.

The RTS observed manifests itself in MAPS as a slow modulation of the output signal of individual pixels with respect to the time. A meaningful example is illustrated in figure 6.12 (top), which shows the output signal of a pixel after CDS over the time as obtained from $2 \times 10^4$ consecutive events at a temperature of 40 $°C$.

The integration time of the individual events taken in this measurement was $\sim 3.3$ $ms$. Nevertheless, the data transfer from the readout system to the computer generates a substantial dead time, which is not clearly determined. The time is thus provided in arbitrary units, which correspond to the event number. A rough estimate of the true event rate is given with 200 events per second. The leakage current and the signal superpose in the plot. Both are presented in units of $ADC$. For the leakage current, the gain was derived with $\sim 0.25$ $fA/ADC$. The gain of the signal is $\sim 5$ $e^-/ADC$.

Two comments should be made before interpreting figure 6.12 (top).

- As discussed chapter 2.2.4, the output signal of a MAPS-pixel is combined by several contributions. The modulations observed can thus be interpreted as charge injections into the pixel, modulations of the leakage currents of the pixel or voltage modulations in the on pixel amplifier. As discussed later in more detail, there are arguments for the hypothesis that the RTS in MAPS is caused by a modulation of the leakage current of the collecting diode. Even if it remains to be proven, this hypothesis will be used in the following.

- According to the theory of RTS, the modulations are caused by individual crystal defects. It is likely that the detailed properties of a pixel showing RTS depend not only on the type of this defect but also on its microscopic position in a pixel, which usually demands for a statistical treatment. The plots and results shown in this work were obtained in studying only some individual pixels showing RTS. The results obtained should thus be interpreted as instructive examples, which are nevertheless not necessarily representative.

When interpreting the output signal of the pixel shown in figure 6.12 as modulations of the leakage current, one finds it to alternate between three different levels. The current of these levels is $\sim 25$ $fA$, $\sim 45$ $fA$ and $\sim 60$ $fA$. In other pixels, leakage currents alternating between two levels were observed.

The noise of the pixel was found not to strongly depend on the current value. In the example, it increases from 30 $e^-$ to 33 $e^-$ at the highest current level.

## 6.5.2. Potential sources of RTS in MAPS

Despite other options are not fully ruled out so far, a modulation of the leakage current passing the collection diode of the pixels is considered as origin of the RTS. This picture provides a simple straightforward explanation for all effects observed. On the other hand, it postulates the occurrence of an effect in reversed biased diodes, which has so far been established for transistors only.

However, the conclusion is covered by the following considerations:

- A source of RTS located in the collecting diode would cause visible effects by generating leakage currents in the order of ten $fA$. This scenario appears more likely than a source of RTS located in the source follower transistor, as the latter transport a macroscopic current in the order of $mA$. Generating a strong modulation of this current with the fields caused by an individual elementary charge seems unlike.

Figure 6.12.:

*Random Telegraph Signal (RTS) on MIMOSA-2 after an irradiation with $10^{13} n_{eq}/cm^2$ at a temperature of $40\ °C$ and an integration time of $3.3\ ms$.*

*Upper figure:  The output signal of a pixel after CDS over the time of a representative pixel showing RTS. One observes the output signal to jump between three different levels.*

*Lower figure:  The amount of hits indicated within $2 \times 10^4$ events is shown as a function of the pixel number. Few tens of hits were expected for each pixel while the number of indications reaches values above $10^4$. This effect appears if the difference of the equivalent charge between two current levels exceeds the signal threshold.*

- A comparable observation could be caused by a modulation of the conductivity of the reset-transistor. Nevertheless, as it is closed most of the time, a modulation would have to cause an additional leakage current in this transistor. This current would continuously recharge the pixel and thus reduce the indication of the leakage current of the collecting diode. This stands in contrast to the observations, as the indicated leakage current of the RTS-pixels is regularly above the one of usual pixels (see also [57]).

A remarkable point is the presence of three different current values in figure 6.12. Usually, RTS alternating between two levels is reported, which was also observed on MIMOSA-2. According to the theory of RTS, the levels of the current are defined by a crystal defect changing its quantum state by electron or hole capturing, which naively leads to a system with two charge states. The reason for the existence of the third state is not clarified. One may speculate about the defect modulating the current to have more than two charge states, which exists for some radiation induced defects. Alternatively, the current might be generated by the superposed effect of two independent defects. In this second scenario, one would however expect the presence of a fourth current level, which was not observed.

### 6.5.3. Consequences for the detector operation

In spite of not having a strong impact on the noise, RTS might have serious consequences on the operation of a 3T-pixel. This is because the quantum steps of the leakage current undermine one of the basic assumptions used for analyzing the data of the chip. As discussed in chapter 4.4.4, the isolation of the signal from the leakage current is only possible if the leakage current is constant. This requirement is not fulfilled in a 3T-pixel showing RTS. Assuming the leakage current correction relying on the leakage current generated in the "ground state" of the pixel, an excitation of the leakage current to the first regime would lead to the indication of a signal of $\sim 400 \ e^-$. This is sufficient for exceeding the threshold. A jump to the second level generates in this example a signal of $\sim 600 \ e^-$, which is significantly above the regular signal of a MIP for this chip.

A pixel generating strong RTS becomes therefore a hot pixel which may reach an individual fake rate above 50 %. This is illustrated in figure 6.12 (bottom), which shows the amount of hits from the $^{55}Fe$ source recorded in $2 \times 10^4$ events as a function of the pixel number. A mean hit rate of $\sim 20$ hits per pixel was expected for the full measurement. As a consequence of the RTS, $\sim 1\%$ of pixels show a hit rate exceeding this number by more than five standard deviations.

The complication caused by the "hot" pixels is twofold. On the one hand, the amount of wrong indications caused by RTS can reach the order of the regular occupancy of the detectors. This leads to a serious additional load on the DAQ-system of an experiment. On the other hand, hot pixels are not reliable for measurements and their data will probably be rejected at some point. A serious amount of hot pixels thus also reduces the detection efficiency of the chip.

### 6.5.4. Methods to overcome problems induced by RTS: Temperature dependence

The temperature dependence of RTS provides an interesting feature for alleviating unwanted consequences of RTS. It was studied by running a MIMOSA-2 irradiated with $10^{13} \ n_{eq}/cm^2$ at different temperatures ranging from $-20 \ ^\circ C$ to $+40 \ ^\circ C$. The amount of "active" RTS-pixels was counted for each of these runs. A pixel was defined as active, if its hit rate exceeded the mean hit rate of all pixels by more than five standard deviations. As illustrated in figure 6.13, the amount of significant pixels increases strongly with the temperature.
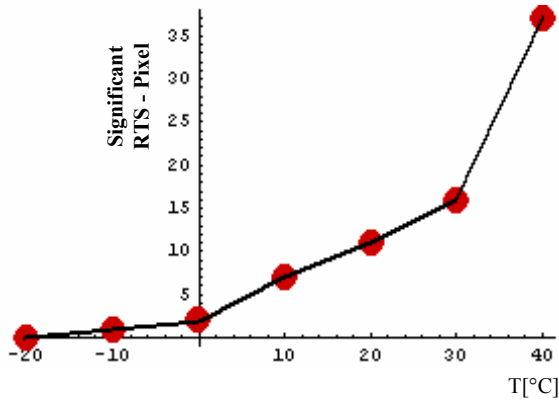
Figure 6.13.:
*The number of observed "active" RTS-pixels as a function of temperature. The data was taken on MIMOSA-2 irradiated with $10^{13}$ $n_{eq}/cm^2$. The integration time was set to 3.3 ms. A RTS pixel is defined as active, if its indicated hit rate is more than 5 standard deviations above the mean hit rate of all pixels.*

In a second step, RTS-pixels, which were identified at high temperature 40 $°C$, were monitored at low temperatures. As illustrated in figure 6.14, a weak RTS could also be observed for low temperatures $-20$ $°C$. The difference between the regimes is however reduced to the order of the thermal noise. A change of the regime is thus insufficient to pass the discrimination threshold and no fake hits are indicated.

Note that the time between two changes of the state of the pixel appears larger than in the high temperature case. This is compatible with [57] but was not studied systematically.

### 6.5.5. Summary and conclusion

Random Telegraph Signal has been observed in the output signal of individual pixels of a MIMOSA-2 chip being irradiated with $10^{13}$ $n_{eq}/cm^2$. This effect is explained in literature by a variation of the charge of individual lattice defects, which are caused by electron/hole capturing. The fields caused by the additional charge manipulate currents in the environment of the defect.

In MAPS, RTS is probably caused by modulations of the leakage current of the collecting diodes. This hypothesis is compatible with all observations made but alternative explications remain to be ruled out.

The effect forms a risk for the operation of irradiated detectors, as up to 1 % of the pixels were observed to become hot. The fake hit rate of some of these hot pixels exceeded 50 %. The corresponding fake hit rate may lead to a substantial unwanted load on the DAQ system. Moreover, as the data provided by the pixels is not reliable, their presence also reduces the detection efficiency of the detector.

It was observed, that the amplitude of RTS is reduced down to the level of thermal noise when cooling the chip. This forms one option to overcome the unwanted effects of RTS, as the hot pixels become (to some extend) operational again. Alternatively, the use of SB-pixels would be helpful, as this pixel adapts itself efficiently to the leakage current. Indeed, RTS was so far not observed for these pixels.

Nevertheless, it remains to be worked out if the use of SB-pixels alone is sufficient to overcome the problem. This is because the time the pixel requires to adapt itself to the new leakage current may reach some tens of *ms*. In some particular cases, RTS fluctuations on a comparable time scale were observed (see figure 6.15).

Additional studies are thus recommended before operating MAPS irradiated with a substantial ($\gg 10^{11}$ $n_{eq}/cm^2$) non-ionizing dose at high temperatures.
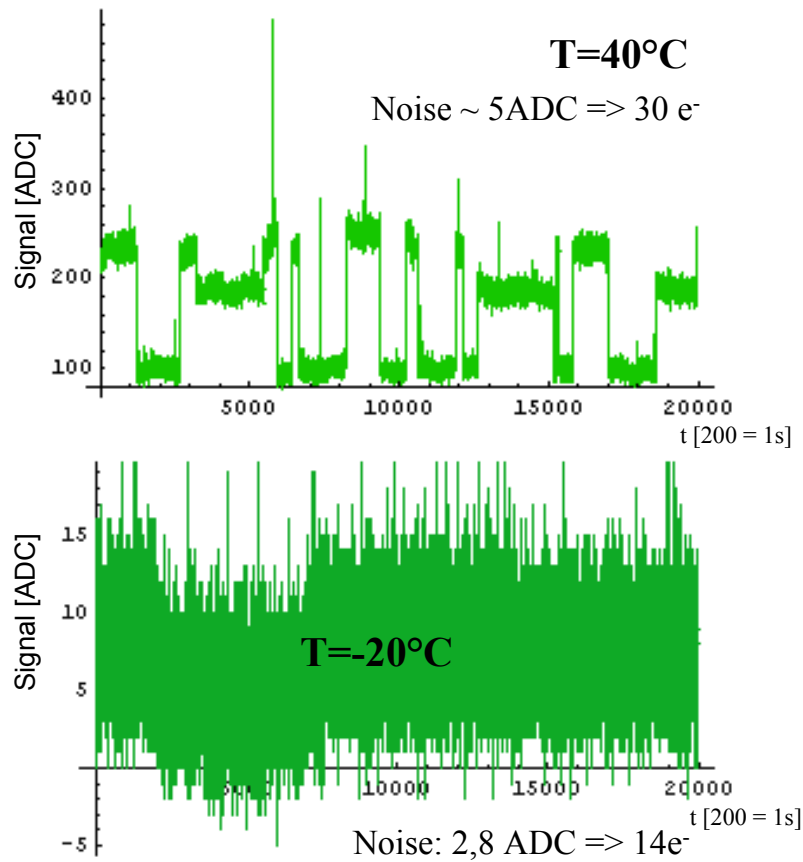
Figure 6.14.:
*Random Telegraph Signal (RTS) on MIMOSA-2 after an irradiation with $10^{13}$ $n_{eq}/cm^2$ and an integration time of 3.3 ms. The RTS pattern of the same pixel at a temperature of 40 °C and −20 °C is shown. One observes the distance between two current levels is reduced at low temperature.*
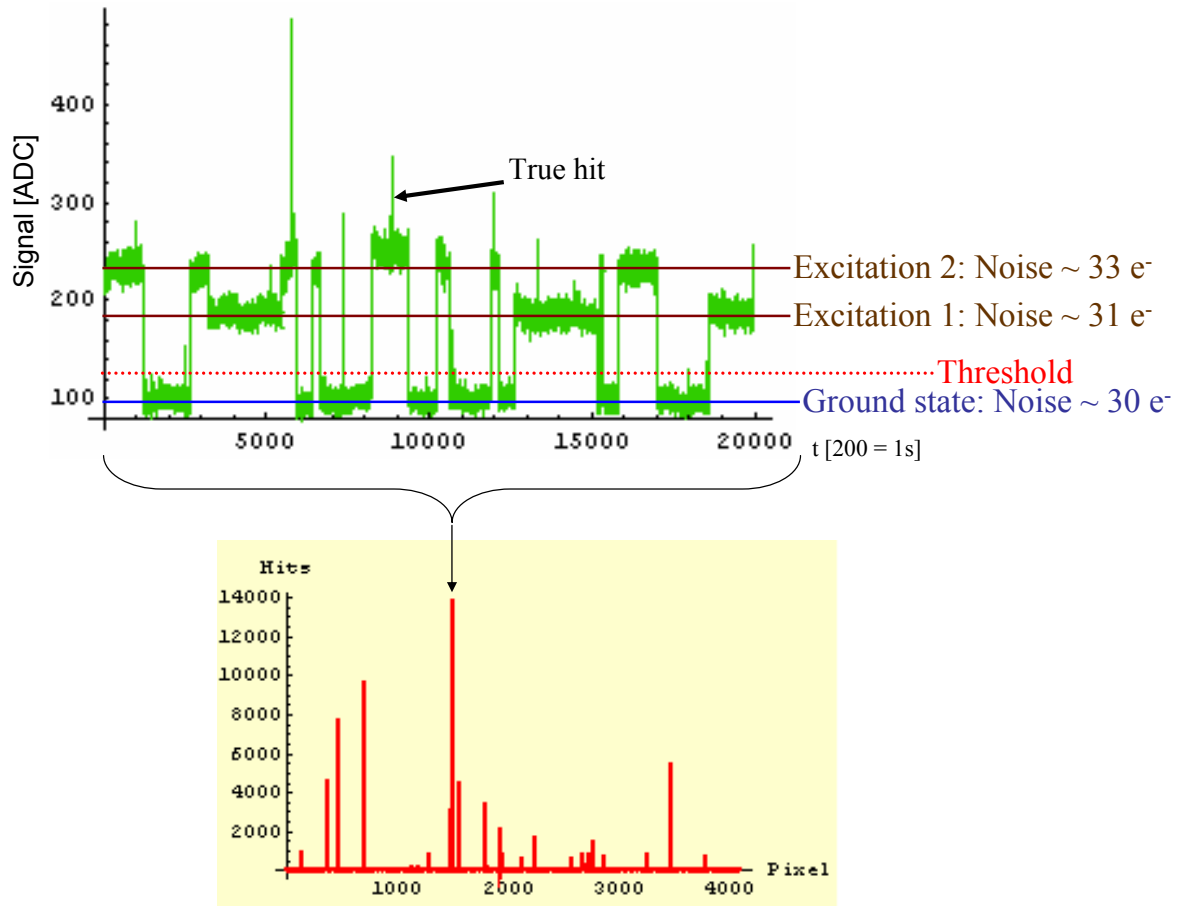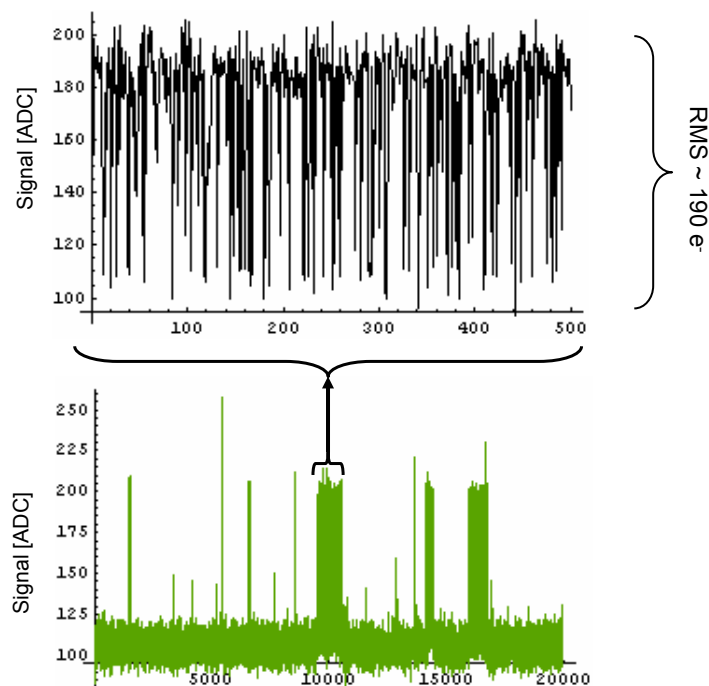


Figure 6.15.:
*Random Telegraph Signal (RTS) on MIMOSA-2 after an irradiation with $10^{13}$ $n_{eq}/cm^2$ at a temperature of 40 °C and an integration time of 3.3 ms. The output signal is plotted as a function of the time. In the zoom (upper plot) one observes fast changes between two regimes, which may reach a time scale comparable to the time constant of SB-pixels.*

## 6.6. Summary and conclusion on non-ionizing radiation tolerance

The radiation tolerance of MAPS against non-ionizing radiation tolerance has been studied. The performances of different irradiated pixels in terms of charge collection efficiency (CCE), leakage current, noise and detection efficiency for minimum ionizing particles were compared with the ones of non-irradiated pixels. Systematic measurements were performed on several consecutive prototype generations to understand the origin of radiation effects and to evaluate ways to alleviate their consequences.

The dominant radiation effect was a drop of the CCE of the pixels, which was observed after IRDs of some $10^{11}$ $n_{eq}/cm^2$. In combination with a moderate increase of the pixel noise, this deteriorated signal over noise ratio (S/N) of particle signals in the detector. According to beam tests done with $\sim 120$ $GeV$ pions and $\sim 5$ $GeV$ electrons, the losses in S/N caused a crucial drop of detection efficiency for minimum ionizing particles above an IRD of $\sim 2 \times 10^{12}$ $n_{eq}/cm^2$. Moreover, Random Telegraph Signal (RTS) was observed on one heavily ($\sim 10^{13}$ $n_{eq}/cm^2$) irradiated MIMOSA-2 chip. As the amplitude of the RTS was sufficient to exceed the discrimination threshold of the pixel, it turned up to $\sim 1$ % of the pixels into hot pixels. Substantial increases of the leakage currents of the pixels were also observed. As their absolute values remained reasonably small, the shot noise generated was substantially less crucial then in the case of ionizing radiation.

In analogy to the observations made in the context of ionizing radiation hardness it was found that moderate cooling ($\sim -20$ °$C$) of the chips has a beneficial effect on several parameters. It reduces the leakage currents of the pixels as much as the corresponding shot noise. Moreover, the amplitude of RTS shrinks below the discrimination threshold and the hot pixels turn back to normal operation. As expected from the observations on detectors irradiated with ionizing doses, running the detector with small integration times can strengthen the beneficial effects of cooling.

The dominant limitation of the tolerance of MAPS against non-ionizing doses, the deterioration of the signal charge, originates from the shrinking of the lifetime of signal electrons irradiated silicon. If this lifetime falls to the order of the time required for charge collection, a substantial part of the signal charge recombines before reaching the sensing diodes. Two strategies to alleviate the consequences of this effect were studied:

Shortening the diffusion paths by increasing the density of the sensing diodes came out to provide a substantial benefit as the charge collection time is reduced. Reducing the size of the pixels from 40 $\mu m$ to 20 $\mu m$ led to an increase of their radiation tolerance of roughly one order of magnitude. The use of pixels with a pitch below the values addressed is likely to allow for further significant progresses. A shortening of the diffusion paths may also be reached by using more than one diode per pixel. This option, which is of interest if one cannot further diminish the pixel pitch, alleviates the radiation-induced deterioration in S/N with drawbacks in terms of higher pixel capacity and smaller initial S/N.

In a second study it was tried to maximize the number of initial signal charge by using a thick sensitive volume. It was observed that that the use of a thicker epitaxial layer increases the initial signal of the detector but also its vulnerability to radiation damage. The latter is presumably because the increased thickness of the detector also lengthens the diffusion paths of the signal charge. It seems likely, that the best thickness of the epitaxial layer is in the order of $10 - 20$ $\mu m$. This question is however still subject to ongoing studies.

Despite the studies performed allowed obtaining a deeper understanding of the consequences of non-ionizing radiation damage of MAPS, their radiation tolerance could be only moderately increased. This is because the dominant effect, the deterioration of the lifetime of signal electrons, is fundamental process of semiconductor physics. Moreover, the first MIMOSA-prototype featured by chance an almost optimal pixel design as its pixels were relatively small (20 $\mu m$) and each

equipped with up to four diodes, which collected their signal from an epitaxial layer of 14 $\mu m$ thickness.

Nevertheless, the limits of radiation hardness of MAPS are not yet reached. It seems likely that further fine tuning of the pixel design, (e.g. reducing the pixel pitch to 10 $\mu m$) will allow improving the radiation hardness of MAPS from nowadays value ($\sim 2 \times 10^{12}$ $n_{eq}/cm^2$) to a value of $\sim 10^{13}$ $n_{eq}/cm^2$.

In a long time perspective, dramatic progresses might be reached, if it was possible to collect the charge with an electric field instead of using thermal diffusion. This however requires modifications in the doping of the epitaxial layer. As this parameter is not accessible to the users of the CMOS-processes, modifying it seems not feasible without an active interest and contribution from industry.

A second potential breakthrough might be reached by operating the detector at cryogenic temperatures [78]. As at those temperatures the re-emission of trapped electrons is dramatically slowed down, a significant amount of traps might become filled and inactive after absorbing signal charge for a first time. For consecutive hits, the number of active traps might shrink dramatically which would restore the CCE of the detector.

The feasibility of cryogenic detector operation and applying electric fields are meanwhile under study. However, it is too early to predict if one of the approaches will provide the expected progresses. Until this is clarified, the plans for CBM have to assume a radiation tolerance of $\sim 10^{13}$ $n_{eq}/cm^2$ for MAPS, which is roughly two orders of magnitude below the initial requirements. The radiation tolerance of MAPS against non-ionizing doses is therefore likely to form a crucial bottleneck for the open charm physics at CBM within the the preliminary measurement concept of CBM. Nevertheless, this concept assumed the use of the very radiation hard but only moderately precise hybrid pixel detectors. It was therefore not yet optimized for the very precise but only moderately radiation hard MAPS. As discussed in the following chapter, a revision of the detector concept allowed for matching the requirements on the MAPS with their abilities. Physics simulations based on on this new concept demonstrated that, despite of their moderate radiation tolerance, MAPS provide an instrument to match the physics goals of CBM in terms of open charm physics.

# 7. Detection of open charm with a MAPS based vertex detector: A simulation study

In this chapter, a simulation study of the feasibility of open charm meson reconstruction with a CBM MVD based on MAPS is performed. Relying on the technological information presented in the former chapters, an updated running scenario is proposed and translated into a simulation model. The radiation doses and the selectivity of the detector is studied and a new MVD-geometry is proposed. Finally, results on the reconstruction expected performances of the CBM-experiment for open charm are presented.

## 7.1. Introduction: The simulation strategy

### 7.1.1. The proposed running scenario

Comparing the performances of MAPS detectors with the preliminary requirements of CBM presented in section 1.4, the limitations of those detectors in terms of readout speed and radiation tolerance seem incompatible with the concept of the experiment. The lifetime of the detector chips is in the order of few days for the full luminosity of the SIS300 accelerator[1]. This is sufficient for an impressive statistics, which reaches the order of $10^{12}$ collisions. Nevertheless, this number is significantly below the ambitious, initial goals.

The anticipated time resolution of MAPS will be $\sim 10~\mu s$, which is insufficient to separate individual nuclear collisions at full collision rate. A pile-up of up to $\sim 100$ nuclear collisions is therefore expected within one individual integration period of the detector. The resulting high track density is likely to overload the track finding algorithms and to generate a significant number of falsely identified tracks. Their presence might generate numerous false secondary vertex signatures, which can produce a very large background for the measurement.

This implies that, the use of the full collision rate might deteriorate the quality of open charm measurements in CBM, because the benefit of the additional statistics would be dominated by the drawbacks in terms of additional background arising from event pile-up. This holds in particular as the statistics is limited by the lifetime of the detector.

To account for this, a revised concept for open charm measurements was developed and its feasibility was investigated by detailed simulation studies. The concept allows fulfilling the open charm physics program of CBM despite of the the limits of the detector technology. Its basic assumption is that the high nominal collision rate of CBM, which is mandatory for studying J/Ψ-mesons in CBM, is not necessary for measuring open charm if a MAPS based vertex detector is used. Besides the technical constraints already mentioned, this assumption is justified because of the substantially higher production multiplicity of open charm with respect to J/Ψ and the very different strategies used for particle reconstruction.

Both, open charm and J/Ψ decay before reaching the detectors. However, energy and momentum conservation allow to reconstruct their momentum and mass from the properties of the

---

[1]Technical data on the SIS300 accelerator are given in section 1.2.

daughter particles. In the reconstructed invariant mass distribution, the particles of interest will form a peak on top of combinatorial background[2].

The significance of this peak is given by

$$Sign. = \frac{N_S}{\sqrt{N_S + N_B}} \approx \sqrt{N_{ev}} \cdot \frac{n_S}{\sqrt{n_B}} \qquad (7.1)$$

where $N_S$ stands for the total amount of correctly identified particles and $N_B$ for the amount of background pairs, which were incorrectly identified as signal. The amount of correctly and falsely identified particles per event are expressed with $n_S$ and $n_B$. $N_{ev}$ represents the number of events (nuclear collisions) available from the experiment. The approximation in equation 7.1 assumes $N_B \gg N_S$ and will be used here for simplicity[3].

Equation 7.1 shows that one can ameliorate the significance of the signal either by measuring a large number of collisions ($N_{ev}$) or by improving the selectivity ($\frac{n_S}{\sqrt{n_B}}$) of the experiment. The first option aims to obtain good significance by the statistical power of a high number of reconstructed particles. This is the only choice, if the background in the decay channel of interest cannot be efficiently reduced. The latter is the case for $J/\Psi \rightarrow l^+ + l^-$ and motivated the high beam intensities foreseen for CBM. The open charm reconstruction at CBM has to face the opposite situation. $N_{ev}$ is limited because of the constraints in terms radiation tolerance of MAPS, but the option to reconstruct the displaced secondary decay vertex of charmed mesons allows for very efficient background suppression. It is thus possible to reach an excellent $\frac{n_S}{\sqrt{n_B}}$, which reduces the required statistics $N_{ev}$.

Given the technical constraints of nowadays vertex detector technology, one cannot achieve highest $N_{ev}$ and highest $\frac{n_S}{\sqrt{n_B}}$ at the same time. It is therefore likely that a dedicated high luminosity run for $J/\Psi$ and a separate moderate luminosity but high precision measurement of open charm might provide better results for both observables than one single run, which would provide only a bad compromise between luminosity and precision. Following those considerations, it is proposed to separate the measurements of $J/\Psi$ and open charm as following:

- For the $J/\Psi$ measurements, the full collision rate of FAIR should be used. As the vertex detector provides little helpful information for this observable, it can be removed without diminishing the signal quality. The constraints from the radiation hardness of the remaining experiment is by orders of magnitude below the one of the vertex detector as for example the main tracker of CBM is more distant to the target and receives therefore substantially lower radiation doses. Moreover, dedicated radiation hard detector technologies can be used in the main tracker, as the requirements in spatial resolution and material budget are alleviated with respect to the ones of the vertex detector.

- For open charm measurements, the use of a precise vertex detector is mandatory and background suppression is of crucial importance. To assure it, the pile-up in this vertex detector must be reduced by decreasing the beam intensity until most precise tracking and secondary vertex identification is reached. The statistical power of the measurement remains unchanged as it is limited by the lifetime of the vertex detector. The outstanding selectivity ($\frac{n_S}{\sqrt{n_B}}$) will allow achieving excellent results on open charm despite of the limited detector lifetime.
  A further improvement of the results might be reached by replacing regularly the most exposed parts of the vertex detector. This appears possible because the fixed target geometry of CBM allows for an easy access. Moreover, the costs will be limited as the surfaces of the

---

[2]Combinatorial background is formed by pairs of particles, which are uncorrelated but show random correlations, which make them appearing in the invariant mass region of the expected signal.

[3]As shown later, in our case $N_B$ is smaller than $N_S$.

vertex detector stations are relatively small and MAPS can be produced in relatively cheap industrial mass production.

### 7.1.2. Questions addressed by the detector simulations

The revised concept proposed in the previous section reduces the requirements on the radiation hardness of MAPS by orders of magnitude. This is because the detector is not affected by the additional doses of the J/Ψ-runs and because of the regular replacements. Nevertheless, the vertex detector has still to stand significant radiation doses to reconstruct a reasonable amount of open charm particles. The feasibility of reconstructing open charm using a MAPS-based MVD had thus to be confirmed by simulations.

The simulations aimed to study if the radiation tolerance and time resolution of MAPS are sufficient to match the physics goals of CBM within the proposed running scenario. A focus was laid on questions of radiation tolerance and detector lifetime, as one can eliminate the pile-up caused by the limited time resolution of MAPS when reducing the beam intensity. Moreover, the early state of the simulation software of CBM did not yet allow for addressing the issue of pile-up with sufficient precision. The reconstruction of $D^0$ mesons[4] through their hadronic decay into a $(K^-, \pi^+)$-pair $(D^0 \to K^- + \pi^+)$ was used as a benchmark for the detector. Because of its short lifetime, the $D^0$ is much more difficult to detect then the other open charm mesons addressed by CBM.

The requirements on the number and purity of reconstructed particles were chosen to allow for measuring the elliptic flow of open charm. This observable is considered as the most challenging part of the corresponding physics program of CBM. It is commonly believed[5] that reconstructing $\sim 10^4$ $D^0$-mesons with good significance will allow for accessing this observable. The ability to reconstruct this number of particles within its lifetime was therefore set as preliminary requirement for an individual vertex detector.

### 7.1.3. The approach of the simulations.

The amount of $D^0$s detected by an experiment can be obtained as:

$$N_{D^0} = Mult.(D^0) \cdot b \cdot N_{Int} \cdot \epsilon_{geo} \cdot \epsilon_{reco} \tag{7.2}$$

where $Mult.(D^0)$ stands for the $D^0$ production multiplicity, $b$ for the branching ratio, $\epsilon_{geo}$ for the geometrical acceptance of the detector, $\epsilon_{reco}$ for its reconstruction efficiency and $N_{Int}$ for the integrated number of collisions of a run. Note that we assume $N_{ev} = N_{Int}$ in the following, which is equivalent to the statement that the length of each "open charm" run will be dictated by the lifetime of one individual vertex detector station. $\epsilon_{geo}$ is defined as the number of $D^0$ particles, for which both daughter particles are emitted within the geometrical acceptance of the experiment divided by the total amount of the $D^0$-mesons produced. $\epsilon_{reco}$ is given by the number of reconstructed $D^0$-mesons after applying all selection cuts divided by the number of $D^0$-mesons within the geometrical acceptance of the experiment.

In order to evaluate the total amount of $D^0$s detected within the lifetime of one vertex detector, one has first to know the corresponding number of collisions. This number is limited by the

---

[4]Note that in this work, $D^0$ and $\bar{D}^0$ are not explicitly distinguished. Normalizations are made for the summed production multiplicities of both particles.

[5]So far, this number bases on reasonable but preliminary assumptions. In particular the interplay between the required amount of reconstructed particles and the purity of the signal remains to be studied. More refined feasibility studies, in particular for the elliptic flow, will have to be performed in future.

radiation tolerance of the detectors:

$$N_{Int} = \frac{R}{d} \tag{7.3}$$

with $R$ the radiation tolerance in $n_{eq}/cm^2$ or in $kRad$ and $d$ the radiation dose per collision given in units of $n_{eq} \ cm^{-2} \ coll.^{-1}$ or $kRad \ coll.^{-1}$ respectively.

Two separated simulation studies, one addressing the radiation doses $d$ impinging the detector and one evaluating its detection efficiency ($\epsilon_{geo} \cdot \epsilon_{reco}$) are required for estimating the total amount of reconstructed $D^0$-particles within the detector lifetime. The production multiplicity and the branching ratio of $D^0 \to K^- + \pi^+$ were obtained from literature. The radiation tolerance $R$ of MAPS is discussed in the previous three chapters of this work. In this chapter it is assumed that the envisaged radiation hardness of $10^{13} \ n_{eq}/cm^2$ can be reached.

Besides estimating the performance of the CBM standard vertex detector, it was also studied, if a refinement of the geometry of the vertex detector could allow for an improved performance. This consisted in finding a good compromise between the need for a good secondary vertex resolution and a long lifetime of the vertex detector. While a good resolution demands for installing the detector close to the target, a large distance reduces the radiation doses, which limit its lifetime.

In the following, we will first introduce the CBM simulation framework. The detailed simulation procedures used for evaluating the radiation dose and the detection efficiency will be discussed separately, as they are widely independent from each other. The results of both simulations will be discussed hereafter. Combining them, it will be shown that slight modifications of the STS-layout could improve the overall performances of CBM for open-charm measurements. Finally, a first estimate on the performances in terms $S/B$-ratio, detection efficiency and number of reconstructed $D^0$-mesons will be given.

## 7.2. The simulation procedure

### 7.2.1. The simulation software

The new and innovative simulation software CbmRoot [58, 59] was used to perform the simulations of the CBM-detector. This software is based on the Virtual Monte Carlo (VMC) package [60] and allows interfacing the analysis framework ROOT [64] with detector simulation engines like GEANT-3 [61] and GEANT-4 [62].

The particular strong point of the VMC is that the different detector simulation engines are interfaced with an universal standard for input and output. The user may therefore build his particle generators, geometry definitions and analysis codes based on this standard, ignoring the particularities of the individual engines. This allows to test efficiently the different engines against each other, which is particularly helpful to identify potential weak points in those complex software packages. Moreover, the analysis codes used for simulation can be developed in the framework of ROOT, which provides an established standard for the analysis of experimental data. It is likely that the analysis codes developed for the simulation may also be used to some extend for analyzing the experimental data. Details on CbmRoot can be found in the Web [63].

The general simulation chain, which will be used in CBM-Root, is illustrated in figure 7.1. It contains the following instances:

- Event and particle generators, which provide the input of the detector simulation. Depending on the generator used, complex nuclear collisions are simulated. Complementary generators use simple models to provide particular particles, which are not for example (yet) addressed in the collision simulations.

| | |
|---|---|
| D⁰ generator Thermal model | Simulation of the D⁰ being emitted from the fireball |
| Background generator URQMD | Simulation of the "ordinary" particles being emitted from the fireball |
| Monte Carlo Code GEANT 3 / GEANT 4 | Propagation of particles through the CBM experiment. Output: MC-Points |
| Detector Models Hitproducer | Simulation of the detector electronics and its answer to an impinging particle. Output: MC-Hits |
| Realistic Track Finder, e.g. Cellular Automatom | Code to identify the hits being generated by the same particle. Only data provided by the detector Simulator (MC-Hits) is used. |
| Track fitter e.g. Kalman-Filter | Code to fit the particle trajectory (including p and charge of the particle) on base of the hits. |
| Primary & Secondary Vertex Fitter | Code to identify decay vertices on the base of intersections of fitted tracks |
| Analysis code | Applying selection rules for Particle reconstruction, produce final distributions. |

Figure 7.1.:
*The simulation chain of Cbm-Root as foreseen for the finalized simulation package.*

- Detector simulation packages (GEANT), which are to propagate the generated particles through the different sub-structures of the CBM-experiment. They simulate particle decays and interactions between the particles and matter. If the particles pass a sensitive structure (a detector of the CBM-experiment) the interaction point is recorded as a so-called Monte Carlo point (MC-point).

- Detector models, which are to simulate the response of the detector, which is hit by a particle. They loop over all MC-points and simulate the detector responses depending on the dedicated detector technology. The output of those models (MC-hits) forms an interpreted high-level representation of the electronics signal and contains the parameters of interest (hit position, time, etc.). Unlike MC-Points, MC-hits account for the features of the particular detectors including their inefficiencies.

- Track finders, which are to recognize which MC-hits are generated by the same particle trajectory. The track finding algorithms used in the simulation may also be used in the off-line data analysis of experimental data. Provided a sufficient speed, they will also serve for the real time track finding, which is required for the foreseen displaced vertex trigger.

- Track fitters, which are to fit these hits in order to reconstruct the particle trajectory. Moreover, the track fitters are needed to reconstruct the primary collision vertex and to scan the data for potential secondary vertices.

- Analysis codes, which are to reconstruct different physics observables. Those codes test hypothesizes on the recorded tracks and apply selection criteria on the data in order to reject combinatorial background.

| | |
|---|---|
| **D⁰ generator Thermal model** | Simulation of the $D^0$ being emitted from the fireball |
| **Background generator URQMD** | Simulation of the "ordinary" particles being emitted from the fireball |
| **Monte Carlo Code GEANT 3** | Propagation of particles through the CBM detector. Output: MC-Points |
| **Detector Models Gaussian Smearing** | Simulation of the detector electronics only by gaussian smearing of the hit position |
| **Ideal track finding for p> 1 GeV/c** | Identification is done using data provided by the Monte Carlo Code. Fast, not possible in the experiment. Tracks p < 1 GeV /c are rejected |
| **Track fitter e.g. Kalman-Filter** | Code to fit the particle trajectory (including p and charge of the particle) on base of the hits. |
| **Primary & Secondary Vertex Fitter** | Code to identify decay vertices on the base of intersections of fitted tracks |
| **Analysis code** | Applying selection rules for particle identification, produce final distributions. |

Figure 7.2.:
*The simulation chain of Cbm-Root as used for this work. The preliminary elements of this chain are emphased.*

The simulations done in this work were performed with an early version of CbmRoot, which provided only a part of the features mentioned above. Parts of the software were still missing, others were not yet optimized for performance which limited the statistics accessible in the simulation. To account for this, a simplified simulation chain was used (see figure 7.2). It was based on simplified but reasonable detector models. For the MAPS detectors, a dedicated digitizer was provided within this work but only few of its features could be used as the implementation of the corresponding interface in the tracking software was still ongoing.

The tracking software (track finder and track fitter) was already fully available. Nevertheless, the track finder was still too slow for a practical use. It had to be replaced by a fast ideal track finder, which used information provided by the simulation engine for track reconstruction. The realistic track and secondary vertex fitter was fortunately not affected and could be used, while the position of the primary vertex was determined based on MC-data. An early version of the analysis software for $D^0$-reconstruction was available but had to be optimized to improve its execution time.

The radiation dose simulation was not affected by the limits of the early CbmRoot, as it relies exclusively on the particle generators and the GEANT-3 simulation packages. These parts of CbmRoot were already stable and only few modifications were required for performing the simulation. Nevertheless, a dedicated model weighting the energy deposit of particles impinging the detectors had to be developed. Moreover, CbmRoot had to be modified to display also neutral particles like neutrons.

### 7.2.2. The simulation model of the STS

The geometries of the STS, which were simulated in this work, are based on the CBM standard geometry as introduced in chapter 1.3.2. This standard geometry will be referred as *Geo1* in the following. It represents the STS with seven silicon disks of a thickness of 200 $\mu m$ having no substructure. A hole in the center of the disks allows for the passage of the beam. This beam hole limits the inner acceptance of the CBM STS to a polar angle of $\sim 3$ ° with respect to the beam axis. The outer acceptance corresponds to a angle of $\sim 25°$.

Different modifications of the vertex detector stations (stations 1-3 of the STS) were investigated. This was to estimate the effect of material budget and spatial resolution of the detector stations on the selectivity of CBM for open charm. Spatial resolutions of $3 \mu m \times 3 \mu m$ and $6 \mu m \times 6 \mu m$ were chosen to simulate optimistic and pessimistic MAPS performances, respectively. Moreover, "hybrid pixel detectors" with resolutions of $30 \mu m \times 30 \mu m$ (CMS pixels) and of $12 \mu m \times 60 \mu m$ (ATLAS pixels) were simulated in a qualitative way. The rectangular ATLAS pixels were simulated twice, with their long side oriented parallel to the x – and the y – axes repectively. The spatial resolution of the silicon strip detector stations was assumed to be $10 \mu m \times 10 \mu m$. The resolution of the detectors was simulated by Gaussian smearing of the hit position.

Some modifications aimed at an improved compromise between the selectivity and the radiation doses impinging the vertex detector. As discussed later on in this chapter, the radiation doses are particularly high close to the beam axis and in the target area. Consequently it was tried to move the detectors away from these regions without substantially deteriorating the secondary vertex resolution of the system. Both, the inner radius of the detector stations and the distance between target and first station were systematically varied in order to find the best combination. In most cases, the inner acceptance angle of the first station was chosen bigger than the value of $\sim 3°$ representing the acceptance of the full CBM experiment[6]. This modification was done to avoid the strong radiation fields close to the beam axis. It does not affect the inner acceptance angle of the full vertex detector, as the missing segment remains covered by the stations located more downstream. Nevertheless, because of the higher lever arm for multiple scattering, a reduced secondary vertex resolution is expected for the subset of tracks, which misses the first station.

The different detector configurations investigated in this work are listed in table 7.1. Their design was motivated by the following considerations:

- Like for the standard geometry (Geo1), the first station of the geometries Geo2, Geo3, and Geo6 is located at $z = 5 \ cm$ from the target. Different diameters of the beam hole, which potentially reduce the radiation dose impinging the first station, were investigated.

- In the geometries Geo4, Geo5 and Geo10, the distance between the first station and the target was systematically varied. This was to study whether moving away the detector from the target might be beneficial.

- Geo11 and Geo12 were used to study whether moving the first station to $z = 10 \ cm$ combined with increasing its beam hole could have a beneficial effect.

### 7.2.3. Representation of the global CBM experiment in the simulation

In the present simulations, only the STS was used for the reconstruction of open charm. The detectors other than the STS were represented as passive material only. This latter was of importance for the radiation dose simulations as neutrons being backscattered from massive

---

[6]This is also a feature of the first station of the standard geometry.

| Name | Geo1 | Geo2 | Geo3 | Geo4 | Geo5 | Geo6 | Geo10 | Geo11 | Geo12 |
|---|---|---|---|---|---|---|---|---|---|
| **Station 1** | | | | | | | | | |
| Position [mm] | 50 | 50 | 50 | 25 | 75 | 50 | 100 | 100 | 100 |
| $R_{Inner}$ [mm] | 5.5 | 10 | 10 | 5.5 | 5.5 | 10 | 5.5 | 11 | 20 |
| $R_{Outer}$ [mm] | 25 | 25 | 25 | 25 | 37.5 | 25 | 50 | 50 | 50 |
| **Station 2** | | | | | | | | | |
| Position [mm] | 100 | 100 | 100 | 50 | 100 | 100 | 150 | 150 | 150 |
| $R_{Inner}$ [mm] | 5.5 | 5.5 | 10 | 5.5 | 5.5 | 8 | 7.5 | 11 | 20 |
| $R_{Outer}$ [mm] | 50 | 50 | 50 | 50 | 50 | 50 | 75 | 75 | 75 |
| **Station 3** | | | | | | | | | |
| **Position [mm]** | 200 | 200 | 200 | 200 | 200 | 200 | 200 | 200 | 200 |
| $R_{Inner}$ [mm] | 10.5 | 10.5 | 10.5 | 10.5 | 10.5 | 10.5 | 10.5 | 11 | 20 |
| $R_{Outer}$ [mm] | 100 | 100 | 100 | 100 | 100 | 100 | 100 | 100 | 100 |
| **Resolution** | | | | | | | | | |
| $3\ \mu m \times 3\ \mu m$ | X | X | X | X | X | X | X | X | X |
| $6\ \mu m \times 6\ \mu m$ | X | X | X | X | X | X | X | X | X |
| $30\ \mu m \times 30\ \mu m$ | X | X | X | X | X | X | X | X | X |
| $12\ \mu m \times 60\ \mu m$ | X | - | - | - | - | - | - | - | - |
| $60\ \mu m \times 12\ \mu m$ | X | - | - | - | - | - | - | - | - |
| **Thickness** | | | | | | | | | |
| $100\ \mu m$ | X | X | X | X | X | X | X | X | X |
| $200\ \mu m$ | X | X | X | X | X | X | X | X | X |
| $300\ \mu m$ | X | X | X | X | X | X | X | X | X |
| $1000\ \mu m$ | X | - | - | - | - | - | - | - | - |

Table 7.1.: List of the vertex detector geometries used in the simulation. All combinations of the geometry of the vertex detector and the spatial resolution and thickness of the individual vertex detector stations marked with an <X> were simulated.

structures have the potential to form a significant contribution. An exception is formed by the the forward calorimeter of CBM. As this detector was not part of the initial design proposal of the experiment, its mechanical structure was not included in this simulation. This is however not expected to have a substantial impact on the results.

However, details on some components are worth mentioning as they have, via multiple scattering and secondary particle generation, an impact on the simulation results:

The *target* was represented by a disk of gold having a thickness of 250 $\mu m$. This thickness is chosen to allow for a 1 % interaction rate between the target and an impinging 25 $AGeV$ gold ion. The flight of the primary particles was started at the origin of the coordinate system, which corresponds to the center of the target.

The *beam pipe* of CBM is represented by a mechanical structure of 0.5 $mm$ of carbon. In the area of the vertex detector, it has an extension which allows for installing the first three detector stations in vacuum. This solution was put to allow the primary beam to propagate in vacuum without introducing unwanted matter between the target and the first three detector stations.

*The magnet* is represented by its mechanical structure and its field. The mechanical structure corresponds to the standard super-conducting dipole magnet of CBM[7]. The field of the magnet is simulated independently from the mechanical structure in CbmRoot. Two magnetic fields representing a standard super-conducting dipole magnet and a magnet with inclined pole shoes (alligator magnet) were initially examined. The field of the alligator magnet was used in most simulations. As it shows a higher strength in the area of the vertex detector, it was considered as more efficient in deflecting $\delta$ - electrons generated by the beam in the target[8].

The cave and in particular the beam dump form another potentially important source of neutrons. They were not simulated, as no quantitative information for them was available.

## 7.3. The simulation of the expected radiation doses in the CBM MVD

### 7.3.1. Radiation sources and their simulation model

As already discussed in detail in chapter 4.1, the interaction between radiation and silicon detectors can be classified in two independent processes. The first one named *ionizing* is caused by electromagnetic interactions between the radiation and the electron cloud of the semiconductor. Through this interaction, charged particles and photons destroy irreversibly atomic bindings at the interfaces between silicon and $SiO_2$ structures in MAPS detectors.

In a second reaction chain, impinging particles displace an atom core from its place in the crystal lattice, which causes a lattice defect in the silicon of the sensing element. Assuming a sufficient energy deposit, this core may collide with other atoms and generate defect cluster. This process is named *non-ionizing* and can be caused by both, the electromagnetic and the strong force. On the other hand, for reasons of momentum conservation, a minimum particle mass is required for this process. This hampers in particular photons from generating non-ionizing damage. Nevertheless, $\gamma$-Rays may contribute with poor probability via the generation of fast secondary electrons.

Charged hadrons and fast electrons constitute the main radiation sources expected in CBM. Being charged and sufficiently massive, they contribute to both, the ionizing and the non-ionizing radiation doses. However, their contribution to non-ionizing radiation is of particular concern.

---

[7]Details on the magnets are described in the appendix of [65].

[8]Note that this choice led to an inconsistency between the mechanical representation and the field of the magnet. This is not expected to have a relevant impact on the results.

*7. Detection of open charm with a MAPS based vertex detector: A simulation study*

A radiation tolerance of MAPS against $\sim 1\ MRad$ ionizing dose and $\sim 2 \times 10^{12}\ n_{eq}/cm^2$ non-ionizing dose has been demonstrated within this work (see chapters 5 and 6). A back of envelop calculation using simplified assumptions shows that this allows tolerating the non-ionizing radiation damage of few $10^{12}$ charged hadrons[9] per $cm^2$. The resistance against ionizing damage is higher and sufficient to tolerate the ionizing dose of $\sim 3.5 \times 10^{13}$ charged hadrons per $cm^2$. The non-ionizing doses were thus considered as being of particular importance for this work and special care was undertaken to simulate precisely this type of radiation. As ionizing doses seem not to form the limiting factor for the lifetime of the detector, a simpler approach could be used to evaluate them.

The radiation dose impinging the vertex detector is presumably formed by three major contributions. The primary particles, which are generated by the nuclear collisions in the target, provides the most important among them. As the primary particles are mostly hadrons, they cause mainly non-ionizing radiation damage.

Moreover, previous simulations [67] showed that an important amount of $\delta$ - electrons is produced when the primary beam passes through the target. The field of the dipole magnet of CBM deflects a part of them before they can reach the vertex detector. Nevertheless, the remaining electrons are sufficiently numerous to be of concern. Electrons generate ionizing radiation damage comparable to a charged hadron. The non-ionizing radiation damage is typically at least an order of magnitude below the value caused by an $1\ MeV$ neutron. The electrons were expected to contribute substantially to the ionizing doses. Their contribution to non-ionizing doses was to be clarified.

A third potential source of radiation is formed by a neutron gas potentially diffusing in the detector volume. Such gas can be formed by neutrons, which are knocked out of nuclear cores by fast particles impinging detector materials. The neutrons in this gas may be slowed down to very low energies before being absorbed. They cause only non-ionizing damage.

Within this work, detailed simulation models for the radiation caused by primary particles and $\delta$ - electrons were developed and used. To simulate the neutron gas the GEANT-3 (used in the CbmRoot simulation framework) was complemented with the GCALOR [66] package[10]. This simulator offers a substantially refined interaction model for slow hadrons, which includes low energy reactions of hadrons and elastic back-scattering of neutrons. This allows simulating particles with a kinetic energy below the GEANT-standard, which is $1\ MeV$. It is thus able to simulate a neutron gas. In order to account for such a gas, the cut-off energy for hadrons was reduced to $50\ keV$, the energy cut-off for electrons was set to $250\ keV$. This corresponds to the minimum energy of electrons required to generate non-ionizing radiation damage.

### 7.3.2. Particle generation for the radiation dose simulations

### 7.3.3. Event and particle generators

The input for the radiation dose simulations was provided by two different particle generators. The particles emitted from the nuclear collisions were provided by the Ultra-relativistic Quantum Molecular Dynamics (UrQMD) [69, 70] model. The latter is a microscopic transport model, which performs a simulation of nuclear collisions. Its output provides the identity, position and momentum of the particles produced in the collision, which is used as input for GEANT. Nuclear

---

[9]Note that fast hadrons generate a slightly lower damage than a $1\ MeV$ neutron.

[10]The usual simulation engine for radiation dose simulations (FLUKA) became available in CbmRoot only after finalizing this study. Preliminary comparisons [68] suggest that the results of both simulation engines are comparable in the particular case of the CBM STS.

collisions with an incident energy of 15 $AGeV$, 25 $AGeV$ and 35 $AGeV$ were used for the radiation dose simulation.

The UrQMD model cannot be used to evaluate the second important source of radiation damage, which is formed by the $\delta$ - electrons being knocked out by the beam from the target. The electrons were thus generated by another particle generator, which is based on a simulation of the underlying physics process with GEANT-3. Gold ions with an energy of 25 $GeV$ were injected into the GEANT-simulation by means of a dedicated ion generator. They were propagated by GEANT through the target. The simulation of the interaction between ion and target produced the $\delta$ - electrons. Note that assuming a 1 % target, one has to combine the $\delta$ - electrons from 100 ions with the hadrons from one UrQMD event. This is because most ions generating $\delta$ - electrons penetrate the target without nuclear collision.

For practical reasons, the radiation generated by primary particles and $\delta$ - electrons were simulated independently from each other. The particles from 5000 collisions represented the particles emitted from the collision. A total of $10^4$ gold ions were injected to the target to generate the $\delta$ - electrons. After their generation and normalization, the radiation maps describing the contribution of primary particles and $\delta$ - electrons were individually generated and added.

### 7.3.3.1. Simulating non-ionizing radiation doses

The particles generated were propagated through the CBM detector using GEANT-3 (+ GCalor). The outcome of the particle transport was the coordinate, at which the particle impinged the detector material. Moreover, the type of the particle and its kinetic energy were delivered. As discussed in chapter 4.1, this information is sufficient to estimate the non-ionizing radiation damage caused by these particles within the NIEL model. To do so, one has to rate the particle with help of the so-called NIEL factor, which normalizes the radiation damage with respect to the one caused by a 1 $MeV$ neutron. Conversion tables [46] for electrons, pions, protons and neutrons were used. Where possible, the values of the tables were fitted and the NIEL factors were obtained from the fit functions.

The fits could be done with good accuracy of few percent with the data set for electrons and protons. For pions, an uncertainty of 10% had to be accepted as resonances in the NIEL factors complicated the fitting procedure. For neutrons, no fit was possible for kinetic energies below 50 $MeV$. A constant factor was thus assumed. This approximation is reasonable since the neutron yield in this energy region is negligible.

All functions generated with the fits are valid for a limited energy-range only. Different assumptions were used in order to handle particles with energies outside of this range:

- *Electrons:* The data on NIEL-factors available range from 300 $keV$ to 200 $MeV$. The fit function obtained in this energy range was extrapolated to the threshold for displacement damage, which is $\sim 260\ keV$. Electrons with a kinetic energy below this value were considered as harmless in terms of non-ionizing dose. For energies above 200 $MeV$, the NIEL factors of electrons go into saturation. Electrons with energy of more than 200 $MeV$ were thus handled as having this energy.

- *Pions:* The data on NIEL-factors available range from 15 $MeV$ to 9 $GeV$. Because of the presence of resonances, the fit is only valid down to 25 $MeV$. The NIEL-factor of particles below this value was set to 0.5 $n_{eq}$. For particles with a higher energy, the function found was extrapolated. This is backed by the low variation of the NIEL factors at high energies.

- *Protons:* The data on NIEL-factors available range from 1 $keV$ to 10 $GeV$ and could be fitted in this energy range. As no hadrons below 50 $keV$ were simulated, this was sufficient for the low energy protons. The resulting fitting function was extrapolated for higher energies.

- *Neutrons:* Even if data for the NIEL factors of neutrons are available down to very low energies, a fit on this data could only be done from 50 $MeV$ to 10 $GeV$. Neutrons below 50 $MeV$ were counted with 1 $n_{eq}$. Extrapolation was used for particles over 10 $GeV$.

The particles mentioned above form the dominant contribution to the non-ionising radiation dose. Nevertheless, other particles, for which no conversion models were available, are present in the environment of the CBM experiment. These particles were handled like following:

- *γ-rays* were ignored as their contribution to non-ionizing radiation damage is negligible.
- *Heavy Ions* and *Nuclear Fragments* were ignored because of their very low number.
- *Muons* were considered to be high-energy electrons, because like electrons they interact through the electromagnetic and the weak force only.
- *Other hadrons*, namely kaons were counted with 1 $n_{eq}$.

### 7.3.3.2. Simulating ionizing radiation doses

As the lifetime of the CBM vertex detector is likely to be limited by the contribution of non-ionizing radiation, the latter had to be evaluated as precisely as possible. From back of envelop calculations it was clear, that the ionizing doses would have lower impact on the detector operation; slightly higher uncertainties arising from a simplified simulation model could thus be accepted.

All hits caused by charged particles were considered to deposit an ionizing energy comparable to a minimum ionizing particle. This energy leads to an ionizing dose of $2.86 \times 10^{-11}$ $kRad$ for one hit per $cm^2$ [71]. Like for the simulation of non-ionizing doses, radiation damage from photons and nuclear fragments was neglected.

### 7.3.3.3. The $\delta$ - electron absorber

The field of the dipole magnet has double effect on the $\delta$ - electrons. As a beneficial effect, it deflects a significant part of the electrons away from the detector stations. On the other hand, some $\delta$ - electrons spiral in the magnetic field and thus hit the station more than once. In order to overcome this problem, it was proposed [67] to install an absorber material outside of the acceptance of the STS. This was intended to absorb spiraling electrons and thus to reduce the radiation doses.

To study this approach, a modified beam pipe [72] was introduced in the simulations and its consequences on radiation doses were investigated. This pipe is modified with respect to the standard one by adding 1 $mm$ of lead at the side of the vacuum vessel. Located outside the acceptance of the detector, this material serves as an absorber.

The effect of this absorber is illustrated in figure 7.3. In the left panel, the situation without absorber is shown. One observes $\delta$ - electrons (blue) spiraling in the STS. In the right panel, absorber material (not shown) is installed at the right side of the beam pipe. The $\delta$ - electrons get strongly decelerated in the detector material. The detector stations are rarely hit more than once by one electron.

### 7.3.4. Results

### 7.3.4.1. Radiation dose simulations for the standard MVD geometry

**Assumptions of this study** The aim of this first step of the radiation dose simulations was to evaluate the radiation doses expected for the standard geometry (Geo1). The radiation doses
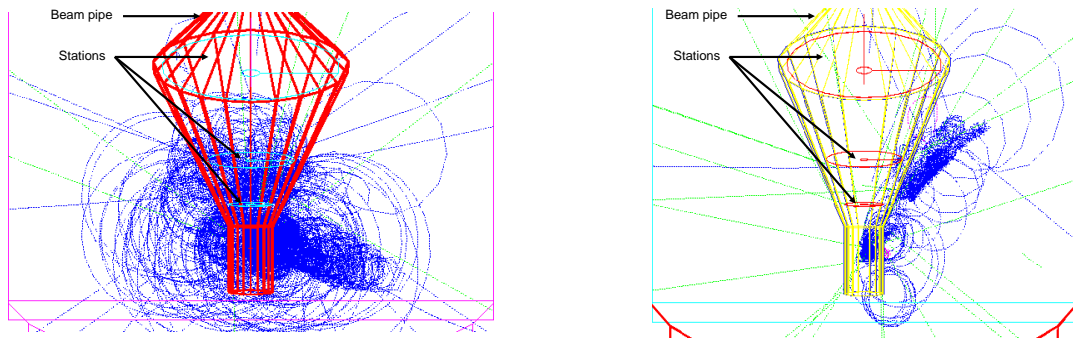
Figure 7.3.: *Effect of an absorber placed aside the beam pipe. The situation without (left) and with (right) absorber is shown. The pictures are taken from [67].*

corresponding to one year of operation of CBM with Au-Au collisions were chosen as baseline for this study.

The radiation dose is proportional to the number of nuclear collisions ($N_{Int}$). This number is given by integrating the collision rate over the time. In order to estimate this value, it is assumed that the operation time (beam on target) of CBM will be $\sim 5 \times 10^6 \ s$ ($\sim 2$ months) per year. Within this time, the full nominal beam intensity of the SIS 300 accelerator is used (i.e. $10^9$ heavy ions per second). Combined with a target with a thickness corresponding to 1 % interaction, one derives a collision rate of $10^7$ collisions per second. This leads to $5 \times 10^{13}$ collisions per year.

It should be mentioned that in this first, exploratory, round of simulations, the radiation dose was evaluated with GEANT-3 alone. The minimum kinetic energy for hadrons in this simulation was thus 1 $MeV$. The contribution of the $\delta$ - electrons and the primary particles were simulated separately. In order to ease the comparison with former studies on particle multiplicity, the first simulations of the radiation dose of primary particles based on the dipole field. For the same reason, the magnetic field of the alligator magnet was used to simulate the $\delta$ - electrons. To avoid potential inconsistencies, the summed radiation doses were addressed with a second round of simulations, where the alligator magnet was used for both kinds of particles. The corresponding results will be discussed more below after introducing the properties of the individual contributions.

**Radiation from particles produced in nuclear collisions in the target (primary particles)** The radiation dose deposited by the primary particles was mapped into $50 \times 50$ bins for each detector station. Consequently, the bin surface depends on the diameter of the station. For example in the case of the first station (diameter of 50 $mm$), the surface of a bin is 1 $mm \times 1 \ mm$.

The results on the radiation tolerance simulation are plotted in figure 7.4. In spite of the presence of a magnetic field, which bends the trajectories of charged particles in the $x$-direction, one finds that the radiation dose is radially symmetric with a maximum close to the beam axis. The same qualitative behavior was also observed for the other STS stations as illustrated in figure 7.5 for the forth (left) and the seventh (right) station.

The radiation dose caused by primary particles was simulated for all seven stations for beam energies of 15 $AGeV$, 25 $AGeV$ and 35 $AGeV$. The results of this study are illustrated in figure 7.6. The radiation doses shown in this figure represent the dose on the most irradiated bin of
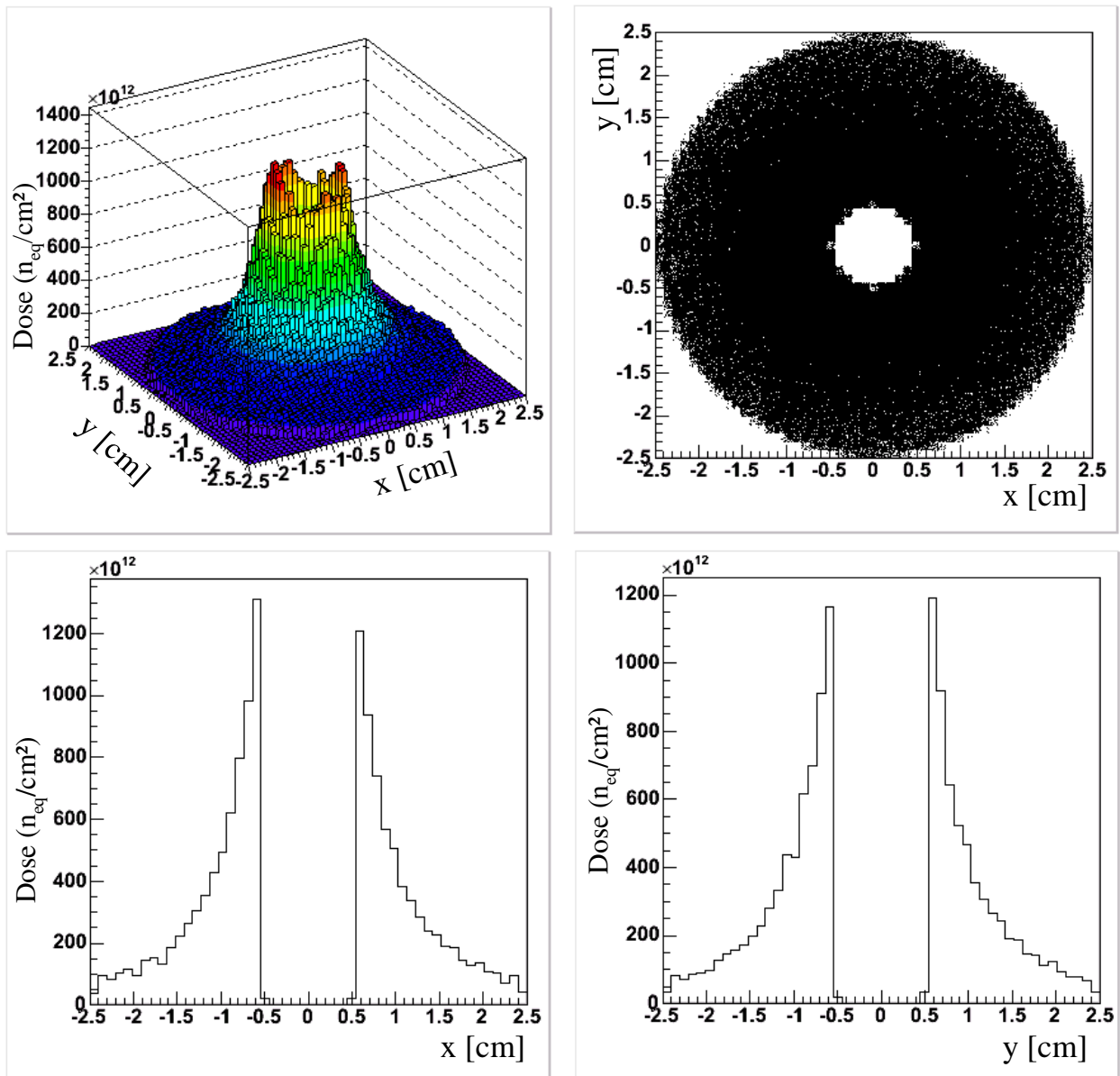
Figure 7.4.: Top left: *Map of the non-ionizing radiation dose without $\delta$ - electrons for the STS station 1 of the standard MVD geometry after one year at nominal beam intensity. The beam axis intercepts the detector plane at $x = y = 0$ cm.*
Top right: *Top view of the radiation dose map. The beam hole can be seen.*
Bottom left: *Cross section of the radiation dose map at $y = 0$ cm.*
Bottom right: *Cross section of the radiation dose map at $x = 0$ cm.*
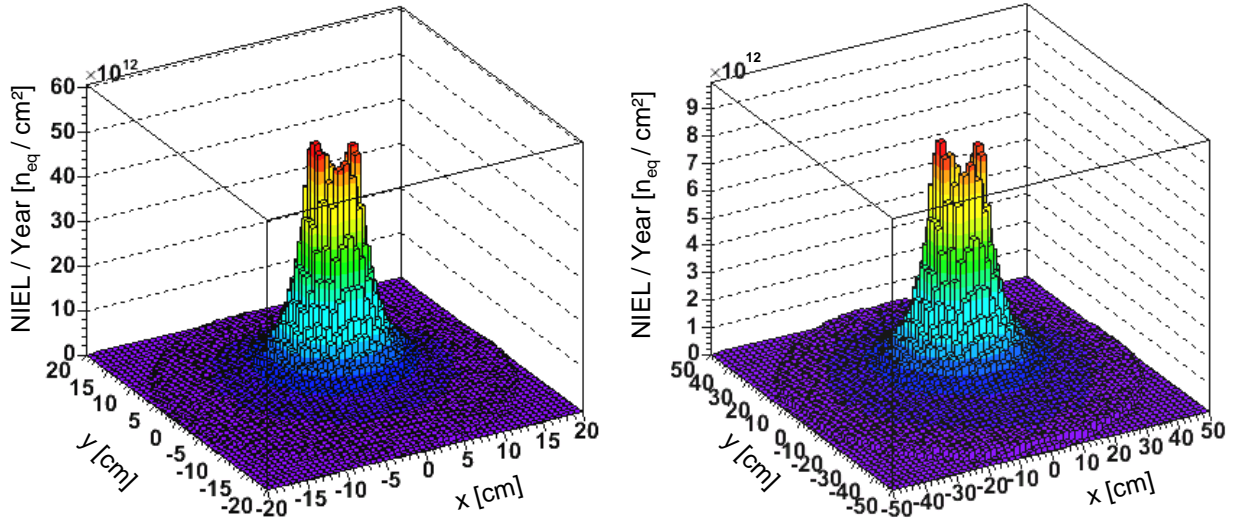
Figure 7.5.: *Distribution of the non-ionizing radiation dose on the STS stations 4 (left) and 7 (right) of the standard MVD geometry. Note the different scales.*

the radiation map, which has a size of 1 $mm^2$ for the first station. This means that most of the surface of a detector is irradiated with substantially lower doses. Note that the contributions of $\delta$ - electrons and neutron gas are not taken into account in figure 7.6.
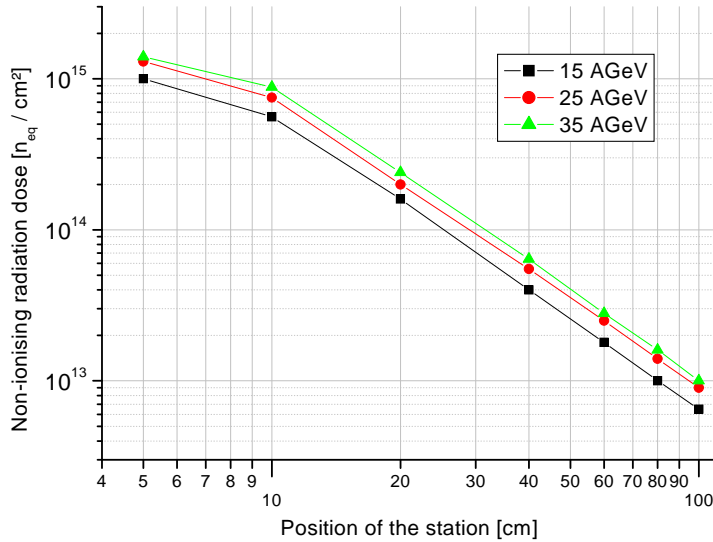


Figure 7.6.:
*Non-ionizing radiation dose in the most irradiated part of the detector stations per year ($5 \times 10^{13}$ nuclear collisions) for the standard STS geometry (Geo1). The dose caused by the primary particles (UrQMD) is shown , $\delta$ - electrons and neutron gas are not taken into account.*

As expected from back of envelop calculations, the maximal non-ionizing radiation dose caused by primary particles is found to be in the order of $10^{15}$ $n_{eq}/cm^2$ for the first station. It decreases roughly according to $1/z^2$, where $z$ stands for the distance between the target and the station. The first station constitutes an exception to this rule because of its larger inner acceptance angle.

The dependence of the radiation dose on the beam energy is found to be modest. Going from 15 $AGeV$ to 35 $AGeV$ the radiation doses increases by $\sim 50\%$. This is due to the higher particle multiplicities.

The contribution of daughter particles of the primary particles, as shown by GEANT-3, was found to constitute $\sim 10\%$ of the radiation damage. Note that this accounts only for secondary

particles with an energy above the cut-off energy ($> 1\ MeV$).

Besides the absolute number of radiation doses, the composition of the particles impinging the first silicon strip station (station 4) was studied. This was motivated by the fact that one can harden silicon strip detectors against radiation by using special oxygen enriched silicon (see section 4.1.3). This is effective against damage from pion and proton irradiation, while the radiation tolerance against neutrons seems not to change. Knowledge on the composition of the radiation field is thus helpful to judge, if this radiation hardening technique could allow improving the lifetime of the strip detectors of CBM. The radiation dose impinging this station came out to be clearly dominated by pions (54%). Neutrons form the next lot with a relative radiation damage of 16%, protons follow with 15%. The relative weight of the radiation damage was found not to vary substantially as a function of the radius. As the contribution of neutrons to the total non-ionizing dose is small, the use of oxygen-enriched material in the CBM strip detectors might be beneficial.

**Radiation doses due to $\delta$ - electrons**   The simulation of the radiation dose due to $\delta$ - electrons is shown in figure 7.7 (left) for the first MVD-station, which is most affected by this type of radiation.
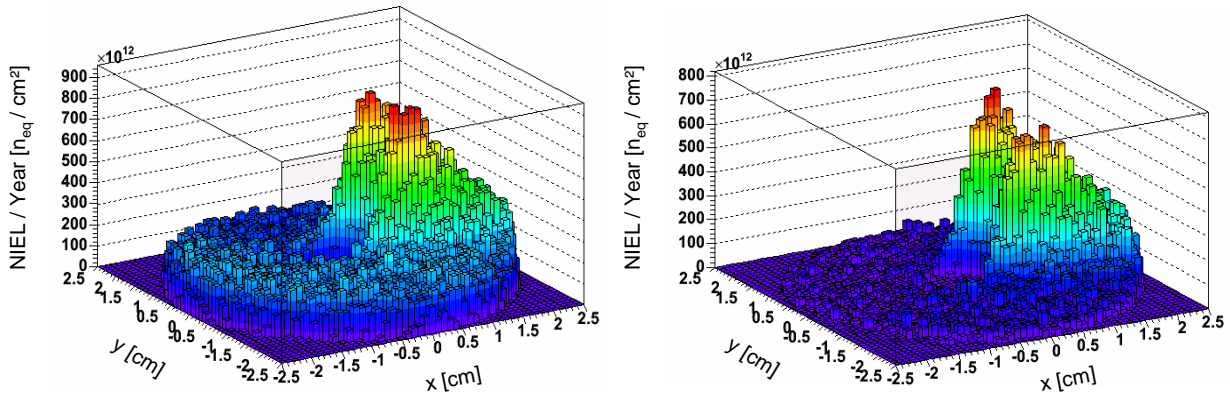


Figure 7.7.: *The radiation dose caused by $\delta$ - electrons in the first MVD-station. In the left panel, the standard geometry of the beam pipe was used. In the right panel absorber was added.*

One observes a concentration of the radiation right of the beam hole, which is probably due to the particular magnetic field. The radiation dose in those hot spots was found to be in the order of $0.85 \times 10^{15} \ n_{eq}/cm^2$. Figure 7.7 (right) shows the radiation damage when adding the absorber for spiraling electrons (see section 7.3.3.3). One observes that the radiation doses in the most irradiated areas are only slightly reduced. On the other hand, the radiation doses (and hit multiplicities) in the region outside the hot spots shrink by roughly a factor of two. This suggests that using an absorber substantially reduces the occupancy of the detectors in this area, which might be very beneficial for track finding.

**Summary** The results of the simulation show that the contribution of the $\delta$ - electrons is not negligible. This is particularly true in the absence of the additional material at the side of the the beam pipe, which is to absorb spiraling $\delta$ - electrons. The effect of this absorber has been studied and found weaker than expected. It has little influence on the maximum radiation doses, probably because the hot spots are dominantly generated by direct radiation. Nevertheless, its presence reduces substantially the occupancy of the stations outside the most irradiated area, which is likely to ease tracking.

The radiation from primary particles was found to concentrate close to the beam axis. As expected, it decreases with distance between first station and target according to $1/z^2$. Increasing this distance offers thus an efficient mean to reduce the radiation dose impinging the detector. Using a bigger beam hole has also a beneficial effect. As we will see later on, this holds in particular for radiation dose originating from primary particles while the effect on the contribution of $\delta$ - electrons is relatively weak.

Summing the contributions of primary particles and $\delta$ - electrons was not possible as they were simulated separately with different magnetic fields. In the following section it will be shown, that the combined radiation dose for the most irradiated area of the first station of the standard vertex detector geometry[11] is 30.2 $n_{eq}/cm^2$. This is equivalent to an annual dose of $1.5 \times 10^{15} \ n_{eq}/cm^2$ at the nominal intensity of SIS300.

### 7.3.4.2. Radiation doses as a function of the vertex detector geometry

The results presented so far were obtained for the standard vertex detector geometry. In this section, we will investigate different other MVD geometries with the aim to obtain a good compromise between radiation doses and detection efficiency. The strategy followed in those simulations was to vary the distance between the target and the detector stations as well as the diameter of the beam hole. The different geometries investigated are listed in table 7.1. Note that only the radiation dose aspects will be discussed here. The impact of the modifications in the detector geometry on the overall performances of the vertex detector will be addressed more below (see section 7.4).

With respect to the simulations discussed in the previous section, slight modifications in the simulation model were undertaken. The same magnetic field (alligator) was used now for simulating all contributions of the radiation dose. Moreover, the simulation was done with the GCalor – engine, which allowed to simulate hadrons down to a kinetic energy of 50 $keV$.

The results in this section are expressed in terms of radiation dose per nuclear collision to ease scaling them to different assumptions on the beam intensity. They will be shown for the most exposed MVD - stations. Note that in some cases (Geo2), the primary particles generated higher

---

[11]Assuming the magnetic field of the alligator magnet.

doses in the second station than the first one. However, because of the contribution of $\delta$-electrons, the highest dose was finally observed on the first station in all geometries.

The radiation map of a combined effect of primary particles and $\delta$ - electrons is shown in figure 7.8 for non-ionizing radiation doses. The left plot shows the radiation doses for a station located at 5 $cm$ featuring a beam-hole with an increased[12] inner radius of $r_1 = 1$ $cm$. As illustrated in the figure, this modification reduced the radiation dose from primary particles by roughly a factor of three. Nevertheless, the effect on the combined radiation dose was only modest, as the contribution of the $\delta$ - electrons was not substantially reduced. The combined dose thus decreased only moderately (23 $n_{eq}/cm^2/coll.$ instead of 30 $n_{eq}/cm^2/coll.$ for the standard geometry).
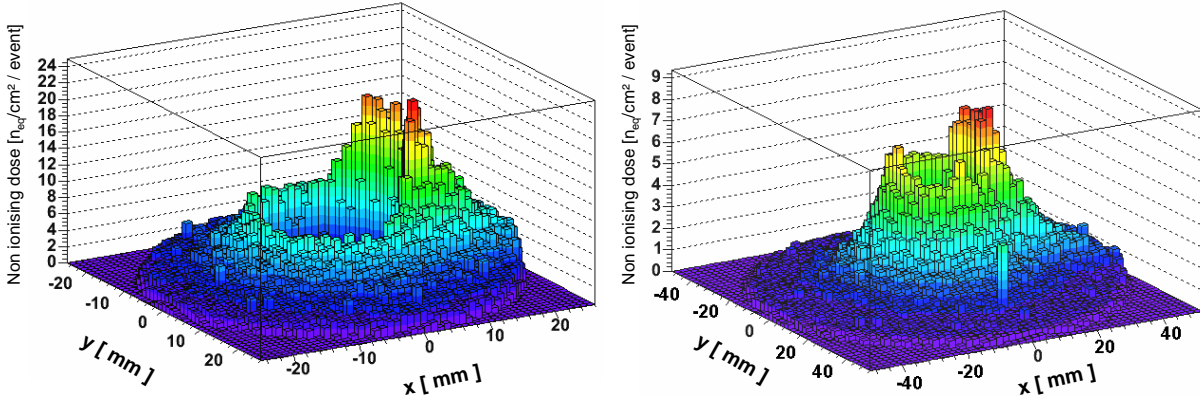


Figure 7.8.:
Left: *Total non-ionizing radiation dose for a MVD - station located at $z = 5$ $cm$ with an inner radius of $r_1 = 1$ $cm$.*
Right: *Total non-ionizing radiation dose for a MVD - station located at $z = 10$ $cm$ with an inner radius of $r_1 = 1.1$ $cm$. Note the different scales.*



Figure 7.9.:
Left: *Total ionizing radiation dose for a MVD - station located at $z = 5$ $cm$ with an inner radius of $r_1 = 1$ $cm$.*
Right: *Total ionizing radiation dose for a MVD - station located at $z = 10$ $cm$ with an inner radius of $r_1 = 1.1$ $cm$. Note the different scales.*
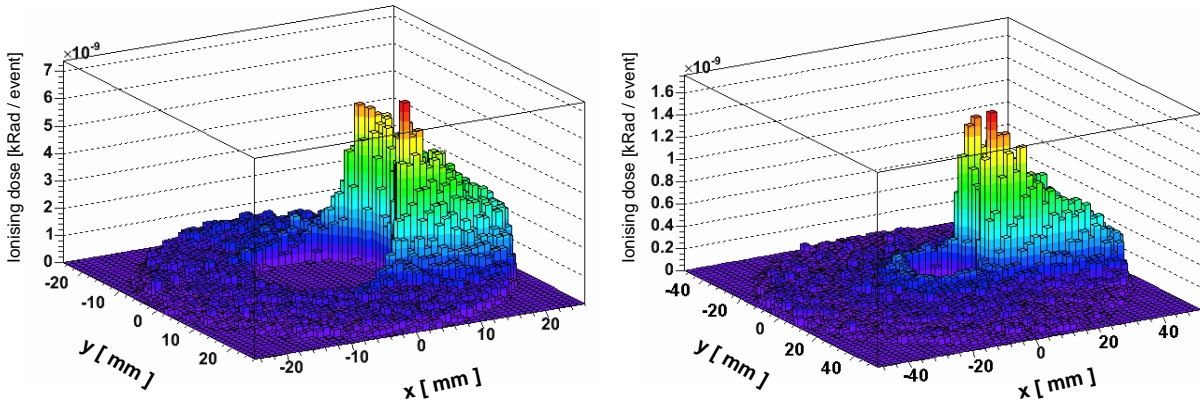
To simultaneously reduce the contribution of primary particles the one of the $\delta$ - electrons, one

---

[12]In the standard geometry of the MVD, the radius is set to $r_1 = 5.5$ $mm$.

may place the first station at $z = 10 \ cm$. This eases the magnetic deflection of the electrons from the first station. Geo 11 combines both, an increased diameter of the beam hole of the first station to $r_1 = 1.1 \ cm$, and a shift of this station to $z = 10 \ cm$. The radiation map for this geometry is shown in figure 7.8 (right). One observes that combining both modifications leads to a significant progress in reducing the radiation doses, which shrink from 30 $n_{eq}/cm^2/coll.$ to 8.5 $n_{eq}/cm^2/coll.$ for this geometry.

The ionizing radiation doses impinging a station located at $z = 5 \ cm$ and $z = 10 \ cm$ are shown in figure 7.9 (left) and (right) respectively. Unlike to the non-ionizing doses, where the contribution of $\delta$ - electrons is reduced by their low NIEL-factor, the ionizing doses are clearly dominated by the electrons.

The radiation doses simulated for the different stations are listed in table 7.2 for the non-ionizing doses and in table 7.3 for the ionizing doses. The contributions of primary particles and $\delta$ - electrons are shown separately. Note that one cannot add the maximal radiation doses given for the individual contributions to obtain the summed radiation dose. This is because the maxima of the two radiation fields are not located at the same position. The maximum combined dose is thus usually smaller than the sum of the maxima of the individual contributions.

The lifetime of the detector is given in table 7.2 in units of nuclear collisions. This lifetime is obtained by dividing the radiation tolerance of the detectors ($10^{13} \ n_{eq}/cm^2$ was assumed) by the non-ionizing radiation doses. Moreover, the ionizing dose expected during the lifetime of the detector is shown in table 7.3. It varies depending on the relative contribution of the $\delta$ - electrons to the non-ionizing radiation dose.

## 7.3.5. Summary and conclusion on the radiation dose simulations

The radiation dose impinging the CBM-MVD was simulated using GEANT3 and GCalor. Contributions of primary particles emitted from the collisions, $\delta$ - electrons generated by the beam in the target and backscattered neutrons were taken into account. Potential neutrons backscattered from the beam dump of CBM were not addressed.

The simulation was done by counting particles impinging the surface of the detector station and evaluating their non-ionizing radiation dose according to the NIEL-model. For the ionizing dose, it was assumed that all charged particles are minimum ionizing. Photons and nuclear fragments were ignored. It was found that the radiation dose impinging the detector may reach up to 340 $MRad$ and $1.5 \times 10^{15} \ n_{eq}/cm^2$ per year of operation at the maximum collision rate. The radiation doses are dominated by particles from the primary collision for the non-ionizing radiation damage. For ionizing radiation damage the main contribution comes from $\delta$ - electrons.

The yearly radiation doses found exceed the non-ionizing radiation tolerance of MAPS, which is estimated to $10^{13} \ n_{eq}/cm^2$, by two orders of magnitude. However, the running scenario discussed at the beginning of this chapter suggests using modest beam intensities for open charm measurements in order to avoid pile-up of events in the detector. In this case, the radiation doses fit the abilities of the detectors for non-ionizing radiation. The ionizing dose expected in this scenario is $\sim 2 \ MRad$ which seems also in reach of the technology.

It was also observed that modifications in the detector geometry could allow reducing the radiation doses by factors up to 6. The benefit of these modifications needs to be balanced against potential losses in terms of reconstruction efficiency. This will be the topic of the coming sections.

| Name | Geo1 | Geo2 | Geo3 | Geo6 | Geo10 | Geo11 | Geo12 |
|---|---|---|---|---|---|---|---|
| **Station 1** | | | | | | | |
| Position [mm] | 50 | 50 | 50 | 50 | 100 | 100 | 100 |
| $R_{Inner}$ [mm] | 5.5 | 10 | 10 | 10 | 5.5 | 11 | 20 |
| Primaries $[n_{eq}/cm^2/coll.]$ | 24.0 | 8.9 | 8.9 | 8.9 | 13.9 | 6.7 | 2.4 |
| $\delta$-electrons $[n_{eq}/cm^2/coll.]$ | 16.5 | 14.9 | 14.9 | 14.9 | 3.6 | 3.6 | 3.0 |
| Combined $[n_{eq}/cm^2/coll.]$ | 30.2 | 22.6 | 22.6 | 22.6 | 14.7 | 8.5 | 5.0 |
| **Station 2** | | | | | | | |
| Position [mm] | 100 | 100 | 100 | 100 | 150 | 150 | 150 |
| $R_{Inner}$ [mm] | 5.5 | 5.5 | 10 | 8 | 7.5 | 11 | 20 |
| Primary $[n_{eq}/cm^2/coll.]$ | 13.9 | 13.9 | 7.1 | 9.7 | – | – | – |
| $\delta$-electrons $[n_{eq}/cm^2/coll.]$ | 3.6 | 3.6 | 3.6 | 3.6 | – | – | – |
| Combined $[n_{eq}/cm^2/coll.]$ | 14.7 | 14.7 | 9.3 | 11.2 | – | – | – |
| "Lifetime" $[10^{11}\ coll.\ ]$ | 3.3 | 4.4 | 4.4 | 4.4 | 6.8 | 12 | 20 |
| Yearly dose $[10^{15}\ n_{eq}/cm^2]$ | 1.5 | 1.1 | 1.1 | 1.1 | 0.74 | 0.43 | 40.25 |

Table 7.2.: *The non-ionizing radiation doses for different MVD geometries (see table 7.1). The doses impinging the second station of Geo10 - Geo12 were not addressed. The results are expressed in terms of radiation dose per nuclear collision. The "lifetime" is expressed in terms of the maximum number of collisions one can measure before replacing the vertex detector.*

| Name | Geo1 | Geo2 | Geo3 | Geo6 | Geo10 | Geo11 | Geo12 |
|---|---|---|---|---|---|---|---|
| **Station 1** | | | | | | | |
| Position [mm] | 50 | 50 | 50 | 50 | 100 | 100 | 100 |
| $R_{Inner}$ [mm] | 5.5 | 10 | 10 | 10 | 5.5 | 11 | 20 |
| Primaries $[\mu Rad/event]$ | 0.9 | 0.3 | 0.3 | 0.3 | 0.5 | 0.3 | 0.1 |
| $\delta$ - electrons $[\mu Rad/event]$ | 6.7 | 6.7 | 6.7 | 6.7 | 1.4 | 1.4 | 1.4 |
| Combined $[\mu Rad/event]$ | 6.7 | 6.7 | 6.7 | 6.7 | 1.6 | 1.6 | 1.3 |
| **Station 2** | | | | | | | |
| Position [mm] | 100 | 100 | 100 | 100 | 150 | 150 | 150 |
| $R_{Inner}$ [mm] | 5.5 | 5.5 | 10 | 8 | 7.5 | 11 | 20 |
| Primaries $[\mu Rad/event]$ | 0.5 | 0.5 | 0.3 | 0.4 | – | – | – |
| $\delta$-electrons $[\mu Rad/event]$ | 1.4 | 1.4 | 1.4 | 1.4 | – | – | – |
| Combined $[\mu Rad/event]$ | 1.6 | 1.6 | 1.6 | 1.6 | – | – | – |
| Lifetime dose $[MRad]$ | 2.2 | 3.0 | 3.0 | 3.0 | 2.2 | 1.9 | 2.5 |
| Yearly dose $[MRad]$ | 340 | 340 | 340 | 340 | 80 | 80 | 60 |

Table 7.3.: *The ionizing radiation doses for different MVD geometries. The doses for the second station of Geo10 - Geo12 were not addressed.*

## 7.4. Choice of the detector geometry

The results of the radiation dose simulation demonstrated that slight variations of the geometry of the vertex detector might have substantial benefit on the lifetime of the vertex detector. This suggested that the compromise between detector lifetime and the selectivity[13] for open charm measurements could still be improved.

In order to do this, one has to evaluate the selectivity for different MVD geometries. This was done with an analytic calculation relying on simulation results on secondary vertex resolution and the invariant mass resolution. Unlike the selectivity of the detector, those two parameters can be assessed with simulations having modest statistics. The semi-analytic approach followed allowed therefore addressing a significant number of geometries, which was required for a systematic study.

Despite of being simplistic, evaluating the performances of the MVD detector on the basis of those two parameters seems justified. As the background suppression is dominantly done relying on the reconstruction of a secondary decay vertex and a cut on the invariant mass of the reconstructed particle, both parameters represent the key features in terms of background suppression. This statement holds if the tracking performance and efficiency is sufficiently good and comparable for all detector geometries. This is fulfilled for all geometries addressed as the main tracker determining it was not modified.

A choice of a good MVD geometry has to rely on a comparison based on a quantity, which reflects both, the lifetime and the selectivity of the detector. The natural quantity of choice is the significance of the reconstructed particle, which can be evaluated based on the detector lifetime, the secondary vertex resolution and the invariant mass resolution obtained by the simulations. This allowed to identify a promising geometry for the MVD, which was then chosen for a full simulation.

In the following, the basic concept used for reconstructing open charm will be introduced and the concept of selection cuts will be presented. Hereafter, the results on the simulation of secondary vertex and invariant mass resolution will be shown before deriving the significance of the signal for open charm for different MVD geometries. The results of the calculation will be discussed and the choice for the detector geometry will be motivated.

### 7.4.1. The approach used for reconstructing open charm

The reconstruction of open charm is done by means of the invariant mass analysis. In the two body decay addressed in this work, which is $D^0 \rightarrow K^- + \pi^+$, the invariant mass of the mother particle is reconstructed from the four-momenta $(E_1, \vec{p_1})$ and $(E_2, \vec{p_2})$ of the daughter particles. This is done according to:

$$m_{inv} = \sqrt{(E_1 + E_2)^2 - (\vec{p_1} + \vec{p_2})^2} \tag{7.4}$$

In order to calculate the invariant mass, one needs information about the momentum combined with knowledge on either the energy or the rest mass of each daughter particle. Information about the momentum of the particles and of their charge sign is provided by the STS-tracker. This is because the trajectory of the particles is bended by a magnetic field provided by the dipole magnet. The momentum resolution of CBM will be in the order of $\sim 1$ % [73].

Information on the rest mass of the daughter particles is more difficult to obtain, as the hadron identification detectors of CBM can distinguish pions and kaons only in a part of the energy range of interest. In the simulation it was therefore assumed that particle identification is available for protons only, which corresponds to a very conservative picture of the hadron identification abilities

---

[13]See section 7.

of CBM. An ad hoc assumption was used on the particle identity, and thus on the mass, of the other particles. It was supposed, that all negatively charged particles are $K^-$ while all positively charged particles are $\pi^+$.

As a priory one cannot identify pion-kaon pairs, the invariant mass is calculated for all possible combinations of positive and negative particles. Each combination of particles is considered as a potential $D^0$ candidate. The number of those candidates is very high. As roughly $10^3$ charged particles pass the detector acceptance in each central collision, one may form $\sim 2.5 \times 10^5$ pairs from each nuclear collision[14]. An efficient automatic selection of $D^0$ from this background is required. This is done by rejecting all candidates, which do not fulfill certain criteria, which are set by the properties of the signal particle one wants to identify. A simplistic but efficient criterion is for example the invariant mass of the particle candidate. One may reject all candidates, which show an invariant mass which is incompatible with the mass of $D^0$. Another major criterion is that the particle pair originates from a secondary decay vertex.

The rejection of candidates corresponding to uncorrelated pairs is done by imposing conditions (cuts) on the selection criteria. Defining good criteria and values for the cuts was one of the key questions of this simulation. The cuts found and the methods used for choosing the appropriate values, will be discussed in detail later on.

### 7.4.2. The simulation of the secondary vertex and the invariant mass resolution of different MVD geometries

The simulation of the secondary vertex resolution and the invariant mass resolution of the CBM-MVD + STS was done with GEANT3. GCalor was turned off to save CPU time. Moreover, for reasons of calculation time, the very time consuming cellular automaton track finder of the simulation framework was replaced by a fast ideal track finder.

The invariant mass resolution and the secondary vertex resolution of a detector can be in principle simulated with $D^0$ particles only. However, the event reconstruction algorithm required embedding the signal into a nuclear collision. The signal, which was generated with the thermal model, which is described in [74] was therefore embedded into a central Au+Au collision with a beam energy of 25 $AGeV$. The latter was provided by UrQMD.

For each detector geometry of interest, $10^4$ events of those composed events were simulated. The daughter particles produced in decays of $D^0$ mesons were selected on the base of Monte Carlo information and used to evaluate the secondary vertex resolution and the invariant mass resolution for each detector geometry.

The simulations were done for a spatial resolution of $3 \times 3$ $\mu m^2$ and $6 \times 6$ $\mu m^2$. Being combined with a material budget of few 100 $\mu m$, this represents MAPS with ADC based, and digital readout respectively. For reasons of completeness, also pixels with a resolution of $30 \times 30$ $\mu m^2$ and $60 \times 12$ $\mu m^2$ were simulated. Being combined with a material budget of 1000 $\mu m$, they represent hybrid pixels with digital readout[15]

The results are shown in figure 7.10 as a function of the detector spatial resolution and the material budget for the standard MVD geometry (Geo1). They show clearly that the secondary vertex resolution degrades if the spatial resolution of the detector deteriorates. One finds that the spatial resolution of $6 \times 6$ $\mu m^2$ combined with very low material budget would be sufficient to keep the secondary vertex resolution in the order of 50 $\mu m$. The latter value was set as preliminary

---

[14]Assuming naively that half of the particles have positive charge and half of them have negative charge.

[15]Note that the typical material budget of hybrid pixels as used at LHC is substantially above 1000 $\mu m$ silicon equivalent per detector station. This unit can be translated to radiation lengths by using the approximation 1000 $\mu m$ $Si \approx 1\%$ $X_0$.
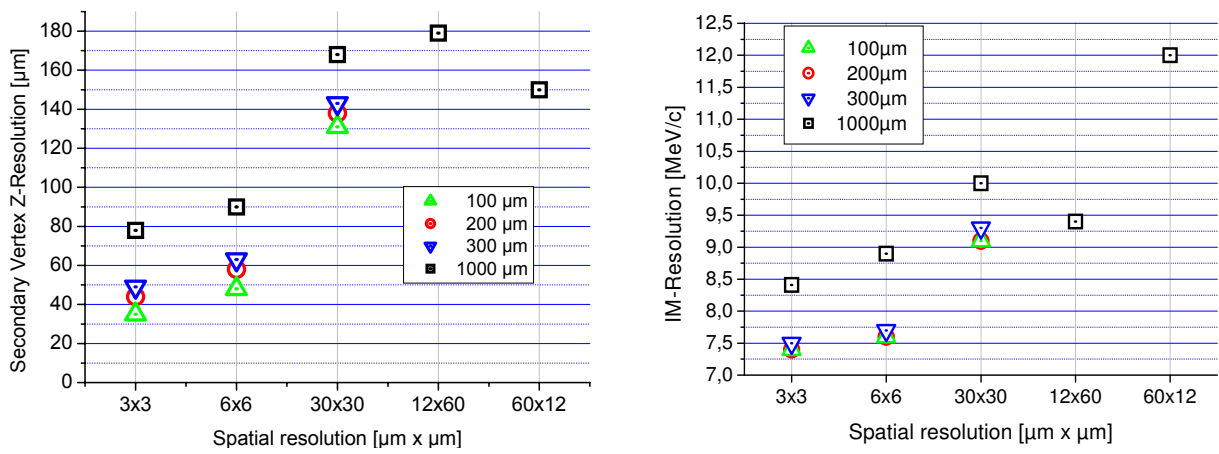
Figure 7.10.: *The secondary vertex resolution (left) and the invariant mass resolution (right) for the standard geometry (Geo1) as a function of detector resolution and material budget (in μm silicon equivalent).*

requirement for the CBM vertex detector [1]. The secondary vertex resolution of the hybrid pixels is typically by a factor of three to five worse than the one of MAPS.

The influence of the material budget is also of importance. The step from a thickness of 100 $\mu m$ silicon equivalent to 1000 $\mu m$ silicon equivalent decreases the resolution by up to a factor of two. Figure 7.10 shows that one can reach the envisaged secondary vertex resolution by using MAPS with a good spatial resolution and with a thickness of few 0.1% $X_0$. This is compatible with the material budget estimated in chapter 3.2.

Concerning the invariant mass resolution, a value between 7 $MeV/c^2$ and 8 $MeV/c^2$ has been reached for all detector designs representing MAPS (see figure 7.10, right). Again, the resolution provided by hybrid pixels is significantly worse. Qualitatively, this suggests that, despite of their high radiation hardness, hybrid pixels will not provide the selectivity required for open charm measurements. Nevertheless, this statement remains to be confirmed by dedicated simulation studies, which were beyond the scope of this work.

As we have seen in section 7.3.4.2, an increase of the distance between the target and the first station of the STS is of particular interest in order to reduce the exposure of the MVD to radiation doses. The secondary vertex resolution has thus been studied as a function of this distance. The outcome of the simulation is shown in figure 7.11 (left). The resolution deteriorates only slowly with increasing distance from 5 $cm$ to 10 $cm$. Provided a good spatial resolution of the stations (3 $\mu m \times$ 3 $\mu m$), the secondary vertex resolution remains below 75 $\mu m$, which is still tolerable.
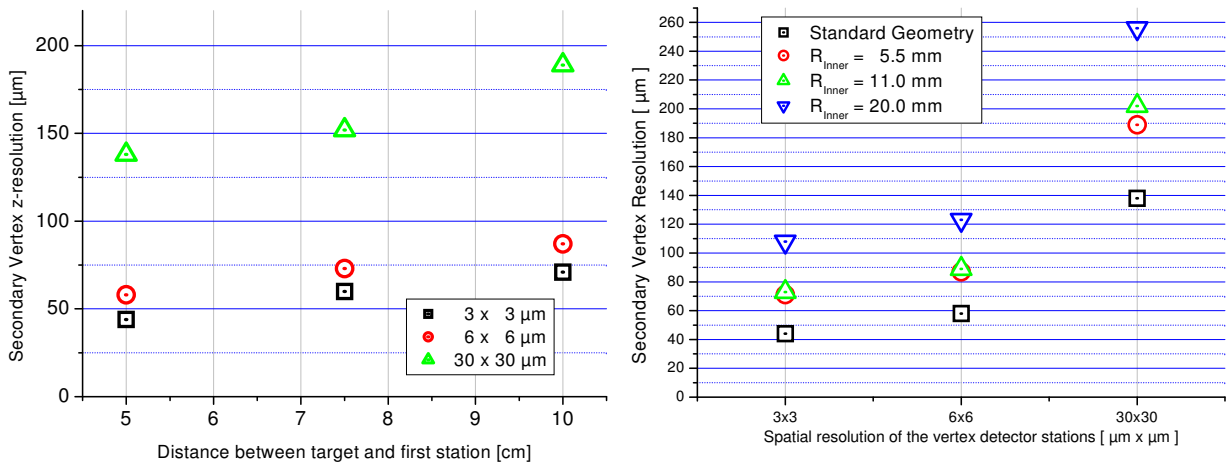


Figure 7.11.:
Left: *The secondary vertex resolution as a function of the distance between the first station and the target. The simulation relies on Geo1 ($z = 5$ cm), Geo7 ($z = 7.5$ cm) and Geo10 ($z = 10$ cm), for different spatial resolutions of the detectors.*
Right: *The secondary vertex resolution for MVD geometries with different inner diameters of the detector stations (Geo10, Geo11 and Geo12). A distance of 10 cm between first station and target was assumed. The resolution of the standard geometry is shown for comparison. A thickness of 200 $\mu m$ was assumed for each vertex detector station.*

The second option to reduce the radiation dose is to increase the radius of the beam hole. The consequences of doing so were also simulated for MVD geometries with a distance of 10 $cm$ between the first station and the target[16]. The consequences on the secondary vertex resolution

---

[16]The results for corresponding MVD geometries with a distance of 5 $cm$ are presented in table 7.4.

are shown in figure 7.11. The resolution does not change significantly if the inner diameter of the station is increased from 5 $mm$ to 11 $mm$. A further increase to 22 $mm$ leads to a dramatic worsening in terms of secondary vertex resolution.

The numerical values of all results obtained are listed in table 7.4.

| Geometry | Geo1 | Geo2 | Geo3 | Geo4 | Geo5 | Geo6 | Geo10 | Geo11 | Geo12 |
|---|---|---|---|---|---|---|---|---|---|
| **Station 1** | | | | | | | | | |
| Position [mm] | 50 | 50 | 50 | 25 | 75 | 50 | 100 | 100 | 100 |
| $R_{Inner}$ [mm] | 5.5 | 10 | 10 | 5.5 | 5.5 | 10 | 5.5 | 11 | 20 |
| $R_{Outer}$ [mm] | 25 | 25 | 25 | 25 | 37.5 | 25 | 50 | 50 | 50 |
| **Station 2** | | | | | | | | | |
| Position [mm] | 100 | 100 | 100 | 50 | 100 | 100 | 150 | 150 | 150 |
| $R_{Inner}$ [mm] | 5.5 | 5.5 | 10 | 5.5 | 5.5 | 8 | 7.5 | 11 | 20 |
| $R_{Outer}$ [mm] | 50 | 50 | 50 | 50 | 50 | 50 | 75 | 75 | 75 |
| **Station 3** | | | | | | | | | |
| **Position [mm]** | 200 | 200 | 200 | 200 | 200 | 200 | 200 | 200 | 200 |
| $R_{Inner}$ [mm] | 10.5 | 10.5 | 10.5 | 10.5 | 10.5 | 10.5 | 10.5 | 11 | 20 |
| $R_{Outer}$ [mm] | 100 | 100 | 100 | 100 | 100 | 100 | 100 | 100 | 100 |
| **SvZ-Resolution** | **Geo1** | **Geo2** | **Geo3** | **Geo4** | **Geo5** | **Geo6** | **Geo10** | **Geo11** | **Geo12** |
| $\sigma = 3 \times 3~\mu m^2$ | | | | | | | | | |
| 100 $\mu m$ Si [$\mu m$] | 35 | – | 51 | – | – | – | – | – | – |
| 200 $\mu m$ Si [$\mu m$] | 44 | 50 | 58 | 34 | 60 | 53 | 71 | 73 | 108 |
| 300 $\mu m$ Si [$\mu m$] | 49 | – | – | – | – | – | – | – | – |
| 1000 $\mu m$ Si [$\mu m$] | 78 | – | – | – | – | – | – | – | – |
| $\sigma = 6 \times 6~\mu m^2$ | | | | | | | | | |
| 100 $\mu m$ Si [$\mu m$] | 48 | – | 69 | – | – | – | – | – | – |
| 200 $\mu m$ Si [$\mu m$] | 58 | 69 | 68 | 45 | 73 | 70 | 87 | 89 | 123 |
| 300 $\mu m$ Si [$\mu m$] | 63 | – | – | – | – | – | – | – | – |
| 1000 $\mu m$ Si [$\mu m$] | 90 | – | – | – | – | – | – | – | – |
| $\sigma = 30 \times 30~\mu m^2$ | | | | | | | | | |
| 100 $\mu m$ Si [$\mu m$] | 131 | – | 162 | – | – | – | – | – | – |
| 200 $\mu m$ Si [$\mu m$] | 138 | 170 | 176 | 126 | 152 | 160 | 189 | 202 | 256 |
| 300 $\mu m$ Si [$\mu m$] | 143 | – | – | – | – | – | – | – | – |
| 1000 $\mu m$ Si [$\mu m$] | 168 | – | – | – | – | – | – | – | – |
| $\sigma = 12 \times 60~\mu m^2$ | | | | | | | | | |
| 1000 $\mu m$ Si [$\mu m$] | 179 | – | – | – | – | – | – | – | – |
| $\sigma = 60 \times 12~\mu m^2$ | | | | | | | | | |
| 1000 $\mu m$ Si [$\mu m$] | 150 | – | – | – | – | – | – | – | – |

Table 7.4.: *The secondary vertex resolution (in μm) for signal pairs as a function of different vertex detector geometries. The details of the geometries are reminded in the upper part of the table. In the lower part, the secondary vertex resolution is given as a function of the spatial resolution of the sensors and of the material budget.*

### 7.4.3. Benchmarking different detector geometries

The simulated values of the secondary vertex resolution and the invariant mass resolution give a first indication on the performances of the different MVD-geometries. This was, however, insufficient for a quantitative comparison of the different geometries, as the consequences of a varied

resolution on the reconstruction performance is not straightforward. In order to allow for this comparison, the expected signal quality for central Au-Au collisions at a beam energy of 25 *AGeV* was evaluated with a back of envelop calculation. Despite the simplicity of those calculations, their results are very close to those achieved with the detailed Monte Carlo simulations, which will be presented later in this chapter.

In the calculations, we take into account the two most important selection criteria required to distinguish signal and background. Those are the reconstructed position of the displaced secondary vertex and the reconstructed invariant mass. The aim of the calculations is to estimate the efficiency of the selection cuts for both, the signal and the background.

In a first step, one estimates the signal efficiency of the cut on the secondary vertex position. To simplify this problem, it is assumed that the velocity of the $D^0$ is equal to the one of the center of mass of the nuclear collisions. According to the decay law, the distribution of their decaying point is given by:

$$n_{D^0}(z) = C_0 \cdot \exp\left(-\frac{z}{\gamma \cdot c\tau}\right) \tag{7.5}$$

In this equation, which is illustrated in figure 7.12, $z$ stands for the distance between the reconstructed secondary decay vertex of the $D^0$ and the primary vertex and $c$ for the speed of light. The Lorentz boost of the center-of-mass for a beam energy of 25 *AGeV* is $\gamma = 3.8$ and the $D^0$ lifetime is $c\tau = 123 \ \mu m$. From this one obtains:

$$\gamma \cdot c\tau = 467 \ \mu m \tag{7.6}$$

$C_0$ is a normalization factor, which will cancel out in the following. In a first step of our calculation, we will derive the fraction $F_{D^0}(z_0)$ of $D^0$-mesons, which decay beyond a point $z_0$. This fraction is given by:

$$F_{D^0}(z_0) = \frac{\int\limits_{z_0}^{\infty} n_{D^0}(z) \ dz}{\int\limits_{0}^{\infty} n_{D^0}(z) \ dz} \tag{7.7}$$

In order to derive the absolute number of $D^0 \to K^- + \pi^+$ decays occurring beyond $z_0$, one has to multiply $F_{D^0}(z_0)$ with total number $(N)$ of accepted $D^0 \to K^- + \pi^+$ decays, which is defined as following:

$$N = Mult(D^0) \cdot b \cdot A \cdot N_{Int} \tag{7.8}$$

Here, $Mult(D^0) = 1.2 \times 10^{-4}$ stands for the production multiplicity of $D^0$ in central collisions, $b = 3.8 \ \%$ represents the branching ratio for $D^0 \to K^- + \pi^+$ and $A \approx 35\%$ stands for the geometrical acceptance of CBM for $D^0$-mesons decaying into pion kaon pairs.

The lifetime of the MVD $N_{Int}$ expressed in terms of central collisions is given by:

$$N_{Int} = \frac{1}{10} \cdot \frac{R}{d} \tag{7.9}$$

Here, $R = 10^{13} \ n_{eq}/cm^2$ the radiation tolerance of the detector and $d$ the radiation dose per collision. The normalization factor $1/10$ is required as we assume $10\%$ of collisions to be central. The number of $D^0$-mesons decaying beyond a point $z_0$ $(N_S(z_0))$ is thus given by:

$$N_S(z_0) = N \cdot F_{D^0}(z_0) = Mult(D^0) \cdot b \cdot A \cdot N_{Int} \cdot \exp\left(-\frac{z_0}{\gamma c\tau}\right) \tag{7.10}$$
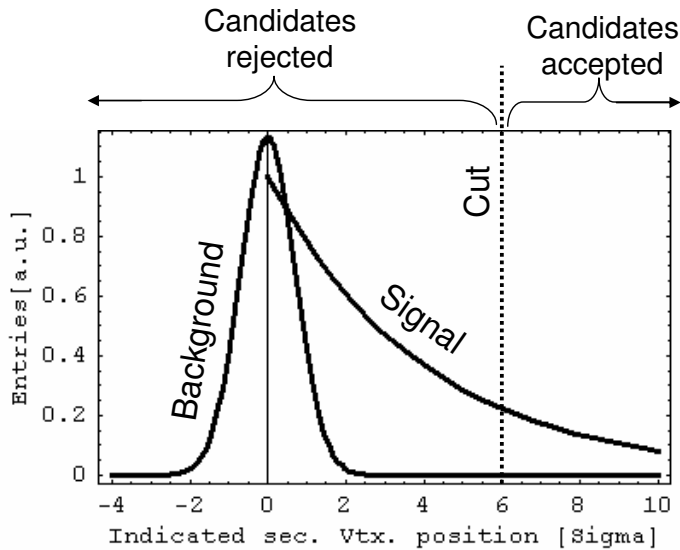
Figure 7.12.:
*Illustration of $n_{D^0}(z)$ (signal) and the corresponding background as a function of the reconstructed position of the displaced secondary vertex (z). This position is given in units of the secondary vertex resolution $\sigma_{SvZ}$. See text.*

As illustrated in figure 7.12, the background distribution is assumed to have a Gaussian shape. For background suppression, a cut on the z-coordinate of the reconstructed secondary vertex of the candidates is assumed. This cut will be applied at the point:

$$z_0 = 6 \cdot \sigma_{SvZ} \tag{7.11}$$

where $\sigma_{SvZ}$ stands for the secondary vertex resolution of the detector. As this cut also rejects signal pairs, the number of $D^0$-mesons passing it is then given by

$$N_S \left(6 \cdot \sigma_{SvZ}\right) = \sigma \cdot b \cdot A \cdot N_{Int} \cdot \exp\left(-\frac{6 \cdot \sigma_{SvZ}}{\gamma c \tau}\right) \tag{7.12}$$

The numerical values for $d$, $N_{Int}$ and $N_S$ are indicated in table 7.5 for some MVD geometries of particular interest. In the table, the signal relative to the one of Geo1 is also shown. This allows testing the effect of the modifications of the MVD-geometries, which were to reduce the impinging radiation dose. One observes that despite of their slightly lower secondary vertex resolution, the modified geometries allow for detecting a substantially higher number of $D^0$'s within the detectors lifetime. The effect of the increased lifetime is thus stronger than the one of the deterioration of detection efficiency and an overall benefit remains.

A conclusion was nevertheless premature without taking into account the background rate. To estimate it, it is assumed that each central Au+Au collision produces roughly 500 positive and 500 negative particles in the detector acceptance. The number of background candidates is then given by:

$$N_{CB} = 500^2 \cdot N_{Int} \tag{7.13}$$

For all these background combinations, one can derive a "secondary vertex" corresponding to the intersection point of the two combined tracks. From the physics point of view, this intersection point is equal to the primary vertex of the nuclear collision. Nevertheless, because of the limits of the detector, it will usually be displayed at a slightly different position: this will be approximated as a Gaussian distribution around the position of the primary vertex (which is located at $z = 0$). The width of this distribution is equal to the secondary vertex resolution $\sigma_{SvZ}$.

As mentioned above, we apply a cut on the distance between primary vertex and reconstructed secondary vertex. The position of this cut is given by $z_0 = 6\,\sigma_{SvZ}$. By doing so, we fix the number

| | Geo1 | Geo 3 | Geo 10 | Geo 11 | Geo 12 |
|---|---|---|---|---|---|
| Sec. Vtx. Res. $[\mu m]$ | 44 | 58 | 71 | 73 | 108 |
| Inv. Mass Res. $[MeV/c^2]$ | 7.4 | 7.4 | 7.7 | 7.8 | 9.2 |
| Rad. Dose $(d)$ $[n_{eq}/coll.]$ | 30.2 | 22.6 | 14.7 | 8.5 | 5.0 |
| Lifetime $(N_{Int})$ [centr. coll] | $3.3 \times 10^{10}$ | $4.4 \times 10^{10}$ | $6.8 \times 10^{10}$ | $11.8 \times 10^{10}$ | $20.0 \times 10^{10}$ |
| Signal $(N_S)$ | 30 k | 34 k | 43 k | 73 k | 80 k |
| $N_S$ / $N_S$(Geo1) | 1.0 | 1.12 | 1.45 | 2.6 | 3.1 |
| BG after SvZ-Cut $(N_{CB_{SvZ}})$ | $1.7 \times 10^6$ | $2.2 \times 10^6$ | $3.4 \times 10^6$ | $5.9 \times 10^6$ | $10.0 \times 10^6$ |
| BG after SvZ & IM-Cut $(N_B)$ | 8 k | 11 k | 17 k | 30 k | 61 k |
| $N_B$ rel. to Geo1 | 1.00 | 1.34 | 2.13 | 3.75 | 7.55 |
| $S/B$ | 3.7 | 3.1 | 2.5 | 2.4 | 1.32 |
| Significance | 154 | 159 | 177 | 228 | 213 |
| $S/B$ rel. to Geo1 | 1.00 | 0.84 | 0.68 | 0.65 | 0.35 |
| Significance rel. to Geo1 | 1.00 | 1.04 | 1.15 | 1.48 | 1.38 |

Table 7.5.: *The characteristic numbers of different potential geometries of the MVD. Note that the numbers on signal ($N_S$) and background (BG) pairs were estimated with a simplistic model. Their absolute values thus underlay substantial uncertainties.*

of surviving background combinations to a value, which is given by

$$N_{CB_{SvZ}} = \frac{N_{CB}}{2} \cdot \left( 1 - Erf\left[\frac{6}{\sqrt{2}}\right] \right) = 1 \times 10^{-9} \, N_{CB} \tag{7.14}$$

This is because the surface of the integral of a Gaussian, which is above 6 $\sigma$ is constant independently of the value of $\sigma$. The numerical values on the background are again shown in table 7.5. Note that only the surface at the positive side of the Gaussian is taken into account.

For both, the signal and the background pairs, the invariant mass distribution of the reconstructed particles can be estimated as following: For the signal, the distribution follows a Gaussian distribution centered around the rest mass of the $D^0$, which is given by $m_{D^0} = 1.864 \, GeV/c^2$. The width of this distribution is defined by the invariant mass resolution ($\sigma_{IM}$), which is a feature of the specific detector. Assuming a perfect Gaussian shape of the distribution, one can state that roughly 95 % of all signal candidates are concentrated in a mass region of interest[17] given by:

$$m_{D^0} - 2\sigma_{IM} < m_{inv} < m_{D^0} + 2\sigma_{IM} \tag{7.15}$$

The invariant mass distribution of the background has, according to simulations, roughly an exponential shape. In the following we will assume this shape to follow

$$n_B(m_{inv}) = P_1 \cdot \exp(-P_2 \, m_{inv}) \tag{7.16}$$

The parameter $P_2 = 1.48 \, GeV^{-1}$ of the exponential was obtained by fitting the invariant mass distribution originating from simulations. The normalization factor $P_1$ will cancel out later on. Similar to equation 7.7 and to equation 7.12, the number of surviving background pairs $N_B$ is given by:

$$N_B = N_{CB_{SvZ}} \cdot \frac{\int_{m_1}^{m_2} n_B(m_{inv}) \, dm_{inv}}{\int_0^\infty n_B(m_{inv}) \, dm_{inv}} = N_{B_{SvZ}} \left[ \exp(-P_2 \cdot m_1) - \exp(-P_2 \cdot m_2) \right] \tag{7.17}$$

---

[17]For simplicity, a signal efficiency of 100 % instead of the correct 95 % was assumed in this calculation.

with $m_1 = m_{D^0} - 2\sigma_{IM}$ and $m_2 = m_{D^0} + 2\sigma_{IM}$. Knowing $N_B$, one can easily extract the $S/B$-ratio

$$S/B = \frac{N_S}{N_B} \tag{7.18}$$

and the significance

$$Sign. = \frac{N_S}{\sqrt{N_S + N_B}} \tag{7.19}$$

The results are listed in table 7.5.

Those results were compared with the outcome of the "full" simulation, which is presented in the next section. The comparison proves a reasonably good accordance between the results of both approaches on the performances of Geo11. The signal and the background are each overestimated by roughly a factor of three with respect to the detailed simulation, the $S/B$ is overestimated by roughly 20 %. The latter is significantly below the uncertainties of the simulations. The results obtained should thus provide a reasonable picture allowing us to judge also the other geometries.

### 7.4.4. Results and Discussion

Several interesting MVD-geometries are compared with the standard geometry Geo1 in table 7.5. Like for Geo1, the first station of Geo3 is located 5 *cm* from the target. The beam hole of the first two stations of Geo3 is increased to a radius of 1 *cm* to avoid the most irradiated areas close to the beam axis without crucially deteriorating the detection efficiencies. The first station of the geometries Geo10, Geo11, Geo12 is located 10 *cm* from the target. Those geometries are distinguished by the radius of the beam hole, which is 5.5 *mm* for Geo10, 11 *mm* for Geo11, and 22 *mm* for Geo12.

From the outcome of the calculations one can see that the study was justified. Even if the $S/B$ of the modified detectors is smaller than the one of the standard geometry, they achieve better results in terms of reconstructed particles and significance of the signal. The detector geometry providing the best compromise between reconstruction abilities and lifetime seems to be Geo11. It reaches the highest significance of all geometries studied. Geo12 shows the second best results but its geometrical acceptance is lower than the one of Geo11, which was not accounted for.

The results shown in table 7.5 suggest that moving the first station of the MVD away from the target improves the performance of the system. The geometries having a distance of 10 *cm* from the target show clearly a better performance than the standard geometry.

Increasing the beam hole has also a positive effect. This effect is reduced for Geo3 as the radiation is dominated by $\delta$ - electrons, which are less concentrated around the beam axis than the primary particles. At a distance of 10 cm, the radiation dose from the $\delta$ - electrons is significantly lower. The effect of increasing the beam hole is stronger. Geo11 and Geo12 show a significantly better performance than Geo10. Overall, Geo11 comes out to provide the best solution for the MVD. It was thus chosen for a full simulation of the CBM experiment, which is discussed in the following section.

## 7.5. A preliminary simulation of the physics performances of CBM

Once an appropriate detector geometry (Geo11) was chosen, the feasibility of doing open charm measurements had to be demonstrated with a dedicated simulation. As already mentioned, the reconstruction of the $D^0$ via the channel $D^0 \rightarrow K^- + \pi^+$ was chosen for this simulation, as this task was considered as particularly challenging. The aim of this simulation was to investigate,

quantitatively the performance of the MVD for $D^0$-meson reconstruction. The results will be presented in terms of the reconstructed number of $D^0$ and the significance and purity (S/B) of the signal.

To obtain those results, a simulation using the simplified simulation chain described in section 7.2.1 was performed. This simplified simulation chain uses ideal track finding and describes the response of the silicon detectors only by a Gaussian smearing of the hit position. As shown in section 7.4.1, the reconstruction of the signal relies on the analysis of the invariant mass of the reconstructed particle and the consecutive use of selection cuts for background rejection.

Within the simulation process it became clear that for simulating the reconstruction of open charm one needs to solve two substantial challenges. The first one is generating and handling the enormous amount of background ($\sim 10^7$ events) required to obtain reliable results. The second one was to define the appropriate selection cuts allowing for an efficient rejection of the combinatorial background. Both points will be addressed in the following sections before discussing the detailed simulation setup and the results obtained.

### 7.5.1. Generating very high background statistics: The super-event approach

Obtaining a reliable simulation result on $D^0$-meson reconstruction requires very high statistics (more than 10 millions of central collisions). Because of CPU time limitations, it is not reasonable to generate such a high number of events with UrQMD. Super-event generation was thus used for these simulations.

This approach was inspired by the event-mixing, which is used for estimating the background in the analysis of experimental data [75]. Super-event generation uses the key idea of event-mixing, which is the generation of combinatorial background from individual tracks. Unlike the classical event-mixing, positive and negative tracks from more than one event are used. As the number of possible combinations between the tracks increases with the square of their number, this allows generating a very high number of background combinations with a limited input. However, one has to be aware that this background is purely combinatorial, e.g. that is formed by random combinations of uncorrelated positive and negative particles. A physics background, due for example to misidentified hyperon decays, cannot be taken into account in this this approach.

This has in first order no effect for $D^0 \to K^- + \pi^+$ as the dominant background is formed by uncorrelated kaons and pions being emitted from the collision. Nevertheless, a small contribution of background is also produced by hyperon decays. As those have a true displaced vertex, their daughter particles are more likely to be accepted by the selection cuts than the uncorrelated particle pairs. Their contribution to the background might therefore become dominant after applying selection cuts. On the other hand, one may hope to reconstruct a part of the hyperons to reject them from the list of $D^0$-candidates in the following. Preliminary results of an ongoing study suggest that doing so might further increase the signal purity with respect to the approach shown here [76].

The background generation using super-events was done by building an artificial event from the tracks of $n = 330$ URQMD-events. The artificial super events were therefore containing approximately $n$ times more positive (and negative) particles. Combining those tracks leads to an increase of a factor of $n^2$ in terms of possible combinations. The statistics reached with such a super event is expressed as $n^2 = 108,900$ events *equivalent*. The unit "events equivalent" is used in order to distinguish statistics reached with normal events (correct description of hyperons) from the one reached with super events.

### 7.5.2. Selection Cuts

The use of highly efficient selection criteria is of crucial importance in the reconstruction of $D^0$-mesons. This is because the number of signal pairs is extremely low as compared to the number of background pairs:

Assuming that roughly $10^3$ charged particles are accepted by the detector and half of them are positively (or negatively respectively) charged, one may form $\sim 2.5 \times 10^5$ pairs from each collision. Assuming a production multiplicity of $1.2 \times 10^4$ $D^0$-mesons per central collision and that the branching ratio of $D^0 \to K^- + \pi^+$ is 3.8 %, one finds that $\sim 2 \times 10^5$ collisions are required to produce one $D^0$ decaying into pion and kaon. As only $\sim 30$ % of them are accepted, one detects one signal pair per $\sim 1.5 \times 10^{11}$ candidates.

The criteria used to distinguish the rare signal from this dense background rely dominantly on the knowledge of the mass of open charm mesons and on the possibility to distinguish their decay vertex from the point of the primary collision. Candidates, which do not match the correct invariant mass, or seem to origin from the primary collision, are rejected. The details of the different selection cuts used in the present simulation will be discussed in the following.

### 7.5.2.1. Cuts on the single tracks

The first set of cuts was applied on properties of the individual tracks. As those cuts can be introduced before combining the tracks, they allow for a significant reduction of the amount of combinations. The definition of selection cuts is illustrated in figure 7.13.
The following single-track-cuts were used in this work:

- *Cut on the particle momentum (p - cut):* This cut accounts for the fact that most daugther particles of open charm mesons have a momentum above $p > 1\ GeV/c$. In the specific context of this simulation, this cut had a second purpose, which was to reduce the uncertainty caused by using the ideal track finder. Doing so is only justified if the efficiency of the realistic cellular automaton track finder of CBM is reasonably close to 100 %. The latter is not fulfilled for particles with $p \lesssim 1\ GeV/c$ which motivated removing them from the simulation.

- *Cut on the transverse momentum ($p_t$ - cut):* This cut is motivated by the fact that the mass of $D^0$ is significantly higher than the one of its daughter particles. A significant amount of kinetic energy is thus set free in the particle decay. This energy is likely to provide an additional transverse momentum $p_t$. Particles generated in a decay of $D^0$ have thus a higher mean $p_t$ than background particles. A minimum transverse momentum of $0.3\ GeV/c$ was requested.

- *Cut on the maximum impact parameter:* In the context of this work, the impact parameter is defined as the distance between the primary vertex at the target plane and the intersection point of a track with this plane. Unlike the background, the daughter particles of an open charm decay are not generated in the nuclear collision but in the decay vertex. It is therefore unlike that an extrapolation of the tracks intersects with the position of the primary vertex. On the other hand, as the lifetime of $D^0$-mesons is limited, the impact parameters should not exceed a certain value.
  An impact parameter below 600 $\mu m$ is requested to exclude tracks originating from hyperon decays.

- *Cut on the minimum impact parameter (PV-cut):* The cut demanding a minimum impact parameter is not done on a fixed distance because the uncertainties of the track extrapolation to the target are very different for different tracks. The cut was thus applied on the impact
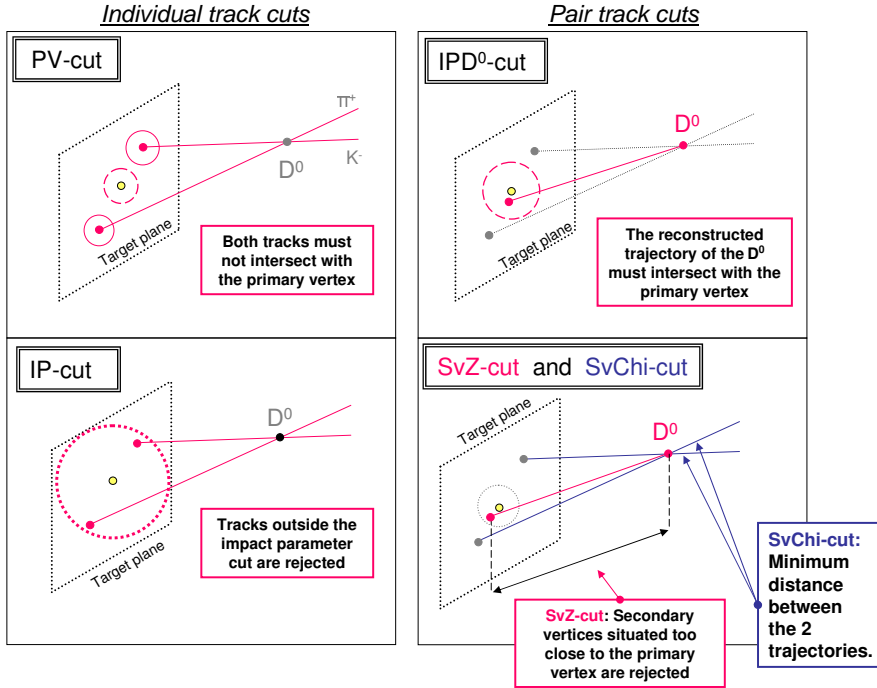
Figure 7.13.:
*The definition of some selection cuts used to extract the signal of open charm. From [77].*

parameter measured in units of this uncertainty, which was displayed by the track fitter. This cut is often referred as "Primary Vertex cut" (PV-cut) in order to distinguish it from a trivial cut on the impact parameter, which does not account for the extrapolation uncertainty.

### 7.5.2.2. Cuts on track pairs

After defining a track pair, parameters like the position of a potential decay vertex and the properties of a potentially reconstructed $D^0$ become accessible. The following selection cuts were applied to each track pair:

- *The SvZ - cut:* This cut on the z-position of the secondary vertex demands for a minimum distance between the reconstructed secondary vertex of two tracks and the primary vertex.
- *The SvChi – cut:* This cut limits the maximal distance between the two tracks at the point of closest approach (secondary vertex). As done before for the PV-cut, this cut takes into account the precision of the extrapolation of the tracks.
- *The IPD⁰ – Cut:* Charmed mesons are emitted from the nuclear collision. Extrapolating their trajectory back from the secondary vertex must thus lead to the primary vertex. This cut on the impact parameter of the reconstructed $D^0$ particle requires the distance between the primary vertex and the extrapolated trajectory of the $D^0$ to be lower than a certain value.

### 7.5.2.3. Finding the appropriate cut values: Definition of the problem and standard method

The selection of $D^0$-candidates is done by imposing cuts on each of the selection criteria defined in the previous sub-section. The values of those cuts nust be defined on the base of a compromise between "background rejection" and "signal efficiency". In few cases, those values were motivated by straightforward arguments. For example, the realistic tracking software showed reduced track finding performance for tracks with a momentum of $p \lesssim 1~GeV/c$. As ideal track finding was used in the simulation, it was justified to reject all tracks with a momentum below this limit.

For most selection criteria, the method used to define the appropriate cut values consisted in two steps: In the first step, a preliminary, loose cut was used for rejecting tracks and candidates, which do obviously not contribute to the signal. This allowed reducing the number of remaining candidates sufficiently, to allow for estimating the definitive cut value with the algorithms described in the next section. This method will be illustrated with a simple example. As one knows that the decay vertex of the $D^0$ must be located downstream the initial collision point, one can immediately exclude all candidates, which indicate a decay vertex upstream of it. This allows in a straightforward way eliminating half of the candidates. However, all candidates required for evaluating the goo cut value remain available.

**The one dimensional approach:**  The method generally used (see for example [74]), which will be named *single cut optimization* in the following, consists in optimizing the significance of the signal by varying the value of a given cut, which is given by:

$$Sign. = \frac{N_S}{\sqrt{N_S + N_B}} \approx \frac{N_S}{\sqrt{N_B}} \tag{7.20}$$

Here $N_S$ stands for the number of signal pairs fulfilling the selection cut. $N_B$ stands for the number of uncorrelated background pairs also fulfilling the selection criterion and are in the $D^0$ invariant mass region. The approximation in equation 7.20 holds if $N_B \gg N_S$ and will be used in the following for simplicity.

In order to optimize the value $c$ of a cut on a parameter $p$ (for example the distance between the primary and secondary vertex) one defines $S(p)$ and $B(p)$ as the distribution of signal and background pairs as a function of the parameter $p$. These functions are illustrated in the upper panels of figure 7.14 for the case of the secondary vertex cut. Assuming in this example a candidate to be signal if a parameter $p$ is above $c$, one finds

$$N_S(c) = \int_c^\infty S(p) \ dp \tag{7.21}$$

$$N_B(c) = \int_c^\infty B(p) \ dp \tag{7.22}$$

The optimal value for an individual cut $c_0$ can be found as the maximum of the function

$$Sign.(c) \approx \frac{N_S(c)}{\sqrt{N_B(c)}} \tag{7.23}$$

This is illustrated in the lower panel of figure 7.14.

**Advantages and limits of the one dimensional approach:**  The method has the advantage to be simple and fast. It allows for identifying a good set of cuts within a reasonable time. Nevertheless, there are some weak points. If more than one selection criterion is applied, the one-dimensional approach can only be used in a sequential way. A background pair can be rejected by more than one cut. The order in which the cuts are optimised might have therefore some importance. To understand this argument in detail, it is worth thinking over the significance as a function of two cuts $c_1$ and $c_2$:

$$Sign.(c_1, c_2) = \frac{N_S(c_1, c_2)}{\sqrt{N_B(c_2, c_2)}} \tag{7.24}$$

Using the single cut optimization method, one has now to set $c_1$ ($c_2$) to a defined value for optimizing $c_2$ ($c_1$), respectively. After having found the optimal condition for the first parameter,
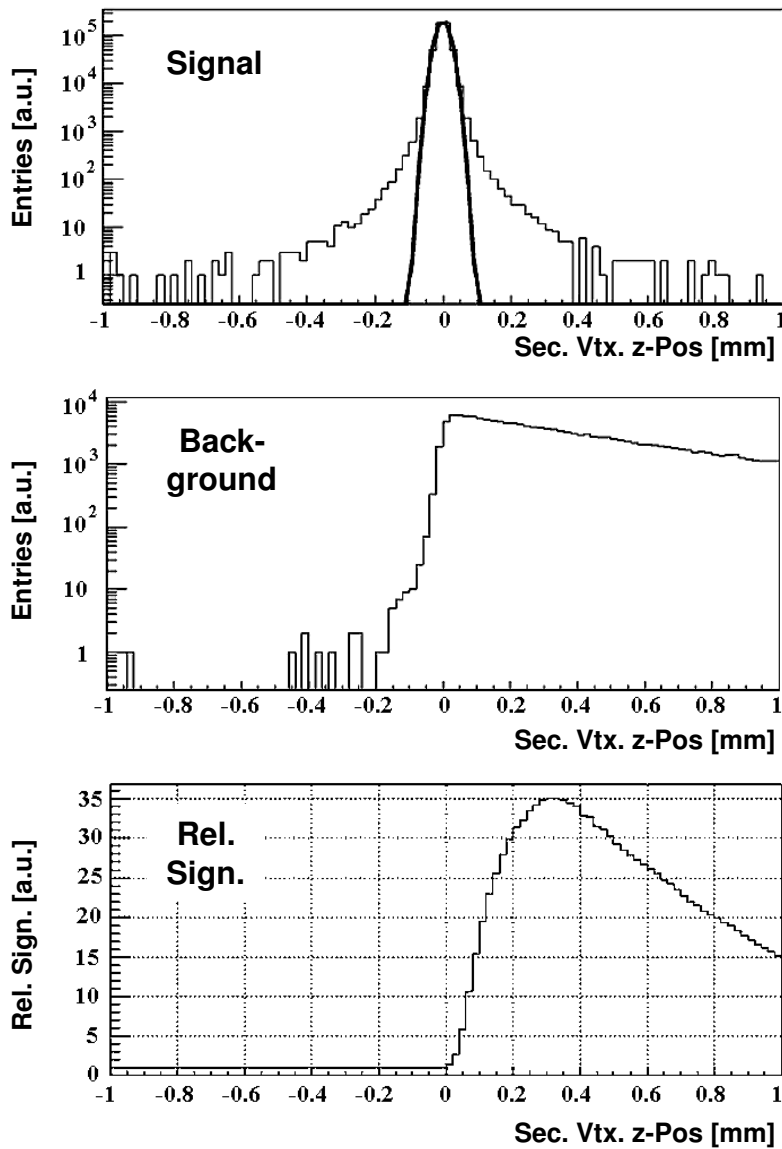
Figure 7.14.:
*Signal (up) and background (middle) distributions of the position of the secondary vertex along the beam - axis. The primary vertex is located at the origin of the coordinate system. The optimum cut value providing the best relative significance (lower plot) can be found at $c_0 = 0.3$ mm. Note than only the shape of the significance plot is meaningful unless signal and background are normalized. Normalization is not required for defining the cut value. From [74].*

one optimizes the second one. As illustrated in figure 7.15, this method does not necessarily find the optimal cuts in the two dimensional case. Moreover, the results depend on the order in which the cuts were applied. This motivated the use of a multidimensional approach.



Figure 7.15.:
*Schematic representation of the problem arising from the use of the single cut optimization method in the multi-dimensional case. The procedure of optimizing one cut after the other corresponds to choosing the paths marked in red within the two dimensional function. One observes that the result depends on the order, in which the cuts are optimized. Moreover, the optimum is not found in this example.*
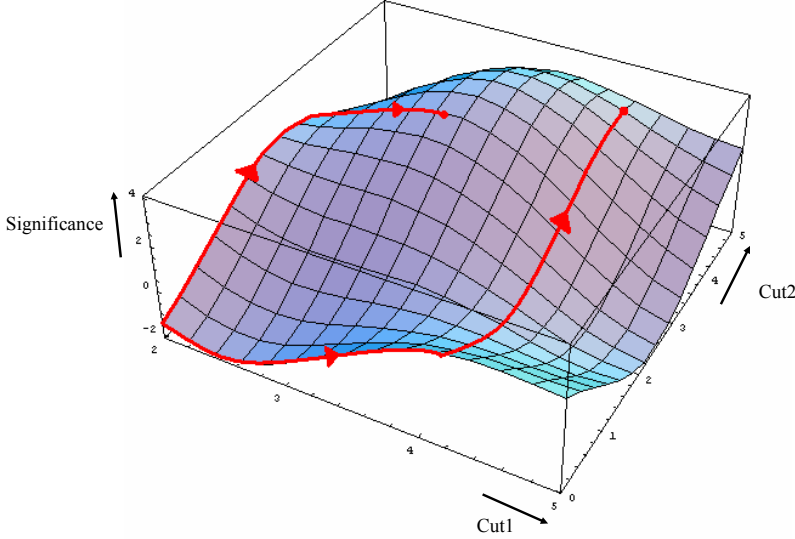
### 7.5.2.4. An algorithm for multidimensional cut optimization

In order to overcome the weak point of the one dimensional approach, it is worth to express the significance of a signal as a function of a vector of cuts, as this was already suggested by equation 7.24. This is justified if the statistics of signal and background is sufficient to neglect discretization. If so, one may write $Sign.(c_1, c_2, \ldots, c_n)$ as a well defined function $Sign.(\vec{c})$. Finding the optimal set of cuts becomes then equivalent to a maximum search on a function $f(\vec{x})$. There are several methods for searching an extreme of such a function.

One of these methods consists in following the derivative $\vec{\bigtriangledown} f(\vec{x})$ of the function towards its extreme. As the analytic form of the function is unknown, this was done in a simplistic but robust way in analogy to deriving the numerical derivative. One obtains this derivative for a sufficiently small, positive number $h$ like:

$$\frac{\partial}{\partial c_i} Sign.(\vec{c}) \approx Sign.(c_1, c_2, \ldots, c_i + h, \ldots, c_n) - Sign.(c_1, c_2, \ldots, c_i, \ldots, c_n). \tag{7.25}$$

In the iterative algorithm used, three points on the function were compared with each other. Those points were defined as following:

$$\vec{c_0} = (c_1, c_2, \ldots, c_i \quad\ , \ldots, c_n) \tag{7.26}$$
$$\vec{c_1} = (c_1, c_2, \ldots, c_i + h, \ldots, c_n) \tag{7.27}$$
$$\vec{c_2} = (c_1, c_2, \ldots, c_i - h, \ldots, c_n) \tag{7.28}$$

In one iteration step, $Sign.(\vec{c_0})$, $Sign.(\vec{c_1})$ and $Sign.(\vec{c_2})$ were compared. The option showing the highest $Sign.$ was chosen as starting point for the next iteration.

As shown in the schema of the algorithm, which is displayed in figure 7.16, the iteration process was continued by improving once all the other cuts (dimensions of $\vec{c}$). Hereafter, the procedure
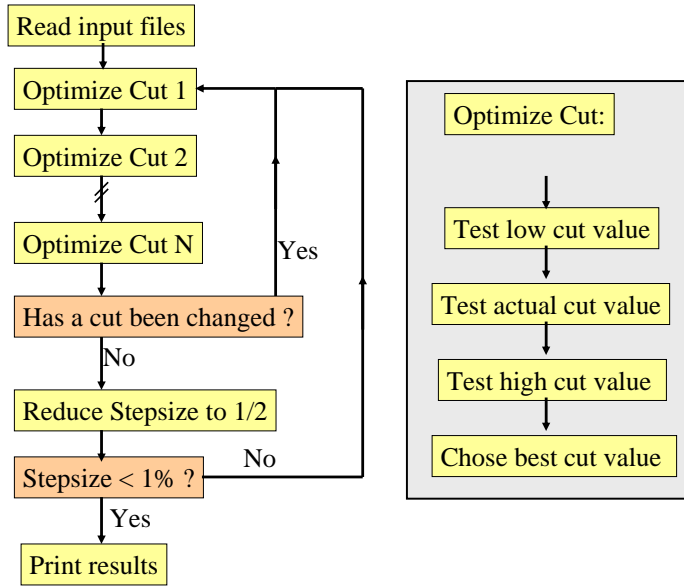
Figure 7.16.:
*Algorithm of the multi dimensional cut optimizer*

was repeated in order to allow the algorithm to approach the maximum in several steps. If no further update of the optimum could be found for a step size $h$, it was considered that the distance between the coordinate reached and the optimum is closer than the step size. A smaller $h$ was used for the next iteration. The algorithm was stopped when reaching a sufficiently small step size. The software based on this algorithm will be named *cut optimizer* in the following.

**Software implementation** The main difficulty in implementing the cut optimizer into CbmRoot was due to the fact that the structure of the CbmRoot files is optimized for processing the events sequentially. Signal candidates are individually accepted or rejected and their invariant mass is stored in a histogram. It is therefore not necessary to keep the data on more than one candidate in the memory. In contrast, evaluating $Sign.(\vec{c})$ requires accessing all candidates simultaneously. This is only possible, if the number of candidates is sufficiently reduced to fit the corresponding data into a file or better into the RAM of a PC.

Given the high number of candidates, this requires an efficient preselection of candidates by means of preliminary cuts. The way to do this was already discussed at the beginning of section 7.5.2.3. The following preselection cuts were applied on single tracks[18]: $p > 1\ GeV/c$, $p_t > 0.3\ GeV/c$ and $PV > 2.4\ \sigma$. As in particular the $PV$-cut is highly efficient, those cuts were sufficient to reduce dramatically the number of candidates. The remaining candidates were written into a file, which was then used as input for the algorithm.

### 7.5.3. Statistics and setup of the simulation

A detailed simulation study was done for Geo11, which is the MVD geometry showing the best performance according to section 7.4. For reasons of CPU time, the simulation relied on ideal track finding but realistic track fitting. The signal was formed by $10^4$ $D^0$-particles. For technical reasons, each of them was embedded into an event formed by a central $Au + Au$ collision. The background was formed by super-events based on 330 central collisions. These super-events are interpreted as $330^2 = 108900$ equivalent events. A total background statistics of $2.4 \times 10^7$ central events (equivalent) was used in the simulations.

---

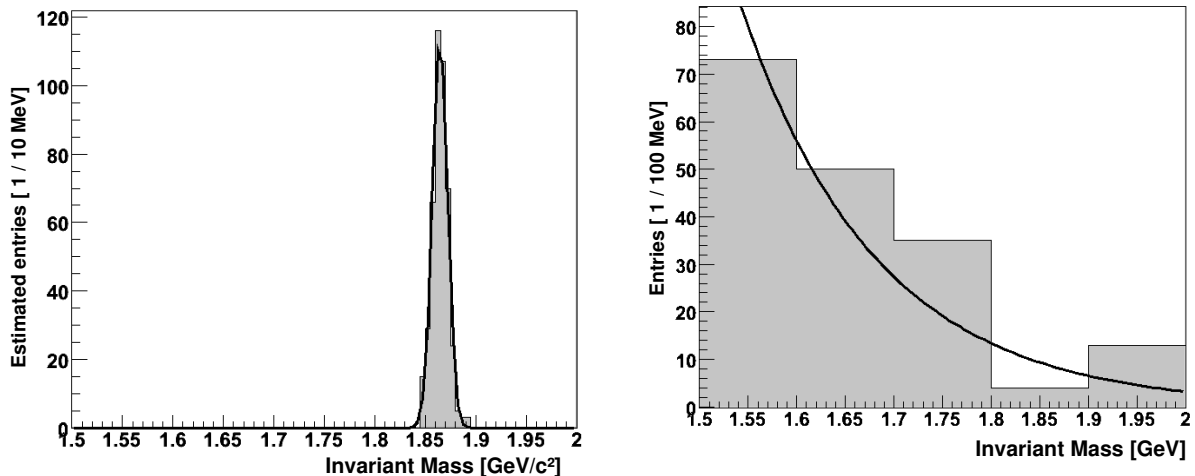[18]The definition of the cuts can be found in section 7.5.2.1.

Figure 7.17.: *The signal (left) and the background (right) invariant mass distributions obtained by applying the selection cuts (see text). Only the invariant mass range between 1.5 $GeV/c^2$ and 2.0 $GeV/c^2$ is displayed. The resulting fitting functions are shown.*

| Cut | Value |
|---|---|
| Momentum-cut | $p > 1\ GeV$ |
| Transverse momentum-cut | $p_t > 1\ GeV$ |
| PV-cut | $PV > 5.292\ \sigma$ |
| SvZ-cut | $774\ \mu m < SvZ < 1\ cm$ |
| SvChi-cut | $SvChi < 1.194\ \sigma$ |
| IPD0 - cut | $IPD0 < 22.3\ \mu m$ |
| Impact parameter cut | $IP < 600\ \mu m$ |

Table 7.6.: *List of the cut values of the major cuts used for $D^0$-reconstruction. The conditions to be fulfilled are shown. The definition of the cuts can be found in section 7.5.2.1.*

The particle identification abilities of CBM were modeled in a simplistic way by rejecting all proton tracks. This is justified by the good proton identification abilities of the time of flight detectors of CBM.

Despite the high statistics used in the simulation, the number of entries remaining in the invariant mass distribution of the background is very low after applying the selection cuts listed in table 7.6. The background distribution was fitted with an exponential function between 1.5 $GeV/c^2$ and 2.0 $GeV/c^2$ to obtain nevertheless a useful background estimate. The background distribution and the fit are shown in figure 7.17 (right). The signal distribution was also fitted. A Gaussian function was used in this case as can be seen in the left panel of figure 7.17.

The resulting fitting functions were used to evaluate the detection efficiency and the S/B ratio. This was done by integrating the signal and the background functions, respectively, within an invariant mass region of interest, which is given by $m_{D^0} \pm 20\ MeV$.

The statistical uncertainty of the background estimate of the simulation was derived by propagating the uncertainties of the fit parameters to the integral. It was observed that the uncertainties of the integral are bigger than the corresponding value. Therefore, no reasonable lower limit is available for the background. However, the parameters of interest in this context are the most probable value and the upper limit of the background rate, which are accessible.

The uncertainties on the signal are negligible with respect to the uncertainties of the back-

ground.

### 7.5.4. Normalization and S/B

Before calculating the S/B, one has to remind that signal and background provided by the generators were not normalized to each other. $10^4$ $D^0$ and $2.4 \times 10^7$ central collisions were used in the simulation. This corresponds to $4.2 \times 10^{-4}$ $(D^0 \rightarrow K^- + \pi^+)$ decays per central collision in the simulation. The expected ratio for the CBM experiment is given by $4.6 \times 10^{-6}$ $(D^0 \rightarrow K^- + \pi^+)$ decays per central collision assuming a production multiplicity of $1.2 \times 10^{-4}$ and a branching ratio of 3.8 %. The events in the simulation were thus enriched with signal as compared with reality. This was done to reach a meaningful signal statistics.

After normalizing the results, the S/B-ratio for $D^0 \rightarrow K^- + \pi^+$ can be derived. It is given by $S/B \approx 2.0$. Accounting for the statistical uncertainties of the background estimate, on finds that the S/B will be > 0.53 with 95 % probability.

Besides the statistical uncertainties already mentioned, this satisfactory result underlies uncertainties, which are due to the assumptions made in the simulation model. The most obvious among them concerns the unknown production multiplicity for open charm at FAIR energies. As no measured data on open charm production is available in the energy region of interest, this uncertainty is considered as sizable.

Moreover, the detector model used in the simulation was still preliminary. The material budget assumed is based on ideal assumptions and might come out to be underestimated. If so, the performance of CBM might be significantly overestimated by the simulation. On the other hand, the CBM particle identification system was only represented by proton rejection. Accounting for the full abilities of this detector might lead to better performances.

Another important source of bias is due to the statistics used in the simulation. The highly efficient selection cuts identified were sufficient almost to remove fully the background. This means that due to a lack of remaining background, potential additional background rejection capabilities of CBM were not accounted for. Following this argument, it seems possible that the simulation shown here underestimates the S/B of the CBM-experiment. This remains to be checked with simulations based on higher statistics.

### 7.5.5. Significance of the signal

The good S/B-ratio achieved indicates that a MAPS based vertex detector can provide the selectivity required for open charm physics at CBM. Nevertheless, this information alone is not sufficient to judge the feasibility of the experiment, as it is not clear if one can measure a sufficient number of collisions before the vertex detector is destroyed by radiation damage. In order to obtain this information, one has to estimate the number of signal and background pairs, the vertex detector will accept within its lifetime. Hereafter, one can calculate the significance of the signal for open charm.

To estimate the amount of signal and the background pairs, we normalized the results provided by the simulation to the lifetime of the vertex detector. This lifetime is given by $\sim 1.2 \times 10^{11}$ central collisions[19].

We found that within the lifetime of the MVD, the number of signal and background pairs would be $N_S = 2.5 \times 10^4$ and $N_B \approx 1.2 \times 10^4$ ($N_B < 3.3 \times 10^4$ with a probability of 95 %). According

---

[19]According to section 7.3, table 7.2. Note that only 10 % of the collisions listed in this table are considered as central ones.
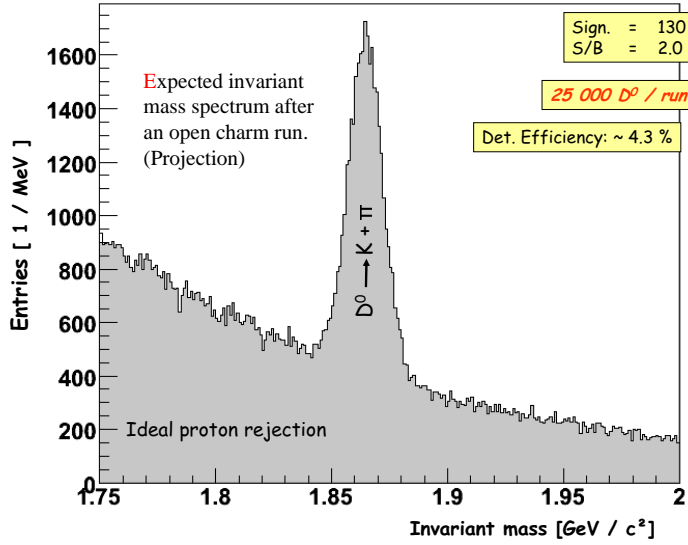
Figure 7.18.:
*Expected invariant mass distribution for a typical CBM-run (see text for details). Note the different bin sizes with respect to figure 7.17.*

to

$$Sign. = \frac{N_S}{\sqrt{N_S + N_B}} \qquad (7.29)$$

one obtains a significance of $Sign. = 130^{+30}_{-40}$. The uncertainty towards lower values was defined by propagating the uncertainty of the background estimate. Towards higher values, the limit is set by the Poisson-fluctuation of the signal in absence of any background.

The results obtained with the simulation ($S/B \approx 2$, $Sign. \approx 130$, $N_S \approx 25000$) suggest that the running scenario proposed will allow for doing excellent open charm physics with CBM. The number of reconstructed mesons is by more than a factor of two above the requirements. Because of the good $S/B$ and significance of the signal, it is very likely that already the statistics collected within the lifetime of one vertex detector will be sufficient for detailed studies of open charm.

The significance of the open charm signal in CBM is illustrated in figure 7.18, which shows the invariant mass distribution in the mass region of interest, as it is expected as a result of a typical CBM-run. This figure was produced based on the fit functions for signal and background shown in figure 7.17. The functions were normalized to the statistics corresponding to the lifetime of the vertex detector. Hereafter, they were added. The fluctuations representing the statistical uncertainties in the bins after measuring $1.2 \times 10^{11}$ central collisions were added by means of a random generator. It has to be pointed out that those fluctuations do therefore *not* represent the uncertainties of the simulation, which has substantially lower statistics.

### 7.5.6. Acceptance of the CBM experiment for $D^0$-mesons

According to the simulation results, the absolute number of reconstructed $D^0$-mesons will be satisfying. However, it remains to be clarified if the acceptance of CBM covers the phase space of interest, e.g. the mid-rapidity region.

Figure 7.19 illustrates the effect of the acceptance for $D^0 \rightarrow K^+ + \pi^-$ in the "transverse momentum - rapidity" plane. The upper panel shows the initial ($4\,\pi$) distribution used as input in the simulations. The mid-panel displays the distribution obtained taking into account the geometrical acceptance of the detector and the lower panel shows the same distribution after applying the selection cuts used for the reconstruction of $D^0$ particles.
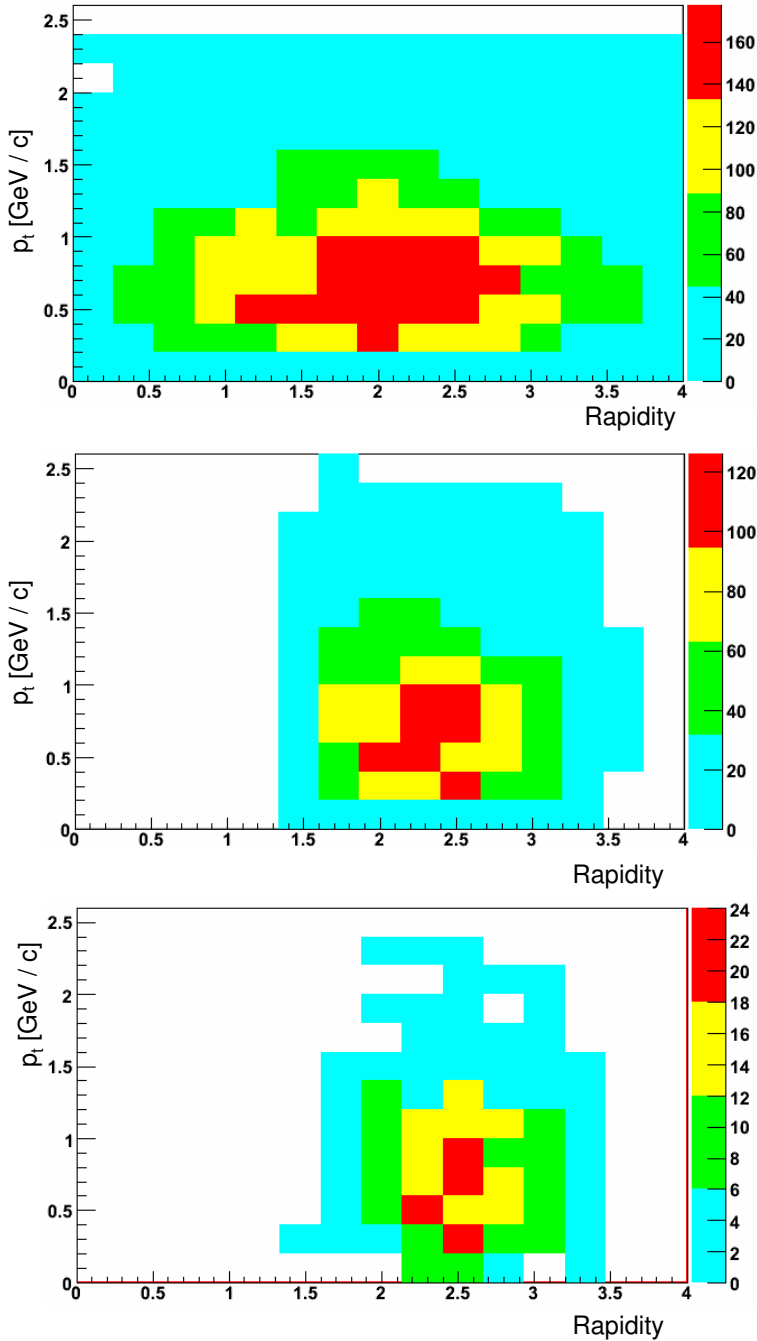
Figure 7.19.:
*Acceptance for $D^0 \rightarrow K^+ + \pi^-$ illustrated in the "transverse momentum - rapidity" plane. The centre-of-mass rapidity is $Y = 2$ at $25$ $AGeV$. Upper panel: Initial $4$ $\pi$ distribution. Mid panel: Same distribution taking into account the geometrical acceptance. Lower panel: Distribution after applying selection cuts.*
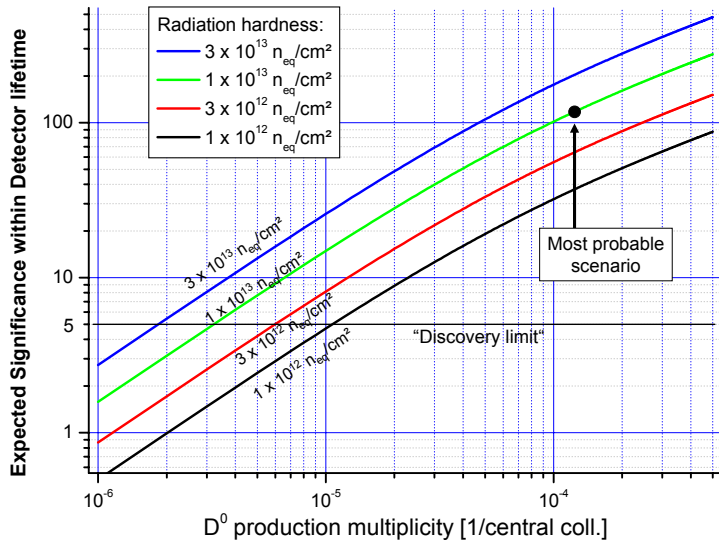
Figure 7.20.:
*Estimated significance of the $D^0$ - signal as a function of the $D^0$ production multiplicity in central Au+Au collisions at 25 AGeV. The results are shown for different assumptions on the radiation tolerance of MAPS-detectors. The point corresponding to the initial assumptions on this work is emphasized ("Most probable scenario"). Moreover, the "discovery limit" for particles, which corresponds to a significance of five is displayed.*

The geometrical acceptance for $D^0$ particles is found to be about 35 %. As can be seen in the mid panel of figure 7.19, the detector allows the coverage of a large fraction of the phase space and in particular the mid-rapidity region, i.e. the region around the center-of-mass rapidity $Y = 2$ .

Applying the selection criteria reduces the number of accepted $D^0$-mesons by a factor of $\sim 8$ but does not affect significantly the phase space coverage as can be seen qualitatively from the comparison of the mid and lower distributions of figure 7.19.

## 7.5.7. Robustness of the results

The results obtained in the previous section demonstrate the feasibility of open charm measurements with CBM using the proposed MAPS-pixel based vertex detector. It is shown that the experiment allows for a good separation of signal and background with a good significance. Nevertheless, this statement holds only, as far as the initial assumptions, which were used in building the simulations, are roughly correct.

Given that some of the parameters used underlay substantial uncertainties, it is worth estimating the consequences of incorrect assumptions. This was done for two of the most crucial parameters, which are the radiation tolerance of MAPS and the production multiplicity of open charm. Both parameters have a straightforward impact on the significance of the open charm signal in the detector. One can therefore easily rescale the simulation results for different assumptions.

The outcome of this study is displayed in figure 7.20, which shows the expected significance of the $D^0$ signal as function of the production multiplicity. The different lines present assumptions on the radiation hardness of MAPS. The assumptions used for the simulation results discussed above are emphasized. One observes that nowadays radiation tolerance $\sim 3 \times 10^{12}$ $n_{eq}/cm^2$ is sufficient to provide a significance of the $D^0$ signal, which is $\sim 60$. If the anticipated radiation tolerance is reached, a significant ($5\ \sigma$) signal for $D^0$ can be measured down to production multiplicities of $\lesssim 4 \times 10^{-6}$ $D^0$ per central collision. This is by a factor of 30 below the expected value.

From this, one can conclude that a very significant signal may be reached even if the radiation tolerance of MAPS or the production multiplicity of $D^0$ are substantially below the expected value. However, the open charm physics potential of the experiment would be limited by low statistics.

## 7.6. Summary and Conclusion

Simulations were undertaken to investigate the feasibility of open charm physics in the CBM experiment using a MAPS-pixel based vertex detector. A running scenario was developed, which focuses on the particular strong points of the MAPS-detectors, formed by their very low material budget and very high granularity. It is proposed to maximize the benefit of those advantages by using reduced beam intensity (to few $10^5$ collisions / s), which will allow overcoming the limits of the technology in terms of readout speed and radiation hardness. The validity of this proposal was demonstrated by the results of simulations.

The simulations were done in two steps, one aiming for an estimate of the radiation doses impinging the vertex detector and a second evaluating the sensitivity of the experiment for open charm. The simulation of the radiation doses show that the radiation hardness of the best performing geometry (referred as Geo11) will allow for the measurement of $1.2 \times 10^{11}$ central collisions.

Unlike the initial geometry of CBM, which features a first vertex detector station $z = 5 \ cm$ downstream the target, the first station of this updated geometry is located at $z = 10 \ cm$. The inner radius of the stations was increased to 11 $mm$. According to the results obtained, both modifications allowed reducing substantially the radiation doses impinging the detector while their selectivity is only modestly reduced. This leads to an improved compromise between long lifetime and high detection efficiency.

A simulation with a high statistics of $2.4 \times 10^7$ background events was done by using super events. This simulation proved the outstanding selectivity of a vertex detector based on MAPS. The results suggest that the lifetime of a vertex detector is sufficient to reconstruct $\sim 2.5 \times 10^4 \ D^0$-mesons with a $S/B = 2.0$ ($> 0.53$ with 95 % probability) and an excellent significance $Sign. = 130^{+30}_{-40}$. As MAPS can be produced in cheap industrial mass production and the detector is easily to access, a regular replacement of the station can be foreseen to enhance the statistics.

Substantial margins are available to do the measurements even if the production multiplicities of open charm or the radiation hardness of MAPS are lower than expected.

The results shown rely on different assumptions, which remain to be confirmed. The probably most important among them is the assumption made on the production multiplicity of $D^0$ for Au+Au collisions at energies of 25 $AGeV$. According to model predictions, a production multiplicity of $1.2 \times 10^{-4}$ was assumed. This value underlays however important uncertainties.

The radiation hardness assumed for MAPS in the simulation was according to our design goals and exceeds nowadays value by a factor of roughly five.

Concerning the assumptions made on the detector geometry, it came out meanwhile that the material budget of the main tracker of CBM was significantly underestimated. Moreover, as discussed in chapter 3.2, refined estimates suggest a material budget of MAPS stations of $300 - 500 \ \mu m$ silicon equivalent instead of the 200 $\mu m$ assumed in this work. The simulation performed tends therefore to overestimate the performances of MVD and STS.

On the other hand, the particle identification abilities of CBM were only considered by assuming a perfect proton rejection. This represents a very pessimistic picture of the performances of the time-of-flight system of CBM. Accounting for the full performances of this detector might substantially improve the results.

Finally, one should note that almost all background produced in the simulation was removed. It was therefore not possible to test, if a better $S/B$ could be reached by applying stricter cuts. Again, better results might be demonstrated with more elaborated simulations based on higher statistics.

Despite of the remaining open issues mentioned above, one can state that CBM being equipped with a MAPS-pixel based vertex detector will provide a unique instrument for studying open charm physics in heavy ion collisions at FAIR energies.

# 8. Summary and conclusion

The work presented in this thesis addresses a key issue of the CBM experiment at FAIR, which aims to study charm production in heavy ion collisions at energies ranging from 10 to 40 $AGeV$. For the first time in this kinematical range, open charm mesons will be used as a probe of the nuclear fireball. Despite of their short decay length, which is typically in the order of few 100 $\mu m$ in the laboratory frame, those mesons will be identified by reconstructing their decay vertex.

The most essential sub-detector for efficient open charm reconstruction is a high resolution micro vertex detector (MVD) installed in the vicinity of the experimental target. Achieving the required spatial resolution conflicts with the necessity to cope with the high particle flux and radiation level inherent to the proximity of the target. Since usual pixel technologies do not provide a satisfactory trade-off between these antagonistic requirements, the adequacy of CMOS Monolithic Active Pixel Sensors (MAPS) was investigated. The objective of the thesis was to demonstrate that these devices could allow to collect, identify and analyze at least 10,000 $D^0$-mesons produced in heavy ion collisions. Such a large sample is expected to allow shedding light on fundamental phenomena such as the appearance of Quark-Gluon Plasma (QGP) and as chiral symmetry restoration.

Demonstrating the necessary sensitivity of a MAPS based MVD required performing R&D to clear up and approach the ultimate performances of the novel MAPS technology. Extensive simulation and design studies were done to refine and improve the design of the MVD. Finally, a high statistics simulation was used to show that the combination of improved MVD and pixel design allows for reconstructing a sufficient amount of $D^0$-mesons.

The R&D discussed in the thesis focused on the radiation tolerance of MAPS, which was still poorly known a few years ago. An $^{55}Fe$-source and minimum ionizing particle beams were used to study the performances of MAPS being irradiated either with neutrons or X-rays. This allowed clarifying, how ionizing and non-ionizing radiation damage manifest themselves in this specific technology. As expected, ionizing radiation dominantly causes an increase of the leakage current of the pixels, which translates into increased shot noise. Non-ionizing radiation generates modest increases in terms of leakage currents but can reduce substantially the lifetime of the signal electrons in the pixel. The latter was found to cause a dramatic drop of the signal if the lifetime of the electrons shrinks below the time required for charge collection.

The performances of irradiated detectors were studied as a function of the operation conditions, i.e. in terms of temperature and integration time of the pixel. It was demonstrated that running the detectors at low temperature ($\lesssim -20°C$) and with short integration time efficiently reduces their leakage currents and noise. This may restore the initial performances of detectors being irradiated with ionizing radiation. For chips being exposed to non-ionizing doses, both measures are helpful to dim the effects of leakage current. However, they have no significant impact on the lifetime of the signal electrons.

The understanding achieved allowed proposing several generations of MAPS pixels with improved radiation hardness. The latter was reached by removing the radiation soft, thick $SiO_2$ in the vicinity of the sensing diode and by putting guard rings around the diode. The modified structure exhibited much better performances after irradiation than previous designs. Moreover, the radiation tolerance against non-ionizing doses was found to improve by almost one order of

magnitude when reducing the pixel pitch by a factor of two, thereby shortening the charge collection time. The modifications allowed to maintain satisfactory detection performances after an exposure to ionizing radiation of $\sim 1\ MRad$ or to a fluence of $\sim 2 \times 10^{12}\ n_{eq}/cm^2$.

Further progress in terms of radiation tolerance might be reached by further reducing the charge collection time of the pixels. This can be done by using a smaller ($< 20\ \mu m$) pixel pitch, a graded epitaxial layer or a collection diode based on deep N-well implantations. Moreover, the drop in the lifetime of signal electrons might be alleviated by operating the detector at cryogenic temperatures. Finally, it remains to be clarified if thermal annealing of the chips might have a beneficial effect. A radiation tolerance of MAPS in the order of $\sim 10^{13}\ n_{eq}/cm^2$ is considered as a realistic estimate for the ultimate performances of this technology.

The feasibility of a massive parallel readout of MAPS, which will presumably allow for a time resolution of $\sim 10\ \mu s$, has been demonstrated in parallel to this work. Though not belonging to the research program presented here, the main outcomes of the development of fast sensors were presented and embedded into the general detector concept.

Despite of the progress achieved, the technological studies showed that MAPS will presumably not reach the time resolution and radiation tolerance required for operating them at the high nominal collision rate of CBM, which may reach $10^7$ collisions per second. This is because the radiation doses caused by this collision rate would shrink the lifetime of the detector to a few days. Moreover, given the time resolution of the chips, pile-up would become a major concern (up to 100 collisions per frame are expected).

It was however demonstrated that a balanced configuration exists where, for lower beam interaction rate, enough $D^0$-mesons can be collected and analyzed to investigate their production properties with a satisfactory sensitivity. To do so, a preliminary concept for integrating individual MAPS chips into a vertex detector station was developed. The concept accounted for the major technological constraints derived from the detector R&D and for the need to operate the vertex detector in vacuum. The latter seems necessary to eliminate the material, which would otherwise be introduced by the beam pipe.

The integration of MAPS into a detector is mainly constrained by the need for good radiation tolerance, which calls for operating the sensors at temperatures of $\lesssim -20\ °C$. An efficient and vacuum compatible cooling system is thus needed. Moreover it was shown, that $\lesssim 50\%$[1] of the surface of MAPS featuring $\sim 10\ \mu s$ time resolution will host data processing circuits. This surface is not sensitive and has thus to be covered with the active surface of a neighboring chip.

In order to account for all requirements, it was proposed to stagger two layers of silicon, which are installed on the opposite sides of a layer formed by micro tubes. The latter provides the necessary mechanical stability and evacuates the heat produced by the sensors by means of liquid cooling. Though the design is considered as preliminary, it provides guidelines for further studies and allows for a first estimate of the material budget of a MVD-station. This estimate suggests that this budget might be as low as a few per-mille of radiation length.

Systematic studies were undertaken to design a well performing MVD made of a few individual detector stations. The geometry of the MVD was tuned in a systematic way in order to find the best compromise between good tagging efficiency (calling for a small distance between target and detector) and low radiation doses (calling for an increase of this distance). The geometries were benchmarked with their ability to reconstruct a maximum number of $D^0$-mesons before the radiation doses exceed the radiation tolerance of the sensors. To do so, the radiation dose per collision and the reconstruction efficiency for $D^0 \rightarrow K + \pi$ were estimated for each geometry considered. It was shown that increasing the distance between target and first detector station

---

[1]This value is presently rather around $\sim 30\%$.

from 5 $cm$ to 10 $cm$ provides a valuable compromise, as the substantial improvement reached in terms of detector lifetime dominates the modest losses in charm reconstruction efficiency.

For the best performing MVD-geometry, a high statistics simulation based on $2.4 \times 10^7$ central Au+Au collisions at a beam energy of 25 $AGeV$, was carried out. A collision rate of about $10^5/s$, which prevents from pile-up effects, was observed to be viable. Assuming the predicted production multiplicity of $1.2 \times 10^{-4}$ $D^0$-mesons per central collision, it was shown that the MVD allows to reconstruct $\sim 2.5 \times 10^4$ $D^0$-mesons, with a $S/B = 2.0$ ($> 0.53$ with 95 % probability) and an excellent significance of $Sign. = 130^{+30}_{-40}$. Those results, which can be obtained within a few months of beam time, fit the physics requirements defined by the CBM-collaboration.

The main systematic uncertainties of the results arise from the early stage of the system integration studies, from the modest precision of the predicted production multiplicities of open charm at FAIR energies and the need to extrapolate the technological progress of the MAPS technology over several years. The consequences of major biases in the estimates used were therefore studied. It was shown that nowadays radiation tolerance of MAPS allows for a significant ($Sign. \geq 5$) reconstruction of $D^0$-mesons for production multiplicities of $\gtrsim 10^{-5}$ mesons per central collision. Assuming the presumed ultimate radiation hardness of MAPS, production multiplicities down to $\gtrsim 5 \times 10^{-6}$ mesons per central collision are sufficient. As however the absolute number of reconstructed particles shrinks, the physics studies achievable would be limited by statistics if the actual production multiplicity misses the predictions by more than a small order of magnitude.

Because of technical constraints, the hadron identification abilities of the time-of-flight system of CBM were not fully accounted for in the simulation presented. Any hadron identification going beyond proton rejection might therefore substantially ameliorate the numbers presented. Moreover, a regular replacement of the most irradiated parts of the vertex detector station can improve the global detection performance substantially. The replacement is considered as feasible taking into account both, system integration and financial aspects.

The beam time required for a measurement would shrink, if some pile-up of nuclear collisions in the MVD could be tolerated. This was so far not studied systematically because of technical and time constraints. However, given the high granularity of MAPS, it seems likely that modest pile-up will have no substantial impact on the detector performances. The limitation may rather come from the central tracker and its track extrapolation abilities.

Concluding, one may state that a MAPS based MVD will allow for doing $D$-physics at CBM. This holds in particular for beam energies of 35 $AGeV$ since the production multiplicities of those mesons increases strongly with energy. For 25 $AGeV$, the simulations of the present work indicate that the necessary performances will be reached but the safety margins are not sufficient to guarantee a satisfactory amount of reconstructed particles if reality departs from the assumptions made in this study by more than a factor of about three.

The feasibility of doing open charm physics at a beam energy of 15 $AGeV$ and of reconstructing the $\Lambda_C$ were not addressed in the thesis. Given the poor production multiplicities of $D$-mesons at this beam energy and the short lifetime of the $\Lambda_C$, reaching the ambitioned sensitivity seems questionable. One may therefore start the physics program of CBM at high beam energies with a MAPS based vertex detector. Doing so will provide the necessary time for developing a second generation MVD relying on newly arising detector technologies, like SOI-detectors or detectors based on vertical VLSI integration. Despite the fact that both technologies are presently still in a very early phase of their development, their conceptual potential justifies considering them for covering the low energy part of the CBM physics program.

*8. Summary and conclusion*

# A. Appendix

## A.1. Preliminary requirements on spatial resolution and material budget of the vertex detector

The requirements on the secondary vertex resolution of the CBM vertex detector are given with $\sim 50\ \mu m$ according to the lifetime of open charm mesons. They have to be compared with the performance of a vertex detector design, which depends dominantly on the spatial resolution of the pixels used, its material budget and geometry. The requirements on the spatial resolution of the pixels and the material budget of the detector stations will be derived in the following in an analytic way. Monte Carlo simulations on the same topic are discussed in section 7.4.2.

Assuming the geometry of the detector as fixed, the secondary vertex resolution of the CBM-STS is dominated by two sources, the resolution of the detector stations $\Delta y$ and the multiple scattering angle $\theta$. This angle describes the bending of the particle trajectory, which is caused by the interaction between the particle and the numerous atoms of the material. Both sources influence the secondary vertex resolution $\Delta z$ according to

$$\Delta z = \Delta z_{mult}(\theta) \oplus \Delta z_{res}(dy). \tag{A.1}$$

Here $\Delta z_{mult}$ represents the uncertainty caused by multiple scattering and $\Delta z_{res}$ stands for the uncertainty caused by the limited spatial resolution of the detectors. The geometry used to derive both parameters is shown in figure A.1. One defines $y_1$ and $y_2$ as the position of the hit caused by the first and second track respectively in the first station. Moreover, $\alpha$ and $\gamma$ are defined as the angles of the tracks with respect to the z-axis. The measurement of these angles is done by combining information of the first and the second station. All four parameters are assumed to underlie an uncertainty.

From figure A.1, one learns that

$$\tan\alpha = \frac{y_1 - y_0}{l} \Rightarrow y_0 = y_1 - l\tan\alpha \tag{A.2}$$

In this equation, $l$ represents the distance between the first station and the intersection of the tracks. In analogy, one derives:

$$\tan\gamma = \frac{y_2 - y_0}{l} \Rightarrow y_0 = y_2 - l\tan\gamma \tag{A.3}$$

By merging both equations, this becomes:

$$l = \frac{y_2 - y_1}{\tan\alpha - \tan\gamma} \tag{A.4}$$

As $z = z1 - l$, this translates into:

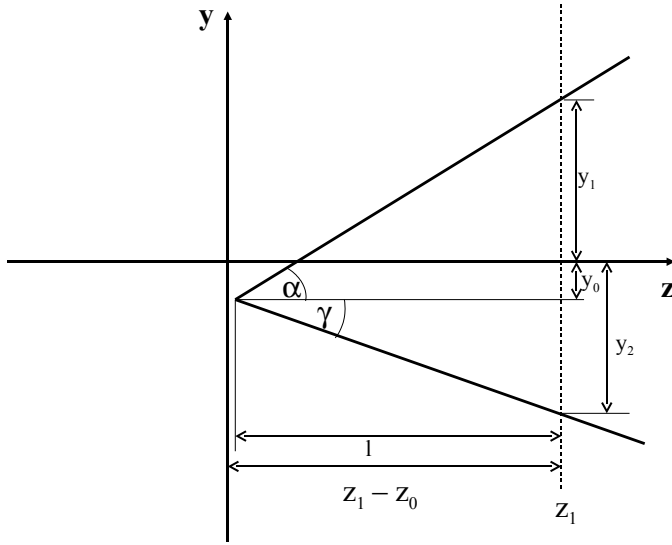$$z = z1 - \frac{y_2 - y_1}{\tan\alpha - \tan\gamma} \tag{A.5}$$

## A. Appendix



Figure A.1.:
*The resolution on the secondary vertex resolution of the STS assumes two tracks to merge close to the target located at the origin of the coordinate system. The tracks are measured by the first station located at $z = z1$, what delivers the impact position $y_1$ and $y_2$. The angles $\alpha$ and $\gamma$ are measured using also the second station (not shown).*

The uncertainty of $z = z(\alpha, \gamma, y_1, y_2)$ is given by $\Delta z$. It can be derived by using the error propagation:

$$\Delta z = \sqrt{\left(\left|\frac{\partial z}{\partial \alpha}\right| \cdot \Delta \alpha\right)^2 + \left(\left|\frac{\partial z}{\partial \gamma}\right| \cdot \Delta \gamma\right)^2 + \left(\left|\frac{\partial z}{\partial y_1}\right| \cdot \Delta y_1\right)^2 + \left(\left|\frac{\partial z}{\partial y_2}\right| \cdot \Delta y_2\right)^2} \tag{A.6}$$

By deriving the partial derivates, one obtains:

$$\Delta z = \sqrt{\frac{(y_1 - y_2)^2}{(\tan \alpha - \tan \gamma)^4} \cdot \left(\frac{\Delta \alpha^2}{\cos^4 \alpha} + \frac{\Delta \gamma^2}{\cos^4 \gamma}\right) + \frac{\Delta y_1^2 + \Delta y_2^2}{(\tan \alpha - \tan \beta)^2}} \tag{A.7}$$

So far, the calculation was made for a universal case. A significant simplification of the problem can be introduced by assuming $\gamma = -\alpha$ and $y2 = -y1$. Moreover, using the approximation $y1 \approx z_1 \tan \alpha$ will be helpful. The simplifications lead to a symmetric problem. As the geometry of both tracks is comparable, it is in first order justified to assume that they also underlay comparable uncertainties ($\Delta y = \Delta y_1 = \Delta y_2$ and $\Delta \alpha = \Delta \gamma$).

Introducing the assumptions into equation A.7 allows simplifying it to:

$$\Delta z = \frac{1}{\tan \alpha} \Delta y \ \oplus \ \frac{z_1}{\cos \alpha \ \sin \alpha} \Delta \alpha \tag{A.8}$$

While $\Delta y$ is given in a straightforward way by the resolution of the detector, the error on the angles is dominantly produced by multiple scattering. If approximating the distribution of the scattering angle $\Delta \alpha$ by a Gaussian distribution, one finds 98% of minimum ionizing particles within a width of the distribution given by

$$\Delta \alpha = \theta = \frac{13.6 \ MeV}{\beta c p} \cdot \sqrt{\frac{x}{X_0 \cos \alpha}} \cdot \left[1 + 0.038 \log\left(\frac{x}{X_0 \cos \alpha}\right)\right] \tag{A.9}$$

where $\beta$, $c$ and $p$ stand for the velocity, the speed of light and the momentum of the particle, $x/X_0$ for the thickness of the detector in radiation lengths and $\cos \alpha$ for the correction required for taking into account the prolongation of the interaction path for particles not passing the

detector vertically.

By introducing equation A.9 to A.8, one obtains

$$\Delta z = \sqrt{\frac{1}{\tan^2 \alpha} \Delta y^2 + \frac{z_1{}^2}{\cos^3 \alpha \, \sin^2 \alpha} \left( \frac{13.6 \; MeV}{\beta cp} \cdot \sqrt{\frac{x}{X_0}} \cdot \left[ 1 + 0.038 \log \left( \frac{x}{X_0 \cos \alpha} \right) \right] \right)^2} \quad (A.10)$$

In order to estimate the resolution on the secondary vertex, one simplifies this equation by assuming $\beta \approx 1$ and $c = 1$. This is justified as the particles produced in the fixed target collision underlay a significant Lorentz boost. Moreover, one sets $\alpha = \arctan\left(1 \; cm / \; 5 \; cm\right) \approx 200 \; mRad$ [1] and assumes the position of the first station to be located at $z_1 = 5 \; cm$. Such one obtains an equation showing the secondary vertex resolution as a function of the material budget and the resolution of the stations and of the momentum of the particle.

$$\Delta z = \sqrt{24.3 \; \Delta y^2 + \frac{124 \; (MeV \; cm)^2}{p^{\;2}} \frac{x}{X_0} \left( 1 + 0.038 \log \left[ 1.02 \; \frac{x}{X_0} \right] \right)^2} \quad (A.11)$$

Analyzing data of a thermal model used within the CBM-simulation framework (see [74]), one finds the momentum of the decay product of the reaction $D^0 \rightarrow \pi + K$ to follow a broad and non Gaussian spectrum. The mean value is given with roughly $p \approx 5 \; GeV$. Using this number, $\Delta z$ can be plotted as a function of the material budget of the stations and of the spatial resolution of the station. This is shown in figure 1.8 for resolutions between 1 $\mu m$ and 30 $\mu m$ and for a material budget of 0.1, 0.2, 0.3 and 1.0 % $X_0$. The figure shows, that a material budget of only few 0.1 % $X_0$ combined with a spatial resolution of $\lesssim 5 \; \mu m$ is required for achieving a secondary vertex resolution $\Delta z = 50 \; \mu m$.

---

[1]This value of $\alpha$ is somehow arbitrary, as the distribution of this parameter shows no a well defined mean value. The choice was motivated by the outcome of more detailed simulations discussed later in this work.

*A. Appendix*

# Bibliography

[1] FAIR - Conceptual Design Report, GSI 2001. Available online: www.gsi.de

[2] S. Heini, "Development of a highly granular, swift and radiation tolerant monolithic pixel sensor", Ph.D. Report, IPHC, under preparation.

[3] The CBM-Collaboration: "Compressed Baryonic Matter Experiment - Technical Status Report - January 2006 (Update)", GSI 2006, Available online: http://www.gsi.de/documents/DOC-2006-Feb-108-1.pdf

[4] P. Senger: "Strangeness and charm of compressed baryonic matter - the CBM experiment at FAIR", J. Phys. G: Nucl. Part. Phys. 31 (2005) S1111–S1114

[5] Bernd Müller: "Physics and signatures of the quark-gluon plasma", Rep. Prog. Phys. 58 (1995) 611-636

[6] T. Matsui, H. Satz: "$J/\Psi$ suppression by quark-gluon plasma formation", Physics Letters B, Volume 178, number 4, page 416.

[7] M.C. Abreu et al. oh behalf of the NA-50 Collaboration: "Observation of a threshold effect in the anomalous $J/\Psi$ suppression", Physics Letters B, Volume 450, Number 4, pp. 456-466

[8] S. Gavin, R. Vogt: "Charmonium suppression by Comover Scattering in Pb + Pb Collisions", Physical Review Letters Vol. 78, Number 6, page 1006

[9] A. Andronic, P. Braun-Munzinger, K. Redlich and J. Stachel, "Charmonium and open charm production in nuclear collisions at SPS/FAIR energies and the possible influence of a hot hadronic medium", arXiv:0708.1488 [nucl-th].

[10] W.Cassing, E.L. Bratkovskaya, A. Sibirtsev: "Open charm production in relativistic nucleus-nucleus collisions", Nucl. Physics A 691 (2001) 753-778

[11] "FAIR, An International Accelerator Facility for Beams of Ions and Antoprotons, Baseline Technical Report September 2006", Available online: http://www.gsi.de/fair/reports/btr.html

[12] Particle Data Group: "Particle Physics Booklet July 2004"

[13] K. Arndt et al.: "Silicon sensors development for the CMS pixel system", NIM-A 511(2003) 106-111

[14] J. Grosse-Knetter on behalf of the ATLAS Pixel collaboration: "The ATLAS pixel detector", NIM-A 568 (2006) 252-257

[15] C.J.S. Damerell: "CCD-based vertex detectors", NIM-A 541(2005)178-188

[16] J. E. Brau: "Investigation of radiation damage effects in neutron irradiated CCD", NIM-A 541 (2005) 117-121

[17] Michael Deveaux , Gilles Claus , Grzegorz Deptuch , Wojciech Dulinski , Yuri Gornushkin and Marc Winter: "Neutron radiation hardness of monolithic active pixel sensors for charged particle tracking", NIM-A, Volume 512, Issues 1-2, 11 October 2003, Pages 71-76

[18] R. Turchetta, J. D. Berst, B. Casadei, G. Claus, C. Colledani, W. Dulinski, Y. Hu, D. Husson, J. P. Le Normand, J. L. Riester, G. Deptuch, U. Goerlach, S. Higueret and M. Winter:"A monolithic active pixel sensor for charged particle tracking and imaging using standard VLSI CMOS technology", NIM-A Volume 458, Issue 3, 11 February 2001, Pages 677-689

[19] G. Claus, C. Colledani, W. Dulinski, D. Husson, R. Turchetta, J. L. Riester, G. Deptuch, G. Orazi and M. Winter: "Particle tracking using CMOS monolithic active pixel sensor", NIM-A Volume 465, Issue 1, 1 June 2001, Pages 120-124

[20] TESLA Technical Design Report, Available Online: http://tesla.desy.de/tdr/

[21] S.M. Sze, "Semiconductor Devices - Physics and Technology", John Wiley & Sons 1985, ISBN: 0471874248

[22] C. Kittel, "Introduction to Solid State Physics", John Wiley & Sons 2004, ISBN: 0471680575

[23] H. Stöcker, "Taschenbuch der Physik", Verlag Harry Deutsch 1998, ISBN 3-8171-1556-3

[24] Povh, Rith, Scholz, Zetsche: "Teilchen und Kerne", 5. Auflage 1999, Springer Verlag, ISBN 3-540-65928-5

[25] G. Lutz, "Semiconductor Radiation Detectors", Springer (1999), ISBN 3-540-64859-3

[26] August Besson, personal communication.

[27] G. Deptuch: "Développement d'un capteur de nouvelle génération et son électronique intégrée pour les collisioneurs futurs - A New Generation of Monolithic Active Pixel Sensors for Charged Particle Detection", PhD Université Louis Pasteur 2002, Available online: http://ireswww.in2p3.fr/ires/recherche/capteurs/index.html (English, french summary)

[28] Grzegorz Deptuch, Wojciech Dulinski, Yuri Gornushkin, Christine Hu-Guo and Isabelle Valin: "Monolithic active pixel sensors with on-pixel amplification and double sampling operation" NIM-A, Volume 512, Issues 1-2 , 11 October 2003, Pages 299-309

[29] G. Deptuch, G. Claus, C. Colledani, Y. Degerli, W. Dulinski, N. Fourches, G. Gaycken, D. Grandjean, A. Himmi, C. Hu-Guo, P. Lutz, M. Rouger, I. Valin, M. Winter: "Monolithic active pixel sensors with in-pixel double sampling operation and column-level discrimination" , IEEE Transactions on Nuclear Science, Volume 51, Issue 5, Part 1, Oct. 2004 Page(s):2313 - 2321

[30] Y.Degerli, G. Deptuch, N. Fourches, A. Himmi, Yan Li, P. Lutz, F. Orsini, M. Szelezniak: "A fast monolithic active pixel sensor with pixel-level reset noise suppression and binary outputs for charged particle detection", IEEE Transactions on Nuclear Science, Volume: 52, Issue: 6, Part 2, page(s): 3186- 3193

[31] W. Dulinski, personal communication.

[32] A. Gay, G. Claus, C. Colledani, G. Deptuch, M. Deveaux, W. Dulinski, Y. Gornushkin, D. GrandJean, A. Himmi, Ch. Hu, I. Valin and M. Winter: "High-resolution CMOS sensors for a vertex detector at the Linear Collider", NIM A Volume 549, Issues 1-3 , 1 September 2005, Pages 99-102

[33] Wojciech Dulinski,Andrea Braem, Massimo Caccia, Gilles Claus, Grzegorz Deptuch, Damien Grandjean, Christian Joram, Jacques Séguinot and Marc Winter: "Tests of a backside illuminated monolithic CMOS pixel sensor in an HPD set-up", NIM A Volume 546, Issues 1-2, 1 July 2005, Pages 274-280

[34] M. Battaglia, D. Contarato, P. Giubilato, L. Greiner, L. Glesener, B. Hooberman: "A Study of Monolithic CMOS Pixel Sensors Back-thinning and their Application for a Pixel Beam Telescome", arXiv:physics/0611081 v1 8 Nov 2006, Submitted to Elsevier Science

[35] Prof. Weischede: "Grundlage zum Verständnis und zur Entwicklung des Tragwerkkonzepts", Vorlesungsscript, Universität Darmstadt

[36] After W. Mann: "Vorlesung über Statik und Festigkeitslehre, Einführung in die Tragwerk-slehre", 2. Auflage, Teubner Verlag, ISBN 351915238X, Page 107

[37] Demtröder: "Experimentalphysik I, Mechanik und Wärme", Springer 1994

[38] Atlas Technical Design Report, CERN 1997

[39] M.Deveaux: "Untersuchungen zur Strahlenhärte von Monolithic Active Pixel Sensoren, Diplomarbeit", Universität Kaiserslautern 2003.

[40] W. Füssel, M.Schmidt and H. Flietner: "Radiation induced degradation of Si/SiO$_2$ structures and the nature of defects", NIM-B65(1992)238-242

[41] W. Füssel, M. Schmidt, H. Angermann, G. Mende, H. Flietner: "Defects at the Si/SiO$_2$ interfaces, their nature and behaviour in technological processes and stress", NIM-A377(1996)177-183

[42] P.Jarron et al. , "Deep submicron CMOS technologies for the LHC experiments", Nuclear Physics B (Proc. Suppl.) 78 (1999) 625-634

[43] W. Snoeys et al., "Layout techniques to enhance the radiation tolerance of standard CMOS technologies demonstrated on a pixel detector readout chip", NIM-A 439 (2000) 349-360

[44] C.J. Dale, P.W. Marshall, G.P. Summers, and E.A. Wolicki, E.A.Burke: "Displacement damage equivalent to dose in silicon devices", Appl. Phys. Lett. 54 (5), 30. Januar 1989

[45] A. Akkerman, J. Barak, M.B. Chadwick, J. Levison, M.Murat, Y. Lifshitz: "Updated NIEL calculations for estimating the damage induced by particles and $\gamma$-rays in Si and GaAs", Radiation Physics and Chemistry 62 (2001) 301-310

[46] A. Vasilescu and G.Lindstroem, "Displacement damage in Silicon, online compilation." http://sesam.desy.de/~gunnar/Si-dfuncs

[47] G.Lindström et. al, "Radiation hard silicon detectors – developments by the RD-48 (ROSE) collaboration", NIM-A 466(2001) 308-326

[48] Michael Moll: "Radiation Tolerant Sensors for Pixel detectors", talk given on the Pixel 2005 international workshop, September 5-8, Bonn, Germany. Slides available under www.physics.ox.ac.uk/LCFI/Sensors/RadDamage_ Moll_ Pixel2005.ppt

[49] El-Sayed Eid, Tony Y. Chan, Eric R. Fossum, Richard H. Tsai, Robert Spanoulo, John Deily, Wheaton B. Byers Jr., and Joseph C. Peden: "Design and Charaterization of Ionising Radiation-Tolerant CMOS APS Image Sensors up to 30 Mrd (Si) Total Dose", IEEE Transactions on Nuclear Science, Vol. 48, No. 6, December 2001.

[50] : Claus, G. Besson, A. Deptuch, G. Deveaux, M. Dulinski, W. Gaycken, G. Grandjean, D. Himmi, A. Jaaskelainen, K. Jalocha, P. Pellicioli, M. Winter, M.: "A portable system for monolithic active pixel sensors characterization", Nuclear Science Symposium Conference Record 2004 IEEE, Volume: 3, On page(s): 1512- 1516 Vol. 3

[51] : Data analysis: Yu. Gornushkin, personal communication.

[52] M.Deveaux, J. D. Berst, J. Bol, W. de Boer, M.Caccia, G.Claus, G.Deptuch, W. Dulinski, G.Gaycken, D. Granjean, L. Jungermann, J.L. Riester, M. Winter: "Charge collection properties of X-ray irradiated Monolithic Active Pixel Sensors". NIM A Volume 546, Issues 1-2 , 1 July 2005, Pages 274-280.

[53] Michal A. Szelezniak, Grzegorz W. Deptuch, Fabrice Guilloux, Sebastian Heini, and Abdelkader Himmi: "Current Mode Monolithic Active Pixel Sensor With Correlated Double Sampling for Charged Particle Detection", IEEE Sensors Journal, Vol. 7, No. 1, January 2007

[54] L.Jungermann: Space-Qualified Electronics for the AMS02 Experiment and Medical Radiation Imaging, PhD-Thesis, University Karlsruhe 2005. IEKP-KA/2005-6

[55] S. Amar-Youcef, A. Besson, M. Deveaux, M. Dorokhov, I. Fröhlich, M. Goffe, D. Granjean, F. Guilloux, S. Heini, J. Heuser, A. Himmi, Ch. Hu, K. Jaaskelainen, C. Müntz, M. Pellicioli, E. Scopelliti, A. Shabetai, J. Stroth, I. Valin und M. Winter: "Strahlenhärte von Monolitic Active Pixel Sensoren (MAPS) im Kontext des CBM-Experimentes". Poster, DPG-Tagung 2006, München.

*Bibliography*

[56] Yu. Gornushkin, G. Claus, W. de Boer, J. Bol, G. Deptuch, A. Dierlamm, W. Dulinski, D. Husson, M. Koppenhöfer, J. L. Riester and M. Winter: "Test results of monolithic active pixel sensors for charged particle tracking", NIM-A Vol. 478, Issues 1-2, Pages 311-315

[57] J. Bogerts et al: "Random Telegraph Signals in a radiation hardened CMOS APS", IEEE Transactions on nuclear science, Vol. 49, No. 1, February 2002

[58] M. Al-Turany, D. Bertini, and I. Koenig: "CBN Simulation and Analysis Framework", GSI Scientific Report 2004, FAIR-EXP-07

[59] M. Al-Turany, D. Bertini, M. Dahlinger, V. Friese, I. Koenig, and F. Uhlig: "Fair-Root/CbmRoot Simulation and Analysis framework", CBM Progress Report 2006 (http://www.gsi.de/documents/DOC-2007-Mar-137-1.pdf)

[60] I. Hrinvacova, D. Adamova, V. Berejnoi, R. Brun, F. Carminati, A. Fasso, E. Futo, A. Gheata, A. Morsch, I. Gonzalez Caballero: "The Virtual Monte Carlo", Proceedings of Computing in High Energy and Nuclear Physics, 24-28 March 2003, La Jolla, California (Project home page: http://root.cern.ch/root/vmc/VirtualMC.html)

[61] "GEANT—Detector description and simulation tool", CERN Program Library Long Write-up W5013, CERN Geneva

[62] The Geant4 Collaboration: "Geant4 - a simulation toolkit". NIM-A 506(2003) 250-303

[63] The CBMRoot Homepage: http://cbmroot.gsi.de/

[64] R.Brun and F.Rademakers,"ROOT An object oriented Data Analysis Framework" ,Nucl. Inst. Method Phys. Res.,VolA389, P81-86,1997. (Homepage: root.cern.ch)

[65] The CBM-Collaboration: "Letter of Intend for the Compressed Baryonic Matter Experiment at the Future Accelerator Facility in Darmstadt". GSI 2004, Available online: www.gsi.de/documents/DOC-2004-Jan-116-2.pdf

[66] C. Zeitnitz and T.A. Gabriel, "The GEANT-CALOR interface and benchmark calculations of ZEUS test calorimeters", NIM A 349 (1994) 106-111.

[67] P. Koczon: "Knock-on Electrons @ CBM", Talk on the CBM collaboration meeting, Oct. 6-8 2004, (http://www.gsi.de/documents/DOC-2004-Oct-182-2.pdf).

[68] D. Bertini, C. Dritsa, personal communication.

[69] S. A. Bass, M. Belkacem, M. Bleicher, M. Brandstetter, L. Bravina, C. Ernst, L. Gerland, M. Hofmann, S. Hofmann, J. Konopka, G. Mao, L. Neise, S. Soff, C. Spieles, H. Weber, L. A. Winckelmann, H. Stocker, W. Greiner, Ch. Hartnack, J. Aichelin and N. Amelin: "Microscopic Models for Ultrarelativistic Heavy Ion Collisions", Prog. Part. Nucl. Phys. 41 (1998) 225-370

[70] M. Bleicher, E. Zabrodin, C. Spieles, S.A. Bass, C. Ernst, S. Soff, L. Bravina, M. Belkacem, H. Weber, H. Stocker, W. Greiner: "Relativistic Hadron-Hadron Collisions in the Ultra-Relativistic Quantum Molecular Dynamics Model", J. Phys. G: Nucl. Part. Phys. 25 (1999) 1859-1896

[71] After Particle Data Group: "Particle Physics Booklet July 2000", Page 224

[72] P.Koczon: Geometry file "pipe180-360-26.geo", Personal communication.

[73] S. Gorbunov, I.Kisel, I.Vassiliev, Analysis of D0 meson detection in AU+AU collisions at 25 $AGeV$, CBMNote, http://www.gsi.de/documents/DOC-2005-Jun-181-1.pdf

[74] V. Friese, "Feasibility of the detection of D0 mesons in the CBM experiment", CBM-PHYS-note-2002-001, http://www.gsi.de/documents/DOC-2005-Aug-36-1.pdf

[75] P. Crochet, P. Braun-Munzinger: "Investigation of background sutraction techniques for high mass dileption physics", NIM A 484 (2002) 564-572.

230

[76] I.Vassiliev, personal communication.

[77] C. Dritsa, "Feasibility study of charmed meson detection in the CBM experiment planned at the future FAIR facility", Master Thesis, IPHC 2006.

[78] K. Borer, S. Janos, V.G. Palmieri, B. Dezillie, Z. Li, P. Collins, T.O. Niinikoski, C. Lourenc, P. Sonderegger, E. Borchi, M. Bruzzi, S. Pirollo, V. Granata, S. Pagano, S. Chapuy, Z. Dimcovski, E. Grigoriev, W. Bell, S.R.H. Devine, V. O'Shea, K. Smith, P. Berglund, W. de Boer, F. Hauler, S. Heising, L. Jungermann, L. Casagrande, V.Cindro, M.Mikuz, M. Zavartanik, C. da Via, A. Esposito, I. Konorov, S. Paul, L. Schmitt, S. Buontempo, N. D'Ambrosio, S. Pagano, G. Ruggiero, V. Eremin, E. Verbitskaya: "Charge collection effeciency of irradiated silicon detector operated at cryogenic temperatures", NIM-A 440(2000) 5-16

*Bibliography*

# Curriculum vitae

**Name:** Michael Deveaux

**Born:** July 7th 1976 in Idar-Oberstein (Germany)

**Parents:** Jürgen Deveaux, Irène Deveaux

**Nationality:** German, French

| | |
|---|---|
| 1996 | Abitur (Gymnasium Kirn) |
| 1996 - 1997 | Alternative national service (Kinder- und Jungendheit Niederwörresbach) |
| 1997 - 2003 | Study of Physics, Technical University Kaiserslautern |
| 1999 - 2003 | Integrated Franch-German studies of Physics in the |
| | Université Louis Pasteur, Strasboug |
| | Technical University Kaiserslautern |
| 2000 | "Licence de phyisque", Université Louis Pasteur |
| 2001 | "Maîtrise de physique", Université Louis Pasteur |
| 2002 - 2003 | Master thesis at the IReS, Strasbourg under the direction of: |
| | H. Schmoranzer (Technical University of Kaiserslautern) |
| | U. Goerlach (Université Louis Pasteur) |
| 2003 | Diplom der Physik (Master of physics equivalent), |
| | Technical University of Kaiserslautern |
| 2003 - 2007 | French-German Ph.D. at the |
| | Institut Pluridisciplinaire Hubert Curien |
| | Université Louis Pasteur, Strasbourg |
| | Johann-Wolfgang-Goethe Universität, Frankfurt/Main |
| | Ph.D. Advisors: |
| | Dr. Marc Winter (Institut Pluridisciplinaire Hubert Curien, Strasbourg) |
| | Prof. H. Stroebele (Johann-Wolfgang-Goethe Universität, Frankfurt/Main) |
| | Prof. J. Stroth(Johann-Wolfgang-Goethe Universität, Frankfurt/Main) |
| | Financement: |
| | Gesellschaft für Schwerionenforschung / Darmstadt (2003 - 2006) |
| | Johann-Wolfgang-Goethe Universität, Frankfurt/Main (2007) |